UC-403

LBL-28171

Lawrence Berkeley Laboratory
UNIVERSITY OF CALIFORNIA

EARTH SCIENCES DIVISION

Audio-frequency Electromagnetic Tomography for Reservoir Evaluation

Qiang Zhou
(Ph.D. Thesis)

October 1989

For Reference

Not to be taken from this room

Prepared for the U.S. Department of Energy under Contract Number DE-AC03-76SF00098.

LBL-28171
Copy 1
Bldg. 50 Library.

DISCLAIMER

This document was prepared as an account of work sponsored by the United States Government. While this document is believed to contain correct information, neither the United States Government nor any agency thereof, nor the Regents of the University of California, nor any of their employees, makes any warranty, express or implied, or assumes any legal responsibility for the accuracy, completeness, or usefulness of any information, apparatus, product, or process disclosed, or represents that its use would not infringe privately owned rights. Reference herein to any specific commercial product, process, or service by its trade name, trademark, manufacturer, or otherwise, does not necessarily constitute or imply its endorsement, recommendation, or favoring by the United States Government or any agency thereof, or the Regents of the University of California. The views and opinions of authors expressed herein do not necessarily state or reflect those of the United States Government or any agency thereof or the Regents of the University of California.

LBL-28171

Audio-Frequency Electromagnetic Tomography for Reservoir Evaluation

Qiang Zhou

(Ph.D. Thesis)

Department of Materials Science and Mineral Engineering
University of California

and

Earth Sciences Division
Lawrence Berkeley Laboratory
1 Cyclotron Road
Berkeley, California 94720

October 1989

This work was supported by the U.S. Department of Energy under Contract No. DE-AC03-76SF00098.

Audio-frequency Electromagnetic Tomography for Reservoir Evaluation

Qiang Zhou

Abstract

A tomographic inversion scheme is developed for interpreting audio-frequency electromagnetic (EM) measurements and for understanding the characteristics of the EM inverse problem. The formulation of this new approach, called EM diffusion tomography, is related to the recent developments in acoustic diffraction tomography. In the frequency domain, however, the significant mathematical difference between the acoustic and the electromagnetic problems is the background wave number which in the acoustic case is real while in the electromagnetic case is complex. By extending the acoustic image reconstruction formulation through the introduction of an inverse Laplace transform as a replacement for the inverse Fourier transform, the method can now be applied to map electrically conductive targets such as saline fluid filled fracture zones in reservoir environments. Since these conductors usually have a small conductivity-thickness product, the Born or Rytov weak scattering approximation can be applied to simplify the problem. This approach is first investigated using a model of two-dimensional (2-D) Cartesian geometry. Following this simple and useful model and using an additional far field approximation, more complex and realistic 2-D cylindrical symmetry and three-dimensional problems are solved. These last two cases are found to be identical to the 2-D Cartesian one if a geometrical correction factor is applied to the data. Therefore, the properties of the reconstructed images for all three models are similar.

The reconstructed conductivity image is found to be a band limited version of the actual conductivity distribution in the wave number domain. The inversion quality can therefore be inferred from the wave number domain coverage which is related to the source-receiver array arrangement and the background wave number or operating frequency. The cross-hole source-receiver configuration has a lower wave number domain coverage and thus a poorer space

domain resolution in the lateral direction than along the vertical. To achieve the best possible resolution in the cross-hole situation, the largest possible operating frequency should be used. For an electrically conductive medium, however, a large source frequency implies severe field attenuation and increased solution instability. On the other hand, the inverse Laplace transform of band limited data is extremely unstable even for noise free data. Thus a suitable constraint such as that of targets which are more conductive than the background (fracture zone mapping application) is extremely helpful in enhancing target resolution and solution stability. To incorporate this constraint, we use a least squares inversion algorithm for image reconstruction instead of an inverse Laplace transform.

The theoretical developments are illustrated with an extensive series of numerical experiments. These are based on a number of hypothetical geological models to illustrate the strengths and weaknesses of electromagnetic diffusion tomography in a variety of situations. In particular we find that the target attitude (the dip angle of a thin conductor) can, in general, be properly recovered. For the cross-hole source-receiver configuration, image resolution in the horizontal direction is directly related to the source operating frequency. Lateral resolution can also be enhanced by including data acquired with a single-hole source-receiver array. Finally, in all the numerical models studied the Rytov approximation is better than the Born approach. These numerical experiments prove audio-frequency EM tomography to be a valid technique for interpreting cross-hole EM observations.

In order to furnish synthetic data for the above inversion experiments, numerical modeling codes are developed using an integral equation approach to simulate the electromagnetic response of the corresponding target geometries. We start with a simple two-dimensional (2-D) Cartesian model, progress to a cylindrical symmetry model and finally treat a three dimensional thin target structure representative of fracture zones. The newly formulated codes are tested against proven numerical solutions under some extreme cases and more importantly against laboratory scale model data. They are found to be both accurate and efficient and can be used to obtain the required numerical data as well as to provide some insight to the inverse problem.

Alex Becker

Acknowledgements

I sincerely wish to express thanks to my thesis advisor Prof. Alex Becker for his support and guidance. I would also like to thank Prof. Frank Morrison for suggesting the cross-hole electromagnetic problem and Prof. Thomas Budinger for reviewing this thesis. Thanks also to Drs. K. H. Lee and N. Goldstein of Lawrence Berkeley Laboratory for helpful suggestions. I have also much benefited from discussions with Mr. Ali Tura on acoustic diffraction tomography. I am grateful to all my fellow Enginnering Geoscience students, especially Ms. Maryla Deszcz-Pan and Mr. Guimin Liu, for their help during the years at Berkeley.

Special thanks to my wife, Tao Wang, for her love and support.

Financial support for this work is provided by U.S. Department of Energy under Contract No. DE-AC03-76SF00098.

Table of Contents

Chapter 1 Introduction *1*
1.1 Electrical properties of fractured media 1
1.2 Geophysical methods for fracture zone characterization 4
1.3 Scope of research work 6
Chapter 2 Two dimensional Numerical modeling and tomographic inversion 12
2.1 Two dimensional (2-D) numerical modeling 12
2.1.1 Mathematical formulation in two-dimensions 13
2.1.2 Numerical solution 15
2.1.3 Test of accuracy 16
2.2 Electromagnetic diffusion tomography 17
2.2.1 Comparison between the EM and the acoustic problems 18
2.2.2 EM modeling versus EM inversion 19
2.2.3 The Born approximation solution 20
2.2.4 The Rytov approximation solution 22
2.2.5 Equivalence of the Born and Rytov approximations 24
2.2.6 Validity of the weak scattering approximation 24
2.3 Numerical construction of the 2-D tomographic image 25
2.3.1 The constrained least squares solution 26
2.3.2 Measure of solution quality 28
2.3.3 Image smoothing 29
2.4 Numerical examples 31
2.4.1 Model parameters for the numerical calculations 31
2.4.2 Comparison between Born and Rytov approximations 33
2.4.3 Dependence on target orientation 34
2.4.4 Dependence on operating frequency 35
2.4.5 Source and receiver array length or space coverage 36
2.4.6 Effect of random noise 36
2.5 Target resolution and wave number domain coverage 37
2.5.1 The wave numbers 38
2.5.2 The cross-hole source-receiver array 39
2.5.3 The Single hole source-receiver array 41
2.5.4 Other configurations 42
2.5.5 Image distortion due to incomplete coverage 43
Chapter 3 Tomographic inversion for a cylindrical symmetry problem 70
3.1 Formulation of the integral equation 70
3.1.1 A cylindrical symmetry model 71

3.1.2 The integral equation 71
3.2 Forward numerical modeling 73
3.2.1 Numerical modeling 73
3.2.2 Verification by physical modeling 74
3.2.3 Influence of the source-receiver array configuration 75
3.3 Inverse solution based on the weak scattering approximation 77
3.3.1 Born approximated integral equation in wave number domain 77
3.3.2 Wave number domain coverage under far field approximation 80
3.4 Tomographic inversion of synthetical data 82
3.4.1 2-D Cartesian model solution after geometric correction 82
3.4.2 Cross-hole source-receiver array configuration 84
3.4.3 Combination of Cross-hole and single-hole source-receiver data 84
Chapter 4 Modeling and tomographic inversion for 3-D thin conductors 100
4.1 The thin sheet approximation 101
4.2 Formulation and solution of the integral equations 102
4.2.1 Integral equation formulation 103
4.2.2 Numerical solution 105
4.3 Verification of the program 105
4.3.1 Numerical checks 105
4.3.2 Comparison with physical modeling 107
4.4 Source-receiver array configuration effects 107
4.4.1 Cross-hole parallel transmitter and receiver 108
4.4.2 Cross-hole fixed transmitter and moving receiver 108
4.4.3 Source and receiver in tandem 109
4.5 3-D electromagnetic tomography 110
4.5.1 Tomographic analysis under weak scattering approximation 110
4.5.2 Solution with an additional far field approximation 114
4.5.3 Numerical examples 116
Chapter 5 Conclusions and recommendations for further research 146
5.1 Conclusions 146
5.2 Recommendations for future work 148
Appendix A Seismic tomographic methods 149
A.1 Ray tomography 149
A.2 Diffraction tomography 150
Appendix B Instability of Laplace transform of band limited data 156
Appendix C Mathematical expressions related to 3-D thin conductors 158
C.1 Green's dyadic function g 158
C.2 Green's dyadic function g_s 160
C.3 Incident fields $\mathbf{E}_n$ and $\mathbf{H}_n$ 162
C.4 Green's function $\mathbf{H}_a$ and $\mathbf{H}_b$ 163
C.5 Numerical solution of the integral equations 164
References 169
Supplement: List of the developed FORTRAN codes 175

Table of illustrations

Figure 1-1-1 The electrical resistivity of natural water (Hearst and Nelson, 1985)

Figure 1-1-2 An example of a fracture zone in a petroleum reservoir (Crary et al, 1987).

Figure 1-1-3 An example of fracture zones found in crystalline rock in a waste repository (Green and Mair, 1983)

Figure 1-1-4 An example of faults and thin permeable zones in a geothermal field (Hulen, 1982; Goldstein, 1985)

Figure 2-1-1 A two dimensional (2-D) model

Figure 2-1-2 An arbitrary 2-D conductor approximated by a set of 2-D thin conductors

Figure 2-1-3 Numerical verification of the 2-D code by approximating a circular cylinder with a number of thin conductors

Figure 2-3-1 Discretization for tomographic inversion

Figure 2-3-2 An example of enhanced resolution with a constrained least squares approach

Figure 2-3-3 Image smoothing scheme

Figure 2-4-1 The two dimensional model for numerical calculation

Figure 2-4-2 Images of a dipping conductor with different reconstruction parameters

Figure 2-4-3 Standard deviation of the inversion results in Figure 2-4-2

Figure 2-4-4 Born images of a dipping conductor with different conductance

Figure 2-4-5 Rytov images of a dipping conductor with different conductance

Figure 2-4-6 Comparison of the standard deviations between the Born and Rytov methods for the $\tau = 0.1\,S$ case

Figure 2-4-7 Images of a conductor with different dip angles [Figure (b) through (d) are reconstructed from exact data while Figure (e) through (g) are from Born data]

Figure 2-4-8 Images of two parallel conductors with different dip angles

Figure 2-4-9 Images of two 60° dipping conductors with a 40m increased horizontal separation as compared to the $\beta = 60^o$ case in Figure 2-4-8

Figure 2-4-10 Images of two 30° dipping conductors under different operating frequencies

Figure 2-4-11 Images of a 45° dipping target reconstructed under different array length

Figure 2-4-12 Images of a 45° dipping target with different levels of random noise in the input data

Figure 2-5-1 Cross-hole wave number domain coverage for $|k_o^2| = 1$

Figure 2-5-2 Cross-hole wave numbers domain coverage for $|k_o^2| = 1/4$ and $1/16$

Figure 2-5-3 Wave number coverage of the model shown in Figure 2-4-1

Figure 2-5-4 Wave number domain coverage for single hole or surface source-receiver configuration

Figure 3-1-1 A cylindrical symmetry model

Figure 3-2-1 Comparison between numerical and physical modeling results for a ring shaped conductor

Figure 3-2-2 Comparison between numerical and physical modeling results for a disk shaped conductor

Figure 3-2-3 Normalized secondary magnetic field response (z-component) for a crosshole VMD source and receiver at the same depth

Figure 3-2-4 Normalized secondary magnetic field response (z-component) for a crosshole fixed VMD source and a moving receiver

Figure 3-2-5 Normalized secondary magnetic field response (z-component) for a tandem VMD source and receiver with fixed vertical separation of 10m

Figure 3-2-6 Normalized secondary magnetic field response (z-component) for a tandem VMD source and receiver with fixed vertical separation of 10m and two frequencies of 5K and 20K Hz

Figure 3-4-1 Comparison of a cylindrical symmetry model reconstructed with the 2-D Cartesian (corrected by a geometric factor) code or with the cylindrical symmetry code

Figure 3-4-2 Reconstructed images of targets with varying lateral extent

Figure 3-4-3 Reconstructed images of targets with varying vertical extent

Figure 3-4-4 Reconstructed images of targets of different conductivity

Figure 3-4-5 Reconstructed image quality as a function of frequency

Figure 3-4-6 Resolution enhancement by combining the transmitted and backscattered fields (the distance between source borehole and target is 10 meters)

Figure 3-4-7 Resolution enhancement by combining the transmitted and backscattered fields (the distance between source borehole and target is 20 meters)

Figure 4-1-1 A 3-D thin conductor model

Figure 4-3-1 Particular model tested for accuracy

Figure 4-3-2 Convergence check

Figure 4-3-3 Reciprocity check

Figure 4-3-4 Accuracy test by variable separation

Figure 4-3-5 Comparison between the new program and program PLATE

Figure 4-3-6 Comparison of physical and numerical modeling (single conductor)

Figure 4-3-7 Comparison of physical and numerical modeling (two conductors)

Figure 4-4-1 Cross-hole parallel source-receiver (one conductor)

Figure 4-4-2 Cross-hole parallel source-receiver (two conductors)

Figure 4-4-3 Cross-hole fixed source and moving receiver (one conductor)

Figure 4-4-4 Cross-hole fixed source and moving receiver (two conductors)

Figure 4-4-5 Single hole moving source and receiver (one conductor)

Figure 4-4-6 Single hole moving source and receiver (two conductors)

Figure 4-4-7 Single hole source-receiver configuration under different operating frequency

Figure 4-5-1 General three-dimensional target with multiple source and receiver boreholes

Figure 4-5-2 Three-dimensional target with only one pair of source and receiver boreholes

Figure 4-5-3 Solution for a dipping thin conductor with the 2-D method using a correction factor derived under far field approximation

Figure 4-5-4 Born approximation solution for a dipping thin conductor

Figure 4-5-5 Rytov approximation solution for a dipping thin conductor

Figure 4-5-6 Standard deviation for the Born and Rytov solutions for the proceeding example

Figure 4-5-7 Images of two horizontal conductors

Figure 4-5-8 Images of two dipping conductors

Figure 4-5-9 Images of two vertical conductors

Figure 4-5-10 Comparison between Born and Rytov approximations for a dipping conductor ($\tau = 1.0S$)

Figure 4-5-11 Comparison between Born and Rytov approximations for a dipping conductor ($\tau = 2.0S$)

Figure A-1 The configuration for cross-hole ray tomography

Figure A-2 The geometry for cross-hole diffraction tomography

Figure A-3 Fourier domain coverage in acoustic diffraction tomography

Figure C-1 The notations on one of the cells in calculating thin conductor EM response

Chapter 1
Introduction

The detection and characterization of major fracture zones, whether natural or manmade, is vital for petroleum production in fractured reservoirs. It is also of great importance for the proper storage of radioactive waste in waste repositories or for the efficient extraction of geothermal energy from geothermal reservoirs. The fracture zones or faults encountered in these applications serve as hydrological pathways along which the crude oil, geothermal energy, or radionuclides migrate.

The purpose of this research is to assess the feasibility of detection and mapping of the fracture zones with a cross-hole electromagnetic technique since these saline fluid filled zones are usually at great depth and are electrically more conductive than the host rock. But, the presence of fractures makes the inference of reservoir properties from electromagnetic measurements much more difficult than would be the case in a conventional isotropic medium. The variations in fracture characteristics, such as size, orientation and others, are so complex that the full description of a reservoir may require other complementary methods.

In this chapter, we review the electrical properties and geometrical parameters of formations which may contain major fracture zones. A survey of the available geophysical techniques and the need for new approaches is also discussed. Then mathematical models are drawn for modeling and inversion studies for the crosshole electromagnetic method.

1.1 Electrical properties of fractured media

It is well known that the electrical resistivity of reservoir rock is representative of its hydrological characteristics. Thus studies have been made, for many decades now, to determine the quantitative relationship between electrical resistivity and the porosity, saturation, or even the permeability in reservoir systems. For an isotropic medium, the most widely accepted fundamental relation between the electrical resistivity and the reservoir porosity is

Archie's empirical formula (1942). However, with the presence of large fracture zones or faults, this relationship may not hold true. Thus other geophysical methods are sought to characterize the fracture system and to provide the information required by hydrologists. Since the host rock and a fracture zone make different contributions to the electromagnetic response, they have to be discussed separately.

There are many factors affecting host rock electrical resistivity. Porosity, saturation, and solution salinity are the most important and commonly considered ones. Others are temperature, pressure, clay and mineral content, wettability, and pore geometry. Thus, a wide range of host rock conductivities can be expected. Archie's experiments (1942) show that the formation resistivity is directly related to that of the formation fluid and that the rock matrix virtually has no effect on it. Thus the electrical conductivity or the salinity of formation fluid was one of the most intensively investigated subjects. Data are available from different sources on a variety of fluid compositions while Figure 1-1-1 illustrates the range of resistivity values of natural water (Hearst and Nelson, 1985). For example, crystalline rocks may have a porosity less than 0.01 so that if the contained fluid is fresh water, one could expect a conductivity as low as $10^{-6}\,S/m$. On the other hand, the conductivity of high porosity (>30%) sandstones saturated with brine could reach up to $0.3\,S/m$. In sedimentary rocks, the typical conductivity is around 0.01 to 0.1 S/m although the variation may span orders of magnitude depending on the particular geological situation. For a geothermal reservoir or a waste repository, much lower host rock conductivities can be expected.

The effects of fracture zones on electromagnetic measurements are also determined by their geometrical parameters. These parameters fall into two categories, i.e. those of a single fracture or a group of fractures. Single fracture parameters include the fracture width, size, nature, and orientation. The multi-fracture parameters refer to their arrangement which includes their distribution and density. For a single fracture, the width or thickness usually varies from microns to millimeters. A single fracture of such a thickness is unlikely to alter the macro electrical property of the medium and borehole geophysical methods can hardly detect its presence except when it intersects the borehole. In reality, there are numerous fractures in the formation. Due to the nature of fracturing process, these fractures are usually oriented in one or a few dominant directions. Adjacent fractures with the same direction can be grouped

into a fracture zone. All these fracture zones constitute a fracture network. Their electrical characteristics are in general determined by the cumulative fracture openings in a fracture zone and the electrical conductivity of the fluid inside the fracture openings.

An example of a fractured petroleum reservoir from Crary et al. (1987) is shown in Figure 1-1-2. Two laterologs, one shallow (LLs) and the other deep (LLd), and a televiewer section are presented. Since the original formation fluid is resistive while the mud filtrate is conductive, the permeable fracture zone corresponds to a significant anomaly on the LLs and LLd logs. Its cause is confirmed by the borehole televiewer as an intensively fractured zone more than 10 meters thick. At the fracture zone, the ratio of the apparent conductivity from LLs over that from LLd is around two. Nevertheless, the logs provide little information about the fracture extent. Other case histories in fractured petroleum reservoirs are provided by Van Golf-Racht (1982) and Nelson (1985).

Examples of fracture detection problems for waste repositories can be found in Green and Mair (1983) and Olsson et al. (1987). Green and Mair (1983) investigated a typical case of fracture zone characterization. They conducted a multidisciplinary investigation of the feasibility of using crystalline rock bodies for the disposal of nuclear waste in Canada. An integrated interpretation of the surface seismic data along with selected borehole logs showed the fracture system depicted in Figure 1-1-3. The electrical conductance of the fracture zones inferred from their results is around 0.01 to 0.1 S. The thickness of the targets ranges from several meters to tens of meters. The granite host is very resistive because of low porosity (Katsube and Hume, 1987).

Numerous cases of fracture zones and faults found in geothermal fields are discussed in an extensive review by Goldstein (1985). Figure 1-1-4 is a three-dimensional geological section of a geothermal reservoir in New Mexico (Hulen, 1982; Goldstein, 1985). It shows the relationship between the various normal faults and the permeable sandstone units within the otherwise low permeability Bandolier tuffs. In general, the permeable zones have tabular shape and are fluid filled.

All these examples show that fracture zones or faults form a network of thin conductors. Because of formation fluid in the openings, they are electrically more conductive than the

background. The thickness-conductivity product of the fracture zones, however, is small (a fraction of a Siemen). The host rock can be either conductive as in a petroleum reservoir or resistive as in a geothermal field or a waste repository.

1.2 Geophysical methods for fracture zone characterization

Fracture detection and evaluation can be accomplished during various operations related to the exploration and production phases of oil field development. The reservoir hydrological system can be best described if one can define the main fracture zones or faults by means of geophysical or other investigations. Conventional surface or borehole geophysical surveys take advantage of the different physical properties associated with fracture zones. Most of the techniques are based on the distortion of electromagnetic or electrical fields by electrically conductive fracture zones or on the attenuation of acoustic energy that accompanies wave propagation across them.

In most situations, surface geophysical techniques can only provide information on fracture zones or faults at shallow depth. Of the surface geophysical methods, high resolution seismic reflection with modern imaging techniques is of great help (Mair and Green, 1981; Palmer, 1982). Electromagnetic (Adam, 1984; Vogelsang, 1987) and resistivity (Flovenz, 1984) methods are used by taking advantage of the high conductivity of fluid filled fracture zones or faults. Self potential anomalies associated with fluid flow along faults or zones of fractured rocks can also be utilized for delineating the targets (Lippmann, et al. 1984). The other available techniques are magnetic (Palmasson, 1976), magnetometric resistivity (Edwards, 1974), and gravity. It is claimed that in most cases a combination of more than one method is necessary for successful fracture characterization.

If the target depth is beyond the reach of surface methods and if a borehole is available, surface to borehole techniques can be used for fracture mapping. VSP (Vertical seismic profiling) is employed to obtain better estimates for the acoustic and elastic properties by measuring both direct and reflected P and S waves (Fehler, 1982). Daniels (1983) investigated the hole to surface resistivity method. The mise-a-la-masse method used by Jamtlid et al. (1984) was shown to be successful for the delineation of fracture zones in crystalline rock.

Subsurface methods, such as logging, coring and hydrological testing, have also been used extensively. Deep boreholes provide the chance to use a wide range of techniques for a closer view of fracture zones, particularly those intersected by the hole. Geophysical well logging and log analysis have received a great deal of attention in this regard (Suau and Gartner, 1980). Zemanek et al. (1969) introduced the borehole televiewer for fracture location. Other logging methods, such as acoustic velocity, acoustic waveform, resistivity, dipmeter, spontaneous potential, temperature, neutron, gamma, and gamma spectral have also been used. A comparison of these logging methods can be found in Paillet (1981) and Crary et al. (1987). The fracture orientation can be determined by a few devices, such as the dipmeter and the acoustic televiewer. Due to the fact that conventional well logging methods have a radius of detection of only a few meters or a few tens meters at most, little information on the fracture extension can be predicted from the well log data alone.

In order to know the geometry and location of targets not intersected by the borehole, newer geophysical techniques are being investigated. Among them, there is the cross-hole seismic method which maps anomalies in velocity distribution (Achenbach, and Viswanathan, 1980; Fehler and Pearson, 1984). Data inversion methods using cross-hole seismic ray (Peterson, 1986) or diffraction (Wu and Toksöz, 1987) tomography are available and can be applied readily. High frequency electromagnetic imaging schemes are under research. Deadrick et al (1982) used high frequency (10 MHz to 100 MHz) cross-hole electromagnetic geotomography in mapping fractures between boreholes separated by 6 to 15 meters. Ramirez and Lytle (1983) investigated alterant tomography which makes use of the changes in electromagnetic attenuation factor caused by forcing tracers into the rock mass. They performed a successful experiment in a fractured granitic rock mass with a borehole separation of 9 meters. The feasibility of such radar system for fracture mapping was also studied by Chang (1984).

Due to high attenuation at the radar frequency, however, a lower operating frequency must be used for the detection of conductive fracture zones between widely spaced holes especially where the host rock is also conductive. Thus the cross-hole audio-frequency electromagnetic method appears to of interest for characterizing conductive fracture zones. This method has been used in mineral exploration (Emerson, 1987) where the interpretation methods are similar to those used for conventional surface data. In this thesis, an analysis will be carried

out of both the modeling and the data inversion for the audio-frequency EM response of conductive targets in a reservoir environment.

1.3 Scope of research work

Three goals are set for this thesis. The first of these embraces the development of computer codes for numerical simulation of the electromagnetic response for three types of target geometries starting with a simple two-dimensional (2-D) case going on to the more complicated cylindrical symmetry model and concluding with a three dimensional thin target model of fracture zones. Next, by analogy with seismic diffraction tomography, we investigate an inversion method for the simple 2-D problem under a weak scattering assumption. Finally, in order to interpret data with cylindrical symmetry or 3-D situations for dipole source excitation, new relations are presented which, with the help of an additional far field approximation, are related to the 2-D solution.

Numerical modeling for two dimensional and cylindrically symmetrical targets usually demands much less sophistication and computer time than a general three dimensional model. However, the programs for three dimensional numerical modeling usually involve enormous computing times. Furthermore, the available programs can only be used for conventional logging applications or surface and airborne mineral exploration problems. Therefore a rapid and accurate quantitative simulation of the cross-hole EM response of conductive thin targets embedded in a conductive host rock is needed. A tabular conductor, such as the typical fracture zone or fault depicted in Figures 1-1-3 and 1-1-4, ranges from tens of meters to several hundred meters in size. They are generally thin with thickness-conductivity products of about a fraction of Siemens or more. The host rock usually has a resistivity in excess of a few tens or hundreds ohm-m. At audio-frequency, these conductors can be assumed to be thin so that only their conductance or the thickness and conductivity product is of importance (Price, 1949; Weidelt, 1981). The advantage of the thin conductor assumption is a considerable saving in computing time. In this study, numerical codes for evaluating the cross-hole electromagnetic response of multiple thin tabular conductors are developed using an integral equation approach.

Once synthetic or physical data are available, it is important to ask what one can infer from the electromagnetic response? In other words, in order to resolve the associated geological problem, the geophysical inverse solution must be considered. As computing facilities improve, more and more attempts at solving electromagnetic inverse problems appear in the literature. Oristaglio and Worthington (1980) used a damped least squares method to invert surface and borehole electromagnetic data for two dimensional electrical conductivity models. Even the more complicated three dimensional situation has now also been attacked (Eaton and Hohmann, 1988). Therefore, the focus here is not on the solution of a similar problem with a variation in the application but rather on the understanding of some of the fundamental inversion characteristics. We propose to take our lead from recent developements in acoustic tomography (Wu and Toksöz, 1987) in order to formulate a new approach to interpreting electromagnetic data. This technique which we call electromagnetic diffusion tomography attempts to form an image of the electrical conductivity of the subsurface. It is from this image that one can estimate the target parmaters such as orientation, conductance or size. Since many physical and mathematical obstacles still stand in the way of a fully automatic "inversion box" physical approximations and constraints must be used in any inversion process. Our technique is based on the Born or the Rytov weak scattering approximation which is valid under many circumstances especially when the fracture or invasion zone which are considered here have small conductance and/or a weak conductivity contrast with the host rock.

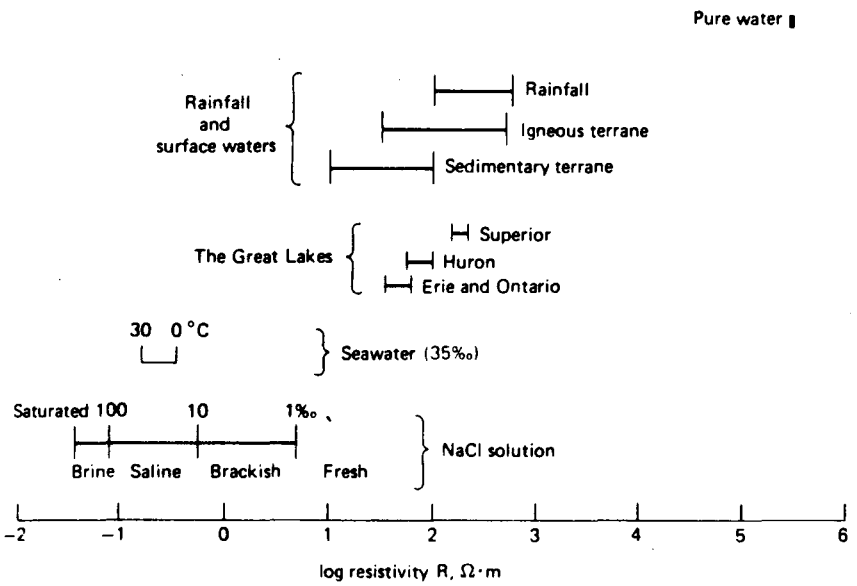

Figure 1-1-1 The electrical resistivity of natural water (Hearst and Nelson, 1985)

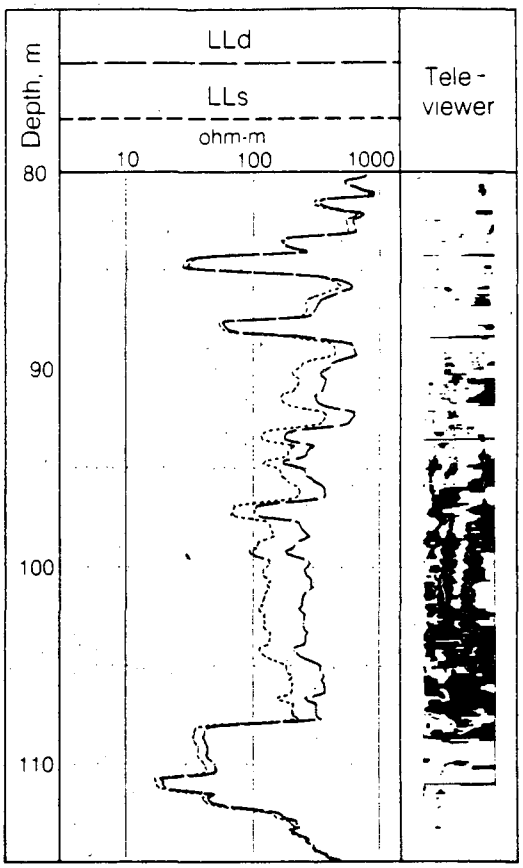

Figure 1-1-2 An example of a fracture zone in a petroleum reservoir (Crary et al, 1987).

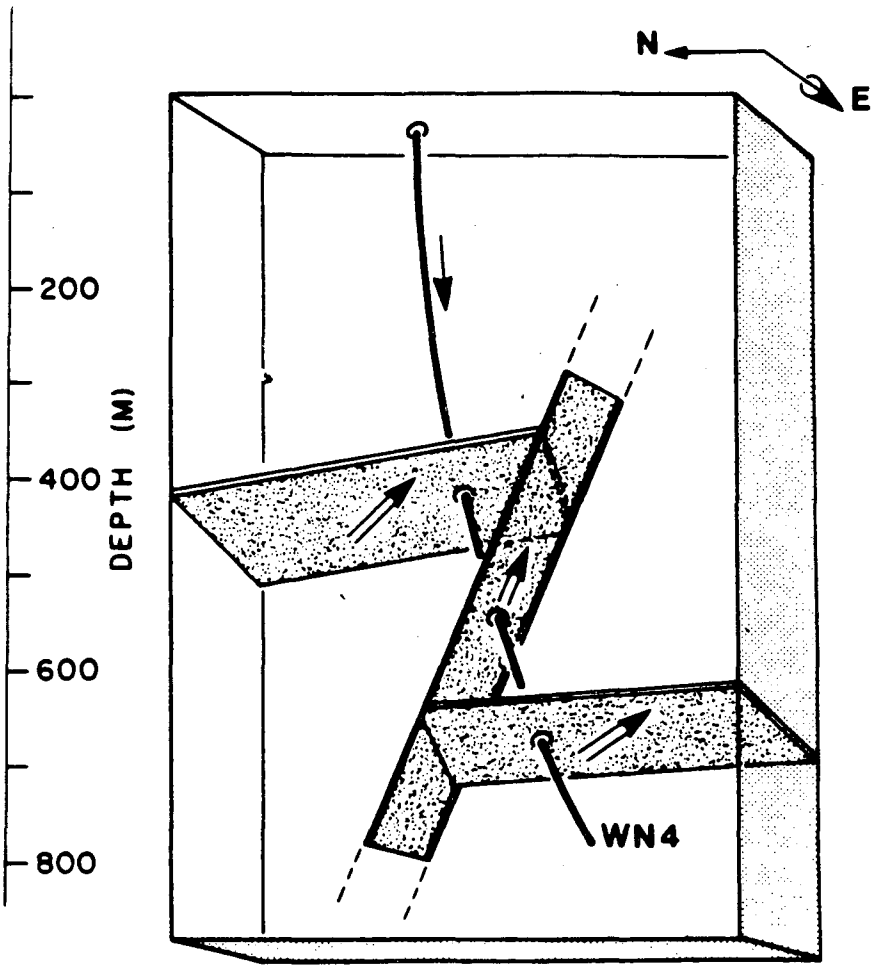

Figure 1-1-3 An example of fracture zones found in crystalline rock in a waste repository (Green and Mair, 1983)

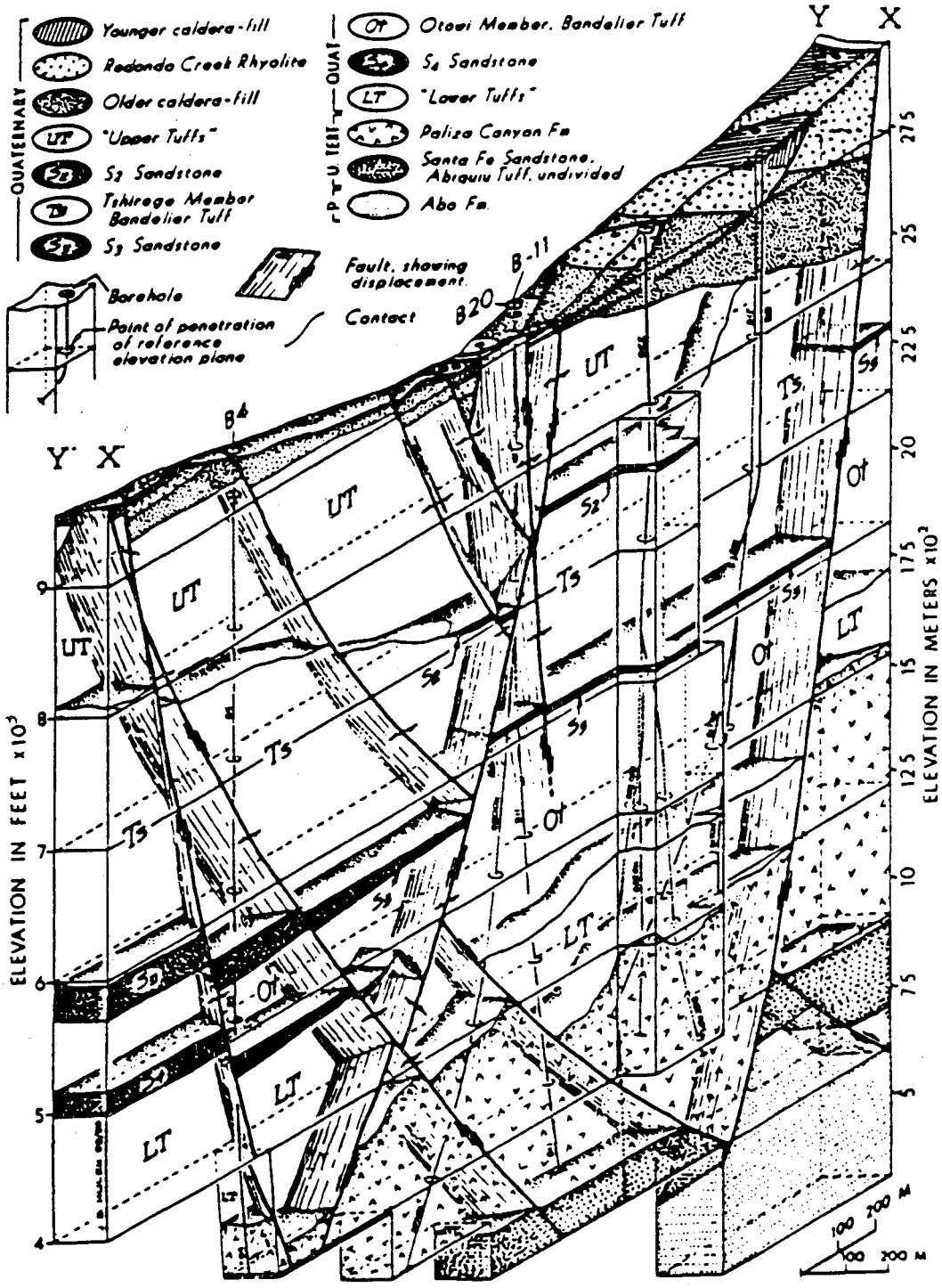

Figure 1-1-4 An example of faults and thin permeable zones in a geothermal field (Hulen, 1982; Goldstein, 1985)

Chapter 2
Two dimensional numerical modeling and tomographic inversion

There is evidence of increasingly sophisticated attempts to make geophysical inversion an essentially mathematical process, thus transferring the burden from the interpreter to the computer. These efforts presumably will make the interpretation process less of an art and more of a science (Treitel and Lines, 1988). In this context, tomography, or the formation of a cross sectional image of an object, is one of the intensively studied inversion techniques. In geophysical applications, tomographic inversion is the estimation of the subsurface geological structure from a large number of systematic physical measurements.

Because of much research and the acoustic wave nature of the problem, seismic tomography has advanced to a stage of practical or near practical application (Peterson, 1986; and Wu and Toksöz, 1987 among the others). Little, however, is known of tomographic inversion of audio-frequency electromagnetic (EM) data. Thus a comparison of the mathematical and physical aspects of the audio-frequency electromagnetic and the acoustic seismic problems is useful in developing the EM inversion techniques. In this chapter in order to elucidate the characteristics of low frequency electromagnetic or diffusion tomography we consider a simple two-dimensional case. More realistic but complicated models energized by dipole sources will be discussed in Chapters 3 and 4. Before discussing tomographic inversion, we examine the forward numerical solution of the electromagnetic problem that is needed to provide the synthetic data for use in the inversion analysis.

2.1 Two dimensional (2-D) numerical modeling

The forward modeling of the electromagnetic response of a two dimensional target is simple and straight forward. Its implementation in mineral exploration has already been investigated by Hohmann (1971) and the others. Here it is considered for a specific cross-hole configuration where the targets are thin-sheet conductors (Price, 1949). In this section, we first

establish an integral relation between the conductivity distribution and the secondary response. Then the numerical calculation of the EM response of conductive targets is implemented to generate synthetic data for the inversion studies.

2.1.1 Mathematical formulation in two-dimensions

The background medium is assumed to be conductive and homogeneous with two dimensional conductive targets embedded in it. An infinitely long electric current source lies along the strike direction of the anomalous body and is harmonic in time. The secondary electromagnetic response is calculated in Cartesian coordinates defined such that the y axis is in the strike direction and x and z are perpendicular to the strike.

Since the operating frequency is low, say below $20K\ Hz$, and the medium is conductive, the displacement current is negligible (Ward and Hohmann, p136, 1988). The Maxwell equations in frequency domain (assuming a time dependency $e^{i\omega t}$) are

$$\nabla\times\mathbf{H} = \sigma\mathbf{E} + \mathbf{J}_s\ , \tag{2-1-1a}$$

and

$$\nabla\times\mathbf{E} = -i\,\omega\mu\,\mathbf{H}\,, \tag{2-1-1b}$$

where $\mathbf{E}$ and $\mathbf{H}$ are the electric and magnetic fields respectively. $\mathbf{J}_s$ is the source current density and σ is the conductivity. μ is the magnetic permeability which is assumed to be of the free space value. The angular frequency is denoted by ω.

Since we are considering a two-dimensional case with a current line source along the strike direction of the inhomogeneity, there only exists one component of the electric field. This electric field component is in the y-direction and is denoted by E. A scalar differential equation can be derived from equation (2-1-1) for a unit current source excitation,

$$\nabla^2 E - i\,\omega\mu\sigma E = i\,\omega\mu\,\delta(\mathbf{r}-\mathbf{r}_s)\,. \tag{2-1-2}$$

$\mathbf{r}$ and $\mathbf{r}_s$ are the observation and the source positions respectively.

Next, define a scalar Green's function G which satisfies

$$\nabla^2 G - i\,\omega\mu\sigma_o G = -\delta(\mathbf{r}-\mathbf{r}')\,, \tag{2-1-3}$$

where σ_o is a constant reference conductivity. Multiplying equation (2-1-2) by G and equation (2-1-3) by E and taking their difference, we have

$$G\,(\nabla^2 E - i\,\omega\mu\sigma E) - E\,(\nabla^2 G - i\,\omega\mu\sigma G) = G\; i\,\omega\mu\,\delta(\mathbf{r}-\mathbf{r}_s) + E\;\delta(\mathbf{r}-\mathbf{r}')\,.$$

After integrating both sides of above equation over a surface that excludes the inhomogeneities, we arrive at

$$E(\mathbf{r}) = E^p(\mathbf{r}) + \iint (G\;\nabla^2 E - E\;\nabla^2 G\;)\,ds\;,$$

where E^p is the primary electric field and is given by

$$E^p(\mathbf{r}) = -i\,\omega\mu\,G(\mathbf{r},\mathbf{r}_s)\,.$$

Next, apply 2-D Green's identity to transform from a surface integral to a line integral.

$$E(\mathbf{r}) = E^p(\mathbf{r}) + \int_c (G\frac{\partial E}{\partial n} - E\frac{\partial G}{\partial n})\,dl\;, \tag{2-1-4}$$

The boundary of the inhomogeneity (Figure 2-1-1a) and the boundary at infinity ($x^2+z^2 \rightarrow \infty$) define c, the path of integration. On the infinite boundary, the line integration disappears. The direction n is normal to the boundary.

We only consider thin conductors here, which according to Price (1949) and Weidelt (1981) can be defined by their thickness and conductivity product or the conductance. To make the approximation valid the electric field on the target should have but little change across the target thickness. The extent of validity of the thin target approximation has also been studied by Joshi et al. (1988) and they concluded that the thickness should be less than half the skin depth in order to correctly approximate a steeply dipping dike by a thin plate. After defining τ to be the conductance and $\mathbf{n}'$ to be the unit vector perpendicular to the conductor (Figure 2-1-1b), **H** and **E** fields on the target satisfy (Weidelt, 1981)

$$[\,\mathbf{n}'\times\mathbf{H}\,]_-^+ = \tau\,\mathbf{E}\,. \tag{2-1-5}$$

Physically, this means that the difference of the tangential magnetic fields on two sides of the thin conductor equals the induced current in the target. In this 2-D problem, the saving in computing time with the use of thin conductor approximation is insignificant since the problem itself is very simple. However, in calculating the EM response of 3-D thin targets in Chapter

4, this simplification makes the numerical computation within reach.

Since both the electric field E and the derivative of the Green's function G are continuous across each thin conductor, the line integration around the target boundary on the second term, $E\,\frac{\partial G}{\partial n}$, of equation (2-1-4) yields zero. With the relationship given in equation (2-1-5), equation (2-1-4) can be further simplified into

$$E(\mathbf{r}) = E^p(\mathbf{r}) - i\,\omega\mu \sum_{m=1}^{ns} \int_{l_m} \tau_m\, G\, E\, dl, \tag{2-1-6}$$

where τ_m is the conductance of the $m-th$ target and ns is the number of thin conductors. The integration is carried out along each target and then is summed up for all of them.

The solution for the 2-D Green's function is the same as the field in a homogeneous medium produced by a unit current source and can be found from Ward and Hohmann (1988, p179),

$$G(\mathbf{r},\mathbf{r}') = \frac{1}{2\pi} K_o(ik_o\,|\mathbf{r}-\mathbf{r}'|), \tag{2-1-7a}$$

or from the relationship between K_o and $H_o^{(2)}$ (National Bureau of Standards, 1972, p375)

$$G(\mathbf{r},\mathbf{r}') = -\frac{i}{4} H_o^{(2)}(k_o\,|\mathbf{r}-\mathbf{r}'|), \tag{2-1-7b}$$

where K_o and $H_o^{(2)}$ are respectively the modified Bessel and Hankel functions of second kind of order zero. k_o is the background wave number ($k_o^2 = -i\,\omega\mu\sigma_o$).

2.1.2 Numerical solution

To solve the problem numerically, each thin target is assumed to be of different but constant conductance τ_m. The thin conductors are discretized into l_m small segments. On each segment, the electric field E is considered to be constant. If one lets $\mathbf{r}$ approach the point $\mathbf{r}_{i,j}$ of $j-th$ cell on the $i-th$ target, equation (2-1-6) can be written as

$$E_{i,j} = E_{i,j}^{\,p} - i\,\omega\mu \sum_{m=1}^{ns} \sum_{n=1}^{l_m} \tau_m E_{m,n} \int_{l_{m,n}} G(\mathbf{r}_{i,j},\mathbf{r})\, dl\,. \tag{2-1-8}$$

If $\mathbf{r}_{i,j}$ is not equal to $\mathbf{r}$, a Simpson integration scheme is used for evaluating the integration on

the Green's function over the $n-th$ cell of the $m-th$ thin target. Otherwise the integration is carried out analytically on the first term of the asymptotic expansion of the Green's function.

Equation (2-1-8) is a linear system of equations for the electric field. The electric field on these thin conductors is obtained by solving the resulting matrix equation. The electric response elsewhere can now be obtained by inserting the solution from equation (2-1-8) into a discretized version of equation (2-1-6).

For completeness, we also introduce here the Born approximation which tells us that in a weak scattering situation, one can approximate the total electric field inside the integral by the primary field, or $E = E^p$. With that approximation, equation (2-1-6) becomes

$$E(\mathbf{r}) = E^p(\mathbf{r}) - i\,\omega\mu \sum_{m=1}^{ns} \int_{l_m} \tau_m\, G\, E^p\, dl\,.$$

The numerical solution of the Born approximation solution can be carried out by discretizing the above equation as in equation (2-1-8).

$$E_{i,j} = E_{i,j}^p - i\,\omega\mu \sum_{m=1}^{ns} \sum_{n=1}^{l_m} \tau_m E_{m,n}^p \int_{l_{m,n}} G(\mathbf{r}_{i,j}, \mathbf{r})\, dl\,.$$

Because there is no unknowns in the right hand side, the solution of this equation is a straight forward summation and no matrix equation solution is needed.

2.1.3 Test of accuracy

The accuracy of the developed code is tested. First the convergence is checked by varying the number of cells on the target. Then reciprocity is also found to be satisfied by interchanging the source and receiver. More importantly, the accuracy of the 2-D solution for thin targets is checked against a semi-analytical solution for the EM response of a 2-D circular cylinder in a homogeneous space.

Let us consider the integral equation governing the EM response of general two dimensional conductors (Hohmann, p329, 1988; note the difference in the factor before the integration sign due to a different definition of the Green's function).

$$E(\mathbf{r}) = E^p(\mathbf{r}) - i\,\omega\mu \int_S (\sigma - \sigma_o)\, E(\mathbf{r}')\, G(\mathbf{r}, \mathbf{r}')\, ds'\,, \qquad (2\text{-}1\text{-}9)$$

where σ_o is the background reference conductivity. Since the induced current is in the strike direction, we can divide this arbitrarily shaped conductor into thin conductors (Figure 2-1-2) without cuting through the induced current. On each thin slice, the thin conductor approximation is valid. Thus the whole target can be taken as a model consisting of a number of thin conductors. Equation (2-1-9) then becomes

$$E(\mathbf{r}) = E^p(\mathbf{r}) - i\omega\mu \sum_{m=1}^{ns} \int_m [(\sigma - \sigma_o)\Delta_m] E(\mathbf{r}') G(\mathbf{r}, \mathbf{r}') dl \ , \qquad (2\text{-}1\text{-}10)$$

where Δ_m is the thickness of the $m-th$ slice. $[(\sigma - \sigma_o)\Delta_m]$ is the product of excess conductivity and thickness and can be denoted as a conductance τ_m. Thus equation (2-1-10) and the equation (2-1-6) are virtually identical and the EM response can then be evaluated using the thin conductor program. By the way, this approach of calculating the fields for a general two dimensional target is not the most efficient one. Our reason for doing so is to verify the thin-conductor numerical code by comparing its output to an analytical solution for a 2-D cylinder.

An example of the electric field anomaly due to the presence of a cylinder is given in Figure 2-1-3. A cylinder of 20 meter diameter and 0.11 S/m conductivity is divided, either horizontally or vertically, into 10 thin conductors of 0.2 Siemens each (Figure 2-1-3a). The background conductivity is 0.01 S/m. The source strength is $\frac{1}{-i\omega}$. The same response is also calculated by using a semi-analytical solution for a circular cylinder. (*Dr. K. Lee**, personal communication). Figure 2-1-3b shows the comparison which verifies the accuracy of the numerical program.

2.2 Electromagnetic diffusion tomography

The diffusive nature of audio-frequency electromagnetic field in a conductive medium usually renders conventional geophysical ray tomography invalid. It is therefore worthwhile to make a comparison between the audio-frequency electromagnetic and acoustic wave fields to find any similarities and differences. From this discussion, we can develop a conductivity inversion scheme which is similar to diffraction tomography but deals with the diffusion

* Earth Sciences, Lawrence Berkeley Laboratory, Berkeley, CA 94720.

phenomenon. In this respect, we closely follow the formulation for acoustic diffraction tomography outlined by Wu and Toksöz (1987). A Born or a Rytov approximation which implies a weak scattering situation linearizes the system and thus simplifies the problem.

2.2.1 Comparison of the EM and the acoustic problems

Physically, the audio-frequency EM field in a conductive medium is a diffusive wave and the acoustic pressure field is a propagating wave. That is if a pulse is sent through a homogeneous medium the acoustic signal is received after a time delay with the source signal shape retained. On the other hand an EM signal is smoothed out and appears instantaneously (neglecting the displacement current) at the receiver. Because of the differing nature of these physical phenomena, it is impossible to adapt a technique such as a acoustic travel time ray tomography (Appendix A.1) to audio-frequency electromagnetic problem.

Mathematically, for the two dimensional case, the electric field $E(\mathbf{r})$ in a source free region satisfies the following scalar differential equation (Hohmann, p334, 1988)

$$\nabla^2 E(\mathbf{r},t) - \mu\sigma(\mathbf{r})\frac{\partial E(\mathbf{r},t)}{\partial t} = 0. \tag{2-2-1a}$$

Here $\sigma(\mathbf{r})$ is the electrical conductivity. The acoustic wave field $u(\mathbf{r})$ in the source free region obeys the equation (Yilmaz, p507, 1987)

$$\nabla^2 u(\mathbf{r},t) - \frac{1}{C^2(\mathbf{r})}\frac{\partial^2 u(\mathbf{r},t)}{\partial^2 t} = 0, \tag{2-2-1b}$$

with $C(\mathbf{r})$ denoting the sound velocity. Thus, the mathematical difference shows up in the time derivative. The EM equation has a first order derivative in t while the seismic equation has a second order.

Define a Fourier transform pair as

$$f(k) = \int_{-\infty}^{+\infty} f(x)\, e^{-ikx}\, dx\,; \tag{2-2-2a}$$

$$f(x) = \frac{1}{2\pi}\int_{-\infty}^{+\infty} f(k)\, e^{+ikx}\, dx\,. \tag{2-2-2b}$$

If a Fourier transform with respect to time is applied to equations (2-2-1a) and (2-2-1b), they

become

$$\nabla^2 V(\mathbf{r}) + k^2(\mathbf{r}) V(\mathbf{r}) = 0. \tag{2-2-3a}$$

Here, $V(\mathbf{r}) = E(\mathbf{r})$ for the EM problem and $V(\mathbf{r}) = u(\mathbf{r})$ for seismic problem. And

$$k^2(\mathbf{r}) = \frac{\omega^2}{C^2(\mathbf{r})} \tag{2-2-3b}$$

for the seismic case, while

$$k^2(\mathbf{r}) = -i\,\omega\mu\sigma(\mathbf{r}) \tag{2-2-3c}$$

for the electromagnetic field; ω represents the angular frequency. Equation (2-2-3) shows that the EM and seismic problems are essentially the same except that the EM case involves a complex wave number while in the seismic case it is real. Physically, the complex wave number implies a severe attenuation of the electromagnetic field. On the other hand, a real wave number means no attenuation so that the acoustic signal is only weakened by geometrical spreading. Because diffraction tomography is based on equation (2-2-3a) or equation (A-3) in Appendix A.2, the acoustic inversion technique, extended to a complex propagation constant, should be applicable to audio-frequency electromagnetics.

2.2.2 EM modeling versus EM inversion

To understand the difficulties of electromagnetic inversion let use examine the integral relationship between the conductivity distribution and the secondary response. Let $E(\mathbf{r},\mathbf{r}')$, $E^p(\mathbf{r},\mathbf{r}')$, and $E^s(\mathbf{r},\mathbf{r}')$ be respectively the total, the primary, and the secondary electrical field at $\mathbf{r}$ due to a source at $\mathbf{r}'$ with

$$E(\mathbf{r},\mathbf{r}') = E^p(\mathbf{r},\mathbf{r}') + E^s(\mathbf{r},\mathbf{r}').$$

Rewrite the integral relation in equation (2-1-9)

$$E^s(\mathbf{r}_g,\mathbf{r}_s) = -\int_S k_0^2\, O(\mathbf{r}) E(\mathbf{r},\mathbf{r}_s)\, G(\mathbf{r}_g,\mathbf{r})\, dxdz\ . \tag{2-2-4a}$$

Where $\mathbf{r}_s$ and $\mathbf{r}_g$ are the source and receiver coordinates. The background wave number $k_0^2 = -i\,\omega\mu\sigma_0$ and the object function $O(\mathbf{r})$ is defined as

$$O(\mathbf{r}) = 1 - k^2(\mathbf{r})/k_0^2 = 1 - \sigma(\mathbf{r})/\sigma_0. \tag{2-2-4b}$$

Equation (2-2-4a) is a Fredholm integral equation of the second kind, which relates the object function $O(\mathbf{r})$ to the electric field anomaly. In the forward modeling problem, the object profile $O(\mathbf{r})$ is known everywhere. After discretizing the integration, equation (2-2-4a) is essentially a linear system of equations for the unknown field. Although computationally its solution may be difficult in some cases (say for a general 3-D problem) due to the inadequacy of computing power, the solution for the electric field is in principle straight forward. On the other hand, in the inverse problem to solve for $O(\mathbf{r})$, the field values of E^s or E are only known over a limited set of space points which usually lie outside the object volume of interest. In order to solve for the object function profile, one has to, in principle, solve for both the object function and the electric field inside the volume. Since the resulting equation is not linear, the inverse problem is rather complicated.

One way of simplifying the problem is to use a weak scattering assumption which approximates the electric field inside the integral with the primary field. Then, the only unknown is the object function $O(\mathbf{r})$ or the medium property $\sigma(\mathbf{r})$. Since the targets (fracture zones) under consideration are thin and their conductance is small, such an approximation should be acceptable in the cases considered here.

2.2.3 The Born approximation solution

In order to simplify the nonlinear equation (2-2-4a) for inversion purposes, a weak-scattering Born approximation,

$$E(\mathbf{r},\mathbf{r}_s) \approx E^p(\mathbf{r},\mathbf{r}_s), \tag{2-2-5}$$

is employed to approximate the field inside the object volume. For a unit (1 ampere) source strength, $E^p(\mathbf{r},\mathbf{r}_s) = -i\,\omega\mu G(\mathbf{r},\mathbf{r}_s)$ and equation (2-2-4) becomes

$$E^s(\mathbf{r}_g,\mathbf{r}_s) = i\,\omega\mu \int_S k_0^2\, O(\mathbf{r})\, G(\mathbf{r},\mathbf{r}_s)\, G(\mathbf{r}_g,\mathbf{r})\, dxdz\ . \tag{2-2-6}$$

Note that the Hankel function in (2-1-7b) can be expressed as (Morse and Feshback, p823, 1953)

$$H_o^{(2)}(k_o\,|\mathbf{r}-\mathbf{r}'|) = \frac{1}{\pi}\int_{-\infty}^{+\infty} \frac{1}{\gamma}\, e^{-i\gamma(x-x')}\, e^{ik_z(z-z')}\, dk_z\ , \tag{2-2-7a}$$

where $\gamma^2 = k_o^2 - k_z^2$. Then its Fourier transform in z direction is

$$\int_{-\infty}^{+\infty} H_o^{(2)}(k_o\,|\mathbf{r}-\mathbf{r}'|)\,e^{-ik_z z}\,dz = \frac{2}{\gamma} e^{-i\gamma(x-x')-ik_z z'}. \tag{2-2-7b}$$

Thus, for a cross hole geometry, if one takes Fourier transforms of equation (2-2-6) along the source and receiver lines, i.e. with respect to z_g and z_s respectively,

$$E^s(x_g, k_g; x_s, k_s) = \frac{-i\,\omega\mu k_o^2}{4\gamma_g\gamma_s} e^{(i\gamma_s x_s - i\gamma_g x_g)} \int_S O(\mathbf{r}) \exp[-i(\gamma_s-\gamma_g)x - i(k_s+k_g)z]\,dxdz, \tag{2-2-8}$$

where k_s and k_g are the Fourier domain wave numbers corresponding to z_s and z_g and

$$\gamma_s^2 = k_0^2 - k_s^2; \qquad \gamma_g^2 = k_0^2 - k_g^2. \tag{2-2-9}$$

x_s and x_g are the horizontal coordinates of the vertical boreholes.

These steps are similar to those taken in acoustic diffraction tomography. While the seismic case is based on the use of real wave number k_0^2, the electromagnetic problem requires its complex equivalent so that further parallelism is inappropriate. Note that, in the seismic application, γ_s and γ_g are real numbers because k_0 is real and k_s and k_g are smaller than k_0 (Appendix A.2). For the electromagnetic field in a conductive medium, k_s and k_g are also real but k_0 is now complex. Therefore, the following substitutions are made,

$$k_s + k_g = k_z\ ; \qquad i(\gamma_s - \gamma_g) = s_x. \tag{2-2-10}$$

Equation (2-2-8) now takes on the form,

$$E^s(x_g, k_g; x_s, k_s)\,\frac{4\gamma_g\gamma_s}{-i\,\omega\mu k_o^2} e^{(-i\gamma_s x_s + i\gamma_g x_g)} = \int_S O(\mathbf{r}) \exp[-s_x x - ik_z z]\,dxdz\ . \tag{2-2-11}$$

Define a Laplace transform pair (Gradshteyn and Ryzhik, p1142, 1980) as following

$$f(s) = \int_0^{\infty} f(x)\,e^{-sx}\,dx\ , \tag{2-2-12a}$$

where $f(x)$ is zero for $x < 0$, and $\int_0^{\infty} |f(x)|^2\,e^{-2\tau x}\,dx$ is finite for $\tau > \tau_0 \geq 0$.

$$f(x) = \frac{1}{2\pi i} \int_{\tau-i\infty}^{\tau+i\infty} f(s)\,e^{+sx}\,ds\ , \tag{2-2-12b}$$

for $x > 0$ and $\tau > \tau_0$.

Since the inhomogeneities are contained within a finite volume, one can always shift the origin to make $O(\mathbf{r}) = 0$ for $x < 0$ and also to ensure that $\int_0^\infty |O(x,z)|^2\, dx$ with $\tau_0 = 0$ remains finite. Thus we can say that one can solve for $O(\mathbf{r})$ by taking the inverse Fourier transform in k_z and inverse Laplace transform in s_x of the left hand side of equation (2-2-11) so that,

$$O(\mathbf{r}) = \frac{1}{(2\pi)^2 i} \int [E^s(x_g, k_g; x_s, k_s) \frac{4\gamma_g \gamma_s}{-i\,\omega\mu k_o^2} e^{(-i\gamma_s x_s + i\gamma_g x_g)}] \exp[\, s_x x + i k_z z\,]\, ds_x\, dk_z\,, \quad (2\text{-}2\text{-}13)$$

where γ_s, γ_g, k_s, and k_g can all be expressed in k_z and s_x. The seismic equivalent is equation (A-13) given by Wu and Toksöz (1987) and Soumekh (1983). Thus, in principle, the cross borehole electromagnetic inverse problem is solved.

2.2.4 The Rytov approximation solution

The Rytov approximation is another widely used weak scattering approximation for simplifying the integral equation in seismic applications (Devaney, 1981; Cheng, 1984). A similar procedure can also be applied to the electromagnetic inverse problem. As before,

$$E(\mathbf{r}, \mathbf{r}') = E^p(\mathbf{r}, \mathbf{r}') + E^s(\mathbf{r}, \mathbf{r}')\,, \quad (2\text{-}2\text{-}14)$$

where E, E^p, and E^s are respectively the total, primary, and secondary fields at $\mathbf{r}$ due to a source at $\mathbf{r}'$. Now let

$$E(\mathbf{r}, \mathbf{r}') = e^{\psi(\mathbf{r}, \mathbf{r}')}; \qquad E^p(\mathbf{r}, \mathbf{r}') = e^{\psi_p(\mathbf{r}, \mathbf{r}')}. \quad (2\text{-}2\text{-}15)$$

Substitute equation (2-2-15) into (2-2-3a). For a homogeneous medium, we have

$$(\nabla\psi_p)^2 + \nabla^2\psi_p = -k_o^2. \quad (2\text{-}2\text{-}16)$$

For an inhomogeneous medium, we have

$$(\nabla\psi)^2 + \nabla^2\psi = -k_o^2\,[\,1 - O(\mathbf{r})\,], \quad (2\text{-}2\text{-}17)$$

where k_o and $O(\mathbf{r})$ are the background wave number and the object function, which are defined in the previous section. Let

$$\psi_s = \psi - \psi_p, \tag{2-2-18}$$

and subtract equation (2-2-16) from equation (2-2-17),

$$2\nabla\psi_p \cdot \nabla\psi_s + \nabla^2\psi_s = k_o^2[O(\mathbf{r}) - (\nabla\psi_s)^2/k_o^2]. \tag{2-2-19}$$

Now if the problem satisfies the Rytov approximation, i.e.

$$\left|\frac{1}{k_o^2}(\nabla\psi_s)^2\right| \ll \left|O(\mathbf{r})\right|, \tag{2-2-20}$$

equation (2-2-19) becomes

$$2\nabla\psi_p \cdot \nabla\psi_s + \nabla^2\psi_s = k_o^2 O(\mathbf{r}). \tag{2-2-21}$$

Introduce $W(\mathbf{r},\mathbf{r}')$ so that

$$\psi_s = W(\mathbf{r},\mathbf{r}')/E^p(\mathbf{r},\mathbf{r}'), \tag{2-2-22}$$

and put this into equation (2-2-21),

$$\nabla^2 W + k_o^2 W = k_o^2 O(\mathbf{r}) E^p .$$

Therefore for a source at $\mathbf{r}_s$, or (x_s, z_s), and a measurement at $\mathbf{r}_g$, or (x_g, z_g), this equation can be solved to get,

$$W(\mathbf{r}_g,\mathbf{r}_s) = -\int_S k_o^2 O(\mathbf{r}) E^p(\mathbf{r},\mathbf{r}_s) G(\mathbf{r}_g,\mathbf{r})\, dxdz. \tag{2-2-23}$$

Together with equation (2-2-22), equation (2-2-23) can be rewritten into the following form for line source excitation.

$$G(\mathbf{r}_g,\mathbf{r}_s)\psi_s(\mathbf{r}_g,\mathbf{r}_s) = -\int_S k_o^2 O(\mathbf{r}) G(\mathbf{r},\mathbf{r}_s) G(\mathbf{r}_g,\mathbf{r})\, dxdz. \tag{2-2-24}$$

Here ψ_s can be found from the measured secondary response through equations (2-2-14), (2-2-15) and (2-2-18). Since the right hand side of equation (2-2-24) is the same as that of equation (2-2-6) and the left hand side is known from the measurements, we can find the object function $O(\mathbf{r})$ as was done in section 2.2.3 for the Born approximation approach.

2.2.5 Equivalence of Born and Rytov approximations

It can be shown that the Born and Rytov approximations are equivalent if the magnitude of the secondary phase, ψ_s, is small. From equation (2-2-14), (2-2-15), and (2-2-18), we have

$$\begin{aligned} E^s &= E - E^p \\ &= e^{\psi_p + \psi_s} - e^{\psi_p} \\ &= e^{\psi_p}\,(e^{\psi_s} - 1) \\ &\approx E^p\ \psi_s\,. \end{aligned} \tag{2-2-25}$$

Thus one would expect to have similar inversion quality when ψ_s is small. However a difference can be found in their definition. The Born approximation in equation (2-2-5) requires that the secondary field be much smaller than the incident field. This requirement, from equation (2-2-4), demands that the object function and the total extent of the object volume be small. In the Rytov approximation case, equation (2-2-20) says that the secondary phase variation, $|\nabla\psi_s|$, over one $|k_o|$ must be much smaller than the object function $|O|$. Claims that one approximation is better than the other are not few (Devaney, 1981; Slaney and Kak, 1985, among others). We will examine this further in the numerical simulations.

2.2.6 Validity of weak scattering approximation

It is difficult to evaluate the validity of the weak scattering approximation for the two dimensional EM problem. Since all waves can be decomposed into plane waves, a one dimensional problem will be considered instead. Such an approach is not new in optical applications (Keller, 1969; Oristaglio, 1985). Let a plane wave traveling in the x direction with a wave number $k = k_1$ be

$$u^i(x,k) = e^{-i\,k_1 x}.$$

If this plane wave is now in a medium with a wave number $k = k_1 + \Delta$, we have

$$u(x,k) = e^{-i\,(k_1+\Delta)x},$$

where Δ is a small perturbation in k_1. In the weak scattering simplification, $u(x,k)$ is approximated by $u^i(x,k)$. Therefore the relative error introduced is

$$\frac{u-u^i}{u} = 1-e^{ix\Delta}. \tag{2-2-26}$$

After expanding $e^{ix\Delta}$ into series, we arrive at

$$\left|\frac{u-u^i}{u}\right| = \left|1-e^{ix\Delta}\right|$$

$$= 0(|x\,\Delta|), \tag{2-2-27}$$

where '0' denotes 'the order of'. It is clear now that the product of the wave number perturbation and the traveled distance is responsible for the error introduced. The product, $x\,\Delta$, is the key to estimating the validity of the approximation. Furthermore, if one also considers the medium interface, the conductivity contrast is also a factor that affects the validity of any approximations (Oristaglio, 1985)

2.3 Numerical construction of the 2-D tomographic image

In principle, the inverse Laplace and inverse Fourier transform representation of the object function in equation (2-2-13) provides a direct way of evaluating the object function. The problem, however, is that the numerical inverse Laplace transform is extremely unstable. This is not difficult to understand because the high wave number components, which contain noise, are amplified during inversion. However, even for noise free but band limited data, the inverse Laplace transform is also unstable (This is discussed more fully in Appendix B). As pointed out by Bertero (1982), the problem of the numerical inversion of the Laplace transform is severely ill posed. In order to solve for the conductivity structure successfully, precautions have to be taken to ensure the stability of the solution. To reduce the uncertainty in the solution one needs smoothing and constrainting on the solution (Bertero et al, 1983) as required in regularization theory. Since the targets (fracture zones) under consideration are more conductive than the background in our problem, we can incorporate this constraint by discretizing the integral equation given in equation (2-2-8) and solving the resulting constrainted least squares or a quadratic programming problem. The usefulness of that explicit expression for studying the inversion quality will be expounded in a later section.

2.3.1 The constrained least squares solution

Either the wave number domain equation (2-2-8) or space domain equation (2-2-6) can be used to solve for the object function. The reason we select equation (2-2-8) is that its solution can be extended to more complicated target geometries as we will see in the later Chapters.

Integral equation (2-2-8) is first discretized over the area of interest (Figure 2-3-1),

$$E^s(x_g, k_g; x_s, k_s)\frac{4\gamma_g\gamma_s}{-i\omega\mu k_o^2} = \sum_{j=1}^{N} O_j \iint_j e^{-i[\gamma_s(x_j-x_s)+k_s z_j]}\, e^{-i[\gamma_g(x_g-x_j)+k_g z_j]}\, dx\, dz\,, \quad (2\text{-}3\text{-}1)$$

where N is the number of pixels and the integration is carried out on each pixel. O_j is the average of the object function over the $j\ th$ pixel. x_s and x_g are the horizontal coordinates of the vertical boreholes containing source and receiver. This equation can now be written as

$$p_i = \sum_{j=1}^{N} s_{ij}\, O_j\,, \quad (2\text{-}3\text{-}2)$$

with

i --- the $i\ th$ wave number combination of (k_g, k_s),

$s_{ij} = \iint_j e^{-i[\gamma_s(x_j-x_s)+k_s z_j]}\, e^{-i[\gamma_g(x_g-x_j)+k_g z_j]}\, dxdz$, the weighting for $j-th$ pixel,

p_i --- the filtered response or the left hand side of equation (2-3-1).

If we have M wave number combinations, for an N pixel image, a linear system of equations can be obtained.

$$S_1\, O = P_1\,, \quad (2\text{-}3\text{-}3a)$$

where

$S_1 = [s_{ij}]_{N\times M}$, N by M full matrix related to the geometry and wave numbers,

$O = [O_1, O_2, \cdots, O_N]^T$, N element solution vector,

$P_1 = [p_1, p_2, \cdots, p_M]^T$, M element vector of the filtered measurements.

Note that equation (2-3-3a) is complex and can be reorganized into a real system of linear equations. Let

$$S = [Re(S_1), Im(S_1)]^T\,; \qquad P = [Re(P_1), Im(P_1)]^T\,,$$

equation (2-3-3a) becomes

$$S\,O = P \tag{2-3-3b}$$

This linear system of equations relates the electrical conductivity anomaly, or the object function, with the measured secondary field. The Fourier transform used in section 2.2.3 is a plane wave decomposition. The exponential terms in s_{ij} are plane waves with $e^{-i[\gamma_s(x_j-x_s)+k_s z_j]}$ corresponding to a wave incident on the $j\,th$ pixel and $e^{-i[\gamma_g(x_g-x_j)+k_g z_j]}$ corresponding to the scattered one from the same pixel (Figure 2-3-1). The summation from j=1 to N combines the contributions from every pixel.

The linear system of equations in equation (2-3-3) is similar to that used in acoustic ray tomography (Appendix A.1). However, in ray tomography, only the pixels along a straight or curved ray path contribute to the measured response. For the EM problem, a full matrix is required to describe the process. To solve such equations, conventional methods (such as ART algorithm in Huesman et al., 1977) do not work well because the matrix equation is quite unstable. Thus constraints must be introduced to ensure the stability of the solution. In order to solve equation (2-3-3b), we minimize the l_2 norm of the misfit of a particular solution O', or minimize

$$s(O') = ||\,S\,O' - P\,||^2 \tag{2-3-4}$$

subject to constraints

$$L_i \le O'_i \le U_i\,; \qquad i = 1, 2, \cdots, N. \tag{2-3-5}$$

L_i and U_i are the lower and upper bounds respectively. For example, if we set $L_i = -\infty$ and $U_i = 0$ everywhere, we limit the object function to be smaller than zero. In other words, one then only considers the case where the conductivity anomaly is greater than the reference background. The constraints in equation (2-3-5) provide the necessary stability to the problem and, more importantly, can also enhance the target resolution greatly (Stark, 1987).

Equation (2-3-4) can be rewritten into

$$s(O') = O'^T S^T S\,O' - 2P^T S^T O' + P^T P, \tag{2-3-6}$$

where the superscript T denotes the matrix transpose. Equation (2-3-6) is in a quadratic form.

Thus equation (2-3-6) and the constraints (2-3-5) together constitute a quadratic programming problem (Gill et al., 1981; Lawson and Hanson, 1974). Several computer mathematical libraries (for example: HARWELL, NAG, LLSQ) contain subroutines for its solution. The particular one used here is VE04A from HARWELL (Hopper, 1979).

A simple example may be used to show the resolution enhancement obtained by incorporating constraints into the inversion. Figure 2-3-2 shows a one dimensional reconstruction of a δ function from band limited wave number domain data. As we know, the Fourier transform of a δ function (Figure 2-3-2a) is a constant (Figure 2-3-2b). The inverse Fourier transform of this constant of course returns the δ function. However, if we limit the band width in the spectral domain (Figure 2-3-2c), the inverse Fourier transform is a sinc function (Figure 2-3-2d) with its amplitude and width controlled by the wave number domain coverage or band width. Now, instead of the inverse Fourier transform of the band limited data we impose a constraint that the inverted result can not be negative and use a constrained least squares approach in an attempt to recover the space domain δ function from the discretized Fourier transform integral. The outcome is given in Figure 2-3-2d and the δ function is recovered. The band limited inverse Laplace transform can be implemented similarly and both the resolution and stability are enhanced greatly.

2.3.2 Measure of solution quality

When a sum of squares is minimized as in equation (2-3-4), certain statistical quantities can readily be calculated (Hopper, 1979; Menke, 1984). First, the residual variance of P can be estimated,

$$\sigma^2 = \| P - S\, O' \|^2 / (M-k), \tag{2-3-7}$$

where M is the number of linear equations and k is the number of free variables which is defined as those not on the bounds.

Another statistical measure is the variance-covariance matrix for the estimated solution O'. The least squares solution of equations (2-3-3) for the object function is (Menke, p58, 1984)

$$O' = [S^T S]^{-1} S^T P$$

where the superscript "-1" denotes the general inverse of the matrix. Assuming the data (P) are uncorrelated and all are of equal variance σ^2, we then have the variance-covariance matrix

$$[Cov\ O] = [[S^T S]^{-1} S^T]\, \sigma^2 I\, [[S^T S]^{-1} S^T]^T$$

$$= \sigma^2 [S^T S]^{-1},$$

where "I" is an indentity matrix. Then according to definition, the standard deviation of the solution is given by the square roots of the diagonal elements of this matrix. Therefore, the standard deviation of the model parameters depends on the data residual variance (σ^2), which comes from the measurement noise and the model misfitting, and the way in which error is mapped from data to model parameters ($[S^T S]^{-1}$) (Menke, 1984). If the matrix $[S^T S]$ is non-singular, its inverse is only related to the model configuration. However, this matrix is in general singular and its general inverse, ($[S^T S]^{-1}$), is incorporated by constraints. The bound variables are assumed to be known exactly and they have zero variance and covariance (Hopper, 1979).

2.3.3 Image smoothing

Inversion of electromagnetic data in general is non-unique. Also, in the presence of noise, the inversion process is very unstable. Although the constraints mentioned in the last section stablize the computed image, a smoothing step may also be necessary. Any sharp variations in the solution are usually artificial and algorithm dependent since in most cases high wave number information is absent and the noise is forced to be amplified.

Applications of smoothing can be found in EM (Constable et al., 1987) and seismic inversion problems. The use of smoothing techniques to form a better image is introduced in acoustic diffraction tomography (Slaney and Kak, 1985) by partially suppressing the high frequency wave number before reconstruction and in ray tomography (Peterson, 1986) by taking a weighted average over nearby pixels. The parameters used for these purposes are basically empirical. Here we will incorporate smoothing in the quadratic programming problem.

Let the number of divisions of the image area in the horizontal direction be K and in the vertical be L (Figure 2-3-3). Then the total number of pixels is N ($N = K\,L$). We define R_1 and R_2 to be the summations of the differences of the object function between the adjacent

pixels in either horizontal or vertical directions respectively.

$$R_1 = \sum_{l=1}^{L} \sum_{k=2}^{K} (O_{(l-1)K+k} - O_{(l-1)K+k-1})^2 \tag{2-3-8a}$$

$$= \| D_1 O \|^2.$$

$$R_2 = \sum_{k=1}^{K} \sum_{l=1}^{L-1} (O_{lK+k} - O_{(l-1)K+k})^2 \tag{2-3-8b}$$

$$= \| D_2 O \|^2,$$

where $O = [O_1, O_2, \cdots, O_N]$ and D_1 and D_2 are two $N \times N$ matrices. We now would like to minimize R_1 and R_2 in addition to the minimization of the misfit given in equation (2-3-4).

Therefore, the problem in equation (2-3-4) becomes the minimization of

$$s(O') = \| S\, O' - P \|^2 + \lambda_1 \| D_1 O' \|^2 + \lambda_2 \| D_2 O' \|^2, \tag{2-3-9}$$

where λ_1 and λ_2 are Lagrange multipliers which control the smoothness in either horizontal or vertical directions. The larger is λ_1 or λ_2, the smoother is the resulting image. If both λ_1 and λ_2 are zero, equation (2-3-9) reduces to equation (2-3-4). Equation (2-3-9) can now be expanded into

$$s(O') = O'^T (S^T S + \lambda_1 D_1^T D_1 + \lambda_2 D_2^T D_2) O' - 2P^T S^T O' + P^T P\,. \tag{2-3-10}$$

The matrix $D_1^T D_1$ is given by

$$D_1{}^T D_1 = \begin{bmatrix} H_1 & 0 & 0 & \cdots & 0 \\ 0 & H_1 & 0 & \cdots & 0 \\ 0 & 0 & H_1 & \cdots & 0 \\ & & & \cdots & \\ 0 & 0 & 0 & \cdots & H_1 \end{bmatrix}_{L \times L}, \tag{2-3-11a}$$

with

$$H_1 = \begin{bmatrix} 1 & -1 & 0 & \cdots & 0 \\ -1 & 2 & -1 & \cdots & 0 \\ 0 & -1 & 2 & \cdots & 0 \\ & & & \cdots & \\ 0 & 0 & 0 & \cdots & 1 \end{bmatrix}_{K \times K}. \tag{2-3-11b}$$

The matrix $D_2^T D_2$ is defined as

$$D_2{}^T D_2 = \begin{bmatrix} I & -I & 0 & \cdots & 0 \\ -I & 2I & -I & \cdots & 0 \\ 0 & -I & 2I & \cdots & 0 \\ & & & \cdots & \\ 0 & 0 & 0 & \cdots & I \end{bmatrix}_{L\times L} , \tag{2-3-12a}$$

with

$$I = \begin{bmatrix} 1 & 0 & 0 & \cdots & 0 \\ 0 & 1 & 0 & \cdots & 0 \\ 0 & 0 & 1 & \cdots & 0 \\ & & & \cdots & \\ 0 & 0 & 0 & \cdots & 1 \end{bmatrix}_{K\times K} . \tag{2-3-12b}$$

The problem now becomes the minimization of equation (2-3-10) subject to the constraints given by equation (2-3-5).

2.4 Numerical examples

A series of numerical calculations and tests are now conducted to find the limits of the validity and the characteristics of the inversion method outlined in the previous chapter. A comparison between the Born and Rytov inversion approaches and their limitations will be made. The effects of the individual survey parameters such as operating frequency, source or receiver array length, target conductance and attitude will also be discussed. The exact or Born approximated electromagnetic responses used in the reconstructions are generated numerically with the two dimensional modeling code described in section 2.1.

2.4.1 Model parameters for the numerical calculations

The target used in the following examples is two dimensional and is located in a homogeneous conductive background medium (Figure 2-4-1). An infinitely long harmonic electrical current source is placed along the target strike direction. The secondary electrical response is measured. One or two thin conductors are employed in the calculations and each has a thickness-conductivity product of 0.1 S. The target dip length is 80 meters. The cross-hole experiment is simulated for a borehole separation of 100 meters and source or receiver array length of 310 meters. 32 source and 32 receiver positions of equal separation are used to produce all the possible crosshole source-receiver combinations. An image area of 100 meters by 160 meters, which is located in the central part of the source or receiver line, is divided into 10

by 32 pixels. The background medium has a conductivity, σ_o, of $0.01\,S/m$ and an operating frequency of $20K\,Hz$ is used. All these parameters will be kept constant unless otherwise specified in any particular example.

As for the selection of the constraint parameters involved in the inversion, a test run is provided for the purpose. Figure 2-4-2a is a model for a thin conductor dipping at 45°. The object function O_i $(= 1-\sigma/\sigma_o)$ of the $i\ th$ pixel is made to satisfy $L_i < O_i < U_i$ as described in section 2.4.1. The solution for the object function in Figure 2-4-2b is constrained to meet $U_i = 0$ and $L_i = -\infty$ for $i = 1, 2, \cdots, N$ (cf. equation (2-3-5)). These constraints mean that the inhomogeneity is more conductive than the background. This is reasonable in situations where fluid filled fracture exist. The condition imposed on U_i is indispensable for resolution and stability purposes. Although the thin target can be seen in the image fairly well, the outcome can be improved further by additional constraints or smoothing. Since we are considering a weak scattering situation, the contrast between the anomalous body and the background should be reasonably small. If one imposes the condition on the object function that $L_i = -1.0$ for all i, the resulting image is shown in Figure 2-4-2c. Or if one does not want to set any limit on L_i, and instead, uses the smoothing technique discussed in section 2.4.3, the outcome is shown in Figure 2-4-2d. In this example the smoothing parameters λ_1 and λ_2, which are defined in section 2.4.3, are both set equal to 0.03. In all the following analysis in this chapter, we will use the smoothing parameter $\lambda_1 = \lambda_2 = 0.03$ and will leave L_i to be $-\infty$.

Born approximated data are also used to make sure that we are not pushing the limit of Born reconstruction too far. Another image (Figure 2-4-2e) is calculated for the same model parameters as Figure 2-4-2d except that the forward modeling also uses the Born approximation. It is found visually that the quality of this image is about the same as that of Figure 2-4-2d.

Figure 2-4-3 shows the standard deviation of the inversion results shown in Figure 2-4-2. When no smoothing is used and $L_i = -\infty$, the standard deviation (Figure 2-4-3a) is large and the residual variance is equal to 0.201. If constraint on L_i is set to -1.0, a much smaller standard deviation is obtained (Figure 2-4-3b) while the residual variance is about the same. The case with smoothing provides better reliability even if there is no limit on L_i (Figure 2-4-3c)

although with a little bit higher residual variance of 0.227. For Born approximated input data, the standard deviation of the solution is given in Figure 2-4-3d and its residual variance (0.017) is the smallest because the Born inversion model fits the Born modeling data best.

2.4.2 Comparison between the Born and Rytov approximations

In section 2.2 of the last chapter, we have discussed the limitation of weak scattering approximation by examing a simplified analytic case of a plane wave propagating in a nonuniform medium. Since any actual situation is more complex, numerical tests are necessary to compare the images of a thin sheet target of variable conductance reconstructed under the Born or Rytov approximation.

By using the model of Figure 2-4-4a, we calculate the Born reconstruction image for conductance values, τ, of 0.1, 0.2, and 0.4 S respectively. The $\tau = 0.1$ case (Figure 2-4-4b) has already been shown in Figure 2-4-2d. Figure 2-4-4c and 2-4-4d are for 0.2 and 0.4 S conductances respectively. These images are a good representation of the original model except that the $\tau = 0.4\,S$ case defines the thin conductor less accurately. The images reconstructed under Rytov approximation for the same model target conductances are provided in Figure 2-4-5b through Figure 2-4-5d.

It is observed that when the target conductance is small, say $\tau = 0.1S$, the images obtained using either the Born (Figure 2-4-4b) or the Rytov (Figure 2-4-5b) approximations look about the same. With the increase in τ, it is apparent that use of the Rytov approximation (Figure 2-4-5c,d) results in a better reconstruction. The less accurate images in Figure 2-4-4c,d are caused by the invalidity of Born approximation when the target conductance is large. Any further increase in conductance does not yield reasonable results for either Born or Rytov solutions.

The statistical analysis of the standard deviation for the $\tau = 0.1$ case is given in Figure 2-4-6. The Rytov approach has smaller standard deviation than the Born method. For comparison, the residual variance for these two methods is listed in the following table.

Table 2-4-1 Residual variance			
	$\tau = 0.1S$	$\tau = 0.2S$	$\tau = 0.4S$
Born	0.277	2.22	15.6
Rytov	0.108	1.20	9.97

The Rytov approach has a smaller residual variance and is thus better than its Born equivalent.

Since the conductance used in the above examples is 0.1, 0.2, and $0.4S$ and the pixel size in horizontal direction is 10 meters, the anomalous conductivity is approximately 0.02 to 0.05 S/m compared to a background conductivity of 0.01 S/m. Thus the contrast we are talking about is from 2:1 to 5:1. The reason why such a contrast can be handled is that the target is thin. As discussed in section 2.2, the image quality is in general related to both the target size and conductivity. The constraints in the quadratic programming algorithm (section 2.3.1) are also responsible for the enhanced image sharpness.

2.4.3 Dependence on target orientation

The model (Figure 2-4-7a) considered here is the same as the general model described in section 2.4.1 except that the dip angle, β, has values of 0° and 90° in addition to the $\beta = 45^o$ case considered above. The horizontal thin conductor (Figure 2-4-7b) is resolved quite well whereas the vertical one (Figure 2-4-7d) is smeared out in the horizontal direction. The blurring phenomenon is less pronounced for a target with a small dip angle since the smearing effect is approximately in the dip direction. However, when the dip angle is large, say $\beta = 90^o$, this effect deteriorates the reconstructed image. This phenomenon associated with the cross-hole methods was observed by Wu and Xu (1979) in describing their holographic image reconstruction of electromagnetic data collected from physical modeling experiments.

To show that the effect is not caused by the weak scattering Born approximation, examples using Born approximated forward modeling data are provided. Figure 2-4-7e, f, and g are the images corresponding to the target dip angle $\beta = 0^o$, 45°, and 90° respectively. Compared to their corresponding images generated from exact data in Figure 2-4-7b through Figure 2-4-

7d, they are again of the similar quality. Thus the poor resolution in the horizontal direction is not caused by the weak scattering approximation but rather by the physical limitation of the low frequency electromagnetic method using the cross-hole source-receiver configuration.

Two thin conductors are used next to study the target resolution, in the horizontal and vertical directions, in a cross-hole situation. The two targets are parallel to each other and are 40 meters apart in the vertical direction. The dip angle starts at 0° (Figure 2-4-8a) then increases to 30° (Figure 2-4-8b), 45° (Figure 2-4-8c), and 60° (Figure 2-4-8d). Both the 0° and 30° cases provide very good estimates and resolution of the thin conductors. However, as the dip angle increases further to 45° and 60°, the resolution in the horizontally shielded area becomes very poor.

We now separate the two thin conductors by an additional 40 meters in the horizontal direction for the $\beta = 60^o$ case. Figure 2-4-9b is Born approximation image and Figure 2-4-9c is that obtained with Rytov approximation. Both images are fairly good, although the Rytov approach results in a better picture. For reference, a Born inversion of the data generated from Born approximated modeling code is also provided in Figure 2-4-9d. Its quality is close to that of the Rytov inversion result (Figure 2-4-9c) of the exact synthetic data. The resolution in the horizontal direction is better than that in the vertical. By the way, the comparison between Figure 2-4-9b and Figure 2-4-9c is another example showing that the Rytov approximation is superior to the Born one.

2.4.4 Dependence on operating frequency

The model to be discussed is the same as that of Figure 2-4-8b which was evaluated for an operating frequency of $20K\,Hz$ and is replotted in Figure 2-4-10b. As we have seen already the two targets with 30° dip angle are resolved quite well. For a $10K\,Hz$ operating frequency, the reconstructed picture is presented in Figure 2-4-10c. Although the quality is not as good as that shown in Figure 2-4-10b, the two conductive zones are still distinguishable. If the frequency is further reduced to $5K\,Hz$, the image (Figure 2-4-10d) does not represent the original model any more. Thus, wherever possible, a high operating frequency should be utilized. Because of the severe attenuation of the electromagnetic field, there is always a trade-off

between resolution and stability in selecting a suitable operating frequency. In the practical sense, a high frequency signal is usually weak and may be difficult to record.

2.4.5 Source and receiver array length or space coverage

The 100 by 160 meter image area only covers the central half of the 100 by 310 meter area covered by the source and receiver arrays which are 310 meters long each. If this length is reduced, the image quality will be deteriorated accordingly. Because of the diffusive nature of the low frequency electromagnetic field in a conductive medium, the EM field varies slowly over a large space. It is thus expected that the EM case requires a larger array coverage than the corresponding seismic application. Therefore the effect of the source and receiver array length should be investigated.

Figure 2-4-11a shows the model for this study. The image for 310 meter array length (Figure 2-4-3d or Figure 2-4-11b) is basically the same as that reconstructed from an array length of 248 meters and source (or receiver) interval of 8 meters (Figure 2-4-11c). If the array length is further decreased to 186 meters and the source or receiver spacing to 6 meters (Figure 2-4-11d), the resulting picture quality is somewhat reduced although there is no difficulty in defining the conductive target. A worse image is found for the 155 meter array length (Figure 2-4-11e) although the position and dip angle are still discernible. One remedy for overcoming the insufficient space coverage is to extrapolate the measurements by taking advantage of the smooth field variation.

2.4.6 Effect of random noise

Since in the inversion process we constrain the background to be less conductive than the anomalous conductors, the inversion result is relatively stable and not overly sensitive to random noise. This matter can be investigated by adding a randomly generated number to the electrical response so as to simulate random noise. The root mean square of the random number is scaled to be certain percentage of the maximum response with randomly selected negative or positive signs. The average of the random numbers is zero. For the general model, with no noise added, the image of a dipping target (Figure 2-4-12b) is the same as

Figure 2-4-3d. As one increases the percentage of noise to ten (Figure 2-4-12c) or twenty (Figure 2-4-12d) percent, the dipping thin target is still recognizable although some deterioration is obvious. Therefore, despite the non-uniqueness of the electromagnetic inversion result, it is still meaningful if suitable constraints or stability measures are taken.

2.5 Target resolution and wave number domain coverage

In electromagnetic exploration, the detectability of a target has already been investigated to some extent (Fitterman, 1989; McCracken, et. al., 1986a,b). Fitterman (1989) studied the detectability levels for the central induction transient sounding. He pointed out two reasons why even parameters of a layered model may not be resolvable. One is equivalence, which refers to the measured response of two different models being indistinguishable within the constraints of measurement noise over the entire time range of the sounding. The other is that the measurements are not made over a time range where a difference in response occurs. Here, it is found that the source-receiver array arrangement is another important key factor in resolving geological features. From the tomographic point of view, these problems can be analyzed under the weak scattering approximation.

There are two major sources of inaccuracy which limit the quality of the reconstructed images. One of these arises from the limitations of Born or Rytov approximation in the formulation. Its effect can be overcome with the development of a more efficient algorithm and access to a more powerful computing facility. The other is due to different source-receiver array configurations and the operating frequency which is going to be discussed. The latter is related to the physical process itself.

The explicit representation of the object function by equation (2-2-13) allows the convenience of studying the system behavior as is done in diffraction tomography (Wu and Toksöz, 1987; Devaney, 1984). The wave number domain coverage of the object function for different source-receiver arrangements will now be discussed to clarify the demonstrated limitations of the inverted conductivity distribution.

According to equation (2-2-13), if every point in the wave number domain (s_x, k_z) is known the object function can be determined exactly and the inversion yields a unique

solution. However, this is not possible for several reasons. The first of these is that the source and receiver positions are discrete and thus we can only have discrete samples of the object function in its transform domain. The second reason is that the maximum coverage of the object function in the wave number domain is determined by the background wave number corresponding to the frequency used and by the maximum Fourier domain wave numbers k_s and k_g. Another more important fact is that different array configurations result in distinctive patterns of wave number domain coverage.

2.5.1 The wave numbers

For a source array length D_s and a constant source interval Δ_s, the corresponding maximum Fourier domain wave number k_s is π/Δ_s and the wave number increment is $2\pi/D_s$. Thus k_s has values given below,

$$k_s = 0, \pm 1\cdot(2\pi/D_s), \pm 2\cdot(2\pi/D_s), \cdots, \pm \pi/\Delta_s. \tag{2-5-1a}$$

Similarly, for receiver array length D_g and constant sampling interval Δ_g, k_g takes the following values

$$k_g = 0, \pm 1\cdot(2\pi/D_g), \pm 2\cdot(2\pi/D_g), \cdots, \pm \pi/\Delta_g. \tag{2-5-1b}$$

The variables γ_s and γ_g in equation (2-2-13) are defined by equation (2-2-9) and are rewritten here

$$\gamma_s = \sqrt{k_o^2 - k_s^2}; \qquad \gamma_g = \sqrt{k_o^2 - k_g^2}. \tag{2-5-1c}$$

For the convenience in constructing the wave number domain coverage illustrations shown in this section, the maximum k_s or k_g is scaled to unit value, i.e. k_s or k_g varies between -1 and 1.

In order to take advantage of the inverse Fourier transform representation of the object function, $|k_s|$ and $|k_g|$ in the acoustic problem must be smaller than k_o, which means that the evanescent waves are negligible. The electromagnetic problem is not restricted by the background wave number k_o because of the introduction of the complex Laplace wave number s_x and $|k_o|$ can either be smaller or larger than k_s or k_g. Nevertheless, from a practical point of view $|k_o|$ should be smaller than $|k_g|$ or $|k_s|$ because a large k_o implies a severe attenuation of

the EM field in a conductive medium.

Before going into the wave number domain coverage problem for any particular array configuration, let us look at the Laplace or Fourier transform definition. For a real function f(x), the following relationships for the Laplace or Fourier transform can be derived. From the Laplace transform pair defined in equation (2-2-12),

$$f(s^*) = f^*(s), \tag{2-5-2a}$$

which says when $f(s)$ at any point s is known, its value at the complex conjugate point s^* can also be obtained by taking the complex conjugate of $f(s)$. In the same way, from equation (2-2-2a) for the Fourier transform, we have

$$f(-k) = f^*(k), \tag{2-5-2b}$$

which tells us that if the function at k is given, its value at $-k$ is then available.

2.5.2 The cross hole source-receiver array

The first case to be discussed is the cross hole configuration with source and receiver in separate holes and all possible source-receiver combinations. Rewrite equation (2-2-10)

$$k_z = k_s + k_g \; ; \qquad s_x = i(\gamma_s - \gamma_g). \tag{2-5-3}$$

First, let $|k_o^2|$ be of unit value. If we fix k_g, say $k_g = 1.0$, and vary k_s according to the value given in equation (2-5-1b) and calculate γ_s and γ_g with equation (2-5-1c), we know from equation (2-5-3) that k_z and s_x move along an arc (Figure 2-5-1a). The horizontal axis in the figure is either the real or the imaginary part of the Laplace domain wave number s_x and the vertical axis is the Fourier domain wave number k_z. Then another k_g is selected and the same procedure is repeated. Finally these arcs make up the shaded area within which the object function in wave-number domain is covered (Figure 2-5-1b). The maximum s_x and k_z in this example are along the arcs defined by $k_s = \pm 1.0$ or by $k_g = \pm 1.0$ and are shown in Figure 2-5-1a.

It also should be mentioned that the real and imaginary components of s_x are paired and the wave number domain coverage is in three dimensional (k_z and the real and imaginary parts of s_x). The coverage in Figure 2-5-1b is its 2-D projection. If we take a slice, say along $k_z = 1$, of Figure 2-5-1b, the resulting relation between $Re(s_x)$ and $Im(s_x)$ is plotted in Figure

2-5-1c, where only $Re(s_x)$ is shown and the relation in equation (2-5-2) is also applied. The inverse Laplace transform should be carried out along such an curved path.

Figures 2-5-2a and 2-5-2b show the wave number domain coverage for the same cross-hole source-receiver configuration with $|k_o^2|$ now taking the values of 1/4, or 1/16 respectively. As the background wave-number $|k_o|$ becomes smaller, one obtains less coverage in the $Im(s_x)$ direction. The real component of s_x becomes larger as $|k_o|$ gets smaller, which says more information about the object function in x direction is smeared out. Therefore one ought to choose the highest possible operating frequency for the cross-hole source-receiver configuration.

The wave number domain coverage of the object function for the numerical model in section 2.4 can now be evaluated. For the parameters specified for that particular model the results are shown in Figure 2-5-3. It can be seen on the $(k_z\ ,\ Im(s_x))$ plane that the coverage in the x-direction is less than one tenth of its extent in the z-direction. The maximum horizontal wave number corresponds to a space length of more than 110 meters. Due to the severe attenuation associated with higher operating frequency or background wave number, little can be done to further increase the lateral or x-direction coverage. In seismic applications, it is well known that features less than 1/4 wave length usually can not be resolved. If this is also true in EM, one should not expect any horizontal resolution better than 30 meters for this particular example without any prior knowledge of the target. Poor coverage and severe wave attenuation contribute to the need for suitable constraints which enhance the image resolution and stablize the inverse problem.

As indicated in Appendix A for acoustic diffraction tomography, poor resolution in the lateral (x) direction is expected for this cross-hole configuration because of the poor coverage in the horizontal wave number. Furthermore here we have the presence of attenuation due to the complex Laplace domain wave number. Thus poor resolution should be expected in the reconstruction since, physically, the high wave number information of the object function is smeared out along x direction. Mathematically, one has to sacrifice resolution for solution stability in the inversion. Nevertheless, the attenuation itself also contains information on the electrical conductivity of the medium. One simple example is from the comparison between

the conventional acoustic and electromagnetic well logs. A time harmonic sonic wave and a source-receiver pair of fixed separation in a homogeneous medium can not yield enough information to determine the acoustic velocity. Instead, the sonic log must use a pulse signal. On the other hand a time harmonic electromagnetic tool can indicate the electrical conductivity of the medium because of the attenuation in the field amplitude.

It should be pointed out that the expected corresponding seismic image quality is better than that of the EM image because of the fundamental difference in the physical properties involved. Theoretically, in the seismic situation one can increase the resolution by raising the operating frequency and the sampling density. In the electromagnetic application the image quality is limited because of the severe attenuation at high operating frequency. Increased sampling density, in the crosshole EM case for example, improves the vertical resolution somewhat but is of little help in the horizontal direction.

2.5.3 The single hole source-receiver array

With source and receiver in a single borehole and with all the source-receiver combinations, the relation between (s_x, k_z) and (k_s, k_g) is as following,

$$k_z = k_s + k_g \; ; \qquad s_x = i(\gamma_s + \gamma_g) . \tag{2-5-4}$$

The single hole case is different from cross-hole configuration in that the backscattered field is measured instead of the transmitted one. Thus a positive sign before γ_g in equation (2-5-4) takes the place of the negative one in that of equation (2-5-3) to account for the direction of the energy flow.

By varying (k_s, k_g) according to equation (2-5-1), the Laplace-Fourier domain (s_x, k_z) coverage can again be calculated. Figure 2-5-4a shows the coverage for a single frequency with $|k_o^2|$ to be of unit value. Figure 2-5-4b and Figure 2-5-4c show the coverage when $|k_o^2|$ equals 1/4 or 1/16. More coverage can be achieved by employing multiple operating frequencies as it can be seen when one overlaps the coverages in Figure 2-5-4a through Figure 2-5-4c.

2.5.4 Other configurations

Although the source-receiver configurations examined in this section do not directly relate to the theme of this thesis, they are interesting byproducts of the wave number domain coverage analysis. Thus the surface array configuration is similar to the single hole geometry with a 90 degree rotation of the x-z coordinate frame. Therefore for surface multiple source-receiver combination the coverage can also be studied with

$$k_x = k_s + k_g \; ; \qquad s_z = i(\gamma_s + \gamma_g) . \tag{2-5-5}$$

The above expressions are the same as those in equation (2-5-4) except for the switch in x and z.

A special case of a surface array arrangement is the TE mode of the magnetotelluric (MT) method where there is only a single plane wave incident in the vertical direction. Therefore in deriving the object function in section 2.2.3, a plane wave primary field ($e^{-ik_o z}$) is used and it is not necessary to take a Fourier transform over the source line in deriving the explicit expression for the object function. Thus, for a vertically incident wave, we have

$$k_s = 0 . \tag{2-5-6a}$$

If we measure the field over an entire profile and take the Fourier transform along receiver line we have,

$$k_g = 0, \pm 1 \cdot (2\pi/D_g), \pm 2 \cdot (2\pi/D_g), \cdots, \pm \pi/\Delta_g . \tag{2-5-6b}$$

Thus equation (2-5-5) becomes

$$k_x = k_g \; ; \qquad s_z = i(k_o + \gamma_g) . \tag{2-5-7}$$

Another source-receiver configuration of interest is the surface to borehole combination with the sources on the surface along x direction and receivers in a vertical borehole (z direction). By similar procedures as the above cases, the coverage can also be derived but one has to introduce complex Laplace wave numbers s_x and s_z so that

$$s_z = i(k_g + \gamma_s) ; \qquad s_x = i(k_s + \gamma_g) . \tag{2-5-8}$$

Thus inverse Laplace transforms in both x and z directions are needed now.

2.3.5 Image distortion due to incomplete coverage

As discussed above, wave number domain coverage provides guidelines for determining data interpretation quality and for choosing a suitable array for any specific application. If every point in the wave number domain is covered, the object function can be determined exactly. Unfortunately, the above discussion indicates that each different source-receiver array covers a distinct and finite area which is also frequency dependent. Define a function $A(s_x, k_z)$ for the cross-hole situation such that

$$A(s_x, k_z) = \begin{cases} 1 & point\ (s_x, k_z)\ covered \\ 0 & point\ (s_x, k_z)\ not\ covered\ . \end{cases} \tag{2-5-9}$$

If the exact object spectrum is $O(s_x, k_z)$, the spectrum obtained from measurements is

$$O'(s_x, k_z) = O(s_x, k_z) \cdot A(s_x, k_z). \tag{2-5-10}$$

Assuming that the exact image is $O(x,z)$ and the inverted image is $O'(x,z)$, we have according to the convolution theorems for Laplace and Fourier transforms

$$O'(x, z) = O(x, z) * A(x, z), \tag{2-5-11}$$

where $A(x, z)$ is the space domain expression of the covered wave number domain, which can be derived by performing inverse Laplace and Fourier transforms on $A(s_x, k_z)$ for each specific source-receiver array. The sign "*" denotes two dimensional convolution of $O(x, z)$ and $A(x, z)$.

Note that the distortion due to the incomplete wave number domain coverage associated with particular source-receiver array and operating frequency can only make the reconstructed image blurred. The target characteristics, such as the dip angle of the thin conductors in our models, are resolved well because the distortion does not involve any rotation or shift in the wave number domain.

The outcomes from the above theoretical analysis are exactly what we have observed from the numerical experiments in section 2.4. The inversion quality depends on the source-receiver array configuration and the background wave number or the operating frequency. For a crosshole source-receiver array configuration, one should always choose the highest possible

operating frequency. Since as the frequency or the background wavenumber becomes smaller, the wave number domain coverage of the object function in the $Im(s_x)$ direction decreases. The reduced coverage makes the resolution decrease. For this same source-receiver configuration, it is also found that the image resolution is much poorer in the horizontal direction than in the vertical. Smoothing and constraints are extremely helpful in enhancing the target resolution and stablizing the solution.

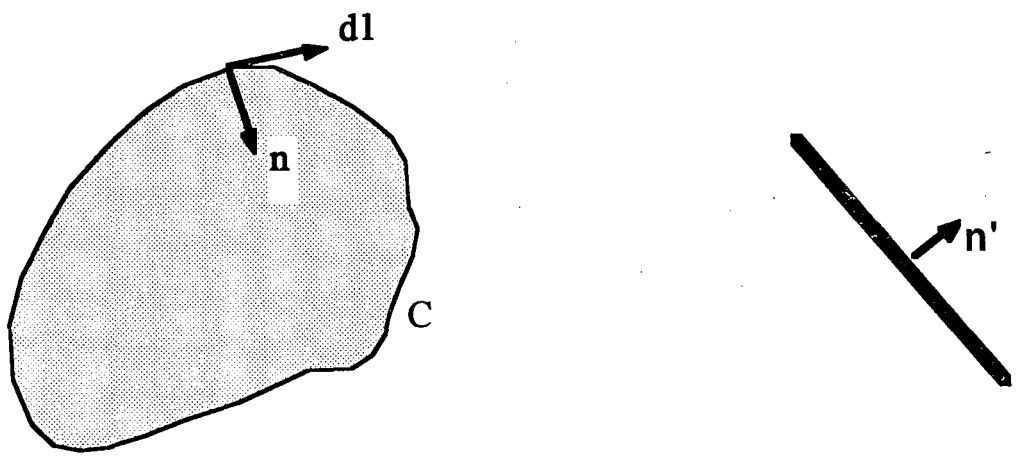

(a) A two-dimensional target

(b) A 2-D thin conductor

Figure 2-1-1 A two dimensional (2-D) model

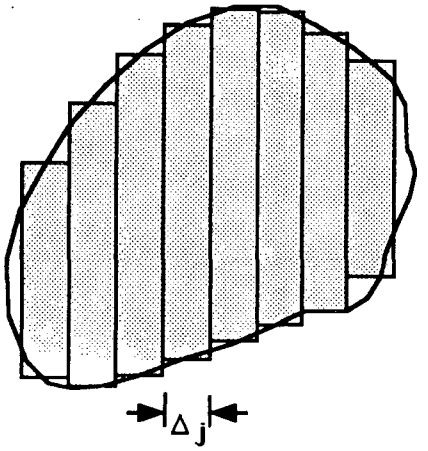

Figure 2-1-2 An arbitrary 2-D conductor approximated by a set of 2-D thin conductors

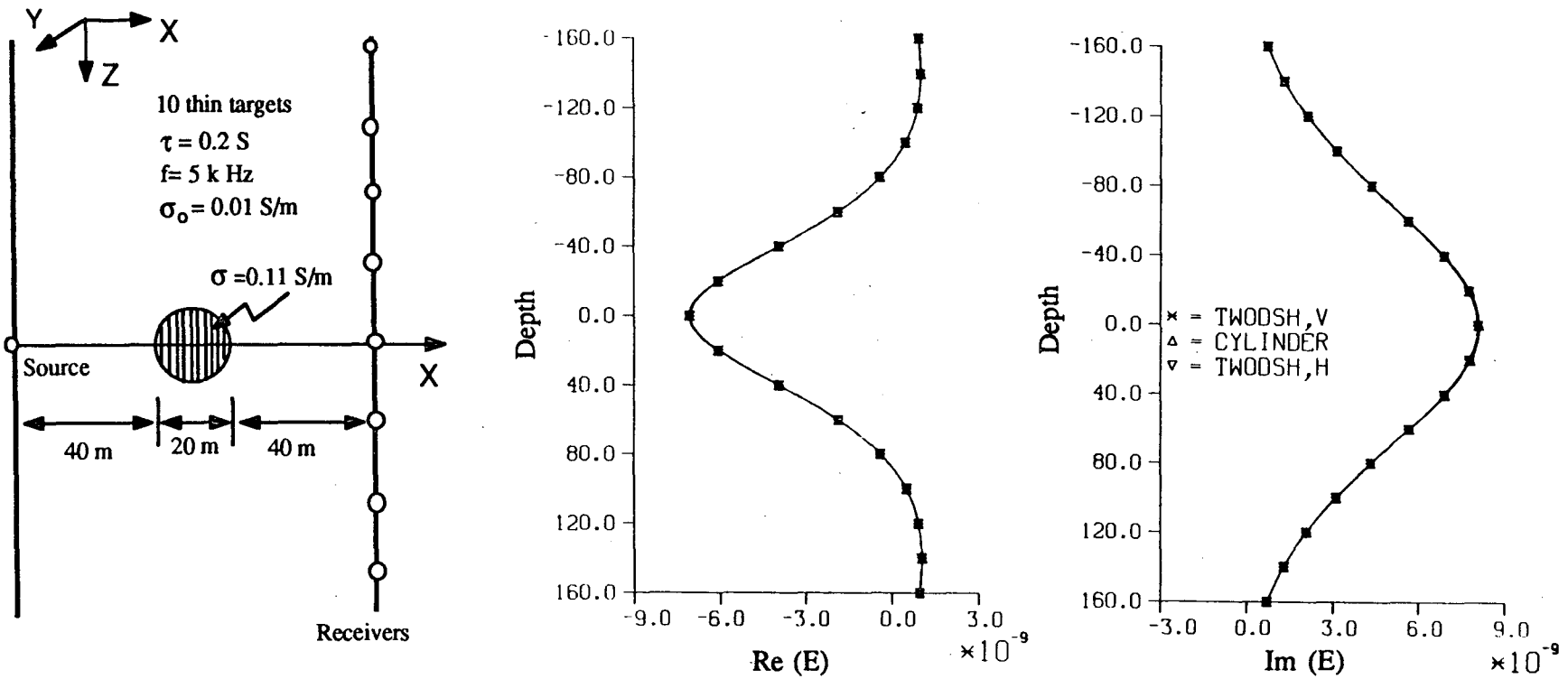

(a) Model

(b) Comparison

Figure 2-1-3 Numerical verification of the 2-D code by approximating a circular cylinder with a number of thin conductors

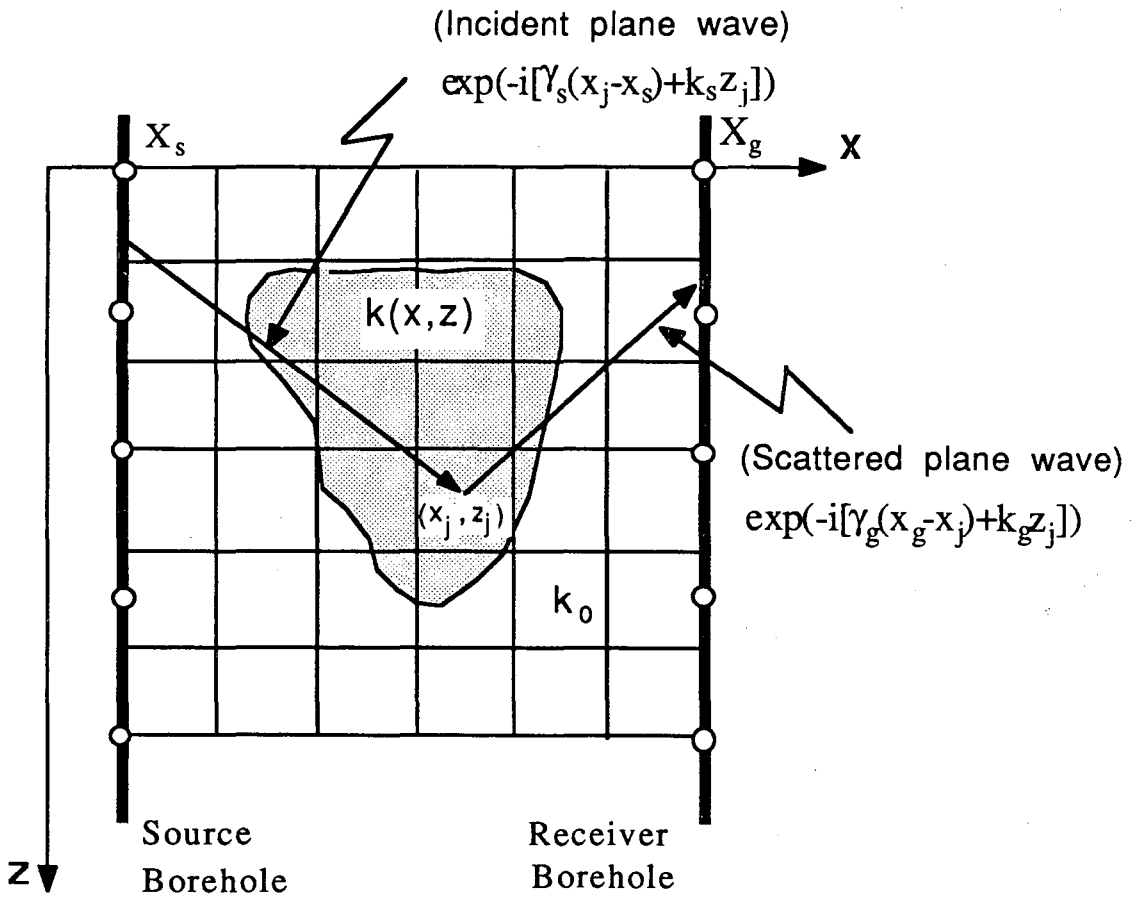

Figure 2-3-1 Discretization for tomographic inversion

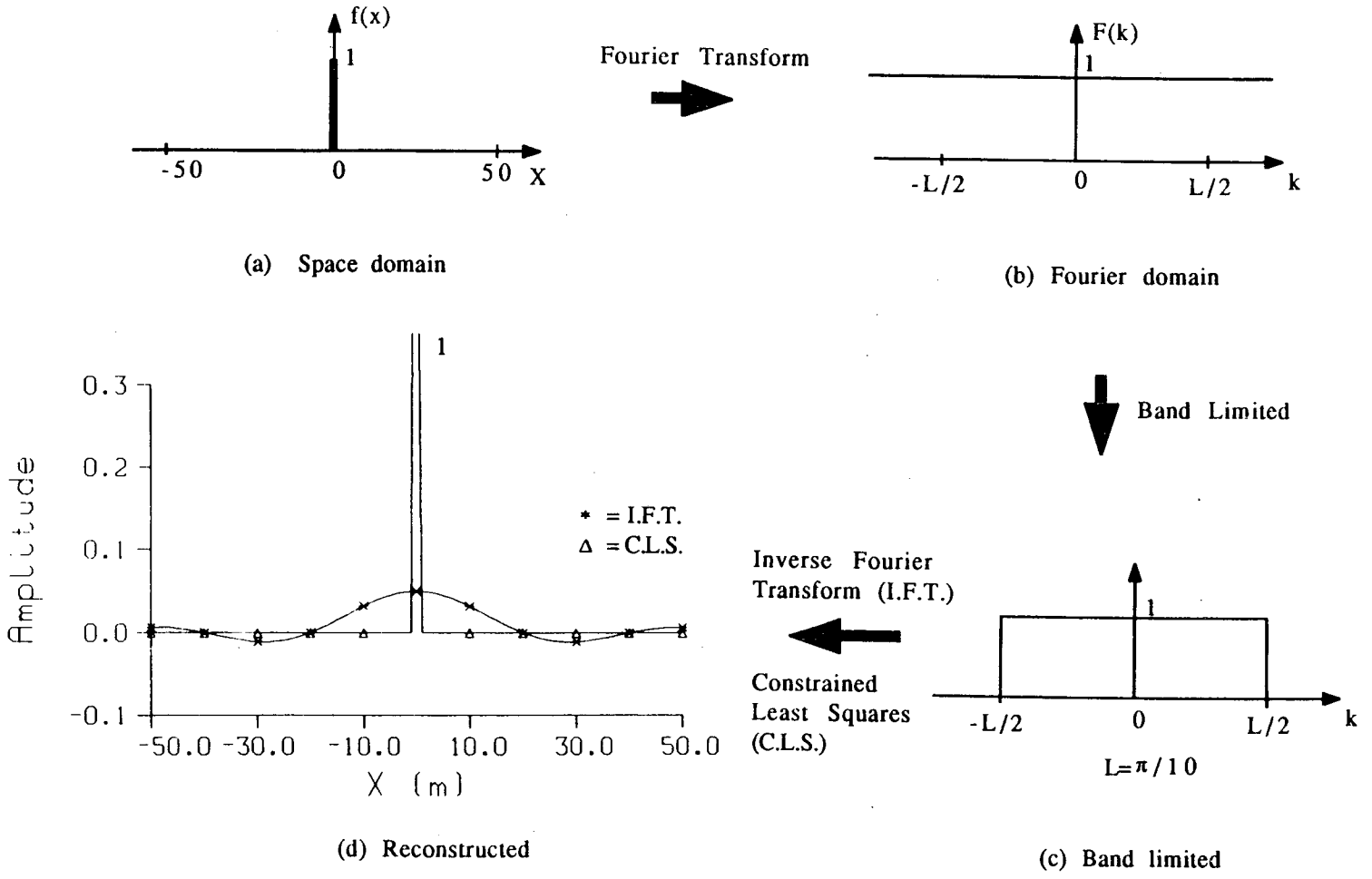

Figure 2-3-2 An example of enhanced resolution with a constrained least squares approach

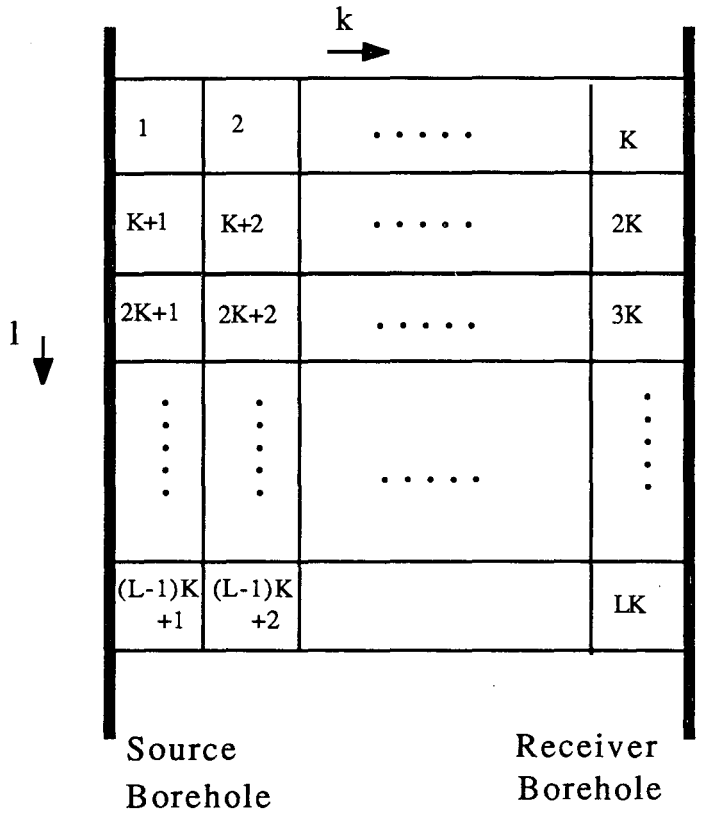

Figure 2-3-3 Image smoothing scheme

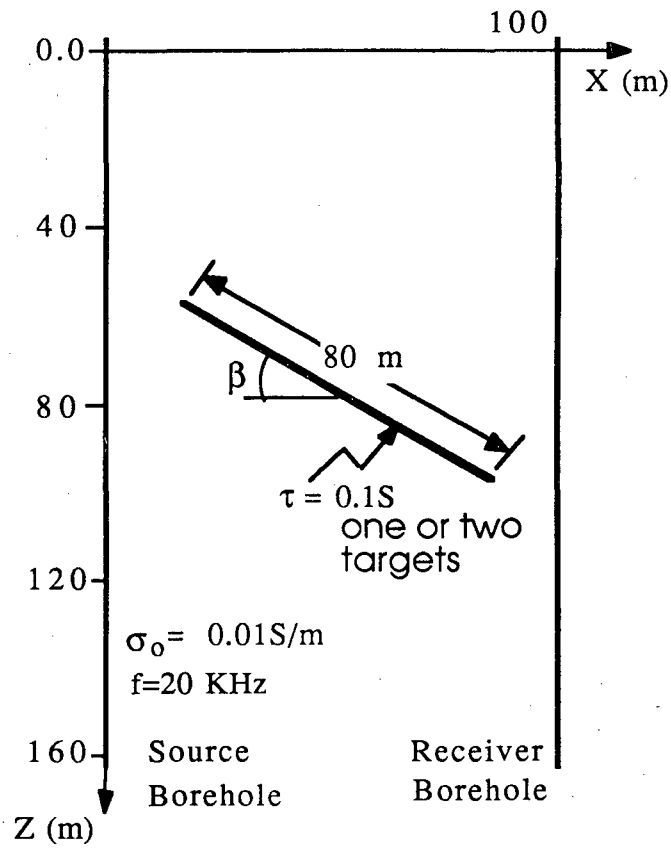

Figure 2-4-1 The two dimensional model for numerical calculation

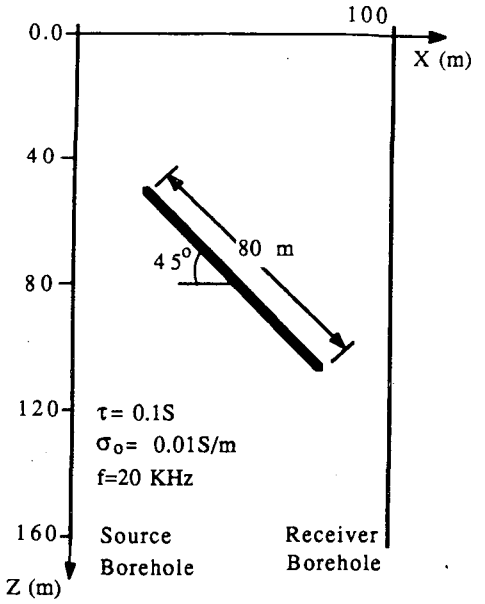

(a) Model

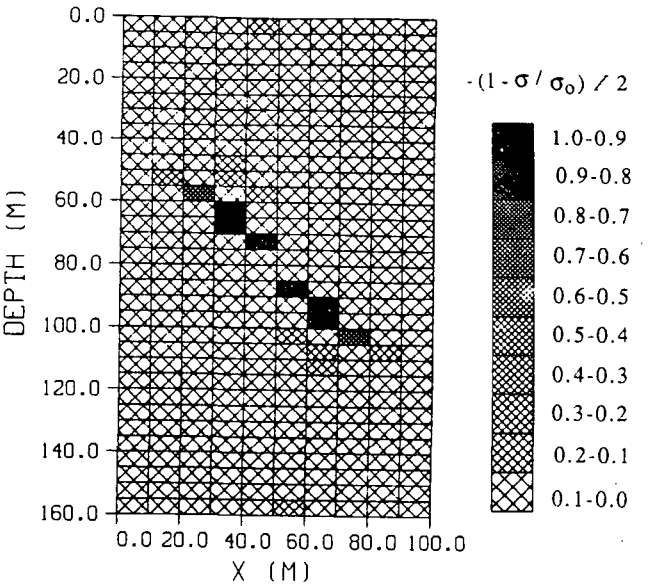

(b) No smoothing, $L_i=-\infty$

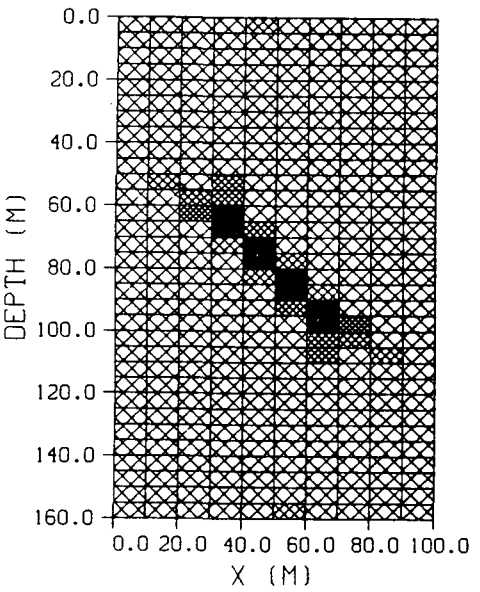

(c) No smoothing, $L_i=-1$

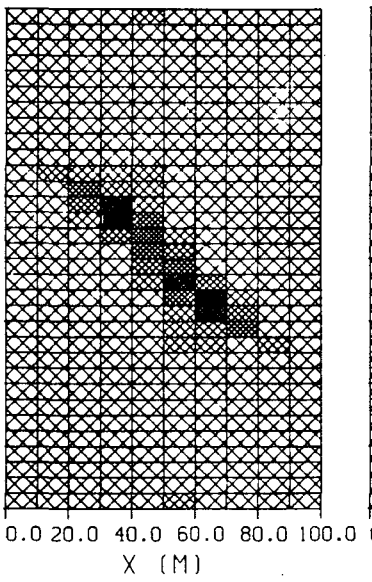

(d) Smoothed, $L_i=-\infty$

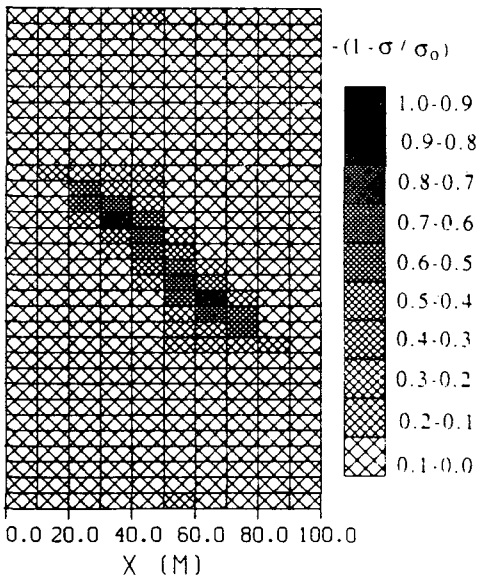

(e) Smoothed, $L_i=-\infty$,Born data

Figure 2-4-2 Images of a dipping conductor with different reconstruction parameters

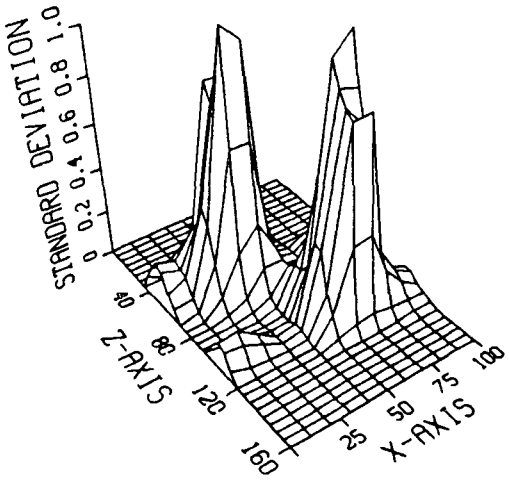

(a) No smoothing, $L_i = -\infty$

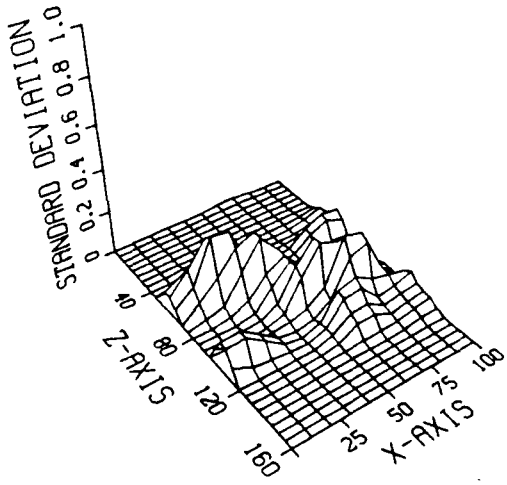

(b) No smoothing, $L_i = -1$

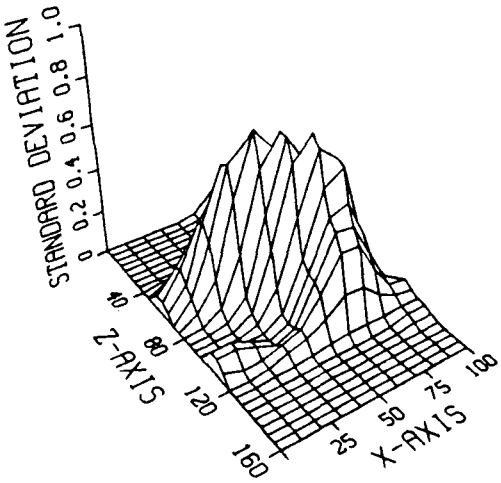

(c) Smoothed, $L_i = -\infty$

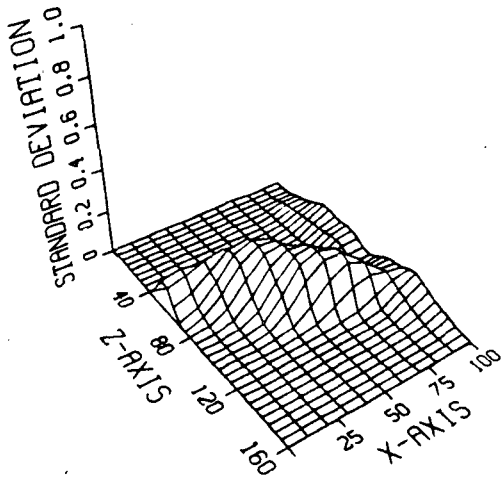

(d) Smoothed, $L_i = -\infty$, Born data

Figure 2-4-3 Standard deviation of the inversion results in Figure 2-4-2

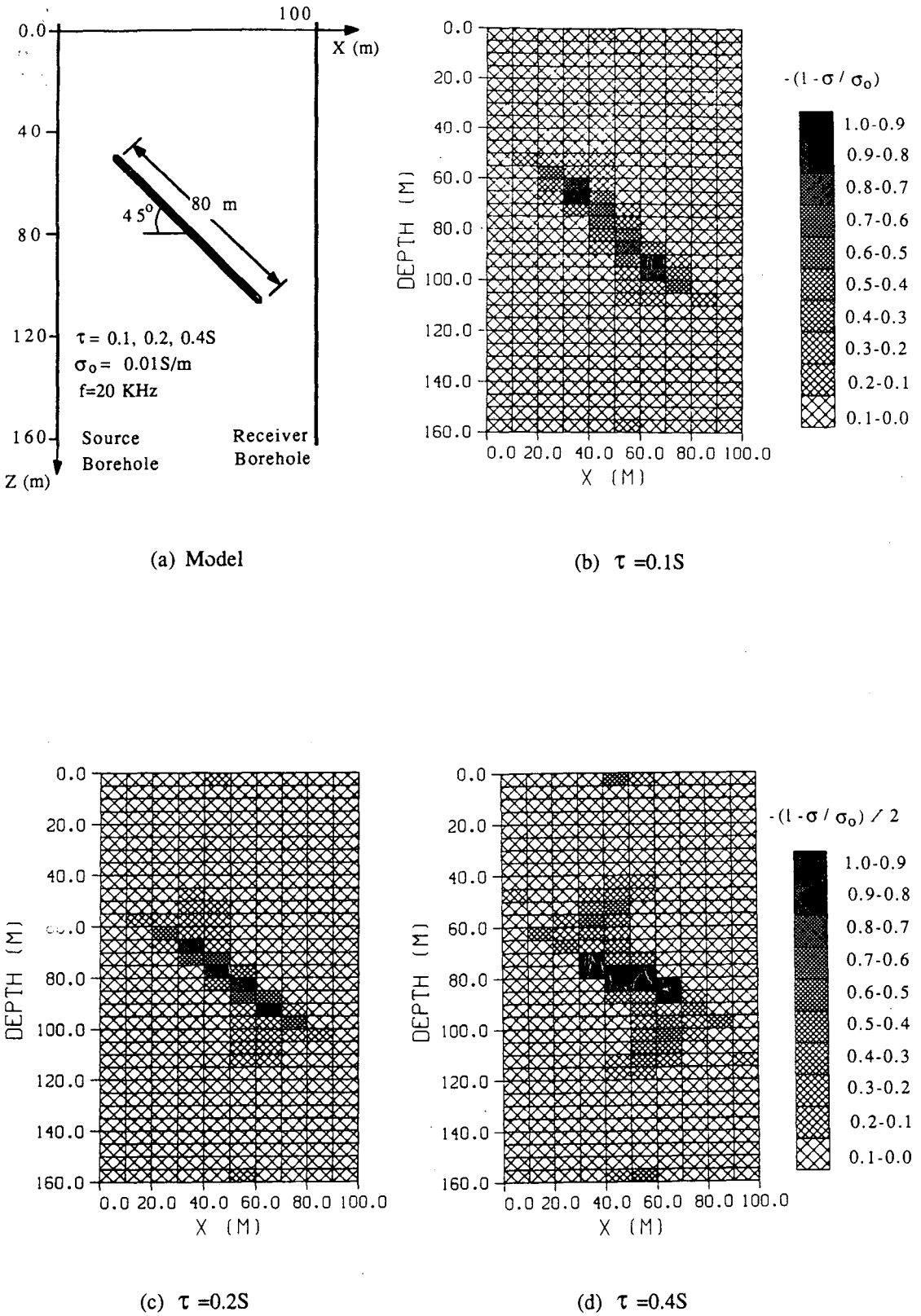

(a) Model

(b) τ =0.1S

(c) τ =0.2S

(d) τ =0.4S

Figure 2-4-4 Born images of a dipping conductor with different conductance

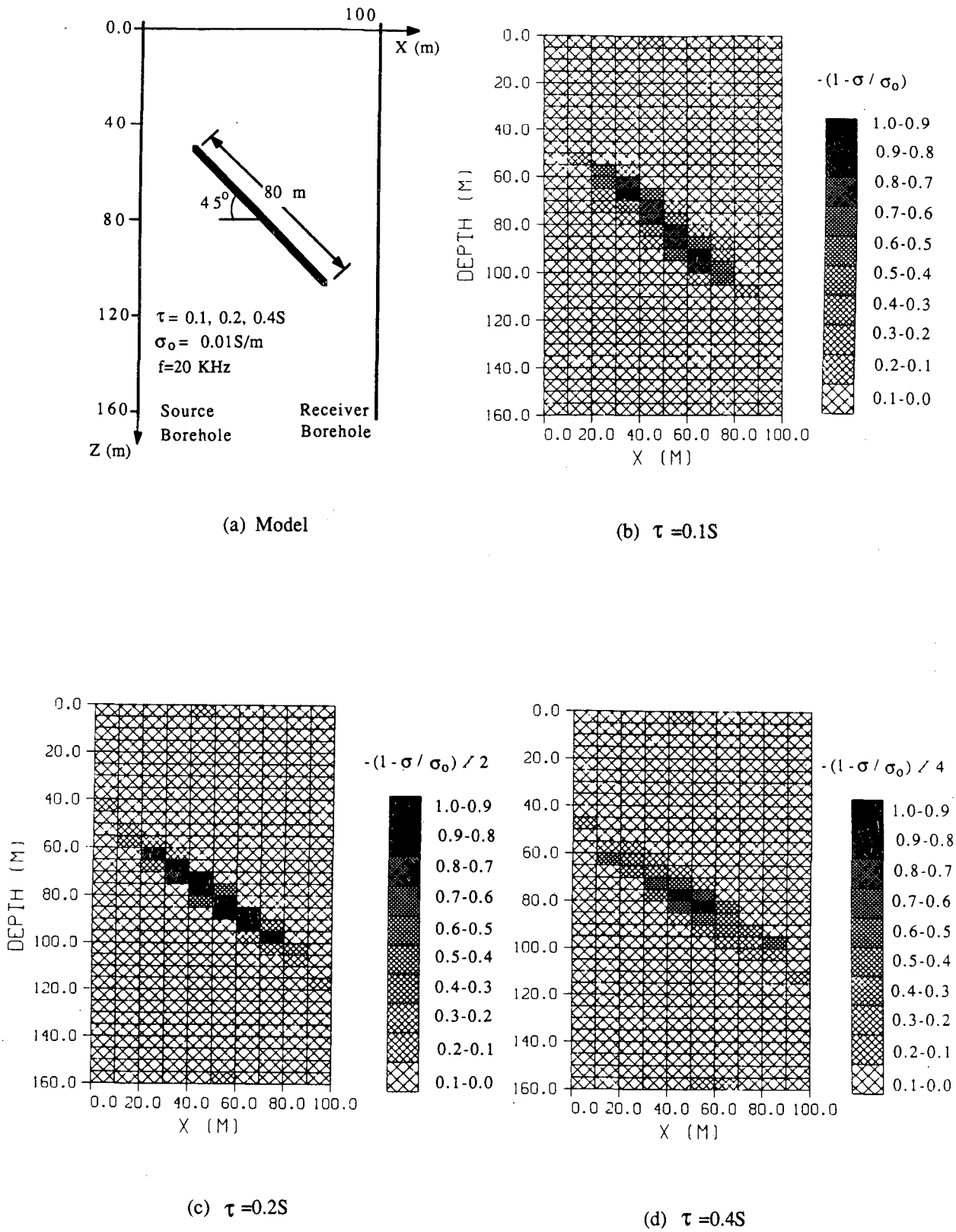

(a) Model

(b) τ =0.1S

(c) τ =0.2S

(d) τ =0.4S

Figure 2-4-5 Rytov images of a dipping conductor with different conductance

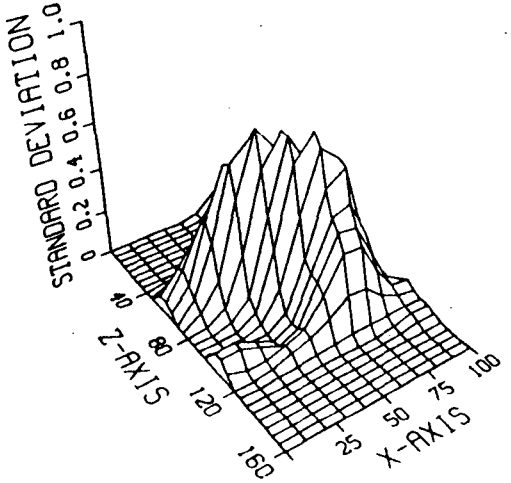

(a) Born approximation

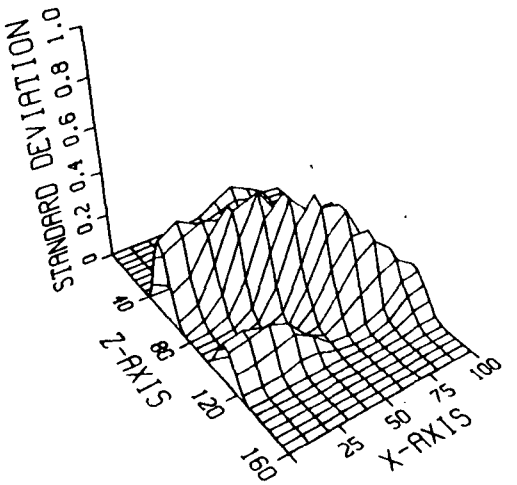

(b) Rytov approximation

Figure 2-4-6 Comparison of the standard deviations between the Born and Rytov methods for the $\tau = 0.1\,S$ case

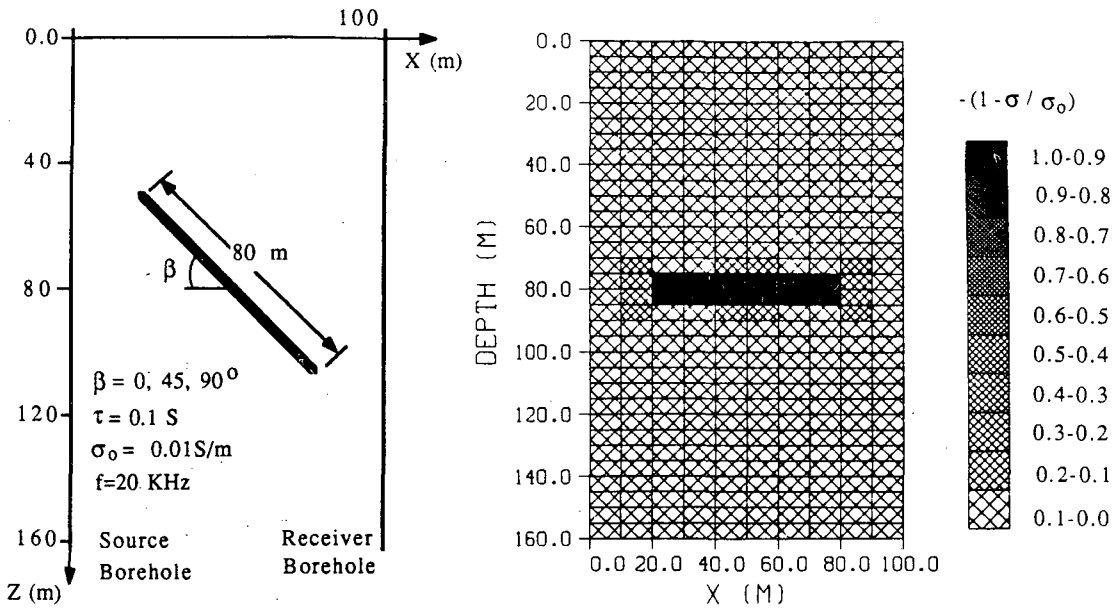

(a) Model

(b) β = 0°

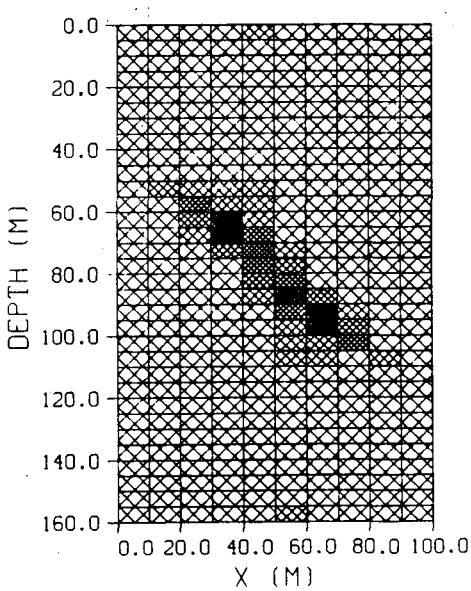

(c) β = 45°

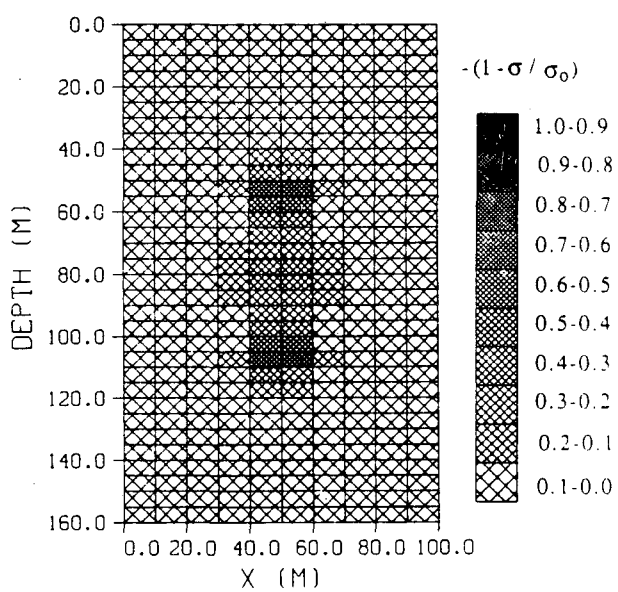

(d) β = 90°

Figure 2-4-7 Images of a conductor with different dip angles [Figure (b) through (d) are reconstructed from exact data while Figure (e) through (g) are from Born data]

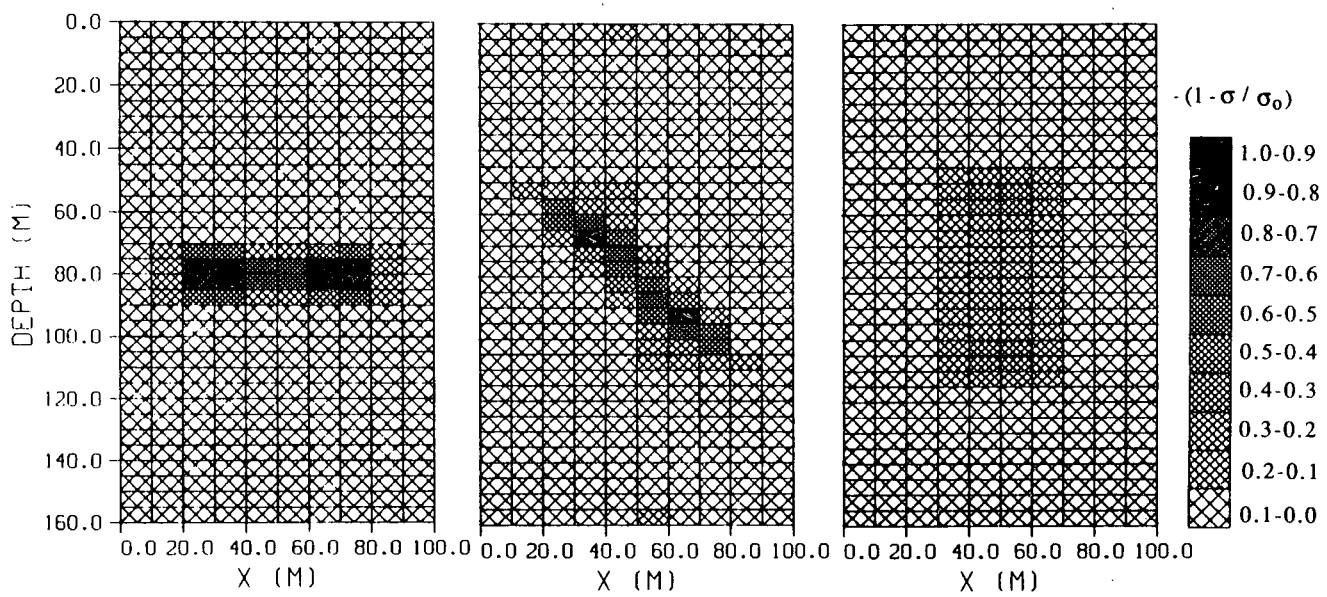

(e) $\beta = 0^o$, Born data (f) $\beta = 45^o$, Born data (g) $\beta = 90^o$, Born data

Figure 2-4-7 Images of a conductor with different dip angles [Figure (b) through (d) are reconstructed from exact data while Figure (e) through (g) are from Born data]

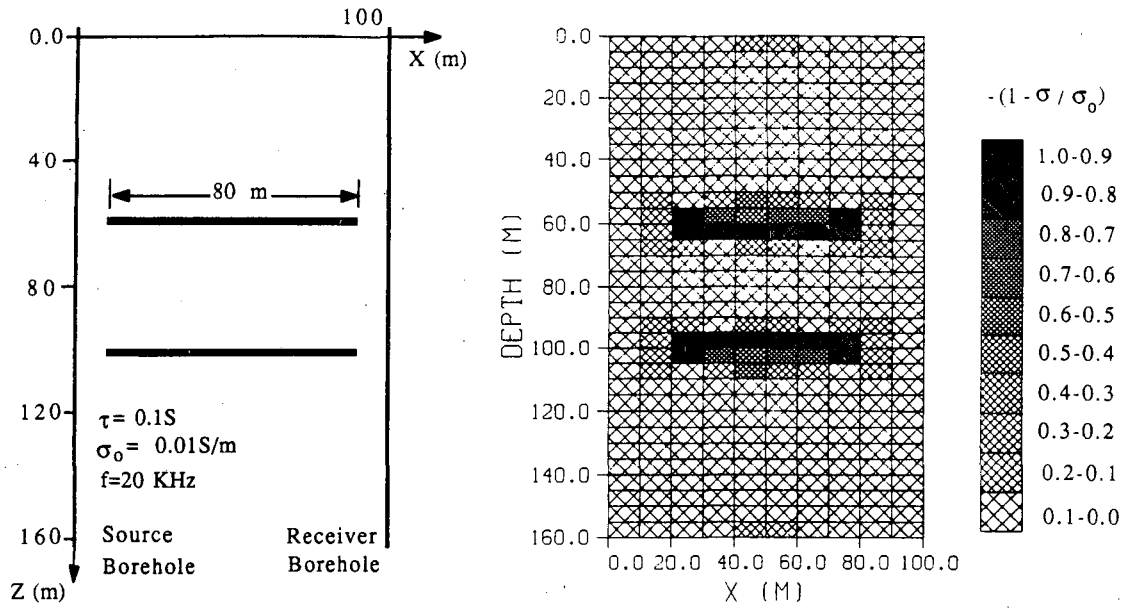

Model Image

(a) $\beta = 0^o$

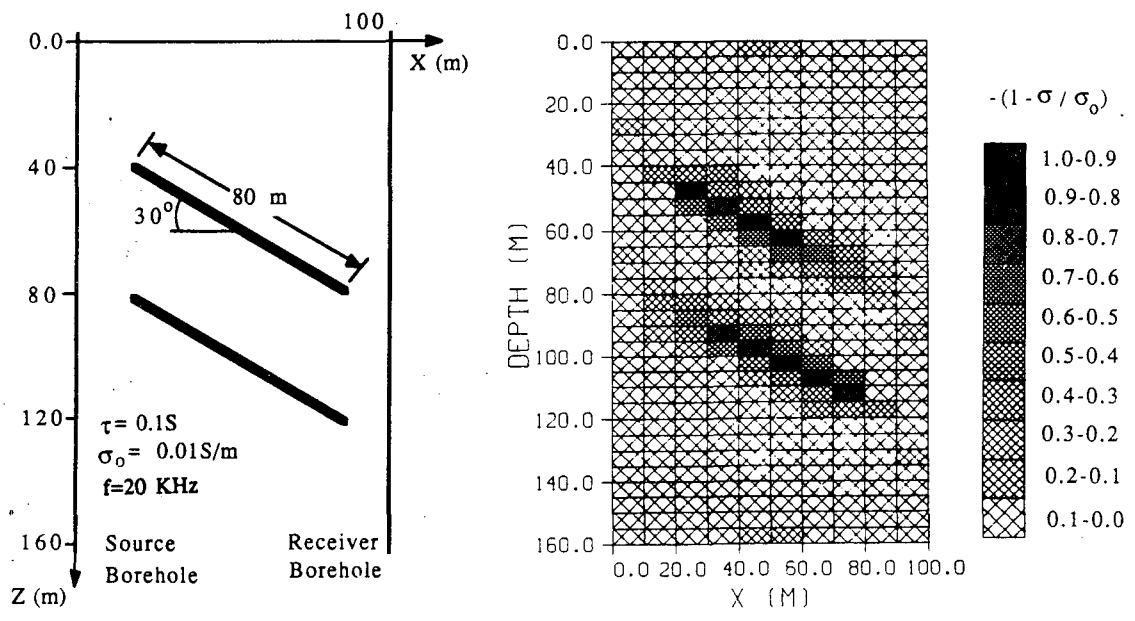

Model Image

(b) $\beta = 30^o$

Figure 2-4-8 Images of two parallel conductors with different dip angles

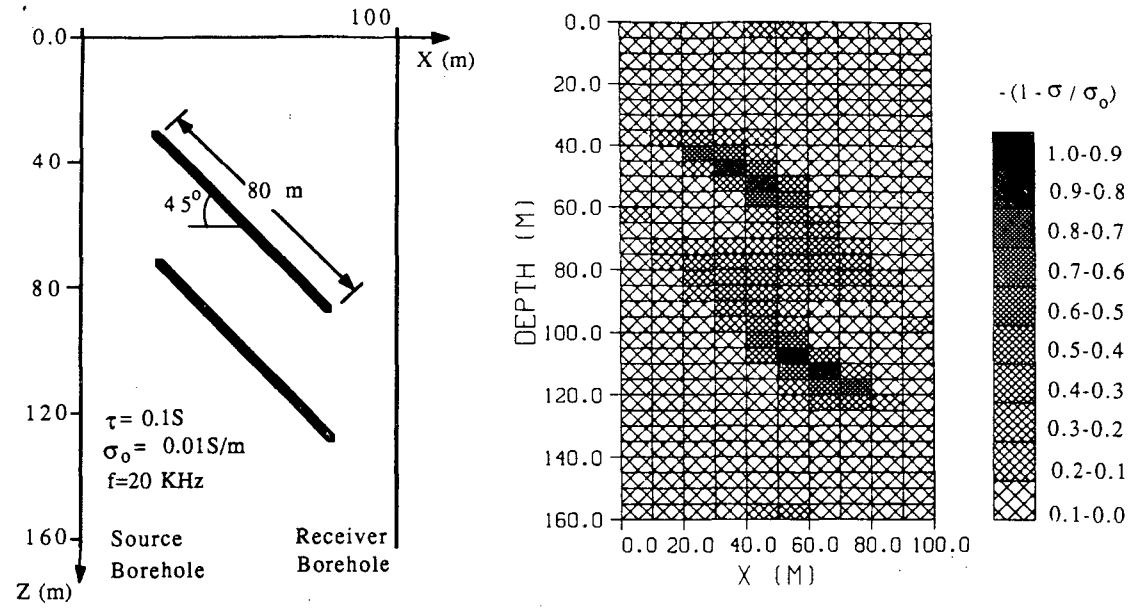

Model Image

(c) $\beta = 45^{o}$

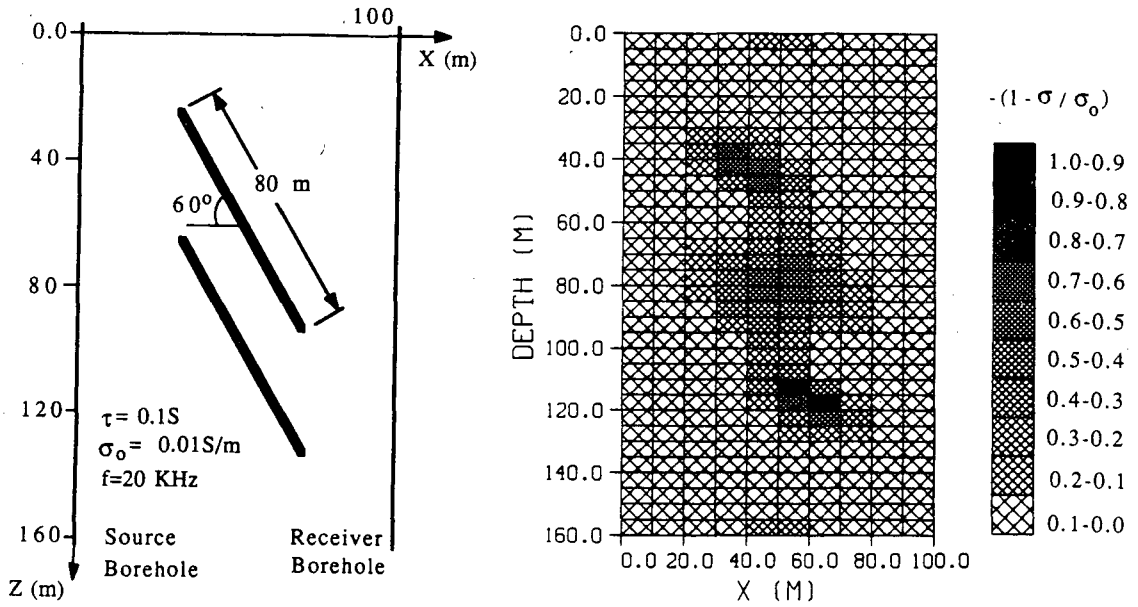

Model Image

(d) $\beta = 90^{o}$

Figure 2-4-8 Images of two parallel conductors with different dip angles

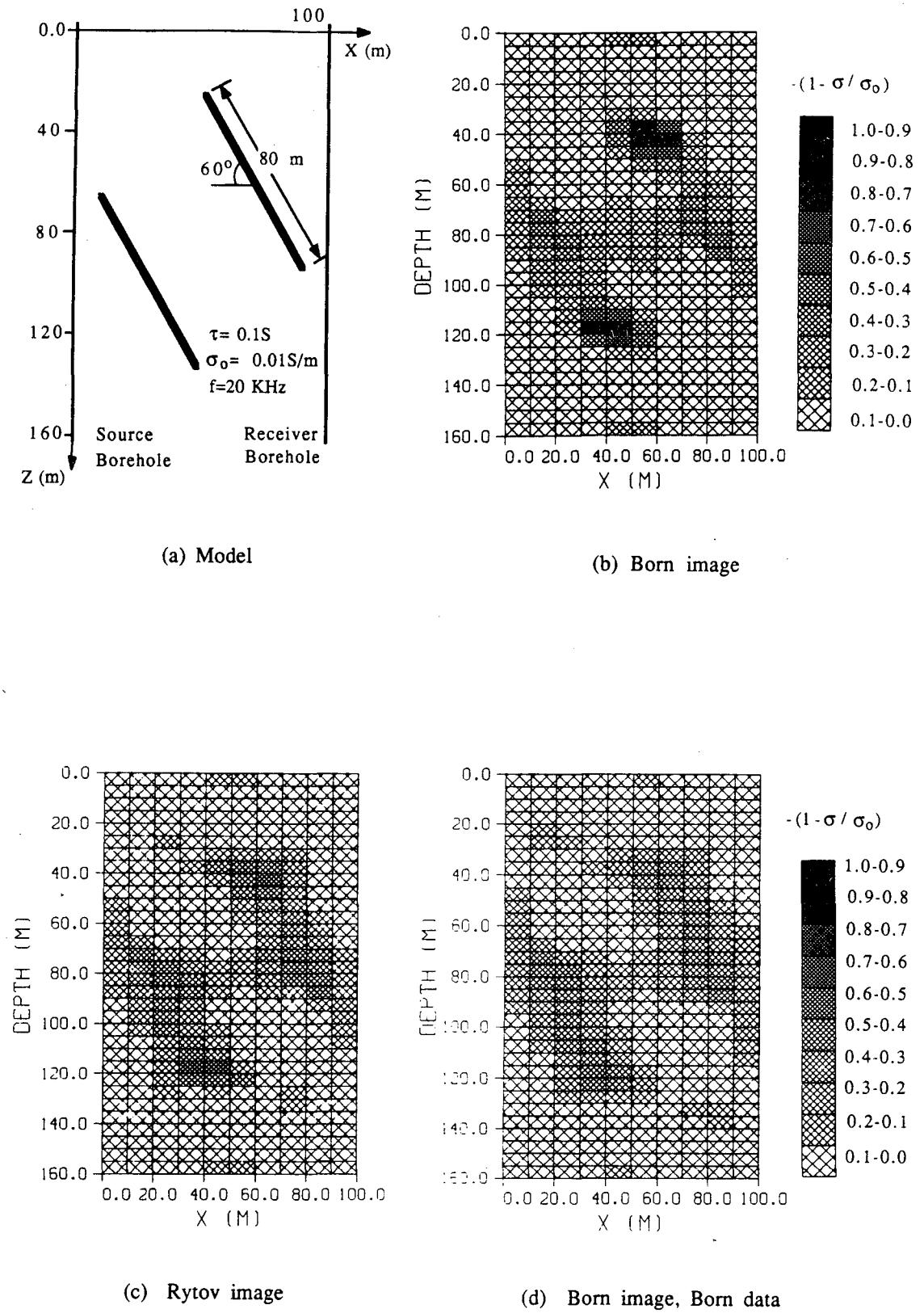

(a) Model

(b) Born image

(c) Rytov image

(d) Born image, Born data

Figure 2-4-9 Images of two 60° dipping conductors with a 40m increased horizontal separation as compared to the $\beta = 60^o$ case in Figure 2-4-8

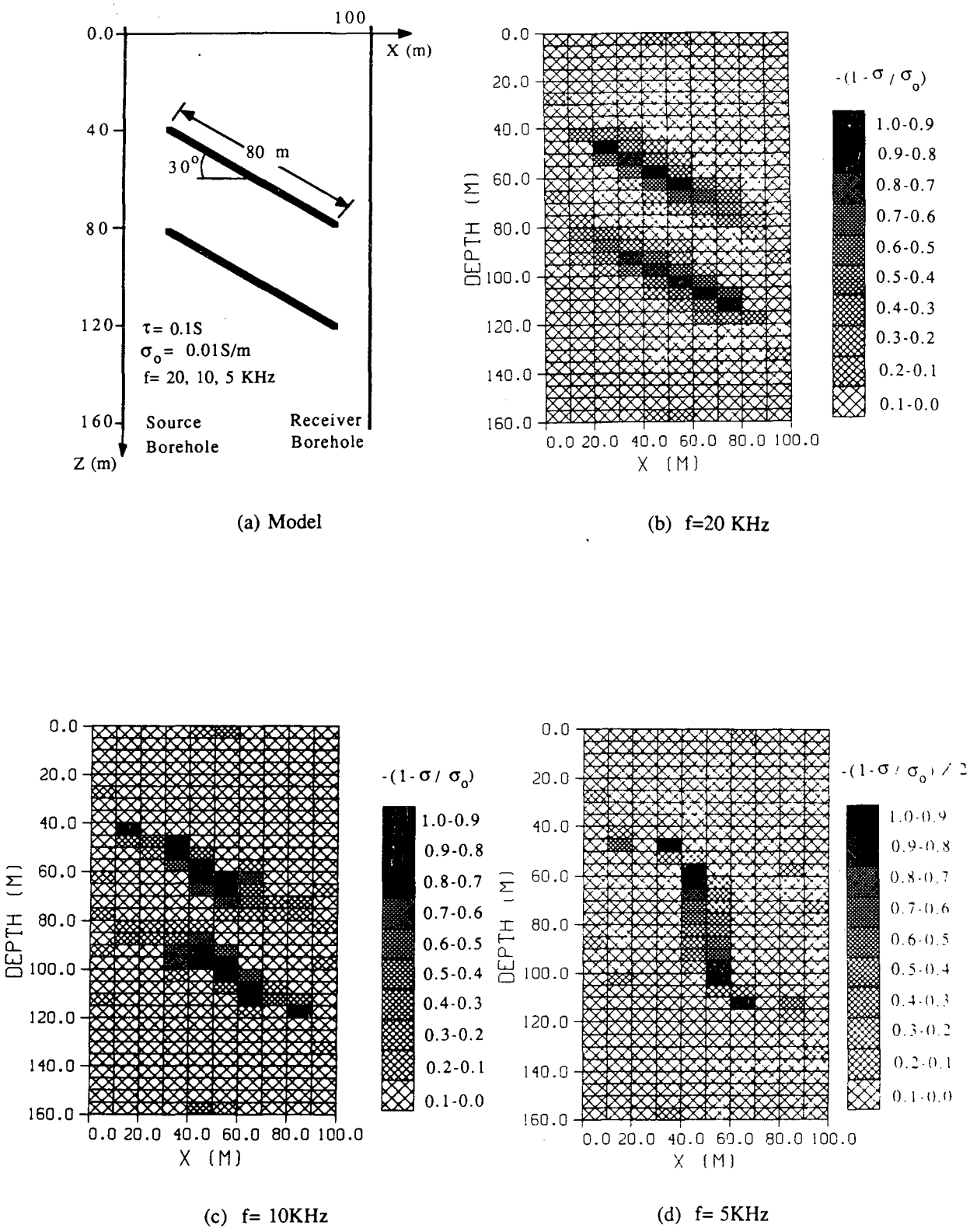

(a) Model

(b) f=20 KHz

(c) f= 10KHz

(d) f= 5KHz

Figure 2-4-10 Images of two 30° dipping conductors under different operating frequencies

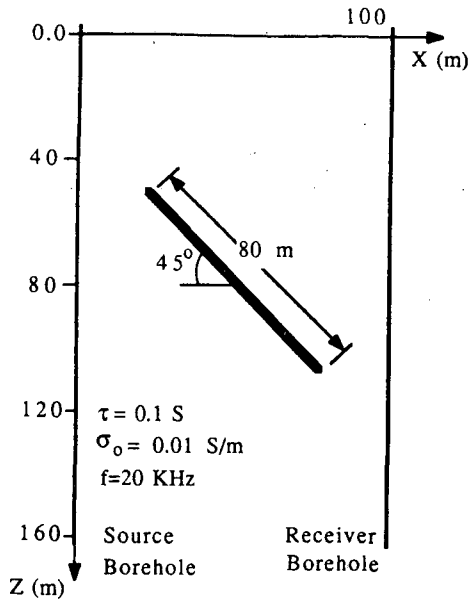

(a) Model

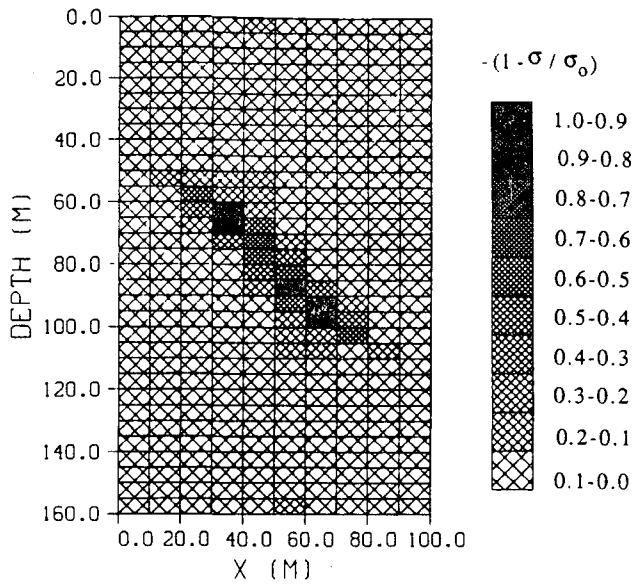

(b) Array length=310m

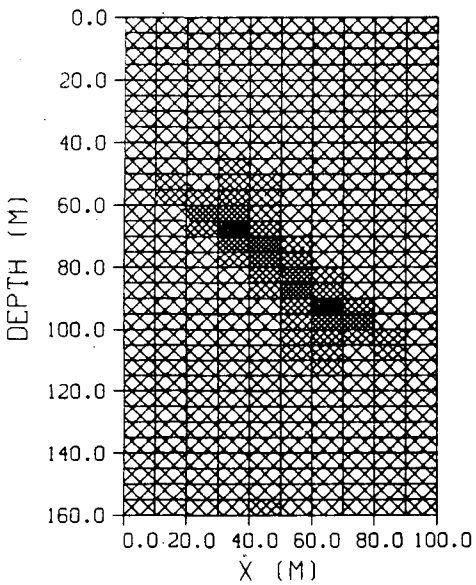

(c) Array length=248m

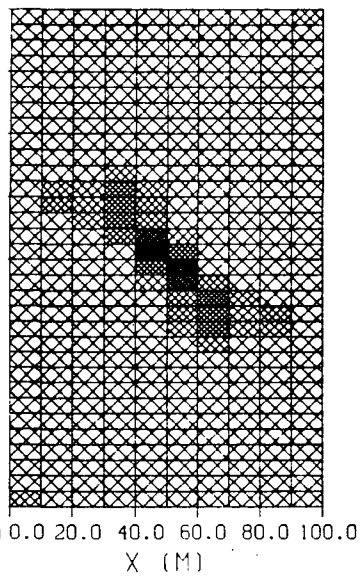

(d) Array length=186m

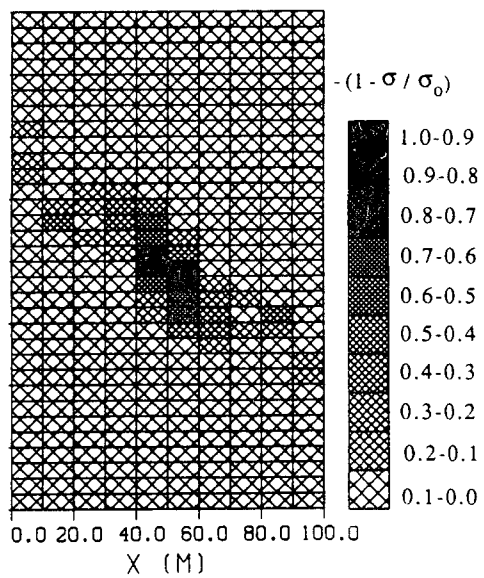

(e) Array length=155m

Figure 2-4-11 Images of a 45° dipping target reconstructed under different array length

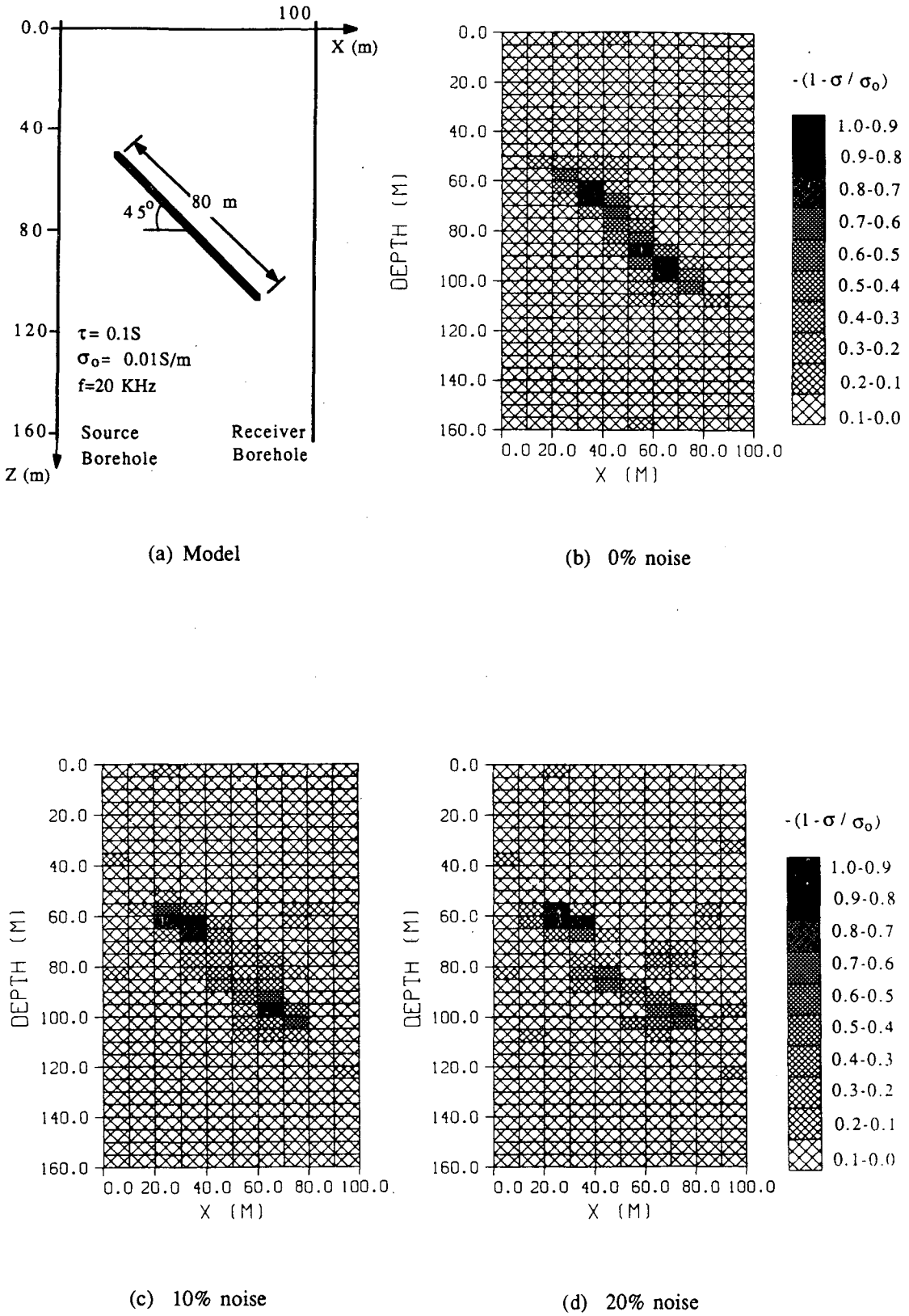

(a) Model

(b) 0% noise

(c) 10% noise

(d) 20% noise

Figure 2-4-12 Images of a 45° dipping target with different levels of random noise in the input data

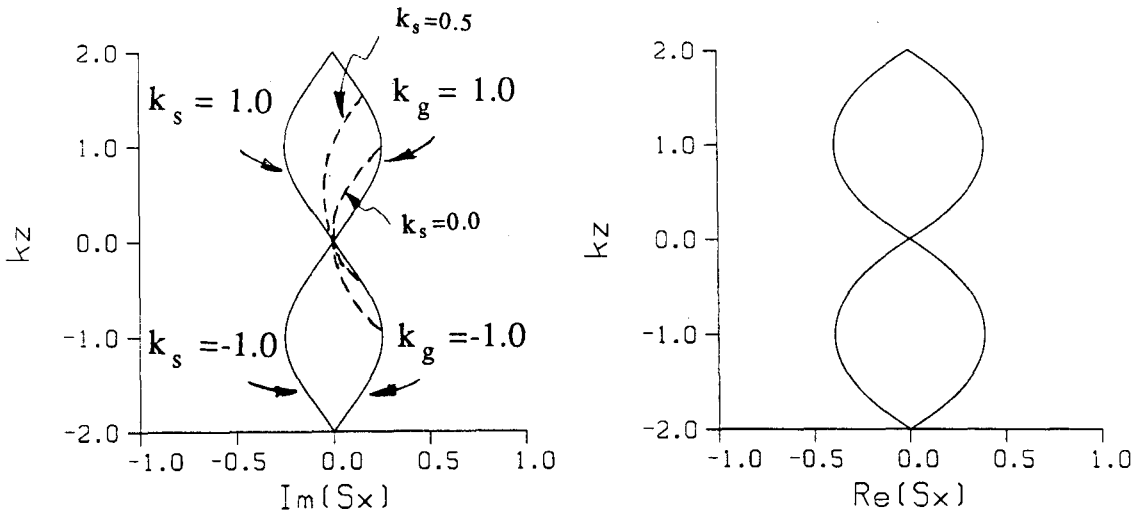

(a) Maximum s_x and k_z for $|k_o|$=1.0

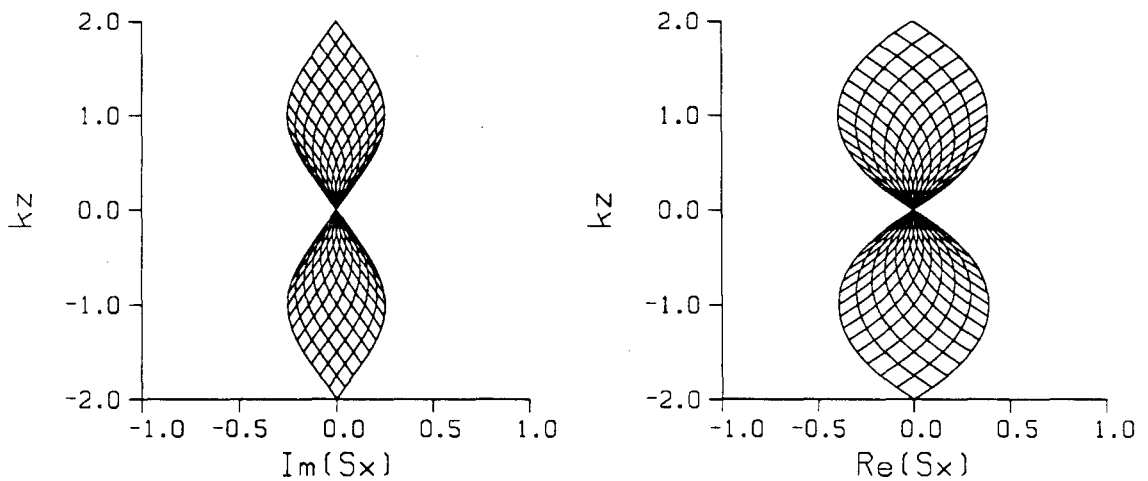

(b) Coverage for $|k_o|$=1.0

Figure 2-5-1 Cross-hole wave number domain coverage for $|k_o^2| = 1$

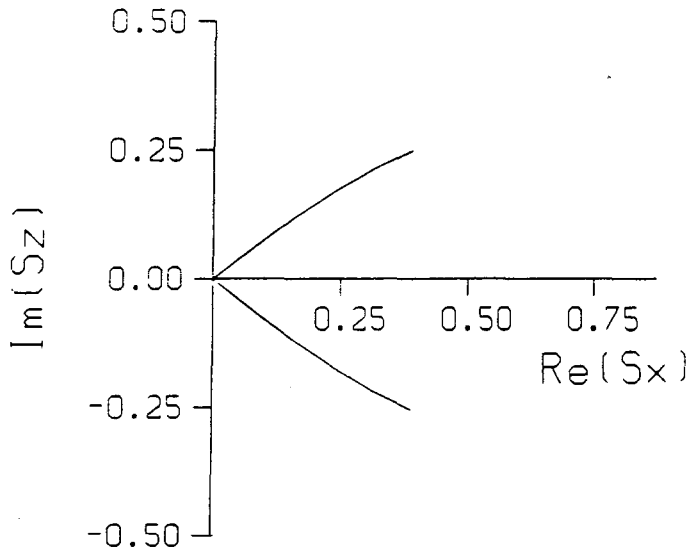

(c) Im(Sx) versus Re(Sx)

Figure 2-5-1 Cross-hole wave number domain coverage for $|k_o^2| = 1$

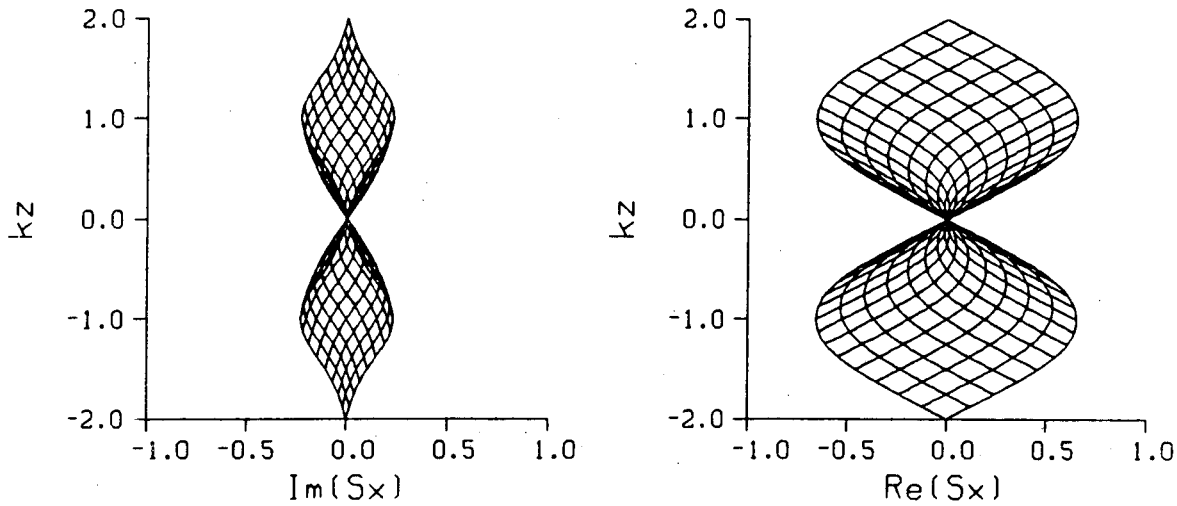

(a) $|k_o| = 1/4$

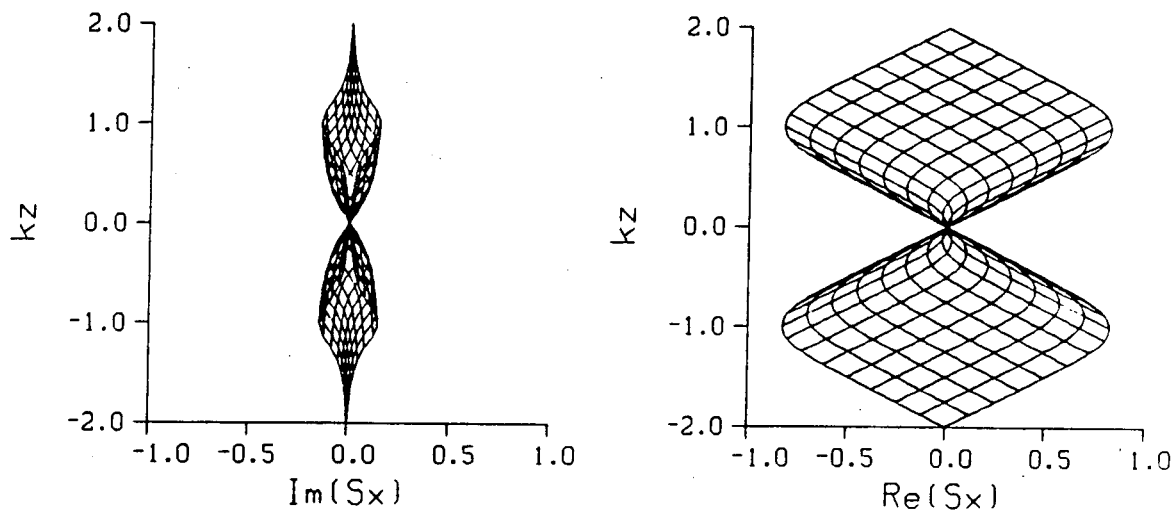

(b) $|k_o| = 1/16$

Figure 2-5-2 Cross-hole wave numbers domain coverage for $|k_o^2| = 1/4$ and 1/16

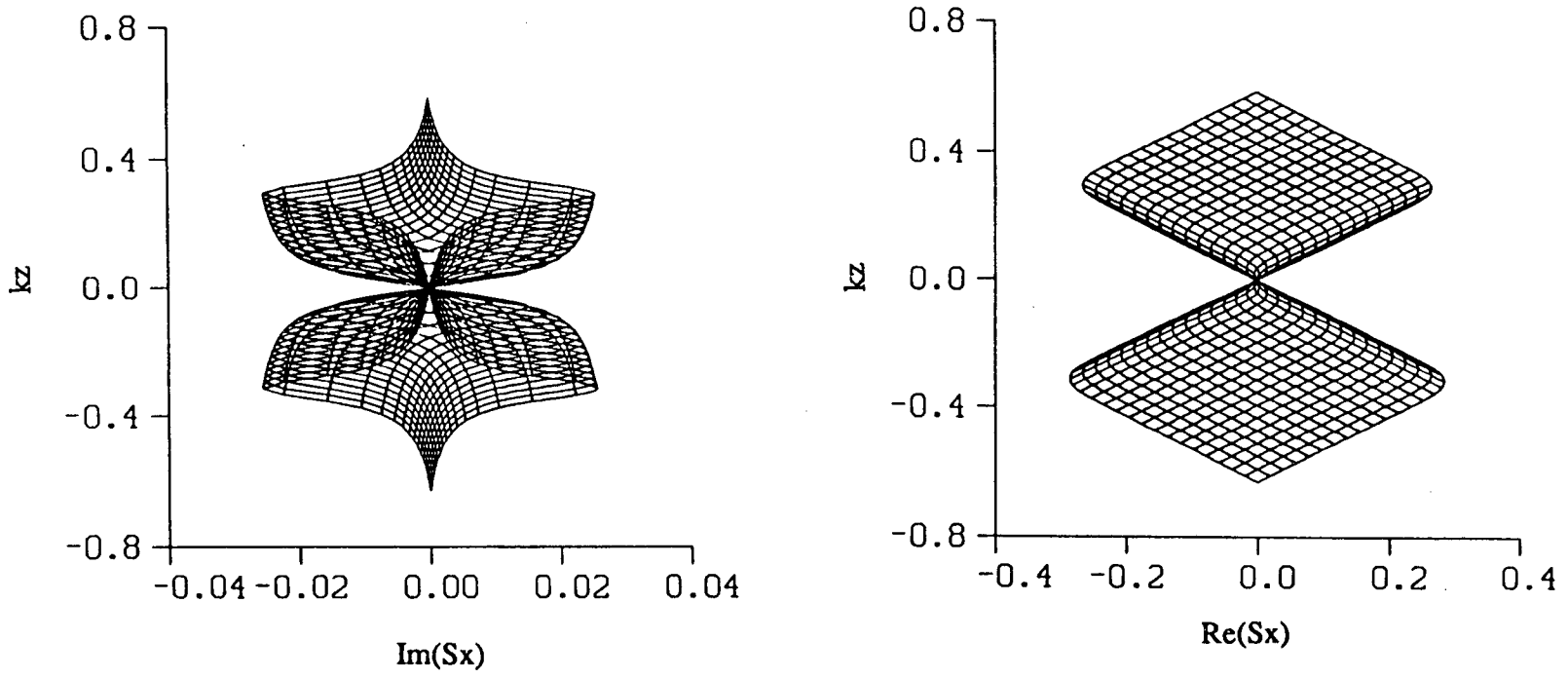

(a) kz - Im(Sx)

(b) kz - Re(Sx)

Figure 2-5-3 Wave number coverage of the model shown in Figure 2-4-1

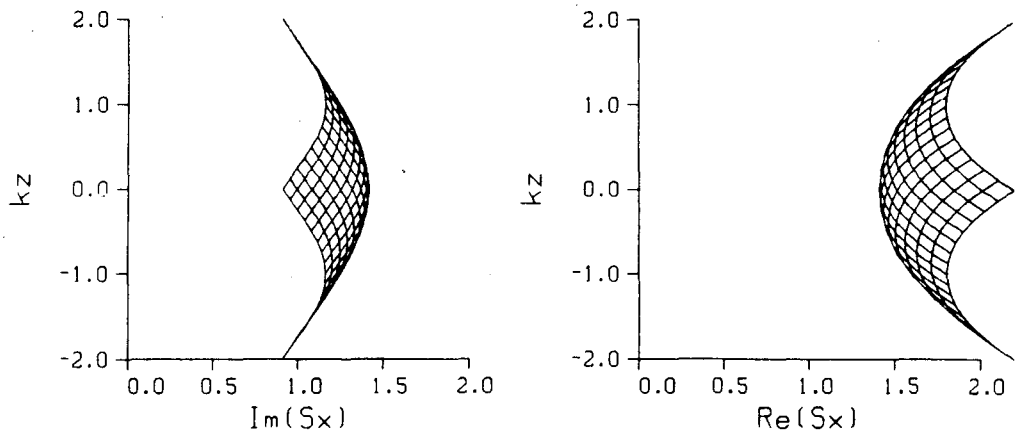

(a) $|k_o| = 1$

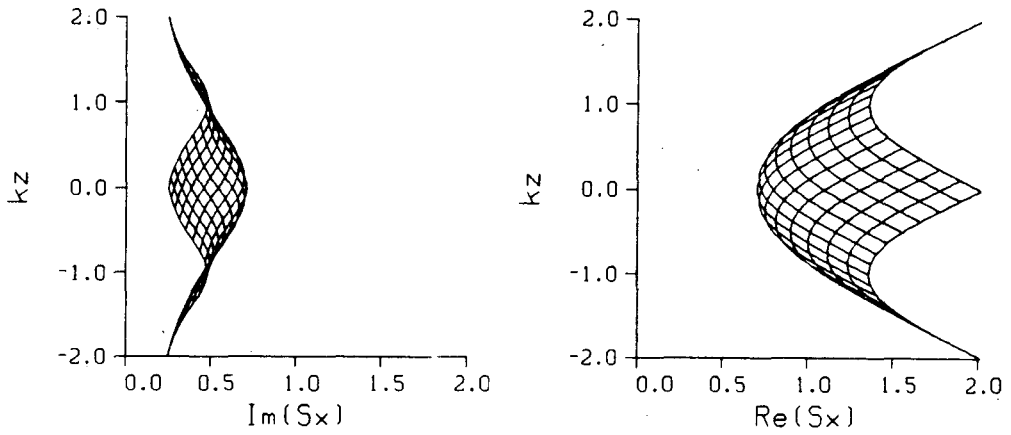

(b) $|k_o| = 1/4$

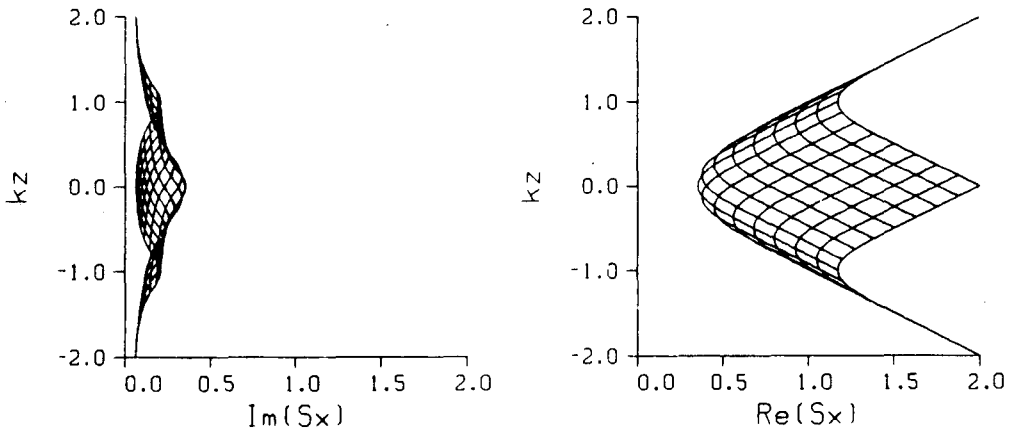

(c) $|k_o| = 1/16$

Figure 2-5-4 Wave number domain coverage for single hole or surface source-receiver configuration

Chapter 3
Tomographic inversion for a cylindrical symmetry problem

In the previous chapter, two-dimensional tomographic inversion has been shown to be successful in characterizing electrically conductive targets which satisfy the weak scattering approximation. Now, this over simplified model will be extended by allowing a dipole source to replace the unrealistic subsurface line source. To allow this source geometry, we choose a simple cylindrical model. If we assume that the target zone displays axial symmetry about the borehole which contains the transmitter, the vertical magnetic dipole source only excites an electrical field in the azimuthal direction which in turn generates the magnetic anomaly at the receiver sites. The resulting scalar equation can now be readily solved.

In the following analysis, the forward modeling code is first formulated and programmed to provide the necessary synthetic data for use in the inversion tests. A tomographic inversion scheme similar to that used for the two-dimensional Cartesian geometry is then developed for conductivity reconstruction. If an additional far field approximation is applied, the wave number domain coverage of the object function for this cylindrically symmetrical problem is found to be exactly the same as that for the two dimensional Cartesian model examined in Chapter 2.

3.1 Formulation of the integral equation

Numerical modeling studies for a conventional logging environment in a cylindrically symmetrical medium have been reported by a number of authors. For example, Zakharov and Nesmeyanov (1979) used an integral equation approach for a layered medium with an invaded zone, while the finite element method was applied to this problem by Anderson and Chang (1982). More recently, a newer method was studied by Pai and Huang (1988) using a generalized Haskell matrix method. All these codes, however, are for the conventional induction logging configuration where the receiver and transmitter are separated by a fixed distance in the

same borehole. Our need for cross-hole source-receiver synthetic data brings with it a numerical modeling problem which can be solved with an integral equation approach.

3.1.1 A cylindrical symmetry model

The cylindrically symmetrical model is shown in Figure 3-1-1. A cylindrical coordinate system is established with z as the vertical axis of symmetry. The background medium is assumed to be homogeneous and has an electrical conductivity of σ_o. The ring shaped conductive target embedded in the homogeneous medium has a conductivity of $\sigma(\mathbf{r})$. Vertical magnetic dipole sources are positioned along the axis of symmetry. It is well known that the vertical magnetic dipole in this situation can only induce current in the azimuthal direction. The secondary magnetic field generated by the induced current is measured in another borehole. Two components of magnetic field will be present, one in the vertical direction and the other in the radial, or horizontal, direction. Since the horizontal component is difficult to measure in a borehole condition, the model analysis will be carried out for the vertical component only. As a matter of fact, in the cylindrical symmetry situation, as will be shown later, the two components contain basically the same information providing observations are made over a long distance in the receiver borehole. From the noise suppression point of view, however, the extra measurements may serve to improve the stability of the inverse problem.

3.1.2 The integral equation

Since for a cylindrically symmetrical medium with magnetic dipole sources along the axis of symmetry we only have an electric field in the azimuthal direction, a scalar equation governing the relationship between conductivity and the electrical response can be deduced. The differential equation for the electrical field E_ϕ derived from the Maxwell's equations in equation (2-1-1) is

$$\nabla^2 E_\phi - \frac{1}{r^2} E_\phi + k^2 E_\phi = i\omega\mu J_\phi, \tag{3-1-1}$$

where J_ϕ is the external current source with current flowing in the azimuthal direction. The magnetic permeability μ is assigned to have the free space value and ω is the angular

frequency used. The medium wave number is k^2 which is equal to $= -i\,\omega\mu\sigma(\mathbf{r})$. $\sigma(\mathbf{r})$ denotes the conductivity distribution. Rearrange equation (3-1-1) into

$$\nabla^2 E_\phi - \frac{1}{r^2} E_\phi + k_o^2 E_\phi = i\,\omega\mu J_\phi + k_o^2 O(\mathbf{r}) E_\phi, \tag{3-1-2}$$

where the background wave number $k_o^2 = -i\,\omega\mu\sigma_o$ with σ_o representing a constant reference conductivity. The object function $O(\mathbf{r})$ is defined as

$$O(\mathbf{r}) = 1 - k^2/k_o^2 = 1 - \sigma(\mathbf{r})/\sigma_o\,. \tag{3-1-3}$$

Next introduce a Green's function G such that

$$\nabla^2 G - \frac{1}{r^2} G + k_o^2 G = i\,\omega\mu\,\delta(\mathbf{r}-\mathbf{r}')\,. \tag{3-1-4}$$

From equations (3-1-2) and (3-1-4) and Green's scalar identity, we derive

$$E_\phi(\mathbf{r}_g, \mathbf{r}_s) = E_\phi^p(\mathbf{r}_g, \mathbf{r}_s) - \int_s \sigma_o O(\mathbf{r}) E_\phi(\mathbf{r}, \mathbf{r}_s) G(\mathbf{r}_g, \mathbf{r})\, dr dz\,, \tag{3-1-5}$$

where the receiver point lies at $\mathbf{r}_g = (r_g, z_g)$ and the source point is located at $\mathbf{r}_s = (r_s, z_s)$. E_ϕ^p $(=G)$ is the primary electrical field. The surface integration is over all the inhomogeneities, or over the area defined by $0 < r < \infty$ and $-\infty < z < \infty$. The Green's function G defined by equation (3-1-4) is the same as the electric field generated by a circular current loop source carrying unit current and can be found from Wait and Hill (1980).

$$G(\mathbf{r}, \mathbf{r}') = i\,\omega\mu \frac{\partial}{\partial r} \frac{r'}{2} \int_o^\infty e^{-\gamma|z-z'|} \frac{J_1(\lambda r')}{\gamma} J_0(\lambda r)\, d\lambda\,, \tag{3-1-6}$$

where $\gamma^2 = \lambda^2 - k_o^2$. $J_0(\lambda r)$ and $J_1(\lambda r')$ are the zero-th and first order Bessel functions of first kind respectively.

To solve for the H-field, one can use equation (3-1-5) and take $\nabla\times(\hat{\phi} E_\phi(\mathbf{r}_g))$ with respect to the observation point $\mathbf{r}_g$. Here, $\hat{\phi}$ is a unit vector in ϕ direction.

$$\mathbf{H}(\mathbf{r}_g, \mathbf{r}_s) = \mathbf{H}^p(\mathbf{r}_g, \mathbf{r}_s) - \int_s \sigma_o\, O(\mathbf{r}) E_\phi(\mathbf{r}, \mathbf{r}_s)\, \mathbf{G}_H(\mathbf{r}_g, \mathbf{r}) dr dz\,,$$

or

$$\mathbf{H}^s(\mathbf{r}_g, \mathbf{r}_s) = -\int_s \sigma_o\, O(\mathbf{r}) E_\phi(\mathbf{r}, \mathbf{r}_s)\, \mathbf{G}_H(\mathbf{r}_g, \mathbf{r}) dr dz\,. \tag{3-1-7}$$

Where $\mathbf{H}^s = \mathbf{H} - \mathbf{H}^p$ and $\mathbf{H}^p$ is the primary magnetic field in a homogeneous whole space generated by a vertical magnetic dipole. Now the Green's function $\mathbf{G}_H$ relates the induced circular current loop with the magnetic field anywhere in the space ($\mathbf{G}_H = (G_{Hr}, G_{Hz})$).

The Green's functions G_{Hr} and G_{Hz} are the same as the magnetic field excited by a unit current loop source in a homogeneous space and also can be found from Wait and Hill (1980).

$$G_{Hr}(\mathbf{r},\mathbf{r}') = -\frac{r'}{2}\frac{\partial}{\partial z}\int_0^\infty e^{-\gamma|z-z'|}\frac{\lambda}{\gamma}J_1(\lambda r')J_1(\lambda r)\,d\lambda; \tag{3-1-8a}$$

$$G_{Hz}(\mathbf{r},\mathbf{r}') = \frac{r'}{2}\int_0^\infty e^{-\gamma|z-z'|}\frac{\lambda^2}{\gamma}J_1(\lambda r')J_0(\lambda r)\,d\lambda. \tag{3-1-8b}$$

If equation (3-1-7) is rewritten into its horizontal and vertical magnetic field components $H_r^s(\mathbf{r}_g,\mathbf{r}_s)$ and $H_z^s(\mathbf{r}_g,\mathbf{r}_s)$ at the receiver point $\mathbf{r}_g$ due to a source at $\mathbf{r}_s$,

$$H_r^s(\mathbf{r}_g,\mathbf{r}_s) = -\sigma_o\int_s O(\mathbf{r})E_\phi(\mathbf{r},\mathbf{r}_s)G_{Hr}(\mathbf{r}_g,\mathbf{r})\,drdz \tag{3-1-9a}$$

and

$$H_z^s(\mathbf{r}_g,\mathbf{r}_s) = -\sigma_o\int_s O(\mathbf{r})E_\phi(\mathbf{r},\mathbf{r}_s)G_{Hz}(\mathbf{r}_g,\mathbf{r})drdz\,. \tag{3-1-9b}$$

3.2 Forward numerical modeling

The electromagnetic response in a cylindrically symmetrical medium is computed to furnish the necessary synthetic data for later inversion analysis. To do this, the integral equation derived in the last section for the electric field on the target is discretized to form a linear system of equations which are then solved by computer. Physical modeling results are used to verify the numerical data.

3.2.1 Numerical modeling

In the forward problem, the object function is given and the unknown in equation (3-1-5) is E_ϕ. Let $\mathbf{r}$ be a point on the target and discretize the inhomogeneity into N cells. The electric field can be readily solved for if one assumes that in each cell the electric field is constant. From equation (3-1-5), the electric field on the j–th cell satisfies

$$E_{\phi_j} = E^p_{\phi_j} - \sum_{i=1}^{N} \sigma_o O_i E_{\phi_i} \int_{i-th\ cell} G(\mathbf{r}', \mathbf{r})\, dr dz \ , \tag{3-2-1}$$

where the integration is evaluated numerically on the $i-th$ cell in both the radial and depth directions. There are N such equations for N unknowns. After solving the system of linear equations for the electric field in all the N cells, the magnetic field can be calculated from equations (3-1-9a) and (3-1-9b). By discretizing these two equations, numerical integrations are carried out over the N cells so that the secondary magnetic field at $i-th$ observation point is

$$H^s_{r_i} = -\sigma_o \sum_{j=1}^{N} O_j E_{\phi_j} \int_{j-th\ cell} G_{Hr}(\mathbf{r}_g, \mathbf{r})\, dr\ dz \tag{3-2-2a}$$

and

$$H^s_{z_i} = -\sigma_o \sum_{j=1}^{N} O_j E_{\phi_j} \int_{j-th\ cell} G_{Hz}(\mathbf{r}_g, \mathbf{r})\, dr dz \ . \tag{3-2-2b}$$

Simpson integration of the Green's function is carried out over each cell to increase the accuracy of the result.

3.2.2 Verification by physical modeling

To verify the numerical computations, two physical modeling data sets are used for the purpose of comparison. Because of the limitations of the available physical modeling facility, only cases with conductive targets in a free space are considered.

The frequency domain relationship between the parameters of a scale model and that of its corresponding full scale system can be found from Frischknecht (1988, p368).

$$\sigma' f' l'^2 = \sigma f\ l^2 ,$$

where f, σ and l are correspondingly the frequency, conductivity and characteristic dimension of the full scale system while f', σ' and l' are those in the scale model.

In this experiment the frequency scaling, or f/f', is set to one. The relation between the characteristic space dimension is 1 cm in the physical scale model to 20 meters in the full scale system ($l/l' = 2000/1$). Thus according to the above formula, the conductivity scaling factor $\sigma/\sigma' = 1/(4\times10^6)$. The material used in the scale model is lead, which has a conductivity of $4.56\times10^6\ S/m$, and therefore $\sigma = 1.14\ S/m$. The digital instrument reading here is accurate up

to the third digit. While the accuracy of the target size and positioning is 5 mm or 1 meter in full scale.

Figure 3-2-1a shows the first full scale model of a ring shaped target with inner and outer radii of 64 and 120 meters respectively. Its thickness is 3.6 meters and its conductivity is 1.14 S/m. The source and receiver are along the axis of symmetry and 120 meters away from, and on opposite sides of, the conductor. Both the source and receiver are fixed and they point in the z-direction. The results plotted in Figure 3-2-1b are the real and imaginary parts of the total magnetic field, normalized by the primary one, as a function of operating frequency.

The second case checked is presented in Figure 3-2-2. The model (Figure 3-2-2a) consists of a circular disk of 10.4 meters thick and 100 meters radius. The target conductivity is 1.14 S/m. The source lies along the axis of symmetry and is fixed at 60 meters from the conductor. The receiver is movable along a line parallel to, and 140m away from, the axis of symmetry. The operating frequency is $3K$ Hz. The numerical and physical modeling comparison is given in Figure 3-2-2b.

Both examples show fairly good agreement between the numerical and physical modeling results. A number of other similar experiments were also conducted for other geometries. The comparison of these numerical and physical modeling results was also satisfactory.

3.2.3 Influence of the source-receiver array configuration

The source-receiver arrays chosen are critical in collecting the necessary information for data interpretation. Our numerical code allows us to demonstrate the characteristics of the different subsurface source-receiver array configurations. A vertical magnetic dipole (VMD) source and vertical magnetic field measurements are considered here because of the vertical borehole orientation. The basic model investigated is a ring-shaped target with a 60m by 20m cross-section. The source borehole is coaxial with the target while the receiver is either in the same well or in another one 100m away. The target conductivity is 0.02 S/m and the background conductivity is 0.01 S/m. An operating frequency of $5K$ Hz is used. These parameters will be kept constant unless otherwise specified.

The first array studied is a cross-hole source-receiver pair moving in parallel down the two boreholes (Figure 3-2-3). The secondary magnetic response is normalized by the amplitude of the primary vertical magnetic field at the receiver. It is found that the two curves corresponding to a source-target separation (D) of 10m or 20m show only a small difference in amplitude. Nevertheless, the anomaly defines the vertical position of the target quite well because it peaks at the target depth.

Next, let us look at the same model (Figure 3-2-4) with a fixed dipole source in one hole and a moving receiver in the other. The rest of the model parameters are the same as those shown in Figure 3-2-3. The amplitude of primary field at the source level is chosen as the normalization factor. Although, the maximum peak-to-peak amplitudes are the same for the two different source-target separations, the curve shapes now show a more significant difference. The response for the target closer to the source has a wider shape. This example shows that the anomaly shape is very important in data inversion. The outcomes in Figures 3-2-3 and -4 suggest that if we use several fixed source positions and take measurements along another borehole, it is possible to resolve a single target. However, in general, the response is very insensitive to the lateral position of the target.

If both the source and receiver are in the same borehole, the electromagnetic response of the targets is found to be much more dependent on the target lateral position. Figure 3-2-5 is an example involving a source-receiver pair with a 10m fixed vertical separation moving in a single hole. As the borehole-target distance varies from 10 meters to 20 meters, a significant change in the response is observed. Thus, to increase the lateral resolution the back-scattered fields should also be measured. Since the curve is normalized by the primary vertical magnetic field of a source only 10 meters away, the relative secondary response is very small although its absolute value is at least of the same order as that for the cross-hole cases.

The effect of different operating frequency on the target response is illustrated in Figure 3-2-6 using the same model as that shown in Figure 3-2-5 with the source-receiver in the same borehole. The target edge is again either 10m or 20m away from the well. Two frequencies of $5K$ Hz and $20K$ Hz are compared. The amplitude of the secondary magnetic response is normalized by the amplitude of the primary field at the receiver site. The ratio of the

maximum amplitudes of 10m and 20m target-borehole separation is about 3.0 for f= 5KHz and 3.7 for f= 20KHz. The contribution from a distant conductor is relatively larger at the lower frequency. Thus, in order to achieve necessary resolution, use of multiple operating frequencies is advisable.

The numerical experiments with different source-receiver array configurations and operating frequencies show that: (1) The cross hole source-receiver array has poor resolution in the lateral direction. (2) Both the shape and the peak-to-peak values of the measured response are important in data interpretation. (3) To resolve the lateral position better, the back scattered field should also be measured, i.e. source and receiver in a single hole. (4) Multiple operating frequencies may increase the resolution, especially in the single hole case.

One should note that these findings regarding array sensitivity reinforce the conclusions derived from the wave number domain coverage approach in the previous chapter for the 2-D Cartesian model. Although the above conclusions are based on a few numerical examples, a more mathematically rigorous analysis would confirm them

3.3 Inverse solution based on the weak scattering approximation

In this section, the integral relation in equation (3-1-9) will be simplified by applying the Born approximation under a weak scattering assumption. Then Fourier transforms are used to find the corresponding wave number domain relationship. With an additional far field approximation, the derived formula is found to be the same as the 2-D expressions discussed in the previous chapters.

3.3.1 Born approximated integral equation in wave number domain

Using a procedure similar to that described for deriving the two-dimensional tomographic inversion, the Born approximation is introduced here by assuming that the problem satisfies the weak scattering condition. After replacing the total electric field $E_\phi(\mathbf{r},\mathbf{r}_s)$ inside the integral sign of equation (3-1-9) with the primary field $E_\phi^p(\mathbf{r},\mathbf{r}_s)$, equation (3-1-9) becomes

$$H_r^s(\mathbf{r}_g,\mathbf{r}_s) = -\int_s \sigma_o\, O(\mathbf{r}) E_\phi^p(\mathbf{r},\mathbf{r}_s)\, G_{Hr}(\mathbf{r}_g,\mathbf{r})\, dr dz \qquad (3\text{-}3\text{-}1a)$$

and

$$H_z^s(\mathbf{r}_g, \mathbf{r}_s) = -\int_s \sigma_o \, O(\mathbf{r}) E_\phi^p(\mathbf{r}, \mathbf{r}_s) G_{Hz}(\mathbf{r}_g, \mathbf{r}) drdz \, . \tag{3-3-1b}$$

The primary electric field for a vertical magnetic dipole source of unit strength can be found from Ward and Hohmann (1988, p176)

$$E_\phi^p(\mathbf{r}, \mathbf{r}_s) = -\frac{i\omega\mu}{4\pi} \left[\frac{r}{R^3} (1 + ik_o R) e^{-ik_o R}\right], \tag{3-3-2}$$

where $R = \sqrt{r^2 + (z - z_s)^2}$ and $r_s = 0$.

For the cross-hole source-receiver configuration, the next step is to take Fourier transforms of equation (3-3-1) with respect to z_s and z_g. Noting that $\mathbf{r}_g = (r_g, z_g)$ and $\mathbf{r}_s = (r_s, z_s)$, we have

$$H_r^s(r_g, k_g; r_s, k_s) = -\int_s \sigma_o \, O(r, z) E_\phi^p(r, z; r_s, k_s) G_{Hr}(r_g, k_g; r, z) \, drdz \tag{3-3-3a}$$

and

$$H_z^s(r_g, k_g; r_s, k_s) = -\int_s \sigma_o \, O(r, z) E_\phi^p(r, z; r_s, k_s) G_{Hz}(r_g, k_g; r, z) \, drdz \, . \tag{3-3-3b}$$

The variables k_s and k_g are the Fourier domain wave numbers corresponding to space domain z_s and z_g values respectively. The transformed primary E-field, $E_\phi^p(r, z; r_s, k_s)$, can be derived readily from equation (3-3-2) from the definition of the Fourier transform and by using a relation provided by Gradshteyn and Ryzhik (formula 6.616.4, p710, 1980)

$$E_\phi^p(r, z; r_s, k_s) = \frac{\omega\mu}{2\pi} \gamma_s \, e^{-ik_s z} K_1(ir\gamma_s), \tag{3-3-4}$$

where K_1 is the first order modified Bessel function of the second kind and γ_s is defined as

$$\gamma_s^2 = k_o^2 - k_s^2 .$$

The transforms of the Green's functions for the magnetic fields are deduced from equation (3-1-8). Two relations from Gradshteyn and Ryzhik (equation 7 of p1147 and formula 6.541 of p679, 1980) are applied in the derivation. The horizontal component of the Green's function in Fourier domain is then given by

$$G_{Hr}(r_g, k_g; r, z) = -irk_g e^{-ik_g z} \begin{cases} I_1(ir_g\gamma_g) K_1(ir\gamma_g); & 0<r_g<r \\ I_1(ir\gamma_g) K_1(ir_g\gamma_g); & 0<r<r_g \end{cases} \tag{3-3-5a}$$

with

$$\gamma_g^2 = k_o^2 - k_g^2.$$

I_1 and K_1 are the first order modified Bessel functions of the first and second kinds respectively. The vertical component of the Green's function in the Fourier domain is

$$G_{Hz}(r_g, k_g; r, z) = -re^{-ik_g z} \frac{\partial}{\partial r} \begin{cases} I_o(ir_g\gamma_g) K_o(ir\gamma_g); & 0<r_g<r \\ I_o(ir\gamma_g) K_o(ir_g\gamma_g); & 0<r<r_g \end{cases}, \tag{3-3-5b}$$

where I_o is the zero-th order modified Bessel function of first kind and K_o is the zero-th order modified Bessel function of the second kind.

In the cross hole case, $0<r<r_g$. Therefore

$$G_{Hr}(r_g, k_g; r, z) = -irk_g e^{-ik_g z} I_1(ir\gamma_g) K_1(ir_g\gamma_g) \tag{3-3-6a}$$

and

$$G_{Hz}(r_g, k_g; r, z) = -ir\gamma_g e^{-ik_g z} I_1(ir\gamma_g) K_o(ir_g\gamma_g). \tag{3-3-6b}$$

Put equation (3-3-4) and equation (3-3-6) into equation (3-3-3) to obtain the following wave number domain relationship between the secondary response and the object function.

$$H_z^s(r_g, k_g; r_s, k_s) = \frac{-k_o^2}{2\pi}\gamma_s\gamma_g K_o(ir_g\gamma_g) \int O(\mathbf{r}) re^{-i(k_s+k_g)z} K_1(ir\gamma_s) I_1(ir\gamma_g)\, drdz \ . \tag{3-3-7a}$$

$$H_r^s(r_g, k_g; r_s, k_s) = \frac{-k_o^2}{2\pi}\gamma_s k_g K_1(ir_g\gamma_g) \int O(\mathbf{r}) re^{-i(k_s+k_g)z} K_1(ir\gamma_s) I_1(ir\gamma_g)\, drdz \ . \tag{3-3-7b}$$

The above equations are for the cross-hole situation but similar relationships can also be derived for other source-receiver combinations.

Now, let us rearrange equation (3-3-7) into

$$\frac{H_z^s(r_g, k_g; r_s, k_s)}{\frac{-k_o^2}{2\pi}\gamma_s\gamma_g K_o(ir_g\gamma_g)} = \int O(\mathbf{r}) re^{-i(k_s+k_g)z} K_1(ir\gamma_s) I_1(ir\gamma_g)\, drdz \tag{3-3-8a}$$

and

$$\frac{H_r^s(r_g, k_g; r_s, k_s)}{\frac{-k_o^2}{2\pi}\gamma_s k_g K_1(ir_g\gamma_g)} = \int O(\mathbf{r}) r e^{-i(k_s+k_g)z} K_1(ir\gamma_s) I_1(ir\gamma_g)\, dr dz \ . \qquad (3\text{-}3\text{-}8b)$$

It is found that the right hand sides of these equations are identical while the left hand sides represent the filtered measurements. Thus, if a data profile along the entire receiver borehole is available, one of the above two equations is redundant. This can also be proven to be true without using the Born approximation.

3.3.2 Wave number domain coverage under far field approximation

In order to understand the quality of the reconstructed image, the wave number domain coverage of the object function is examined by using an asymptotic expansion of the Bessel functions for the far field. From Stinson (1976, p267), we have the following relations for any integer n

$$I_n(x) = \sqrt{\frac{1}{2\pi x}}\, e^x \qquad \text{for } |x| \to \infty \quad \text{and} \quad |x| \gg |n| \qquad (3\text{-}3\text{-}9a)$$

$$K_n(x) = \sqrt{\frac{\pi}{2x}}\, e^{-x} \qquad \text{for } |x| \to \infty \quad \text{and} \quad |x| \gg |n| \qquad (3\text{-}3\text{-}9b)$$

It should be mentioned that the far-field approximation in EM has much less validity than that in seismic method. Because of the severe attenuation of high frequency EM fields in a conductive medium, the argument in $I_n(x)$ or $K_n(x)$ can not be very large in the practical sense. However, analysis shows that the far-field assumption is still acceptable. The following table is for the absolute value of the relative error for the modified Bessel function under the far field approximation (calculated from the handbook by National Bureau of Standards, 1972).

Table 3-4-1 Relative error of the Bessel functions under far-field approximation

	$x = 1$	$x = 2$	$x = 10$	$x = 20$
$K_0(x)$	9.5%	5.3%	1.2%	0.6%
$K_1(x)$	23.%	14.%	3.5%	1.8%
$I_0(x)$	14.%	8.6%	1.3%	0.6%
$I_1(x)$	92.%	31.%	4.0%	1.9%

To be specific for our numerical examples, the absolute value of the arguments, i.e. $|ir\gamma_s|$ and $|ir\gamma_g|$, varies between 0 to about 30. Therefore, it is expected that the outcome is within reasonable error range if the target is a certain distance away from the borehole. The more convincing verification comes from later numerical experiments which show that the approximation is valid.

Using the far field approximation, we can substitute equation (3-3-9) into equation (3-3-8a) to arrive at,

$$H_z^s(r_g, k_g; r_s, k_s)\left(\frac{4i\sqrt{2\pi i}}{-k_o^2\sqrt{\gamma_s}}\right)\sqrt{r_g}\, e^{ir_g\gamma_g} = \int O(\mathbf{r}) e^{-i(k_s+k_g)z}\, e^{-ir(\gamma_s-\gamma_g)}\, drdz \ . \qquad (3\text{-}3\text{-}10)$$

After making the following substitutions,

$$k_s + k_g = k_z \ ; \qquad i(\gamma_s - \gamma_g) = s_r, \qquad (3\text{-}3\text{-}11)$$

equation (3-3-10) becomes

$$H_z^s(r_g, k_g; r_s, k_s)\left(\frac{4i\sqrt{2\pi i}}{-k_o^2\sqrt{\gamma_s}}\right)\sqrt{r_g}\, e^{ir_g\gamma_g} = \int O(\mathbf{r}) e^{-ik_z z}\, e^{-rs_r}\, drdz \ . \qquad (3\text{-}3\text{-}12)$$

A comparison of equation (3-3-12) with the corresponding two-dimensional situation discussed in Chapter 2 immediately shows that this equation is the same as equation (2-2-11) except for the fact that on the left hand sides different weighting factors are applied to the measurements. Therefore, the object function $O(\mathbf{r})$ can be readily derived by the inverse Laplace transform in the lateral direction and the inverse Fourier transform in the vertical direction of equation (3-3-12).

$$O(\mathbf{r}) = \frac{1}{(2\pi)^2 i}\int [H_z^s(r_g, k_g; r_s, k_s)(\frac{4i\sqrt{2\pi i}}{-k_o^2\sqrt{\gamma_s}})\sqrt{r_g}\, e^{ir_g\gamma_g}]\, e^{rs_r}\, e^{ik_z z}\, dk_z\, ds_r\,. \quad (3\text{-}3\text{-}13)$$

Therefore, the most important finding is that the discussion in Chapter 2 on the wave number domain coverage of the object function is also valid here. Inevitably, for the cross-hole source-receiver configuration, we will expect relatively poorer resolution in the horizontal direction than that obtainable along the vertical. For the single hole configuration, where the source and receiver are in the same borehole, expression similar to that of 2-D Cartesian model can also be derived. The wave number domain coverages are identical if a far-field assumption is applied to the cylindrical symmetry model.

3.4 Tomographic inversion of synthetic data

We now go on to the numerical experiments in EM tomography. First, we want to show that the 2-D Cartesian formulation discussed in the previous Chapter can be used in a cylindrically symmetric medium after a geometric correction is applied. Then we consider different source-receiver array combinations without applying the far field approximation.

The cylindrically symmetrical model in these numerical experiments has a background conductivity of $0.01\,S/m$. An operating frequency of $20K$ Hz is chosen. 32 source and 32 receiver positions are used in the cross-hole configuration in all possible source-receiver combinations. The source or receiver spacing is 10 meters. The image area (100m by 160m) is the central part of the $100\,m \times 310\,m$ area covered by the source and receiver array.

3.4.1 2-D Cartesian model solution after geometric correction

Under the additional far field approximation the cylindrical symmetry problem becomes analogous to the 2-D Cartesian one. Equation (2-2-11), after the modification for a geometric factor, can be used to solve it. Rewrite equation (3-3-12) for the cylindrical symmetry model

$$H_z^s(r_g, k_g; r_s, k_s)(\frac{4i\sqrt{2\pi i}}{-k_o^2\sqrt{\gamma_s}})\sqrt{r_g}\, e^{ir_g\gamma_g} = \int O(\mathbf{r}) e^{-ik_z z}\, e^{-rs_r}\, dr dz\ , \quad (3\text{-}3\text{-}14a)$$

and compare to equation (2-2-11) for the 2-D Cartesian model

$$E^s(x_g, k_g; x_s, k_s)\frac{4\gamma_g\gamma_s}{-i\,\omega\mu k_o^2} e^{(-i\gamma_s x_s + i\gamma_g x_g)} = \int_S O(\mathbf{r}) \exp[-s_x x - ik_z z]\, dx dz\ , \quad (3\text{-}3\text{-}14b)$$

where $r_g = x_g$ (the borehole separation) and $x_s = 0$. Then the factor for geometric correction in the 2-D algorithm for the cylindrical symmetry data is then

$$\frac{(4i\sqrt{2\pi i}\,\sqrt{r_g})/(-k_o^2\sqrt{\gamma_s})}{(4\gamma_g\,\gamma_s)/(-i\,\omega\mu k_o^2)} \tag{3-3-15}$$

Figure 3-4-1 shows a horizontal disk model of 80 meter diameter and 10 meter thickness. Its conductivity is twice the background. The synthetic data, i.e. the z-component of the magnetic anomaly with vertical magnetic dipole source excitation, generated for this model is first inverted using the 2-D Cartesian model with a correction for the geometric effect. The resulting image is shown in Figure 3-4-1b. It is found that the target is basically resolved except that the area near the source borehole does not show the correct conductivity value. This is caused by the invalid use of the far field approximation when the target position does not actually satisfy it. Therefore, it is also necessary to program the inversion problem without the far field assumption.

Again, because of the instability of the inverse Laplace transform, equation (3-3-13) can only be utilized to study the system characteristics. The actual way of solving for the object function, $O(\mathbf{r})$, is to discretize the integral equations given by equation (3-3-8) without the far field approximation. The resulting linear system of equations is inverted with the same constrained least squares approach as was used for the two-dimensional Cartesian geometry. One has to note that constraints are most necessary for improvements in both resolution and stability. Figure 3-4-1c shows the new inversion result (without the far field approximation) where it can be clearly seen that the edge close to the source borehole now is resolved much better than previously.

These numerical experiments show that the cylindrical symmetry problem can be treated as a 2-D Cartesian geometry problem after a geometrical factor correction. Although the area near the source or receiver is not well resolved due to the invalidity of the far-field approximation, the approach is still valuable since one is usually interested in the area away from the borehole and the near field area can be resolved by other conventional logging techniques.

3.4.2 Cross-hole source-receiver array configuration

Next, we consider a fictitious enhanced oil recovery problem. The problem can be stated as the monitoring of saline water/oil front in a fracture zone sandwiched in a homogeneous formation. Since the oil has low electrical conductivity while the saline water has high conductivity, the front can be mapped if one can distinguish changes in the conductivity distribution. Figure 3-4-2 (a) gives the model parameters of a simplified problem. The target is 20 meters thick and the anomalous conductivity is assumed to be twice that of the background. Tests are carried out for the migration of the saline water to lateral distances of $Lx = 20, 40, 60, 100$ meters. The z-component of the EM response is used in this calculation and these synthetic data are generated from the exact numerical code calculating the EM response of cylindrically symmetrical medium discussed earlier in this chapter. The reconstructed images shown in Figure 3-4-2 (b) through (e) are not based on the far field approximation. The extent of the high conductivity anomaly can be mapped reasonably well.

We next vary the thickness of the anomalous conductor. The lateral extent is fixed at 60 meters (Figure 3-4-3a). The reconstructed images are shown in Figure 3-4-3b, Figure 3-4-3c and Figure 3-4-3d for thickness, Tz, values of 10, 20, and 40 meters. It is clearly seen that the reconstructed images can show the difference of target position, size, and conductivity reasonablely well. For different target conductivity, a model with a $60m \times 10m$ conductor is studied (Figure 3-4-4a). The reconstructed images are presented in Figure 3-4-4b, c, and d which correspond respectively to the conductivity values of $\sigma = 0.02, 0.04, 0.06 S/m$. The recovered conductivity is found to be smaller than the actual one while the size is larger than the model input. The frequency effect is demonstrated in Figure 3-4-5. For frequency 2.5, 10, and 20 KHz, the reconstructed images (Figure 3-4-5) are little different in quality since the target is horizontal. These three frequencies correspond to a borehole separation to skin depth ratio of approximately 1, 2, and 3.

3.4.3 Combination of cross-hole and single-hole source-receiver data

From the wave number domain coverage analysis of Chapter 2 and the comparison between 2-D Cartesian and cylindrical symmetry models given earlier in this Chapter, better

images should be achieved by combining the measurements of cross-hole and single hole source-receiver arrays. The sources will be assumed to be along the axis of symmetry of the medium while the receivers are either in another hole or in the same one as the source with all the possible combinations.

Figure 3-4-6 and Figure 3-4-7 are the reconstructed images of a 'ring' of a 60m by 20m cross-sectional area. This target is either 10 or 20 meters away from the source borehole. The solutions with the cross-hole source-receiver configuration for these two models are given in Figure 3-4-6b and Figure 3-4-7b. The images are somewhat blurred. The single-hole source-receiver arrangement results in the solutions shown in Figure 3-4-6c and Figure 3-4-7c. The side of the target closer to the source borehole is resolved quite accurately. Nevertheless, due to the attenuation characteristics of the EM wave in a conductive medium, the far side of the target from the single-hole measurements can not be defined correctly. With the combination of both source-receiver array configurations, much better images are arrived at as shown in Figure 3-4-6d and Figure 3-4-7d.

To summarize, we find in this chapter that the cross-hole audio frequency electromagnetic technique can be applied to recover the conductivity image in a cylindrical symmetry situation. Through theoretical and numerical analyses, the recovered conductivity distribution is shown to have similar characteristics to that with 2-D Cartesian geometry. Under the weak scattering and far field approximations, the wave number domain coverage of the object function is identical to that for the 2-D Cartesian geometry discussed in the last chapter. The coverage tells us that the maximum lateral resolution for the cross-hole source-receiver array is directly related to the maximum operating frequency. Due to severe attenuation associated with the high frequency electromagnetic field, however, the maximum operating frequency, and therefore the maximum lateral resolution, is limited. We also find that better images can be constructed by combining the single-hole source-receiver data with those from cross-hole array.

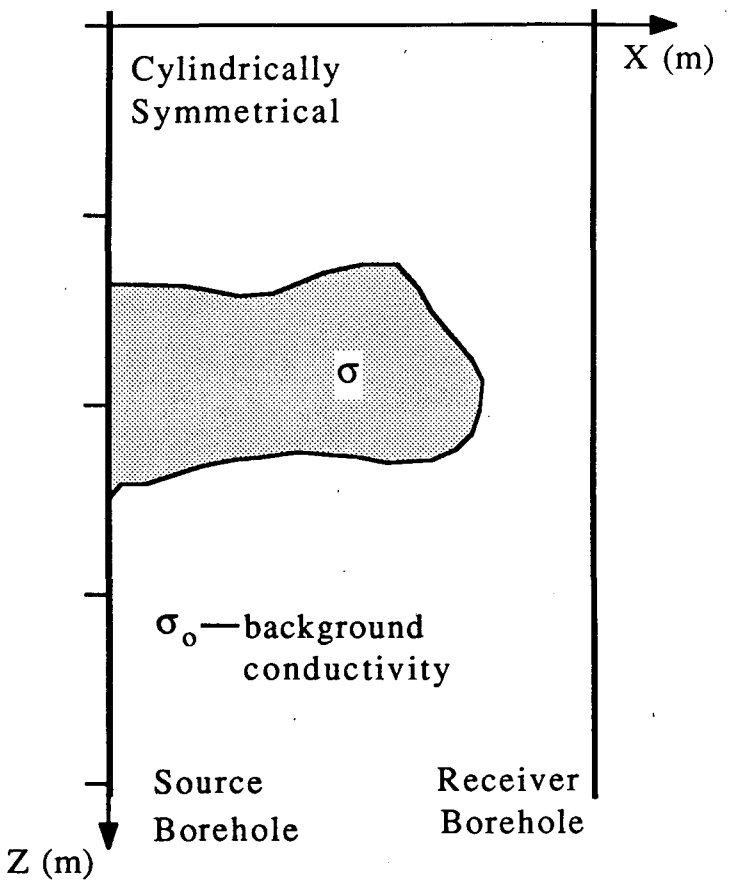

Figure 3-1-1 A cylindrical symmetry model

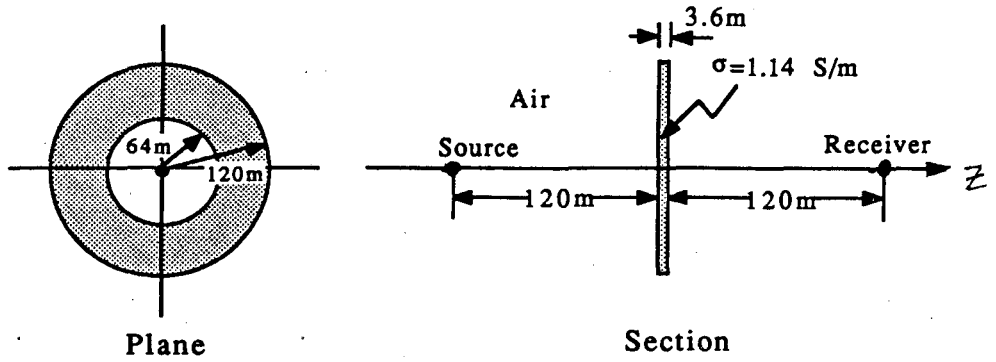

(a) Model

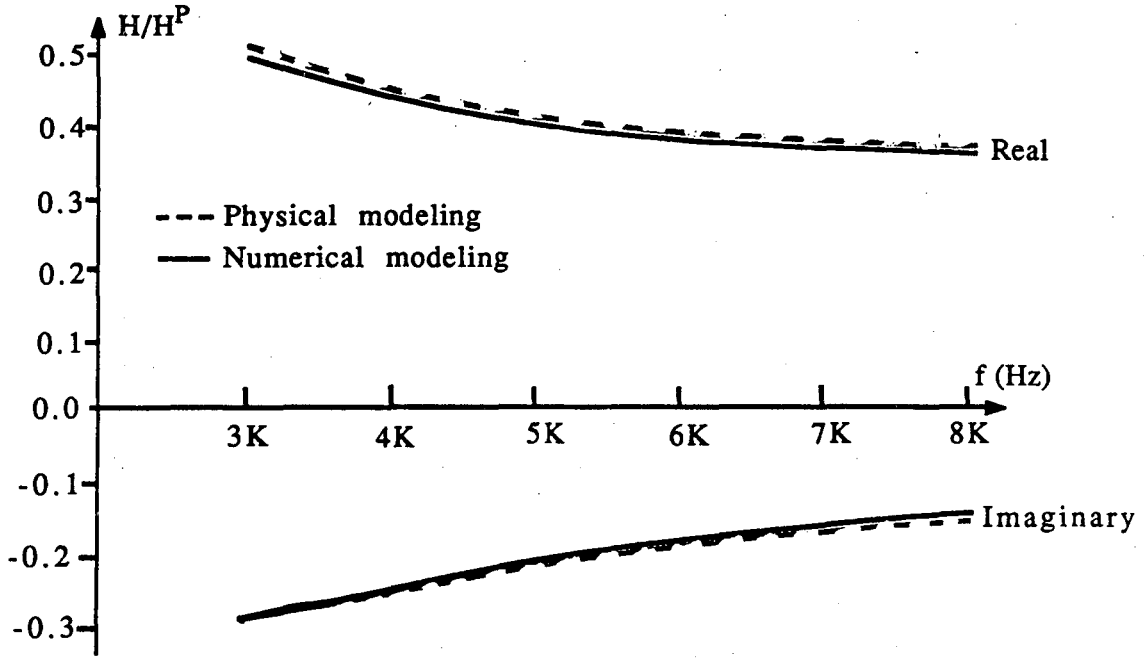

(b) Comparison

Figure 3-2-1 Comparison between numerical and physical modeling results for a ring shaped conductor

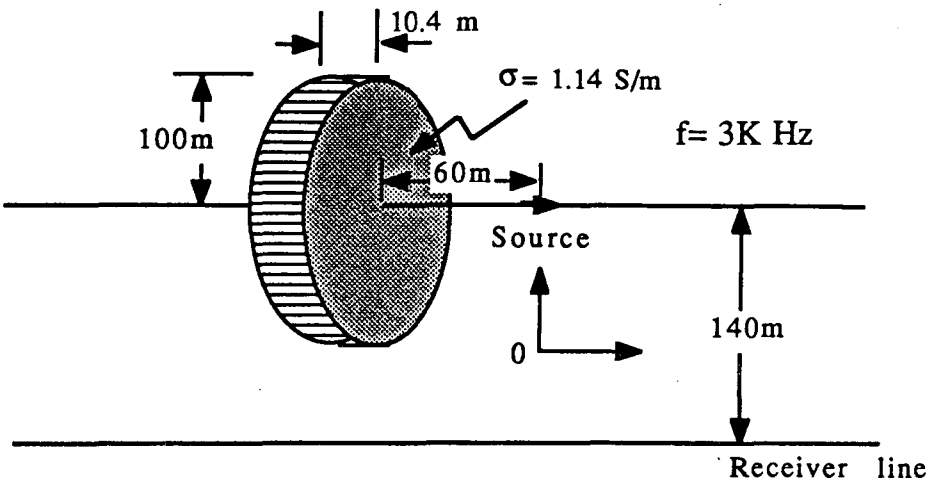

(a) Model

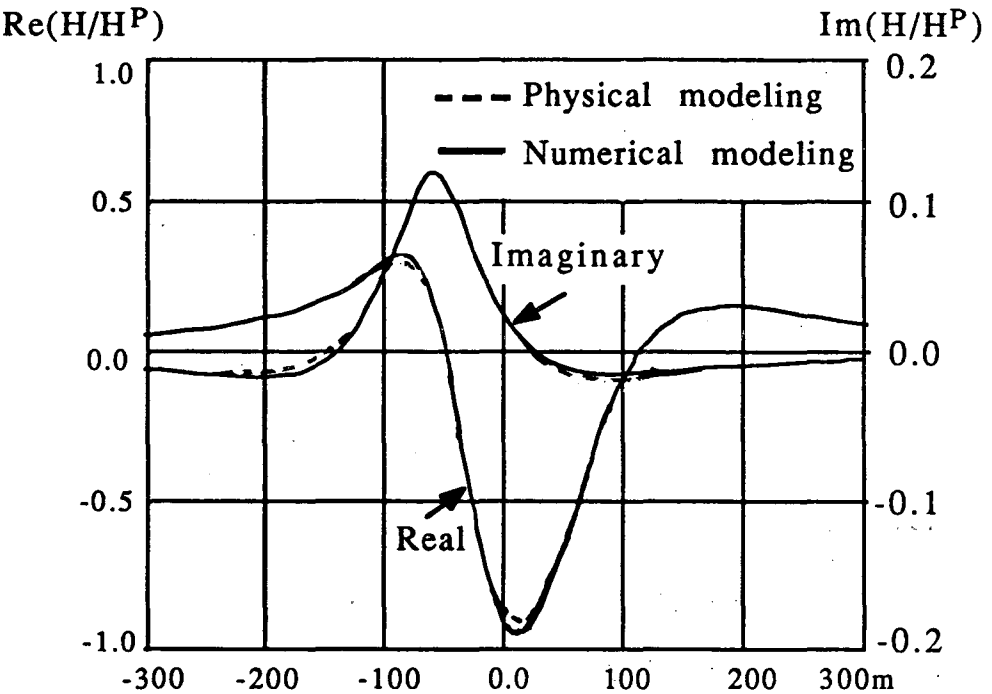

(b) Comparison

Figure 3-2-2 Comparison between numerical and physical modeling results for a disk shaped conductor

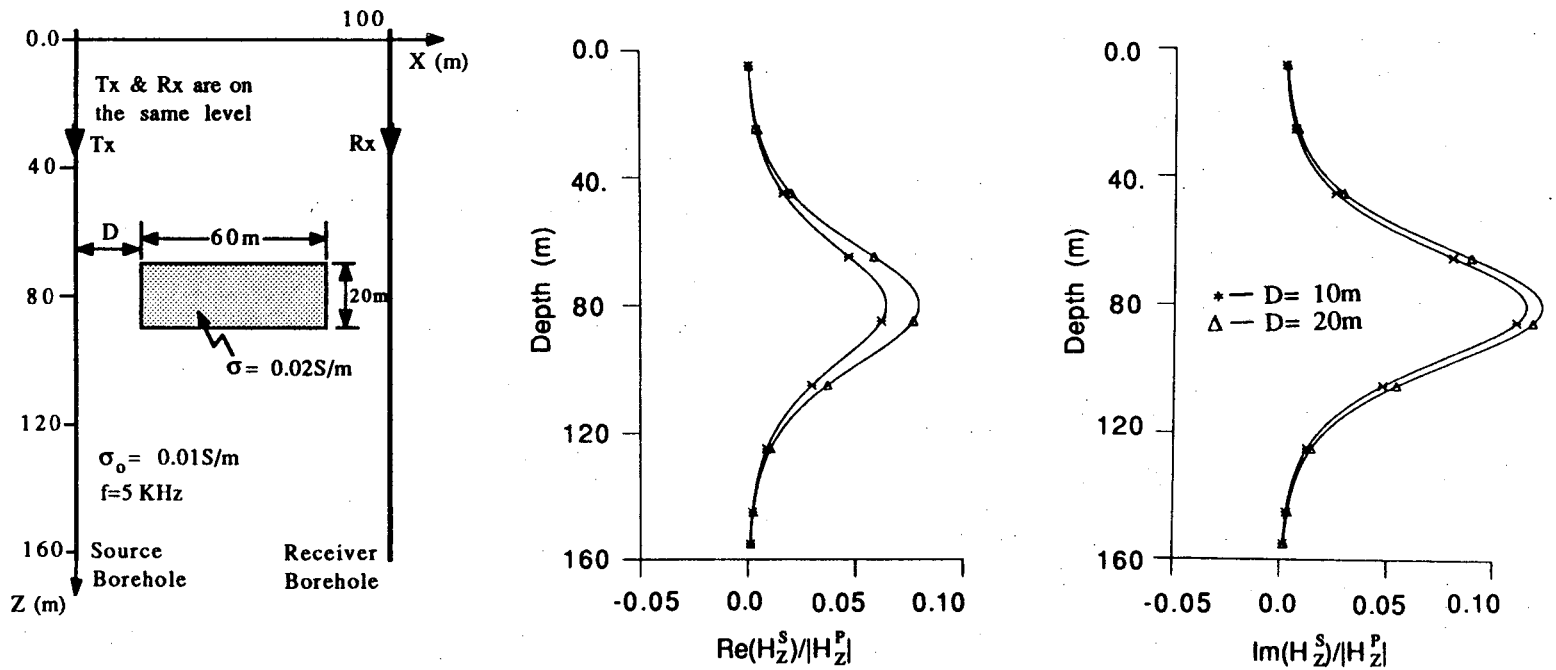

(a) Model

(b) Normalized magnetic field

Figure 3-2-3 Normalized secondary magnetic field response (z-component) for a crosshole VMD source and receiver at the same depth

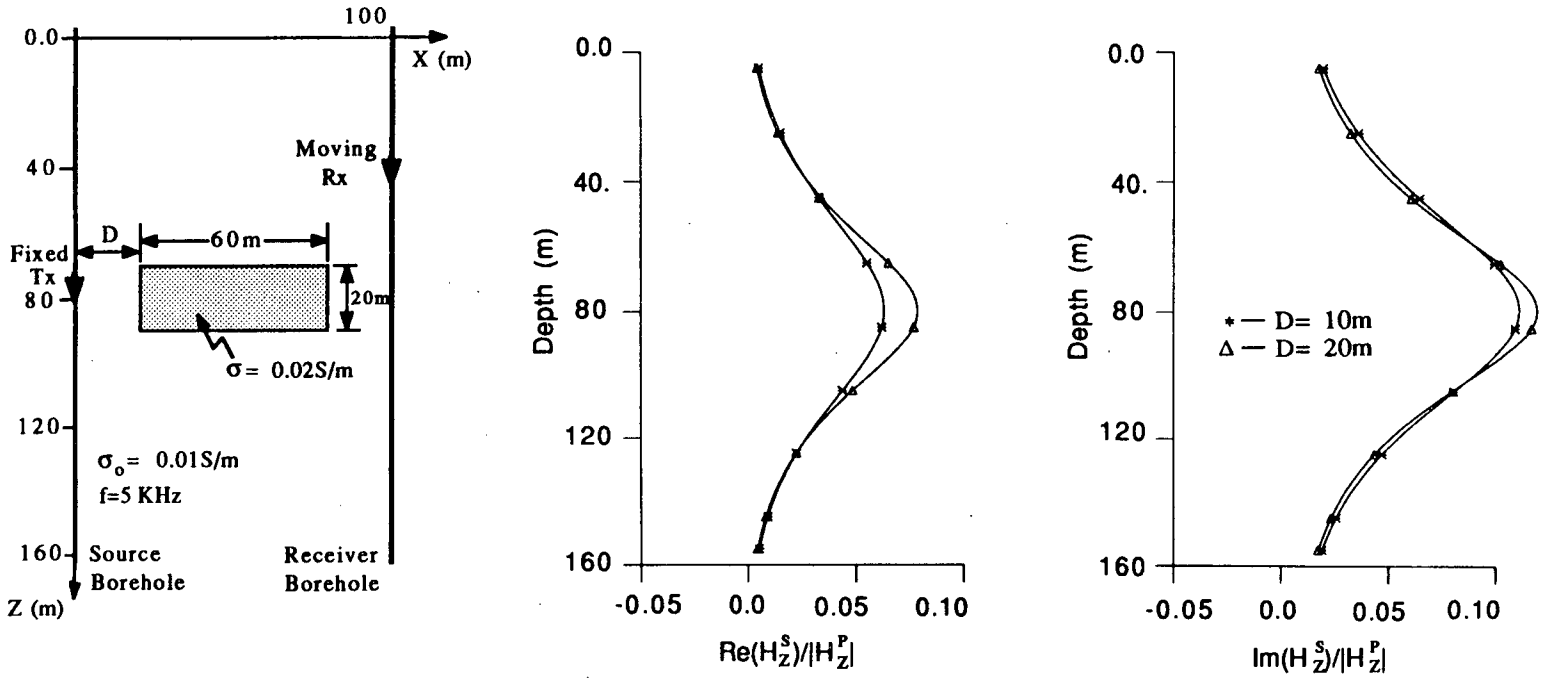

(a) Model

(b) Normalized magnetic field

Figure 3-2-4 Normalized secondary magnetic field response (z-component) for a crosshole fixed VMD source and a moving receiver

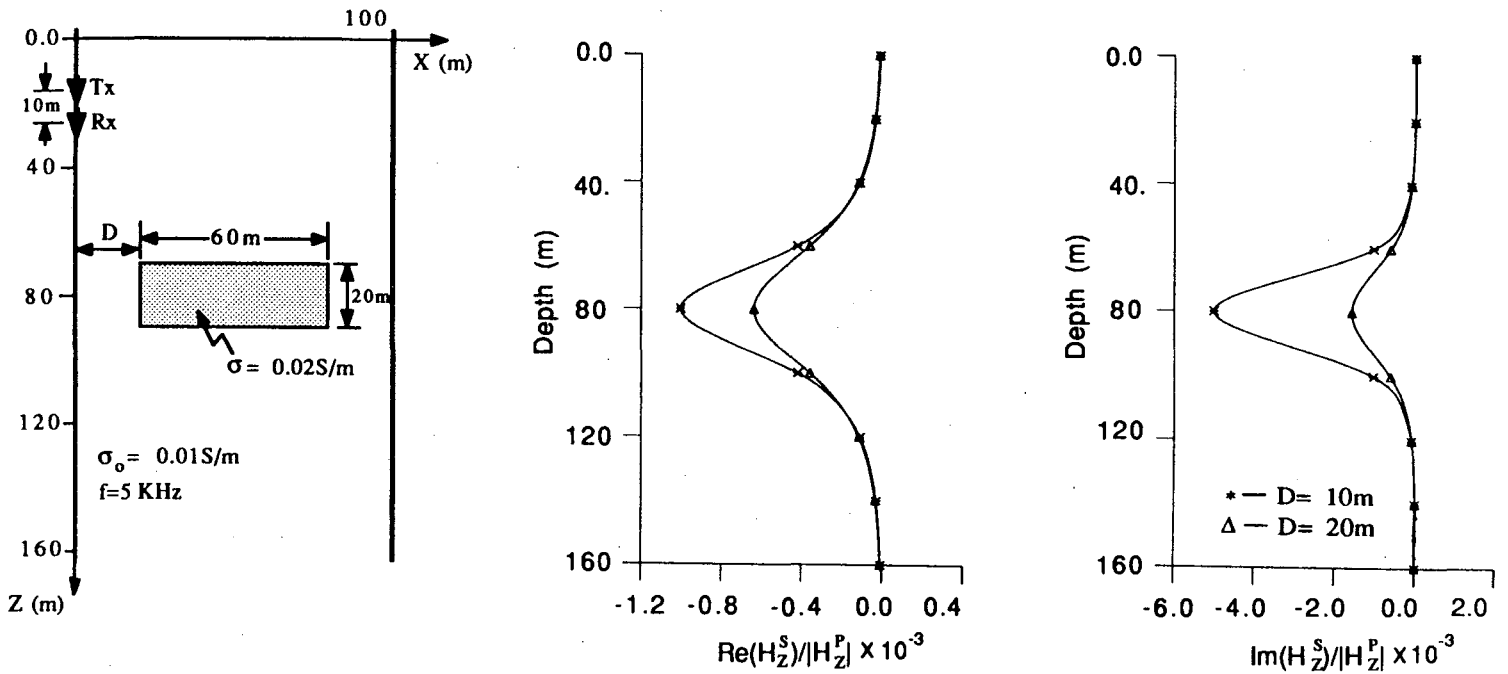

(a) Model

(b) Normalized magnetic field

Figure 3-2-5 Normalized secondary magnetic field response (z-component) for a tandem VMD source and receiver with fixed vertical separation of 10m

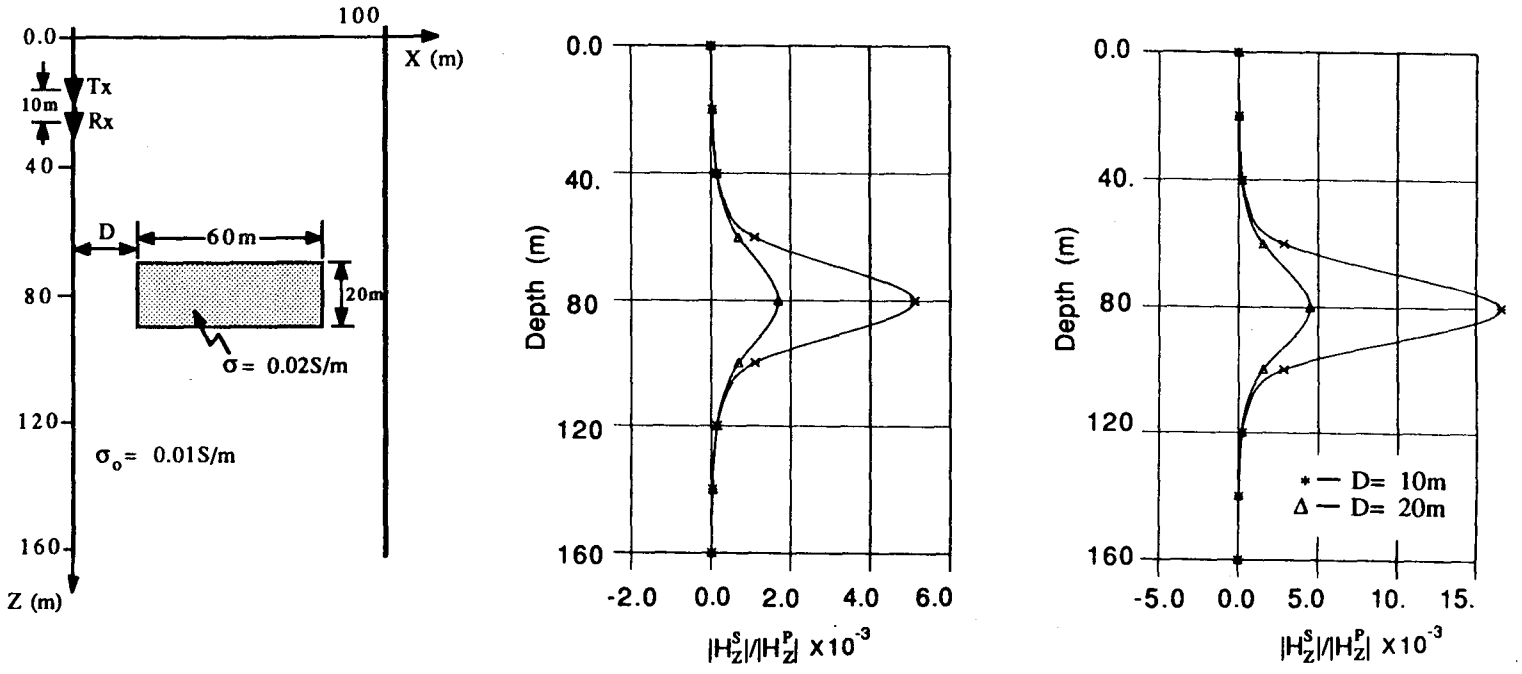

(a) Model

(b) f= 5K Hz

(c) f= 20K Hz

Figure 3-2-6 Normalized secondary magnetic field response (z-component) for a tandem VMD source and receiver with fixed vertical separation of 10m and two frequencies of 5K and 20K Hz

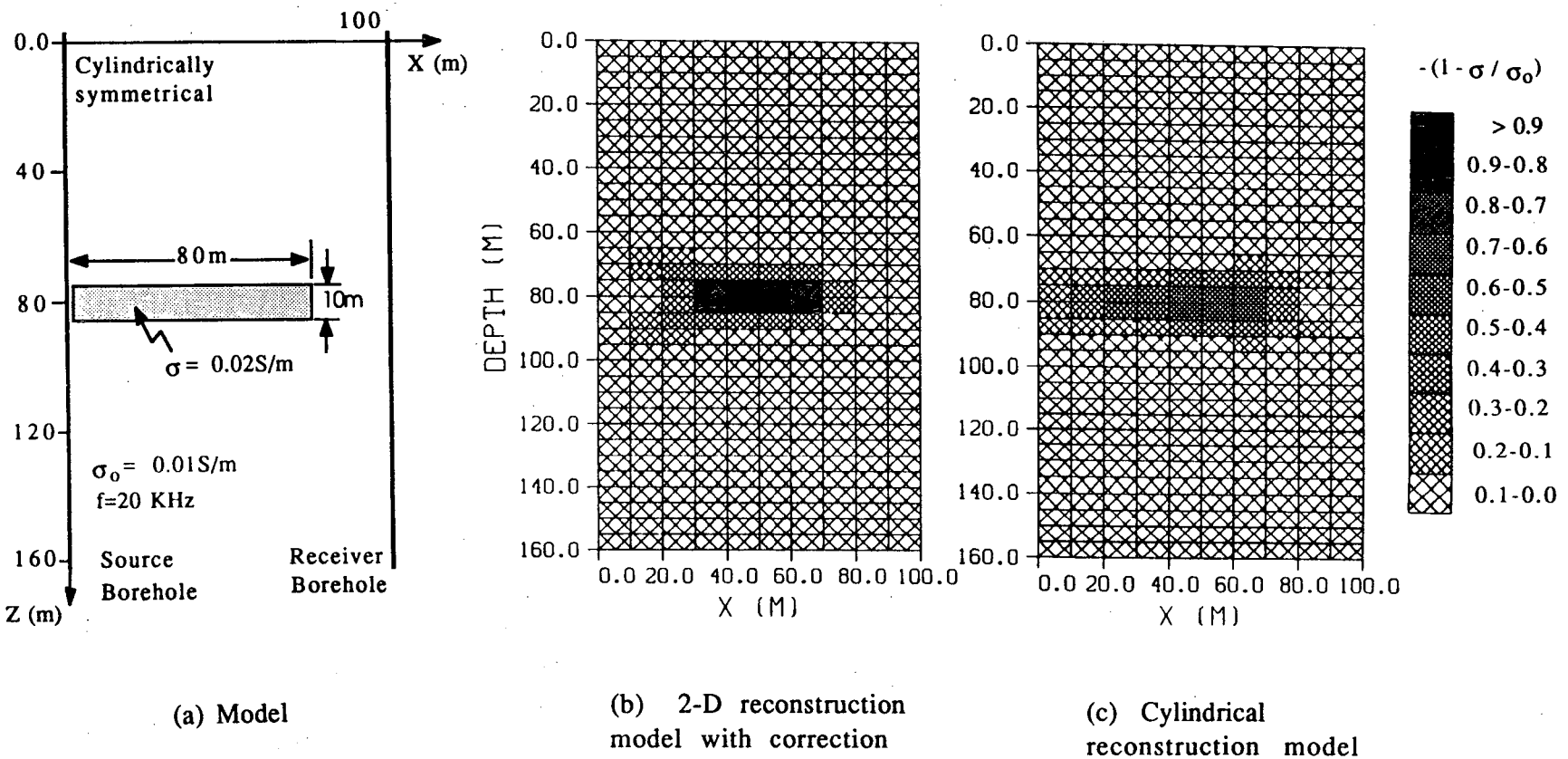

(a) Model

(b) 2-D reconstruction model with correction

(c) Cylindrical reconstruction model

Figure 3-4-1 Comparison of a cylindrical symmetry model reconstructed with the 2-D Cartesian (corrected by a geometric factor) code or with the cylindrical symmetry code

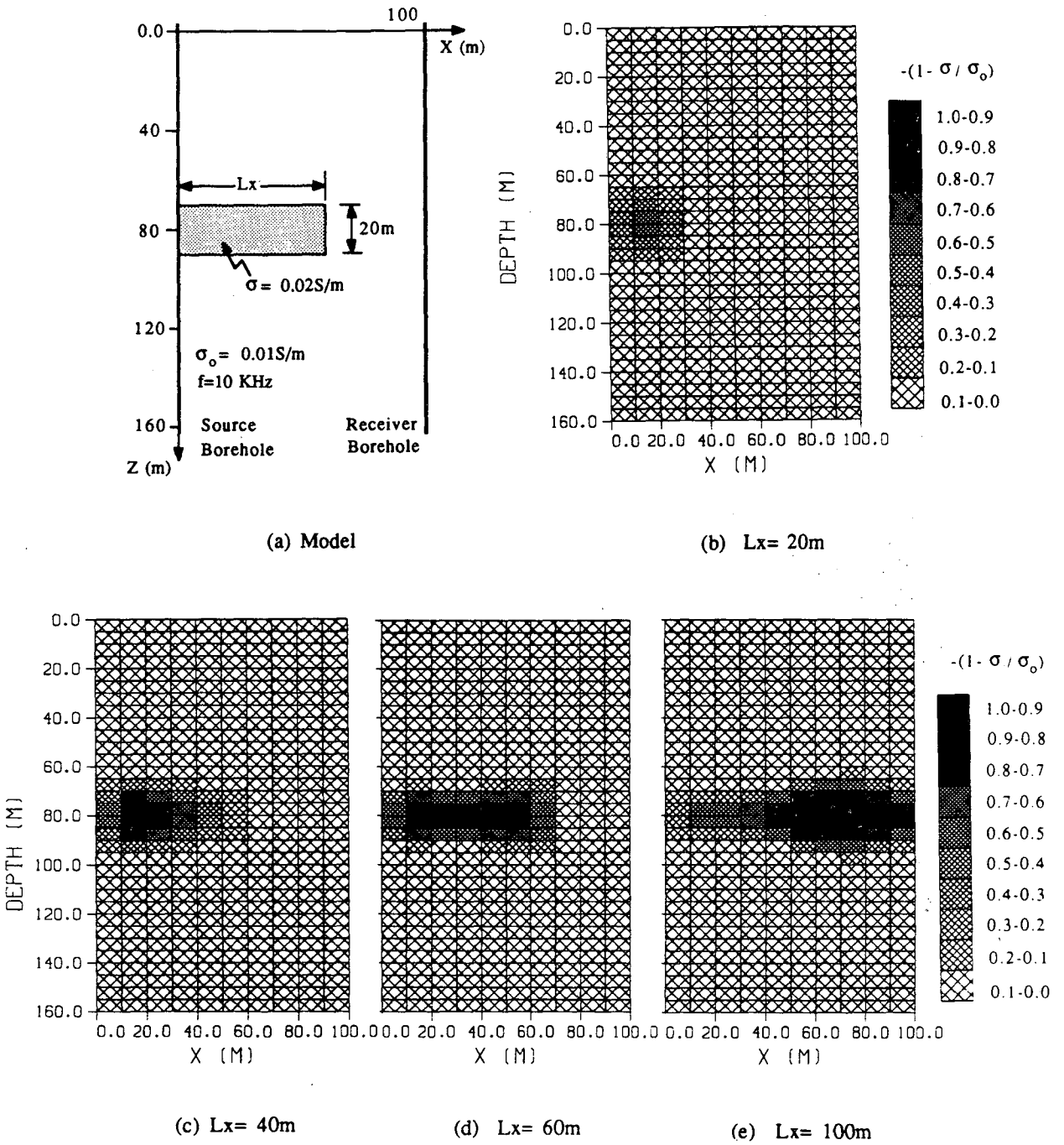

(a) Model

(b) Lx= 20m

(c) Lx= 40m

(d) Lx= 60m

(e) Lx= 100m

Figure 3-4-2 Reconstructed images of targets with varying lateral extent

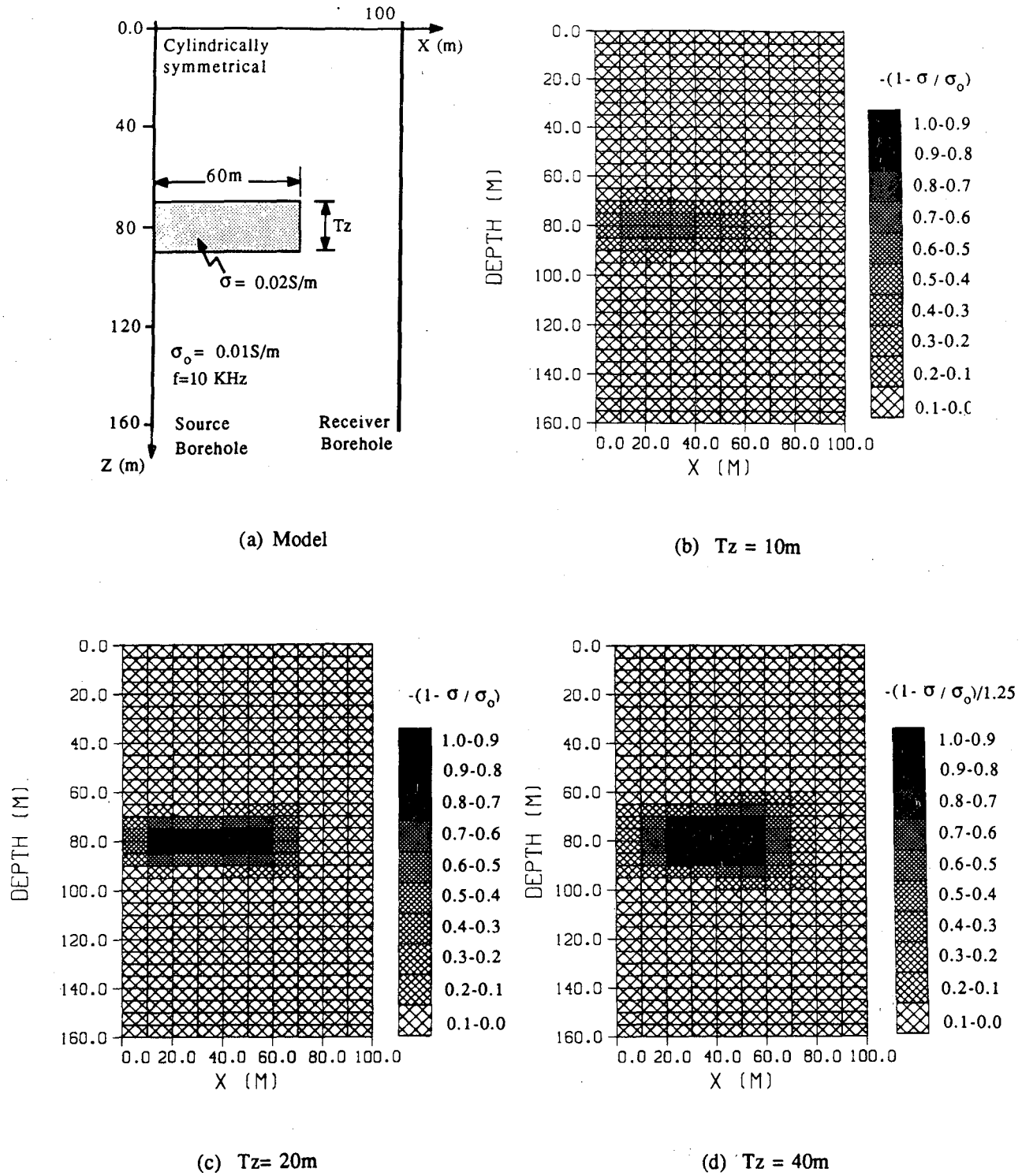

Figure 3-4-3 Reconstructed images of targets with varying vertical extent

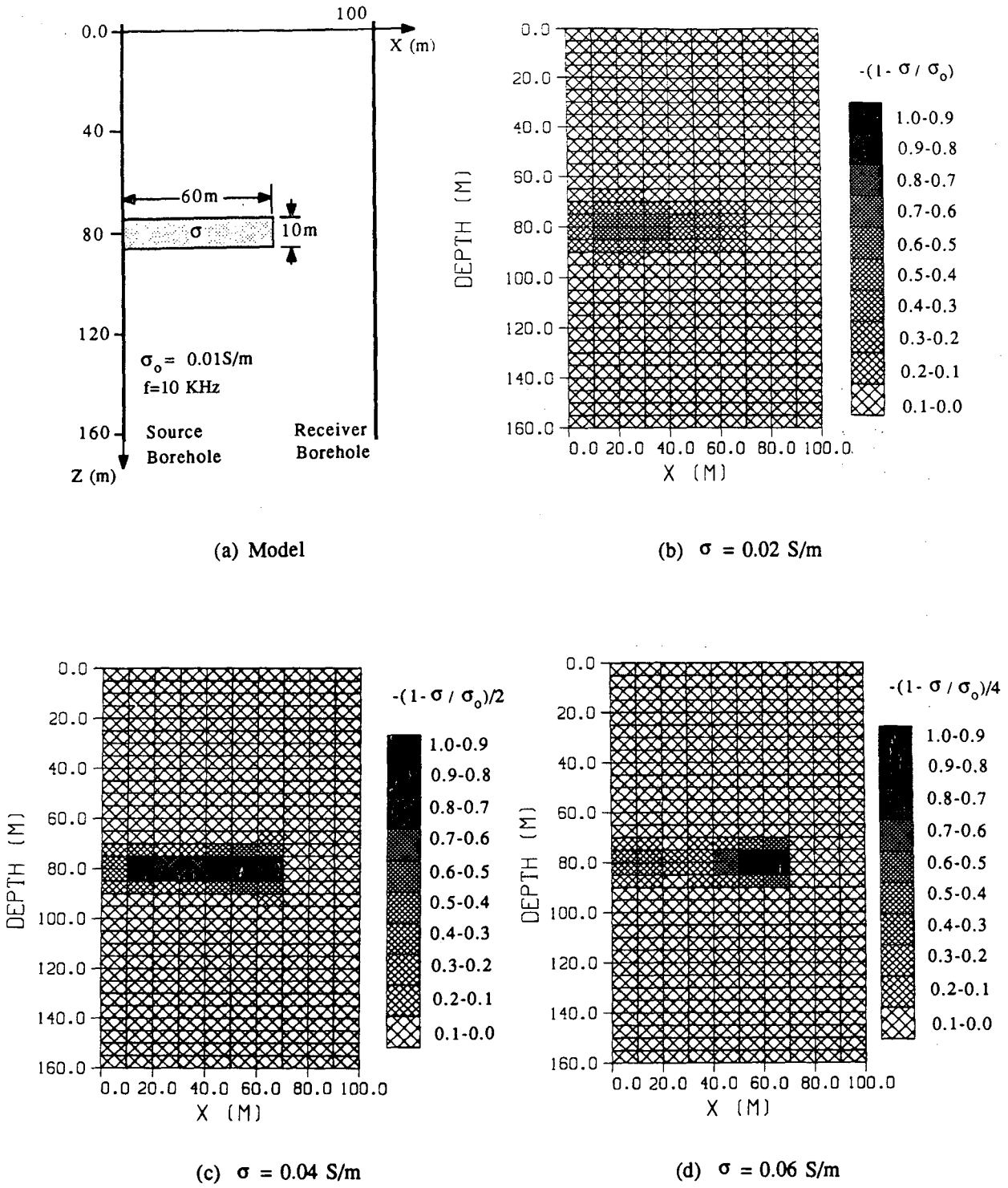

(a) Model

(b) σ = 0.02 S/m

(c) σ = 0.04 S/m

(d) σ = 0.06 S/m

Figure 3-4-4 Reconstructed images of targets of different conductivity

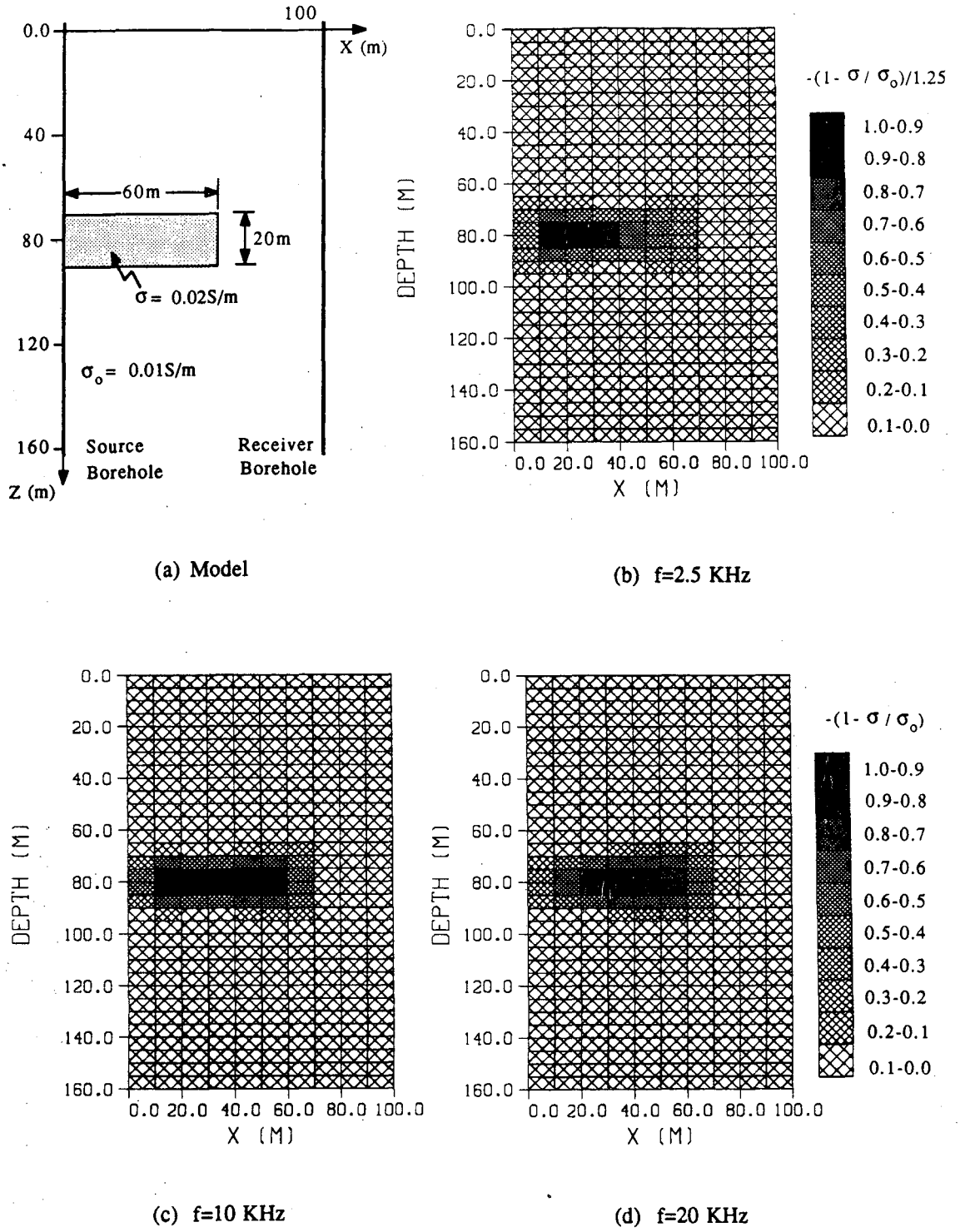

Figure 3-4-5 Reconstructed image quality as a function of frequency

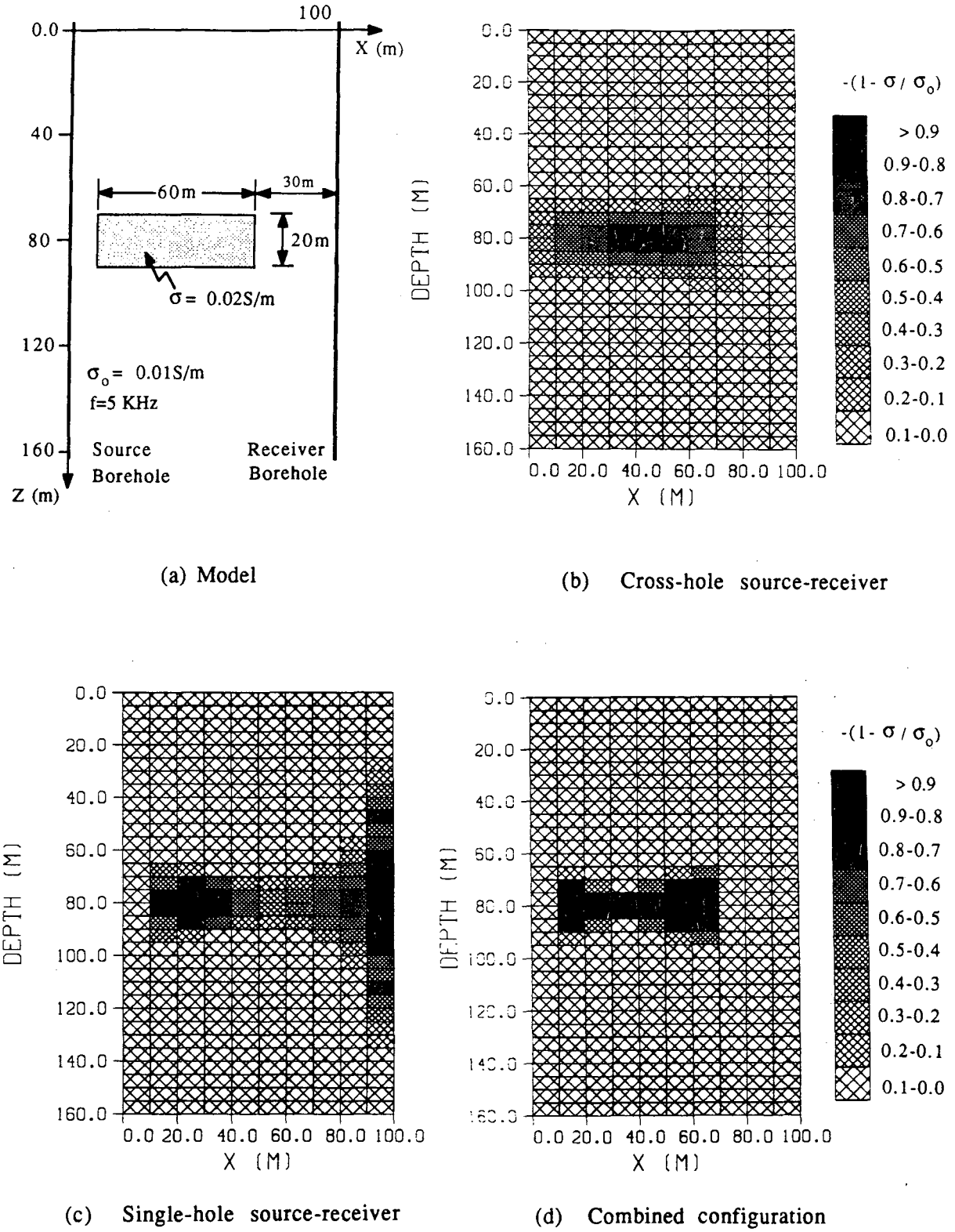

(a) Model

(b) Cross-hole source-receiver

(c) Single-hole source-receiver

(d) Combined configuration

Figure 3-4-6 Resolution enhancement by combining the transmitted and backscattered fields (the distance between source borehole and target is 10 meters)

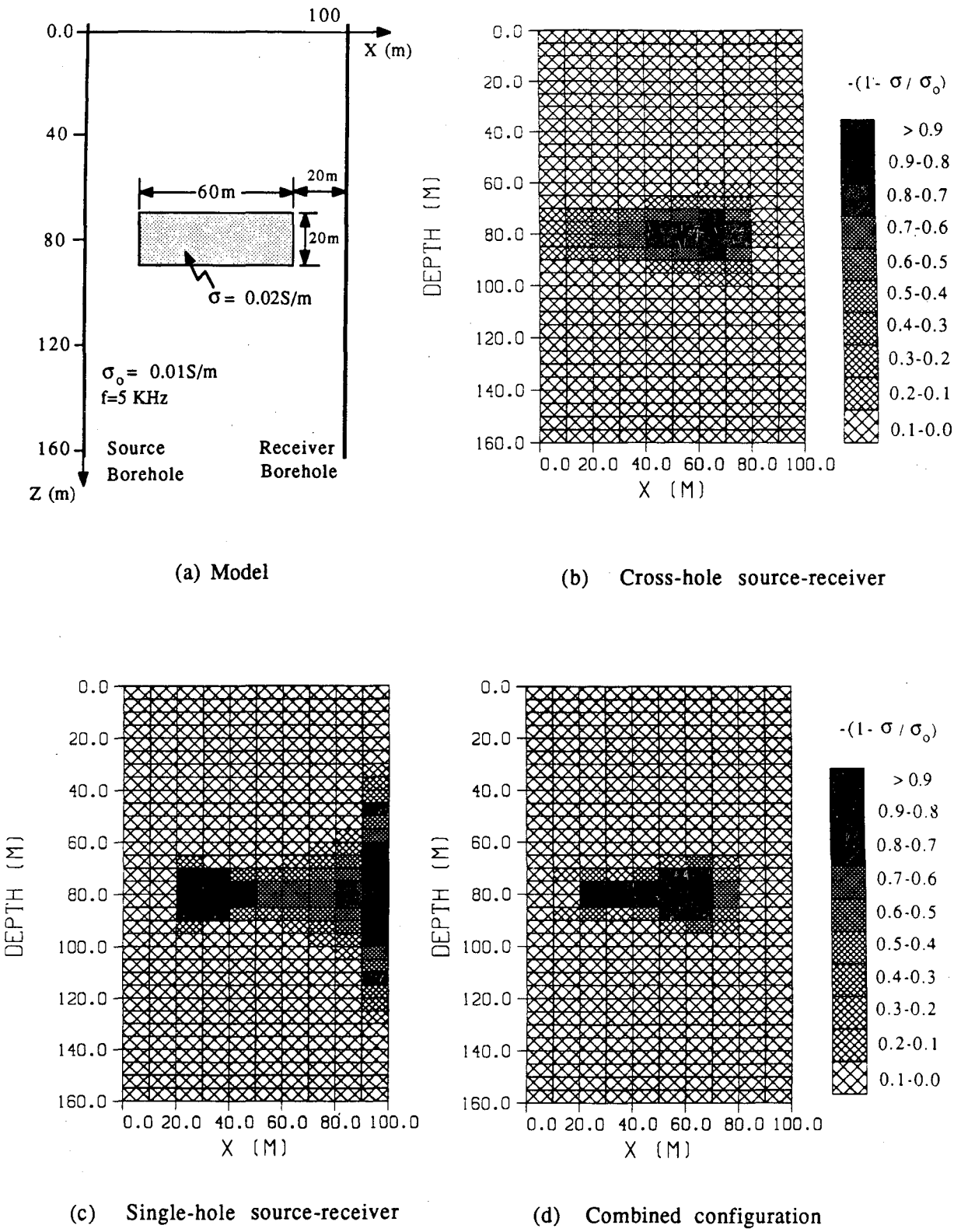

Figure 3-4-7 Resolution enhancement by combining the transmitted and backscattered fields (the distance between source borehole and target is 20 meters)

Chapter 4
Modeling and tomographic inversion for 3-D thin conductors

The 2-D Cartesian and cylindrical symmetry models investigated in the previous two chapters are fundamental and instructive but are insufficient to simulate realistic fracture zones. On the other hand, currently available three dimensional numerical modeling programs (Wannamaker et al., 1984; Weidelt, 1981; Lee et al., 1981; Dyck et al., 1980; to name but a few) for evaluating the electromagnetic response of 3-D conductive targets either involve enormous computing time or are limited to, for example, a surface source and receiver or a single conductor or a free space background. Therefore, it is necessary to develop a rapid and accurate quantitative simulation program for computing the subsurface EM response of multiple thin conductive targets (fracture zones) and a corresponding 3-D inversion method.

Since fracture zones are usually thin, much computational time can be saved by again using the thin sheet approximation (Weidelt, 1981; Price, 1949) which combines the target conductivity and thickness into a single conductance parameter. Numerical modeling of the audio frequency EM response of thin conductive targets embedded in a conductive host rock can be carried out with an integral equation approach which is similar to Weidelt's formulation (1981) for evaluating the EM response of a single such target with source and receiver in the air. The code developed here, however, can be used for modeling of multiple electrically thin conductive conductors detected with a subsurface source and receiver. Both numerical and physical modeling checks of the developed numerical code show that it is acceptably accurate.

Because of the complexity and nonuniqueness inherent to 3-D inversion, the experiments with the forward modeling code can provide some insight into the characteristics of the inversion problem. By examining the calculated electromagnetic response, one can investigate the utility of different array arrangements, such as cross-hole, single hole, tandem moving source-receiver, and fixed source with moving receiver. These numerical experiments are an aid to choosing the right source-receiver combination in order to obtain sufficient information for data

interpretation purposes.

Use of tomographic inversion in a 3-D situation is investigated by assuming that an array of source or receiver boreholes is available. In the more practical case where only one pair of source receiver boreholes exists, an additional assumption must be used in order to make the solution unique and stable. Under the weak scattering and far field assumptions, the inversion characteristics of the 3-D case are found to be similar to those for the 2-D cases discussed in the previous chapters. Finally, we show the results of numerical experiments in locating target representative of electrically conductive fracture zones.

4.1 The thin sheet approximation

As mentioned in the first chapter, numerous papers and reports on the electrical and geometrical parameters of the fracture zones are available. The finding is that the fracture zones of interest are generally thin and are filled with saline water, which makes them more conductive than the host rock. Depending on the geological situation, their thickness-conductivity products range from 0.01 to 1.0 Siemens or more. The host rock may be somewhat conductive as in a petroleum reservoir or resistive as in a waste repository. The size of the tabular conductors ranges from tens of meters to several hundred meters.

The geological situations encountered in these applications suggest the following model for the numerical calculation (Figure 4-1-1). The thin conductors (two in this illustrative model) are represented by rectangular thin sheet like targets of size a_i by b_i, $i=1,2,\cdots,ns$, where ns is the number of sheet-like conductors. The upper edge of the rectangular targets is horizontal. Because these tabular conductors are thin, only the conductance τ_i or the thickness and conductivity product of the fracture zone is of importance. This assumption is justified if the distance from the source to any of the conductors is much larger than the target thickness, the observation point lies not too close to any of the targets and the electromagnetic penetration depth is much greater than the thickness. In other words, the tangential electrical field $\mathbf{E}_s$ on these targets varies slightly across the full thickness. Joshi et al. (1988) discuss the validity of the thin sheet conductor approximation from an analysis of laboratory scale model data. They conclude that the thin sheet assumption is valid if the thickness is less than half the skin depth

in the conductor.

Define three unit vectors $\hat{\mathbf{a}}_i$, $\hat{\mathbf{b}}_i$, $\hat{\mathbf{c}}_i$ such that $\hat{\mathbf{a}}_i$ is in the strike direction of the $i-th$ thin conductor, $\hat{\mathbf{b}}_i$ in the dip direction and $\hat{\mathbf{c}}_i$ is defined by $\hat{\mathbf{a}}_i \times \hat{\mathbf{b}}_i$. For the thin sheet approximation (Price, 1949), we have on the i th thin target

$$[\hat{\mathbf{c}}_i(\mathbf{r}) \times \mathbf{H}(\mathbf{r})]_-^+ = \tau_i(\mathbf{r})\mathbf{E}_{s_i}(\mathbf{r}) \ , \tag{4-1-1}$$

where $\mathbf{E}_{s_i}$ is the tangential electric field and $\mathbf{H}$ denotes the magnetic field. Physically, equation (4-1-1) means that the induced current, $\tau_i(\mathbf{r})\mathbf{E}_{s_i}(\mathbf{r})$, on a thin conductor is equal to the difference of the tangential magnetic fields on the two sides of the thin target.

The conductive targets are assumed to lie in a homogeneous half space of conductivity σ_2. Above the half space, there is an overburden of conductivity σ_1 and thickness D. The strike angle of the $i-th$ target is denoted by γ_i and its dip angle by β_i. The coordinate of the center of the top edge is (X_{1i}, X_{2i}, H_i), where H_i is the depth to the horizontal top of the i th thin conductor from the surface. The source, at a depth of H_{tx}, is harmonic in time ($e^{i\omega t}$). The depth of the receiver is represented by H_{rx}. In the cross-hole case, the separation between the transmitting and receiving wells is X_{dh}.

In all calculations we use a unit dipole moment ($M = 1\ A \cdot turn \cdot m^2$). The displacement current is neglected, and the magnetic permeability is assumed to have the free space value μ_0 of $4\pi \times 10^{-7}$ (H/m). The boreholes whose diameter is assumed to be nil are considered to be vertical and their effects are not taken into account in the calculation.

4.2 Formulation and solution of the integral equations

Our approach to the calculation of the frequency domain magnetic field response is similar to the algorithm developed by Weidelt (1981) who calculated the magnetic field anomaly for a thin conductor and a magnetic dipole source and receiver in the air. Here the EM response of multiple thin conductors with a subsurface source and receiver is going to be investigated.

4.2.1 Integral equation formulation

Beginning with Maxwell's equations and the assumption that the displacement current is negligible,

$$\nabla\times\mathbf{E}(\mathbf{r}) = -i\,\omega\mu_o\mathbf{H}(\mathbf{r}) \ , \tag{4-2-1}$$

$$\nabla\times\mathbf{H}(\mathbf{r}) = \sigma(\mathbf{r})\mathbf{E}(\mathbf{r}) + \mathbf{J}_e(\mathbf{r}) \ , \tag{4-2-2}$$

one arrives at,

$$\nabla\times\nabla\times\mathbf{E}(\mathbf{r}) + k_n^2\mathbf{E}(\mathbf{r}) = -i\,\omega\mu_o\mathbf{J}_e(\mathbf{r}) \ , \tag{4-2-3}$$

where **E** and **H** are the electric and magnetic fields respectively. $\mathbf{J}_e$ is the source current density. And $k_n^2 = i\,\omega\mu_o\sigma_n$. The subscript n has the value of 0, 1, 2 corresponding respectively to the field location in the air, overburden, or the conductive half space.

Let x_1, x_2 and x_3 be a system of Cartesian coordinates so that x_1 and x_2 are parallel to the layer interfaces and x_3 is perpendicular to them. $\hat{\mathbf{x}}_1$, $\hat{\mathbf{x}}_2$, $\hat{\mathbf{x}}_3$ are unit vectors in x_1, x_2 and x_3 directions respectively. Define a Green's function $\mathbf{G}_i$ in a layered medium with i=1, 2, 3 denoting a dipole source oriented in x_1, x_2 and x_3 directions respectively.

$$\nabla\times\nabla\times\mathbf{G}_i(\mathbf{r},\mathbf{r}_o) + k_n^2\mathbf{G}_i(\mathbf{r},\mathbf{r}_o) = \hat{\mathbf{x}}_i\,\delta(\mathbf{r}-\mathbf{r}_o) \ , \tag{4-2-4}$$

where $\mathbf{G}_i = (G_{1i}, G_{2i}, G_{3i})$

Multiply Eq.(4-2-4) by $\mathbf{E}(\mathbf{r})$ and Eq.(4-2-3) by $\mathbf{G}_i$, then integrate their difference in a volume V which consists of the whole space but excludes the volume occupied by the targets. Following Green's vector theorem (Tai, 1971, p6)

$$\int_V \Big[\mathbf{P}\cdot\nabla\times\nabla\times\mathbf{Q} - \mathbf{Q}\cdot\nabla\times\nabla\times\mathbf{P}\Big]\,dv = \int_{\partial V}\Big[\mathbf{Q}\times\nabla\times\mathbf{P} - \mathbf{P}\times\nabla\times\mathbf{Q}\Big]\cdot d\mathbf{s} \ ,$$

we have for i = 1, 2 and 3

$$E_i(\mathbf{r}_o) = -i\,\omega\mu_o\int_V \mathbf{J}_e(\mathbf{r})\cdot\mathbf{G}_i(\mathbf{r}_o,\mathbf{r})dv + \int_V [\mathbf{E}(\mathbf{r})\cdot\nabla\times\nabla\times\mathbf{G}_i(\mathbf{r}_o,\mathbf{r}) - \mathbf{G}_i(\mathbf{r}_o,\mathbf{r})\cdot\nabla\times\nabla\times\mathbf{E}(\mathbf{r})]dv$$

$$= E_{ni}(\mathbf{r}_o) + \int_{\partial V}[(\hat{\mathbf{n}}\times\nabla\times\mathbf{G}_i(\mathbf{r}_o,\mathbf{r}))\cdot\mathbf{E}(\mathbf{r}) - (\hat{\mathbf{n}}\times\nabla\times\mathbf{E}(\mathbf{r}))\cdot\mathbf{G}_i(\mathbf{r}_o,\mathbf{r})]ds \ , \tag{4-2-5}$$

where the primary electric field $\mathbf{E}_{ni}(\mathbf{r}_o)$ is defined by

$$\mathbf{E}_{ni}(\mathbf{r}_o) = -i\,\omega\mu_o \int_V \mathbf{J}_e(\mathbf{r})\cdot\mathbf{G}_i(\mathbf{r}_o,\mathbf{r})dv\ . \tag{4-2-6}$$

∂V, the boundary of V, consists of the boundaries of the thin conductors and the infinite distance surface on which the surface integration disappears. And $\hat{\mathbf{n}}$ is the outward normal unit vector. Since $\nabla\times\mathbf{G}_i$ and $\mathbf{G}_i$ are continuous everywhere for $\mathbf{r}_o$ within V and $\mathbf{r}$ on S_i and the electric field $\mathbf{E}$ satisfies the relations given by the equation (4-1-1) and (4-2-1), equation (4-2-5) now can be reduced to

$$E_i(\mathbf{r}_o) = E_{ni}(\mathbf{r}_o) - i\,\omega\mu_o \sum_{j=1}^{ns} \int_{s_j} \tau(\mathbf{r})\mathbf{G}_i(\mathbf{r}_o,\mathbf{r})\cdot\mathbf{E}_{s_j}(\mathbf{r})ds, \qquad i=1,2 \text{ and } 3\ . \tag{4-2-7}$$

After introducing a Green's dyadic function

$$g(\mathbf{r},\mathbf{r}_o) = [\,\hat{\mathbf{x}}_1,\hat{\mathbf{x}}_2,\hat{\mathbf{x}}_3\,]\begin{bmatrix} G_{11} & G_{12} & G_{13} \\ G_{21} & G_{22} & G_{23} \\ G_{31} & G_{32} & G_{33} \end{bmatrix}\begin{bmatrix} \hat{\mathbf{x}}_1 \\ \hat{\mathbf{x}}_2 \\ \hat{\mathbf{x}}_3 \end{bmatrix}, \tag{4-2-8}$$

equation (4-2-7) then can be written into a vector form

$$\mathbf{E}(\mathbf{r}_o) = \mathbf{E}_n(\mathbf{r}_o) - i\,\omega\mu_o \sum_{j=1}^{ns} \int_{s_j} \tau(\mathbf{r})g(\mathbf{r}_o,\mathbf{r})\cdot\mathbf{E}_{s_j}(\mathbf{r})ds\ . \tag{4-2-9}$$

On the $i-th$ target, the tangential electrical fields are

$$\mathbf{E}_{s_i}(\mathbf{r}_o) = \mathbf{E}_{ns_i}(\mathbf{r}_o) - i\,\omega\mu_o \sum_{j=1}^{ns} \int_{s_j} \tau_j(\mathbf{r})g_s(\mathbf{r}_o,\mathbf{r})\cdot\mathbf{E}_{s_j}(\mathbf{r})ds\ , \tag{4-2-10}$$

where g_s is the Green's function that relates the tangential electrical field to the current distribution on the thin conductors and is discussed in Appendix C. Similarly, the magnetic field at any point anywhere in the space is given by

$$\mathbf{H}(\mathbf{r}) = \mathbf{H}_n(\mathbf{r}) + \sum_{j=1}^{ns} \int_{s_j} \tau_j(\mathbf{r})\mathbf{E}_{s_j}(\mathbf{r}_o)\cdot\nabla\times g(\mathbf{r}_o,\mathbf{r})ds_o\ . \tag{4-2-11}$$

Here $\mathbf{E}_s$ is the total tangential electric field on the conductor, and $\mathbf{E}_{ns}$ is the incident tangential electrical field on the thin target. Likewise, $\mathbf{H}$ is the total magnetic field and $\mathbf{H}_n$ is the incident magnetic field at the point of observation. $g_s(\mathbf{r},\mathbf{r}_o)$ and $g(\mathbf{r},\mathbf{r}_o)$ are the Green's dyadic functions relating the tangential current distribution on the target with the electric field everywhere.

The conductance $\tau(\mathbf{r})$ is the conductivity-thickness product, which is assumed to be a constant over each thin sheet conductor.

4.2.2 Numerical solution

Both the incident fields $\mathbf{E}_{ns}$ and $\mathbf{H}_n$ and the Green's dyadic function g and g_s are related to the dipole fields in a layered medium (3 layers considered here) and are easy to evaluate (Weidelt 1981; Johansen et al., 1979; and Lajoie et al., 1976). After the thin conductors are discretized and $\mathbf{E}_{ns}$ and g_s are calculated, equation (4-2-10) is discretized and solved for $\mathbf{E}_s$, which is then used in equation (4-2-11) together with the calculated $\mathbf{H}_n$ and $\nabla_o \times g$ to obtain $\mathbf{H}$ at the receiver sites. For easy reference, the mathematical details needed for the numerical evaluation are provided in Appendix C.5.

4.3 Verification of the program

Both numerical and physical modeling verification is done to ensure that the developed code is accurate.

4.3.1 Numerical checks

The model used for the numerical verification is shown in Figure 4-3-1 and is symmetrical with respect to the plane defined by the two boreholes. Two identical thin conductors are embedded in a conductive half space of conductivity 0.01 S/m. An overburden of conductivity 0.02 S/m and thickness 20m covers the half space. The two thin targets are discretized into the same number of cells (8×8 on each). Their conductance is $10S$ each and their dip angle is 45°. An operating frequency of $1K\,Hz$ is used. A cross-hole parallel source and receiver pair moves down along the boreholes. The source is a vertical magnetic dipole of unit moment. The other parameters are indicated on the illustration. One of these parameters will be varied in each case to define the computational accuracy. The secondary magnetic field is measured in Ampere/meter.

We know that if the mathematical and numerical approach is correct, then as the number of divisions on each conductor increases, the results should converge. Figure 4-3-2 shows the

results for different numbers of divisions, $N_a \times N_b$ with N_a and N_b denoting the number of cells in the strike and dip directions respectively. It is found that as $N_a \times N_b$ varies from 4×4 to 6×6 to 8×8, the horizontal and vertical magnetic field responses converge. There is almost no difference between the 6×6 and the 8×8 curves. Generally, the minimum number of divisions depends on the conductor size as compared to the background induction number or the operating frequency and the host rock conductivity. The cell size should be smaller than the shortest distance between the source and target or between the target and receiver.

We next verify the reciprocity. Figure 4-3-3 shows the same model but two different sources are used. The symbol "Δ" marks denotes the data profile for the horizontal magnetic response in the right hole for a vertical magnetic dipole (VMD) source on the left. While "+" symbol is used for the vertical magnetic response seen in the left hole for a horizontal magnetic dipole (HMD) source on the right. It is found that both curves match closely.

Yet another way of checking the computational accuracy is by reducing the separation of the two targets. In the limit, the EM response should be the same as that of a single conductor with a conductance that equals the sum of the conductances of the two. Here both targets move toward each other, starting at a horizontal separation of 30 meters, while the dip angle and the other parameters remain fixed. It is evident that the response shown in Figure 4-3-4 for two conductors with a horizontal separation 0.4 meters matches very well with that of a single conductor of conductance $2\times10\ S$ positioned between them. These results verify our expectations.

Numerical checks are also made against the PLATE program by Dyck et al. (1980) for a thin tabular conductor in free space. Figure 4-3-5 shows one of the cases compared. The model consists of a thin conductor of 100 by 100 meters and is symmetrical about the plane defined by the boreholes. The target conductance is 1.0 S and the operating frequency is 1.0 KHz. A unit moment magnetic dipole source is fixed in one hole at a depth of 50m while the secondary magnetic field profile is taken in another hole. In this comparison, the target is divided into 10 by 10 cells in our program. While in the calculation of the PLATE program four eigen-currents (Dyck et al., 1980) are used to approximate the induced current in the target. A good match between these two sets of results is obvious.

4.3.2 Comparison with physical modeling

In addition to the numerical verifications, we also carried out some scale modeling checks for conductors situated in free space. The target material in the physical scale modeling is made of lead. The scaling factors between the parameters of a full scale system and those of the scale model are the same as before (cf. Chapter 4).

$$f/f' = 1/1\,; \qquad l/l' = 2000/1\,; \qquad \sigma/\sigma' = 1/(4\times10^6)\,,$$

where f, σ and l are correspondingly the frequency, conductivity and characteristic dimension of the full scale system while f', σ' and l' are those in the physical scale model.

The full scale system consists of either one or two thin conductors of 300 by 300 meters and is symmetrical about the plane defined by the boreholes. Each target has a conductance of $4.1\,S$. The operating frequency is $3K\,Hz$. The model geometry is shown in the illustrations of the comparison between the numerical and physical modeling results. Figure 4-3-6 shows the results for a single conductor while Figure 4-3-7 contains the data for two thin conductors of same size and conductance. Both illustrations show that the numerical and physical outcomes match each other quite well, so that we conclude that the developed code is both accurate and efficient. For 20 cross-hole source-receiver combinations and a model with two thin conductors buried in a conductive half space with an overburden the computational time is about 60 seconds on an IBM3090 computer. It is about 30 seconds for conductors situated in a homogeneous whole space. More importantly, the developed forward modeling program allows us to calculate numerical data in realistic multi-target situations.

4.4 Source-receiver array configuration effects

As shown in the previous Chapter, the source-receiver arrays chosen are critical in collecting the necessary information for data interpretation. Let us now briefly examine this for the finite thin conductor case. Only a vertical magnetic dipole source and vertical magnetic field measurements are considered because of the borehole orientation. The basic model investigated has one or two thin vertical conductors between two boreholes separated by 150 meters. The targets are perpendicular to and symmetric about the plane defined by the boreholes. Each conductor has a strike length a = 150 m and dip length b = 100 m and a conductance $\tau = 1\,S$.

The whole space background conductivity is assumed to be $0.01\,S/m$. An operating frequency of $10K$ Hz is used. Note also that the secondary magnetic field shown in the following figures are normalized by the amplitude of the whole space field.

4.4.1 Cross-hole parallel transmitter and receiver

The first combination studied is for the cross-hole source-receiver moving in parallel down the two boreholes (Figure 4-4-1). The magnetic response is normalized by the amplitude of the primary vertical magnetic field at the receiver. It is found that the two curves corresponding to a source-target separation (X_s) of 50 m or 100 m are identical because of reciprocity. For a target at $X_s = 75\,m$, the response is still about the same as at the two previous positions. This source-receiver combination is thus insensitive to the lateral position of the target. Nevertheless, the anomaly defines its vertical position quite well.

The above example is for a single conductor. Now suppose there are two parallel identical thin conductors between boreholes (Figure 4-4-2a). Can the cross-hole measurements indicate the changes in the target separation? The secondary magnetic response normalized by the primary field amplitude for vertical thin conductors separated either 50 m or 30 m is plotted in Figure 4-4-2b. It is clear that the difference for these two target separations is small. Thus the parallel source-receiver array is again insensitive to the lateral variations in target position.

4.4.2 Cross-hole fixed source and moving receiver

Let us look at a model (Figure 4-4-3a) with a fixed dipole source in one hole and a moving receiver in the other. The model parameters are shown in the illustration. The amplitude of primary field at the source level is chosen as the normalization factor. Although, the maximum peak-to-peak amplitudes are the same for source-target separation of either 50 or 100 meters, the curve shapes are different. In general, the response for a target closer to the source has a wider shape. This example shows that the anomaly shape is very important in data inversion. The outcome suggests that if we use several fixed source positions and take measurements along another borehole, it is possible to resolve a single target.

When there are two targets present, however, and their separation is varied as shown in Figure 4-4-2, the fixed source and moving receiver cross-hole configuration does not result in any significant change in the magnetic anomaly. The normalization factor is the primary field amplitude at the source level in the receiver borehole. These results tell us that even when one uses all the cross-hole source-receiver combinations it may still be difficult to resolve conductors which shield each other.

4.4.3 Source and receiver in tandem

It has been shown that the cross-hole source-receiver configuration is not very sensitive to lateral conductivity variations. However, if both the source and receiver are in the same borehole, the observed electromagnetic response related to the targets is much more dependent on their lateral position. Figure 4-4-5 is an example for a source-receiver pair with a 15 m fixed vertical separation moving in a single hole near a vertical conductor. As the borehole-target distance varies from 50 meters to 75 meters, a significant change in the response is observed. One might also notice that the imaginary component shows a much smaller change than its real component does. This phenomenon differs from the secondary EM field of a target located in free space where both components change at similar rate as the conductor moves away. In this illustration, the imaginary component is mainly due to the phase shift by the conductive background. In general, there is no way to predict whether one component will show less variability.

For two parallel conductors of 30 m or 50 m separation (Figure 4-4-6), the computed responses also differ clearly. These changes are mainly related to the distance of the nearest conductor to the source-receiver borehole. Thus as shown above, to increase lateral resolution the back-scattered fields should also be measured. Since the curve is normalized by the primary vertical magnetic field of a source only 15 meters away, the relative secondary response is very small although its absolute value is of the same order as that for the cross-hole cases.

The effect of different operating frequency in the single hole case is illustrated in Figure 4-4-7 using the same model as that shown in Figure 4-4-5 for a single vertical conductor with the source-receiver in the same borehole. The target is either 50m or 75m away from the well.

Two frequencies of $10K\ Hz$ and $5K\ Hz$ are used. The amplitude of the secondary magnetic response is normalized by the amplitude of the primary field at the receiver site. It can be seen that the contribution from a distant conductor is relatively larger at the lower frequency. Thus, in order to achieve necessary resolution, use of multiple operating frequencies may be advisable.

Conclusions about the array arrangements and operating frequency for this three dimensional situation are the same as those in section 3.2.3 where the cylindrical symmetry model are investigated through a number of numerical experiments. Since the discussion is limited to a few examples, more mathematical approach is going to be taken next.

4.5 3-D electromagnetic tomography

The inverse problem for any three-dimensional target based on the data collected from one or two boreholes is under-determined and is also much more complicated than its two-dimensional counterpart. The situation is somewhat similar to the elastic problem in the seismic method although here one only needs to solve for a single unknown (electrical conductivity) instead of the multiple parameters (density and Lamé constants) in the seismic method (Beylkin and Burridge, 1989). In this section, we will start with the assumptions that there are two arrays of source and receiver boreholes arranged parallel to each other as shown in Figure 4-5-1 and that the measurements are taken for all crosshole source-receiver combinations. A three-dimensional inverse solution is then derived under the weak scattering approximation. and by assuming the target to be short. Then, with an additional far field approximation, an inverse solution can be found for the crosshole (two borehole) array.

4.5.1 Tomographic analysis under the weak scattering approximation

A Cartesian coordinate system is chosen with the z-axis along the vertical borehole, while x-axis and y-axis are in horizontal (Figure 4-5-1). Following similar steps to those outlined in the previous chapters, an integral equation is first established. From Hohmann (p318, 1988), the electric field $\mathbf{E}(\mathbf{r})$ for a general three-dimensional problem satisfies

$$\mathbf{E}(\mathbf{r}) = \mathbf{E}^p(\mathbf{r}) + \int_v g(\mathbf{r},\mathbf{r}')\cdot(\sigma-\sigma_o)\mathbf{E}(\mathbf{r}')\,dv' \,, \tag{4-5-1a}$$

where $\mathbf{E}^p$ is the primary field, g is the Green's dyadic function, σ is the conductivity distribution and σ_o is a constant background conductivity. The integration is carried out all over the space with respect to the coordinate variable $\mathbf{r}'$. After introducing the secondary field $\mathbf{E}^s$ $(= \mathbf{E} - \mathbf{E}^p)$, the above equation becomes

$$\mathbf{E}^s(\mathbf{r}) = \int_v g(\mathbf{r},\mathbf{r}')\cdot(\sigma-\sigma_o)\mathbf{E}(\mathbf{r}')\,dv' \,. \tag{4-5-1b}$$

To derive the integral equation for the secondary magnetic field, one only needs to take the curl with respect to $\mathbf{r}$ on both sides of equation (4-5-1b) and also make use of the relation in equation (2-1-1b). Thus we have

$$\mathbf{H}^s(\mathbf{r}) = \int_v g_H(\mathbf{r},\mathbf{r}')\cdot(\sigma-\sigma_o)\mathbf{E}(\mathbf{r}')\,dv' \,. \tag{4-5-2}$$

The Green's dyadic function g_H is related to the magnetic field in a homogeneous whole space generated by an electric dipole source pointing in one of the three coordinate directions and can be found from Ward and Hohmann (p174, 1988).

$$G_{xx} = 0; \tag{4-5-3a}$$

$$G_{yx} = \frac{1}{4\pi}\frac{\partial}{\partial z_g}\frac{e^{-ik_oR_g}}{R_g}; \tag{4-5-3b}$$

$$G_{zx} = -\frac{1}{4\pi}\frac{\partial}{\partial y_g}\frac{e^{-ik_oR_g}}{R_g}; \tag{4-5-3c}$$

$$G_{xy} = -\frac{1}{4\pi}\frac{\partial}{\partial z_g}\frac{e^{-ik_oR_g}}{R_g}; \tag{4-5-3d}$$

$$G_{yy} = 0; \tag{4-5-3e}$$

$$G_{zy} = \frac{1}{4\pi}\frac{\partial}{\partial x_g}\frac{e^{-ik_oR_g}}{R_g}, \tag{4-5-3f}$$

where $R_g = \sqrt{(x_g-x)^2+(y_g-y)^2+(z_g-z)^2}$ and $k_o^2 = -i\,\omega\mu\sigma_o$.

Since in the borehole we measure the magnetic field, the following discussion will concentrate on equation (4-5-2). After applying the Born approximation,

$$\mathbf{E}(\mathbf{r}') = \mathbf{E}^p(\mathbf{r}'),$$

under a weak scattering assumption, equation (4-5-2) becomes

$$\mathbf{H}^s(\mathbf{r}) = \int_v g_H(\mathbf{r},\mathbf{r}')\cdot(\sigma-\sigma_o)\mathbf{E}^p(\mathbf{r}')\,dv' \,. \tag{4-5-4}$$

For a vertical (in z-direction) magnetic dipole source excitation, the primary electric field in a homogeneous medium is (Ward and Hohmann, p176, 1988)

$$E_x^p = -\frac{i\omega\mu_0}{4\pi}\frac{\partial}{\partial y}\frac{e^{-ik_oR_s}}{R_s}\,; \tag{4-5-5a}$$

$$E_y^p = \frac{i\omega\mu_0}{4\pi}\frac{\partial}{\partial x}\frac{e^{-ik_oR_s}}{R_s}\,; \tag{4-5-5b}$$

$$E_z^p = 0\,, \tag{4-5-5c}$$

where $R_s = \sqrt{(x-x_s)^2+(y-y_s)^2+(z-z_s)^2}$.

Therefore, the secondary magnetic field at point $\mathbf{r}_g$ or (x_g, y_g, z_g) due to a source at $\mathbf{r}_s$ or (x_s, y_s, z_s) can be rewritten from equation (4-5-4) to read,

$$\mathbf{H}^s(\mathbf{r}_g,\mathbf{r}_s) = \int_v (\sigma-\sigma_o)\,[\,\hat{\mathbf{x}}G_{xy}E_y^p + \hat{\mathbf{y}}G_{yx}E_x^p + \hat{\mathbf{z}}(G_{zx}E_x^p + G_{zy}E_y^p)\,]\,dv \,. \tag{4-5-6}$$

Since the borehole condition usually only allows the measurement of the vertical magnetic field, we will mainly study that component.

$$H_z^s(\mathbf{r}_g,\mathbf{r}_s) = \int_v (\sigma-\sigma_o)\,[\,G_{zx}E_x^p + G_{zy}E_y^p\,]\,dv \,. \tag{4-5-7}$$

With the introduction of equations (4-5-3) and (4-5-5), the above equation can be expressed as

$$H_z^s(\mathbf{r}_g,\mathbf{r}_s) = \frac{i\omega\mu_0}{(4\pi)^2}\int_v (\sigma-\sigma_o)\,[\,(\frac{\partial}{\partial y_g}\frac{e^{-ik_oR_g}}{R_g})(\frac{\partial}{\partial y}\frac{e^{-ik_oR_s}}{R_s})$$
$$+\,(\frac{\partial}{\partial x_g}\frac{e^{-ik_oR_g}}{R_g})(\frac{\partial}{\partial x}\frac{e^{-ik_oR_s}}{R_s})\,]\,dv \,. \tag{4-5-8}$$

Now taking the Fourier transforms with respect to z_g and z_s and denoting the corresponding Fourier domain wave numbers with k_g and k_s, we have

$$H_z^s(x_g, y_g, k_g; x_s, y_s, k_s)$$

$$= \frac{-i\,\omega\mu_0}{16} \int_v (\sigma-\sigma_o)\, e^{-i(k_s+k_g)z} \left[\frac{\partial}{\partial y_g} H_0^{(2)}(r_g\gamma_g) \frac{\partial}{\partial y} H_0^{(2)}(r_s\gamma_s) \right.$$

$$\left. + \frac{\partial}{\partial x_g} H_0^{(2)}(r_g\gamma_g) \frac{\partial}{\partial x} H_0^{(2)}(r_s\gamma_s) \right] dv\,, \qquad (4\text{-}5\text{-}9)$$

where

$$\gamma_s^2 = k_o^2 - k_s^2; \qquad \gamma_g^2 = k_o^2 - k_g^2; \qquad (4\text{-}5\text{-}10a)$$

$$r_s = \sqrt{(x-x_s)^2+(y-y_s)^2}; \qquad r_g = \sqrt{(x_g-x)^2+(y_g-y)^2}; \qquad (4\text{-}5\text{-}10b)$$

and $H_0^{(2)}$ is the zero-th order Hankel function of the second kind. In deriving equation (4-5-9), an identity given in Gradshteyn and Ryzhik (formula 6.616.4, p710, 1980) is applied.

After taking Fourier transforms with respect to y_s and y_g and making use of the relation given in equation (2-2-7b), equation (4-5-9) finally becomes

$$H_z^s(x_g, k_{yg}, k_g; x_s, k_{ys}, k_s) = \frac{-k_o^2}{4} \frac{k_{yg}k_{ys} - k_{2g}k_{2s}}{k_{2g}k_{2s}} e^{-ik_{2g}x_g}$$

$$\int_v O(\mathbf{r})\, e^{-i(k_s+k_g)z}\, e^{-i(k_{ys}+k_{yg})y}\, e^{-i(k_{2s}-k_{2g})x}\, dv, \qquad (4\text{-}5\text{-}11)$$

where the object function $O(\mathbf{r})$ is defined as before, $O(\mathbf{r}) = 1-\sigma/\sigma_o$, and k_{ys} and k_{yg} are the Fourier domain wave numbers corresponding to y_s and y_g respectively. The wave number k_{2s} and k_{2g} are defined as

$$k_{2s}^2 = \gamma_s^2 - k_{ys}^2; \qquad k_{2g}^2 = \gamma_g^2 - k_{yg}^2. \qquad (4\text{-}5\text{-}12)$$

If the following substitutions are made,

$$k_s + k_g = k_z\,; \qquad k_{ys} + k_{yg} = k_y\,; \qquad i(k_{2s} - k_{2g}) = s_x\,, \qquad (4\text{-}5\text{-}13)$$

the object function $O(\mathbf{r})$ can be derived from the inverse Fourier transforms in k_y and k_z and the inverse Laplace transform in s_x of equation (4-5-11). Numerically, however, this is impossible because of the instability of the inverse Laplace transform. Nevertheless, from this expression we see that the inversion characteristics are the same as the previous 2-D Cartesian and cylindrical symmetry models except that there is one more variable.

4.5.2 Solution with an additional far field approximation

Usually only one or two boreholes are available and obviously then the inverse problem is nonunique. Nevertheless, if suitable assumptions and constraints are applied the conductivity distribution on the plane defined by the source-receiver boreholes can be determined. Equation (4-5-9) can be cast into the following form after taking the derivatives,

$$H_z^s(x_g, y_g, k_g; x_s, y_s, k_s)$$

$$= \frac{-k_o^2}{16} \int_v O(\mathbf{r}) \gamma_s \gamma_g \cos(\phi_s - \phi_g) H_1^{(2)}(r_g \gamma_g) H_1^{(2)}(r_s \gamma_s) e^{-i(k_s+k_g)z} \, dv \ , \quad (4\text{-}5\text{-}14)$$

where

$$\phi_s = \sin^{-1}\left(\frac{y-y_s}{r_s}\right); \qquad \phi_g = \sin^{-1}\left(\frac{y_g-y}{r_g}\right). \quad (4\text{-}5\text{-}15)$$

Under the far field approximation, the above equation is simplified by using the following relationship (Stinson, 1976)

$$H_n^{(2)}(x) \rightarrow \sqrt{\frac{2}{\pi x}} e^{-i[x-(\pi/2)(n+1/2)]}, \qquad \text{if } x \rightarrow \infty \quad \text{and} \quad |x| \gg n \ .$$

Now, we have

$$H_z^s(x_g, y_g, k_g; x_s, y_s, k_s)$$

$$= \frac{ik_o^2}{8\pi} \sqrt{\gamma_s \gamma_g} \int_v O(\mathbf{r}) \cos(\phi_s - \phi_g) \frac{1}{\sqrt{r_s r_g}} e^{-ir_s\gamma_s - ir_g\gamma_g} e^{-i(k_s+k_g)z} \, dv \ . \quad (4\text{-}5\text{-}16)$$

Since there is no control in the y-direction, some assumption must be made in order to make the inverse solution unique. Let us assume that the anomalous conductor is located between the source and receiver boreholes and that it is not too close to either the source or the receiver borehole (Figure 4-5-2). The target extension in the y-direction is also assumed to be small when compared to the borehole separation. Therefore,

$$r_s \approx x \ ;$$

$$r_g \approx x_g - x \ ;$$

$$\frac{1}{\sqrt{r_s r_g}} \approx \frac{2}{x_g} \ ;$$

$$\cos(\phi_s - \phi_g) \approx 1 .$$

Under these conditions and after the integration with respect to y, the vertical magnetic anomaly is

$$H_z^s(x_g, k_g; x_s, k_s)$$

$$= \frac{ik_o^2}{8\pi} \sqrt{\gamma_s \gamma_g}\, e^{-ix_g \gamma_g}\, \Delta y\, \frac{2}{x_g} \int_{x-z} O(\mathbf{r})\, e^{-i(\gamma_s - \gamma_g)x}\, e^{-i(k_s + k_g)z}\, dxdz , \qquad (4\text{-}5\text{-}17)$$

where Δy is the width in y-direction within which the target is located. x_g is the borehole separation while x_s is zero. The integration is carried out on the $x-z$ plane.

Equation (4-5-17) is again familiar to us because it is similar to equation (4-4-10) for the cylindrical symmetry case or to equation (2-2-8) for the 2-D Cartesian model. The only difference is a geometric factor. Thus, the remarks made in chapter 2 regarding the wave number domain coverage of the object function $O(\mathbf{r})$ are equally applicable to this three-dimensional case. The wave number analysis also verifies the conclusions drawn from the numerical experiments discussed in the previous section. Studies of other source-receiver configuration can be carried out similarly and their wave number domain coverage and resolution can also be examined.

The above discussion for a finite target of small strike extent is only one of the models that one can use to make the solution unique and stable. I conjecture that other assumptions, such as that the target has infinite extension in the y-direction, should also provide a good solution. The main idea behind the geometrical factor correction is to get rid of one space variable such as the $y-axis$ in a 3-D Cartesian geometry or the azimuthal dependence in a cylindrical symmetry geometry. The geometrical difference between the 2-D line and 3-D point dipole sources is the main reason for this approximation. A similar approach can be found in seismic applications as shown by Esmersoy (1986), Bleistein (1984) and the others.

4.5.3 Numerical examples

The expression given in equation (4-5-17) is similar in form to those for the 2-D Cartesian or the cylindrical symmetry models except for the different weighting factor in the wave number domain transform of the measurements. Thus, one can take advantage of the developed codes in the previous chapters to solve for the 3-D conductivity distribution. Of course, only the conductivity distribution on the plane defined by the source-receiver boreholes will be presented. Anything more than that would be unrealistic without any further assumptions or additional knowledge of the target parameters.

Rewrite equation (4-5-17) for the 3-D far field approximation,

$$H_z^s(x_g, k_g; x_s, k_s) \frac{8\pi}{ik_o^2 \sqrt{\gamma_s \gamma_g}} \frac{x_g}{2\Delta y} e^{ix_g \gamma_g} = \int_{x-z} O(\mathbf{r}) e^{-i(\gamma_s - \gamma_g)x} e^{-i(k_s + k_g)z} \, dxdz \quad \text{,(4-5-18a)}$$

and also rewrite the equation (2-2-11) for the 2-D Cartesian model,

$$E^s(x_g, k_g; x_s, k_s) \frac{4\gamma_g \gamma_s}{-i\omega\mu k_o^2} e^{(-i\gamma_s x_s + i\gamma_g x_g)} = \int_S O(\mathbf{r}) \exp[-s_x x - ik_z z] \, dxdz \quad . \qquad \text{(4-5-18b)}$$

Therefore, the factor for the geometric correction to be used with the 2-D algorithm and 3-D data is

$$\frac{\left[\dfrac{8\pi}{ik_o^2 \sqrt{\gamma_s \gamma_g}} \dfrac{x_g}{2\Delta y}\right]}{(4\gamma_g \gamma_s)/(-i\omega\mu k_o^2)} \qquad \text{(4-5-19)}$$

The model for the numerical calculation consists of a dipping conductor of finite size ($100m \times 80m$) buried in a homogeneous background of conductivity $0.01\,S/m$. The thin target has a conductance of $0.1\,S$. Higher conductances are chosen later to show the validity of the weak scattering approximation. The conductive target is symmetrical about the plane defined by the two vertical boreholes. An operating frequency of $10\,KHz$ is used. The synthetic data is generated with the numerical program discussed earlier in this chapter. Vertical magnetic dipole (VMD) sources are placed in one hole and the vertical magnetic anomaly is measured in the other one which is 100 meters away. The number of sources and receivers is 32×32 with all possible cross-hole source-receiver combinations. Both the Born and Rytov reconstruction methods are tested.

After applying the correction for the geometric factor, the two dimensional inversion scheme is applied to invert the data generated by our 3-D thin conductor modeling code. We also assume in equation (4-5-17) that $\Delta y / x_g = 1.0$. Figure 4-5-3a shows the model of the dipping conductor. Inverse solutions for the conductivity distribution are given in Figure 4-5-3b and c. These results provide reasonable estimates of the target. The residual variance for the inversion is 12.4 for the Rytov and 13.8 for the Born method of approximating the fields on the conductor.

To reduce the dimensionality of the problem, other correction factors for geometric spreading can also be used under various assumptions for the target extent in the strike direction. The geometric difference between the 2-D line and 3-D point dipole sources is one of the main concerns for this approximation. Therefore, one may also use the correction factor appropriate to the cylindrically symmetry model, which uses dipole source, with the 2-D Cartesian coordinate inversion to obtain a solution for the 3-D case. By doing this, one also saves the trouble of setting the value $\Delta y / x_g$ in equation (4-5-17) or in the correction factor of equation (4-5-19).

In Figure 4-5-4 and latter, the same 2-D inversion method is used but with a different correction factor (equation 4-4-15) which is derived for the cylindrical symmetry model. Figure 4-5-4 shows the inversion results for the Born approximation reconstruction for three different dipping conductor models ($\beta = 0^o, 45^o, 90^o$). Similarly, Figure 4-5-5 shows the outcomes for the Rytov approach. Both approximations result in a reasonable representation of the original model. Nevertheless, one should notice that the part of the target closer to the source borehole is not reconstructed as well as the far side of the conductor. These might be caused by the invalidity of the far field approximation when the target is actually close to the source.

The statistical measures are also calculated for the above models. First the residual variance is calculated and is shown in the following table.

Table 4-5-1 Residual variance of the Born and Rytov models			
	$\beta = 0^o$	$\beta = 45^o$	$\beta = 90^o$
Born	0.3133	0.3792	0.3958
Rytov	0.2916	0.2049	0.1961

In all these cases, the Rytov method has smaller residual variance than the Born method which tells that there is a better data fit for the Rytov method. The standard deviation for the Born and Rytov solutions is calculated and shown in Figure 4-5-6. Together with what we have already seen in the residual variance analysis, it is clear that the Rytov approach is superior.

The $\beta = 45^o$ case in Figure 4-5-4 and -5 corresponds to the model in Figure 4-5-3. One can visually notice that there is some improvement in the inversion result by using the present correction method. If one looks at the residual variance for the $\beta = 45^o$ case in the in Figure 4-5-3, -4, and -5, it is evident that the second approach to the geometric factor correction is better.

Models with two thin conductors are also used to study the target resolution in the horizontal or vertical directions for the cross-hole source-receiver array arrangement. The two targets are parallel to each other and are 40 meters apart. Figure 4-5-7 is for the Born and Rytov images of two horizontal sheet conductors. The images of two dipping (45°) conductors are shown in Figure 4-5-8. Those of two vertical conductors are presented in Figure 4-5-9. For the horizontal and dipping target cases, good estimates of model parameters are obtained except for the side near the borehole due to the limitation of the far field approximation. However, the resolution for two vertical conductors shielding horizontally each other is very poor. The deteriorated quality is mainly due to the poor wave number domain coverage of the object function in the horizontal direction under the cross-hole geometry.

A higher target conductance is used next and the outcome of the inversion is shown in Figure 4-5-10 and Figure 4-5-11. In Figure 4-5-10 a target conductance of $1.0S$ is used while in Figure 4-5-11 the conductance is $2.0S$. In these two cases, the Rytov method yields images with nearly correct position and conductance. On the other hand, the Born approximation

solution gives quite poor quality. As the conductance further increased, both methods fail. The Rytov method is valid up to a conductance of $\tau = 2.0S$ but the Born method has a much lower range of validity.

It should be pointed out that the weak scattering approximation applied in the 3-D inversion implies that the channeling current is dominant over the induced current in the target. The assumption is valid for targets situated in a conductive background (Newman et al., 1989). Precaution must be taken if one wants to solve for targets situated in a resistive host rock because the current in the target is inductive and its pattern is totally different from that of channeling current.

In all the examples shown above, the Rytov method has a smaller residual variance and standard deviation than the Born method. These inversion results also show that the theoretical analysis in the previous section is valid. There is poorer resolution in the horizontal direction than that in the vertical for the cross-hole source-receiver configuration. It is also found that the two-dimensional inversion scheme is applicable in the cases of three-dimensional target and source if an approximation is made to correct for the geometric factor.

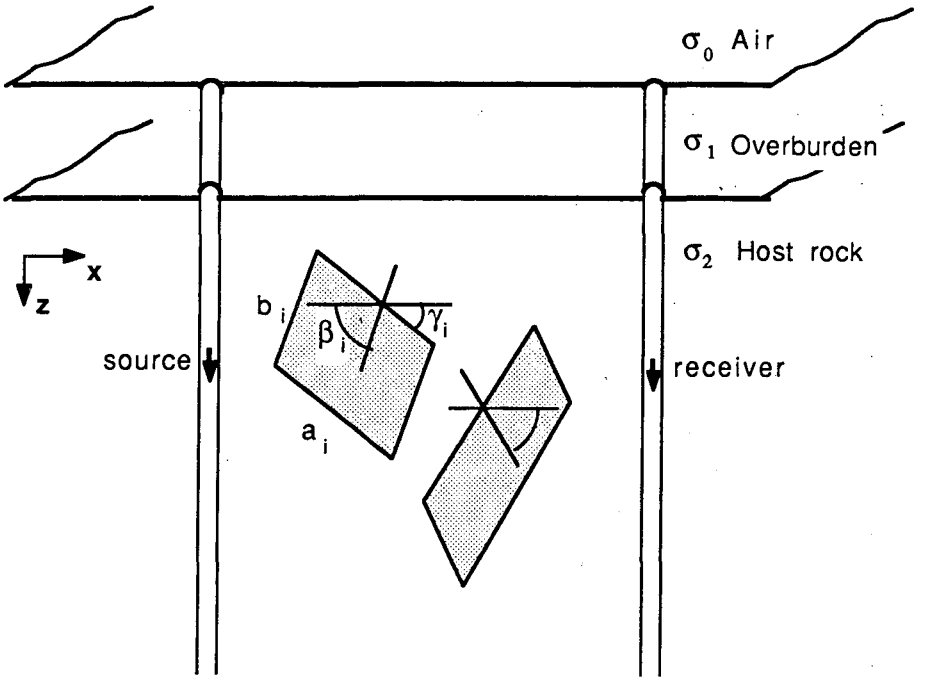

Figure 4-1-1 A 3-D thin conductor model

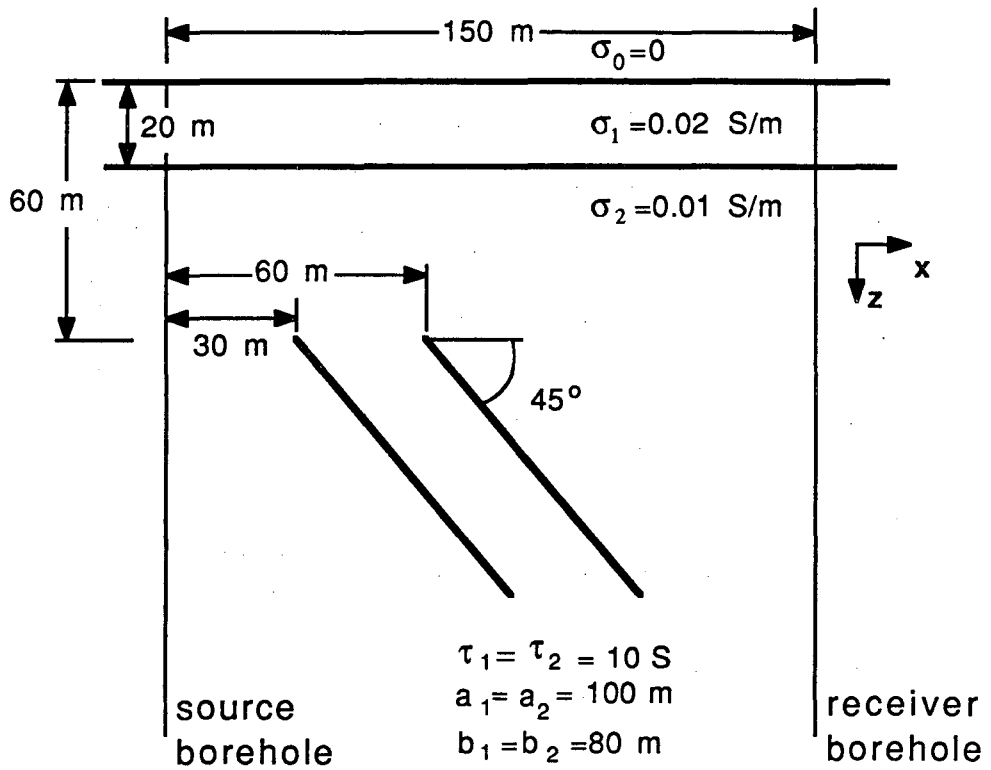

Figure 4-3-1 Particular model tested for accuracy

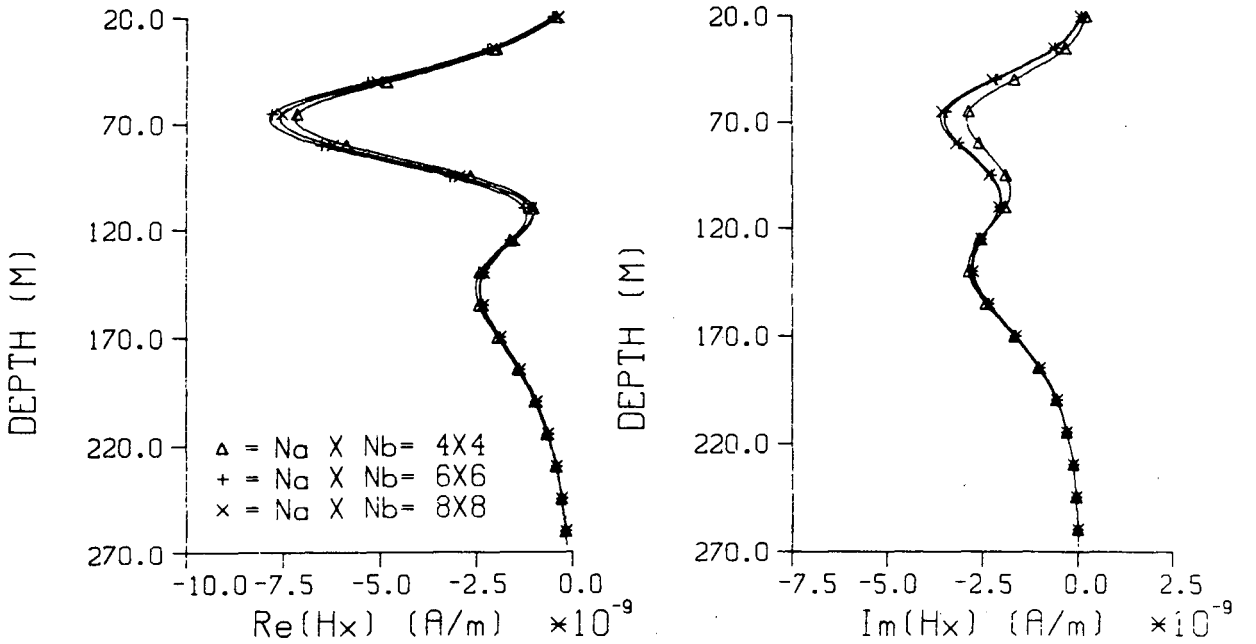

(a) Hx component

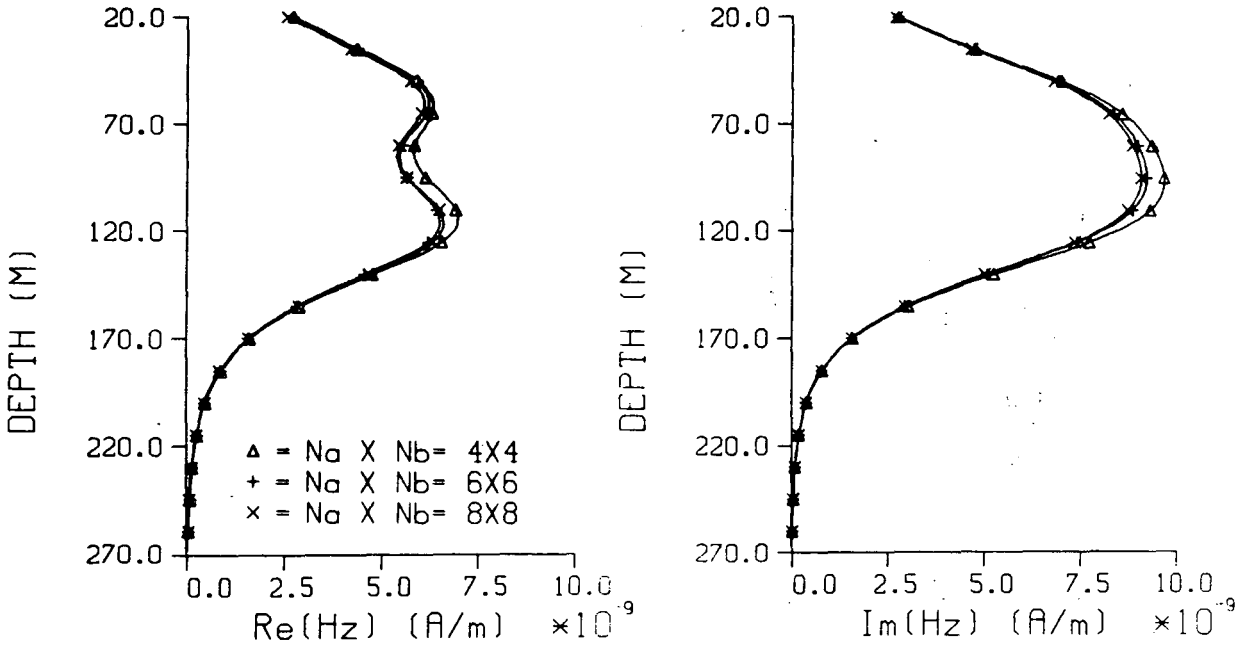

(b) Hz component

Figure 4-3-2 Convergence check

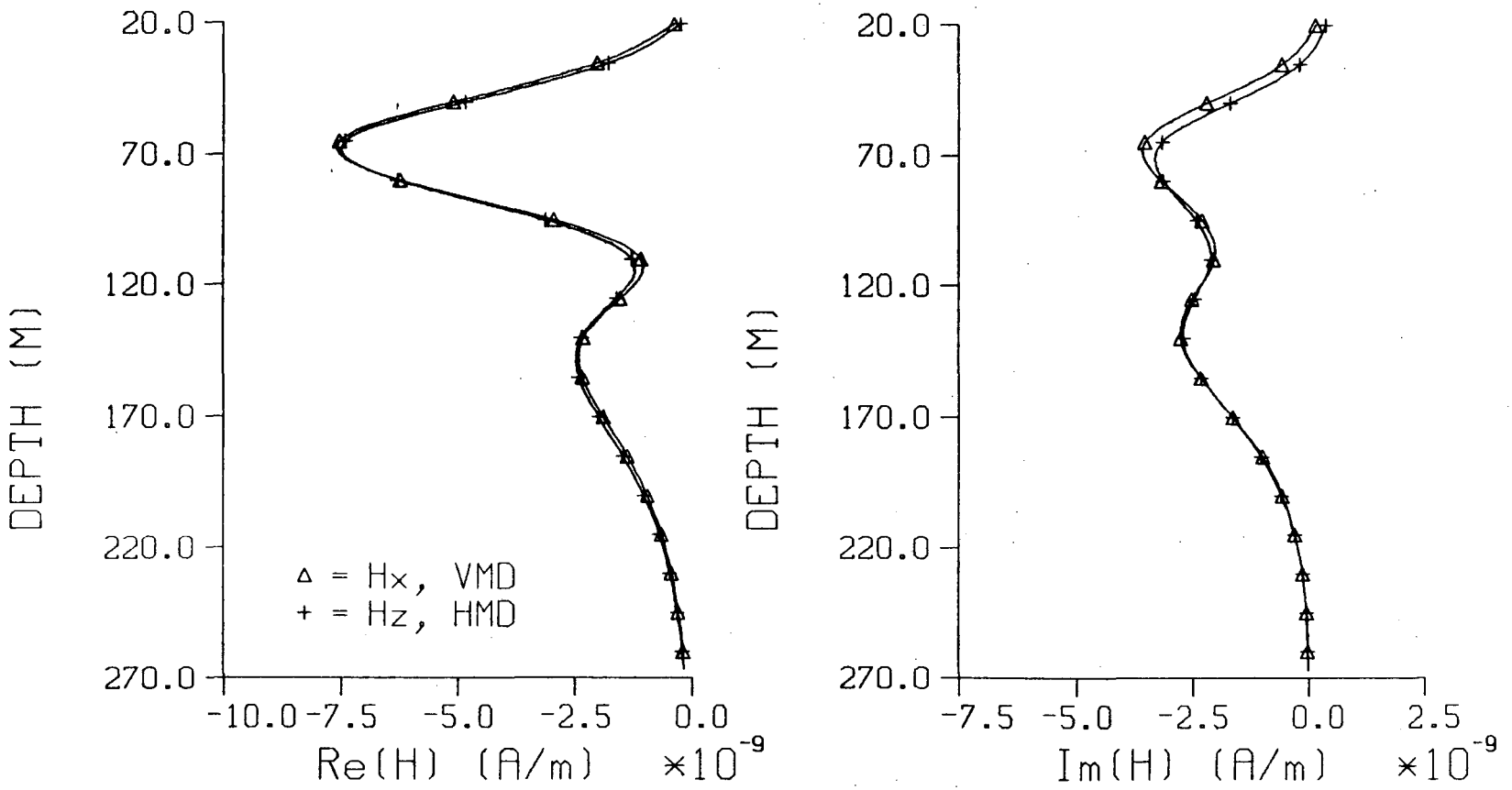

Figure 4-3-3 Reciprocity check

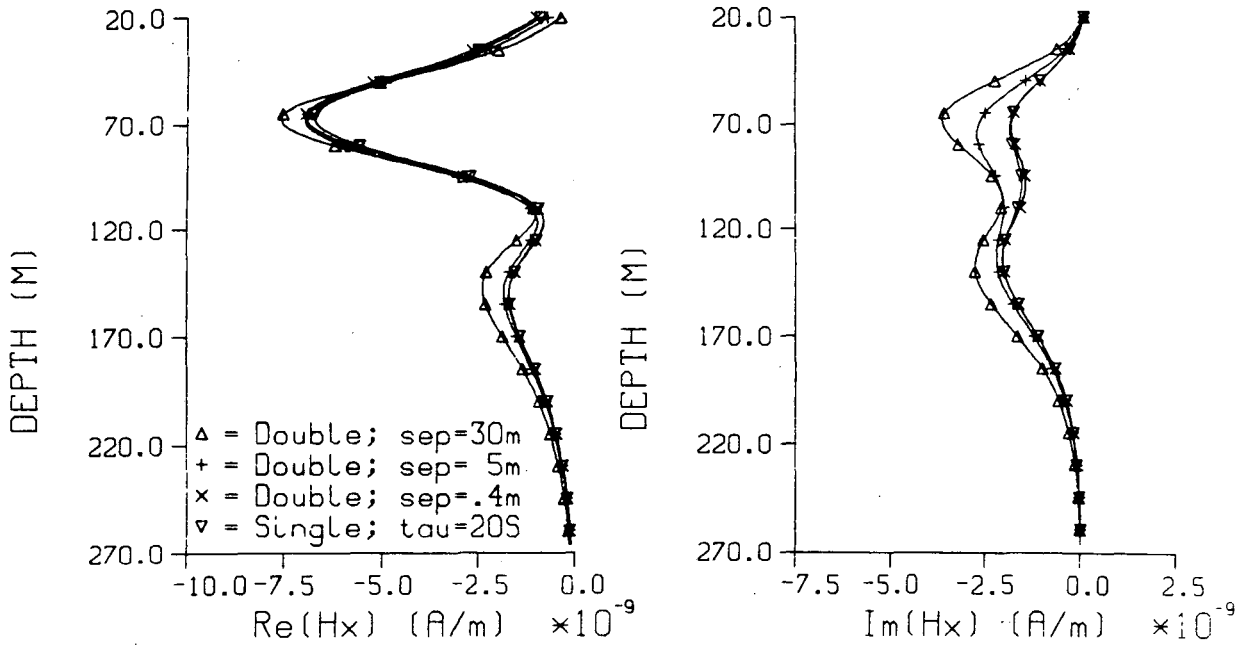

(a) Hx component

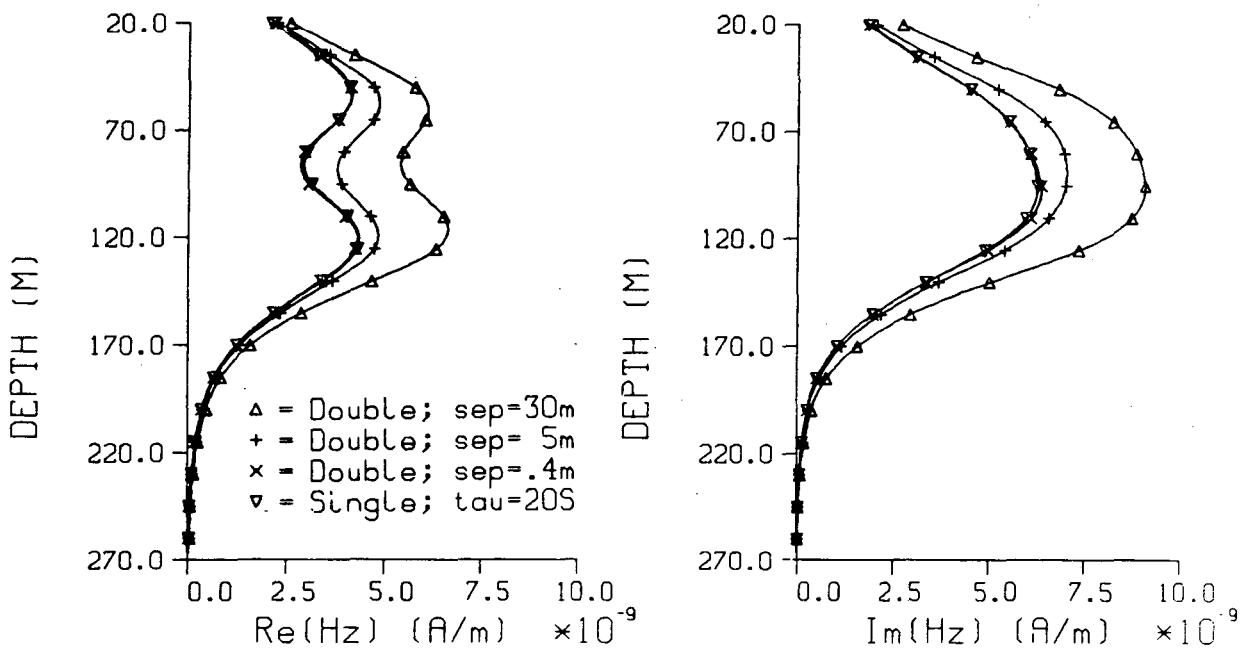

(b) Hz component

Figure 4-3-4 Accuracy test by variable separation

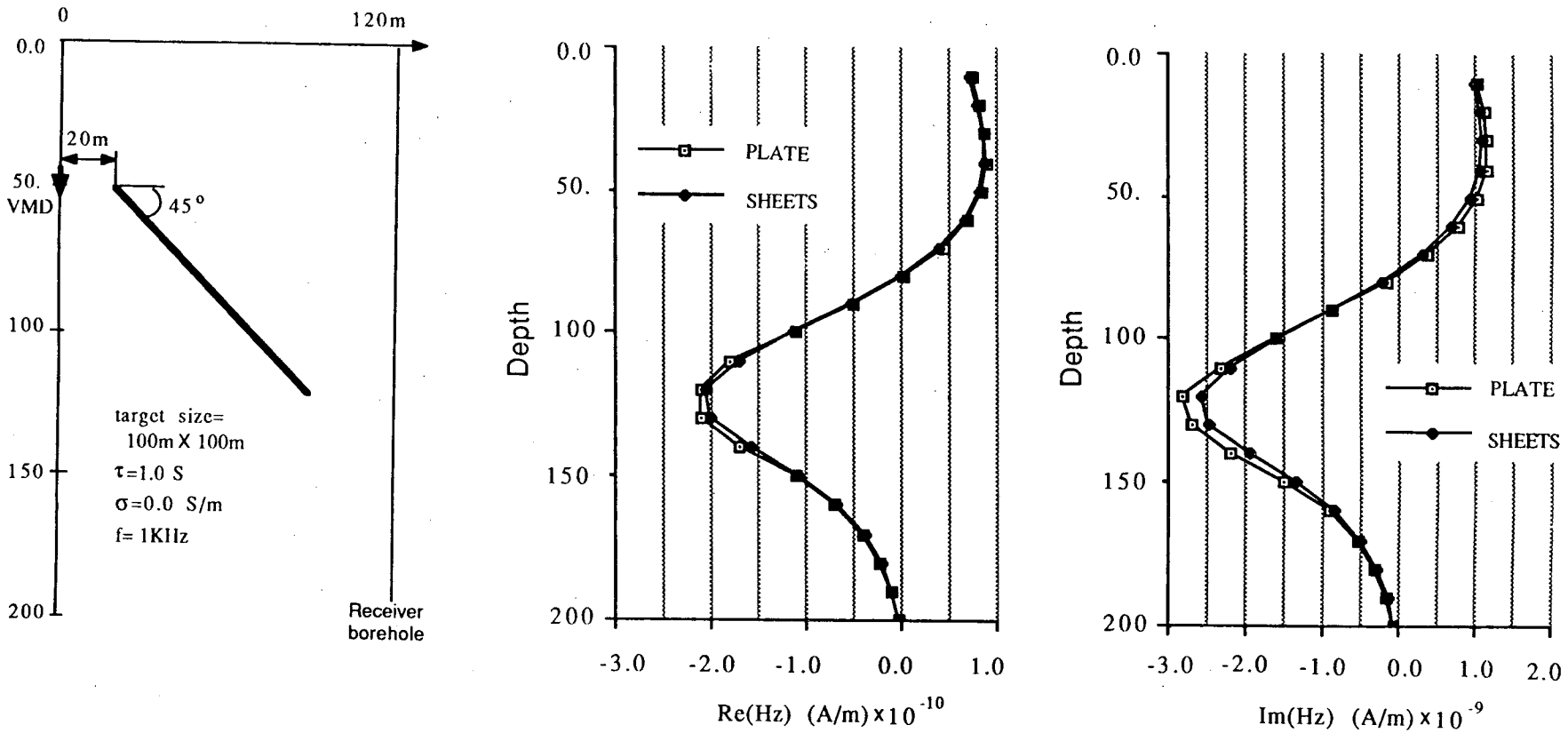

(a) Model

(b) Comparison

Figure 4-3-5 Comparison between the new program and program PLATE

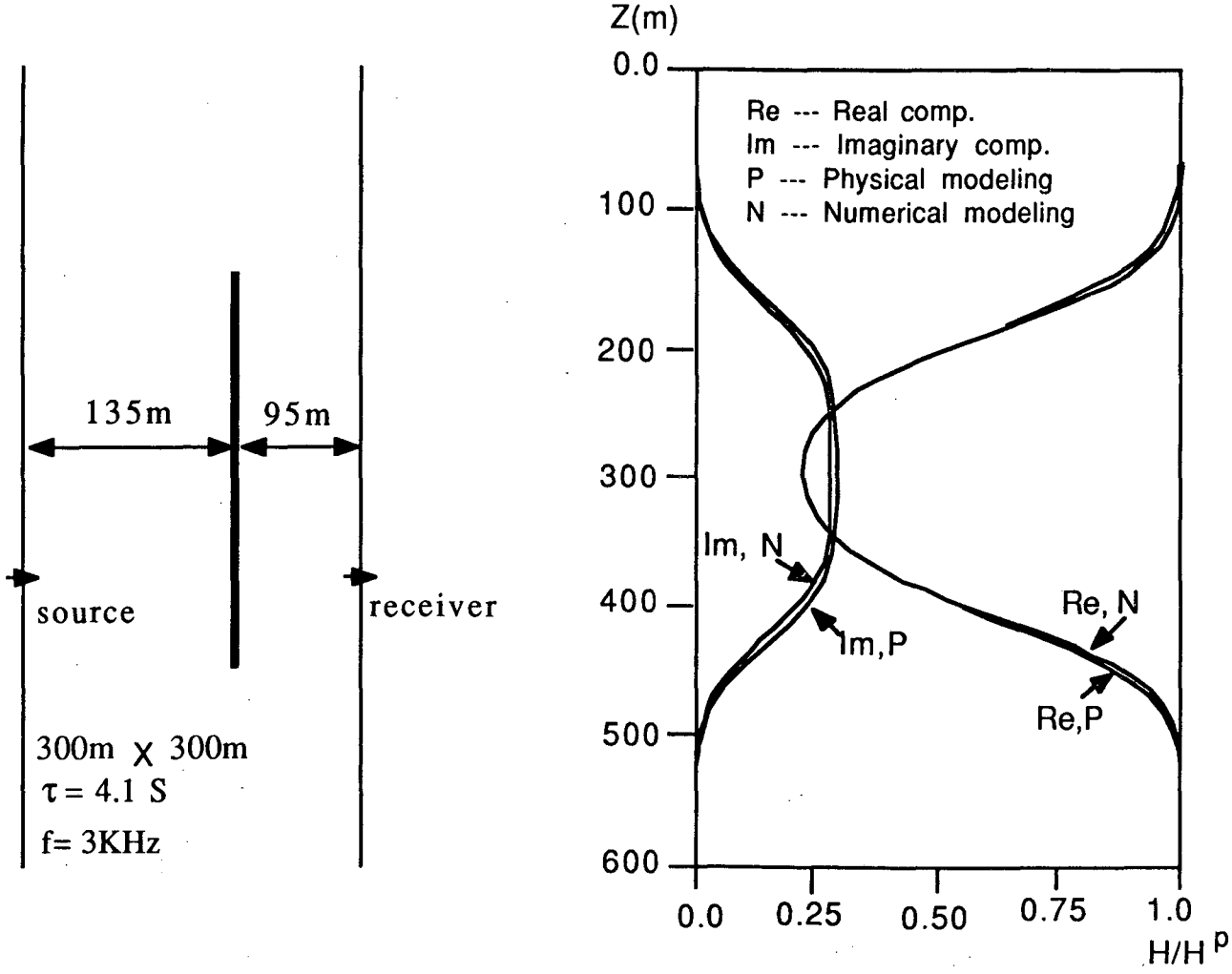

(a) Model

(b) Comparison

Figure 4-3-6 Comparison of physical and numerical modeling (single conductor)

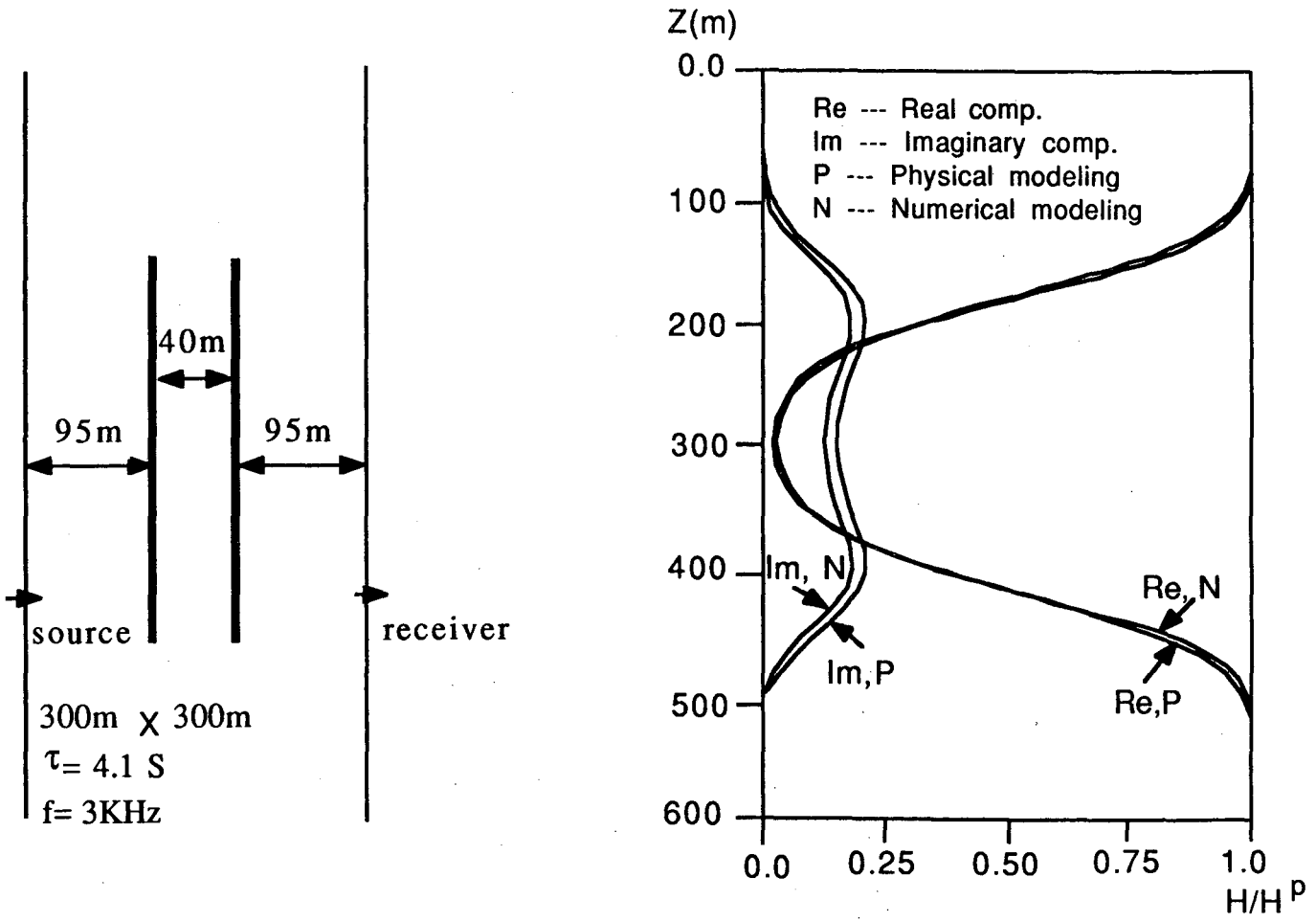

(a) Model

(b) Comparison

Figure 4-3-7 Comparison of physical and numerical modeling (two conductors)

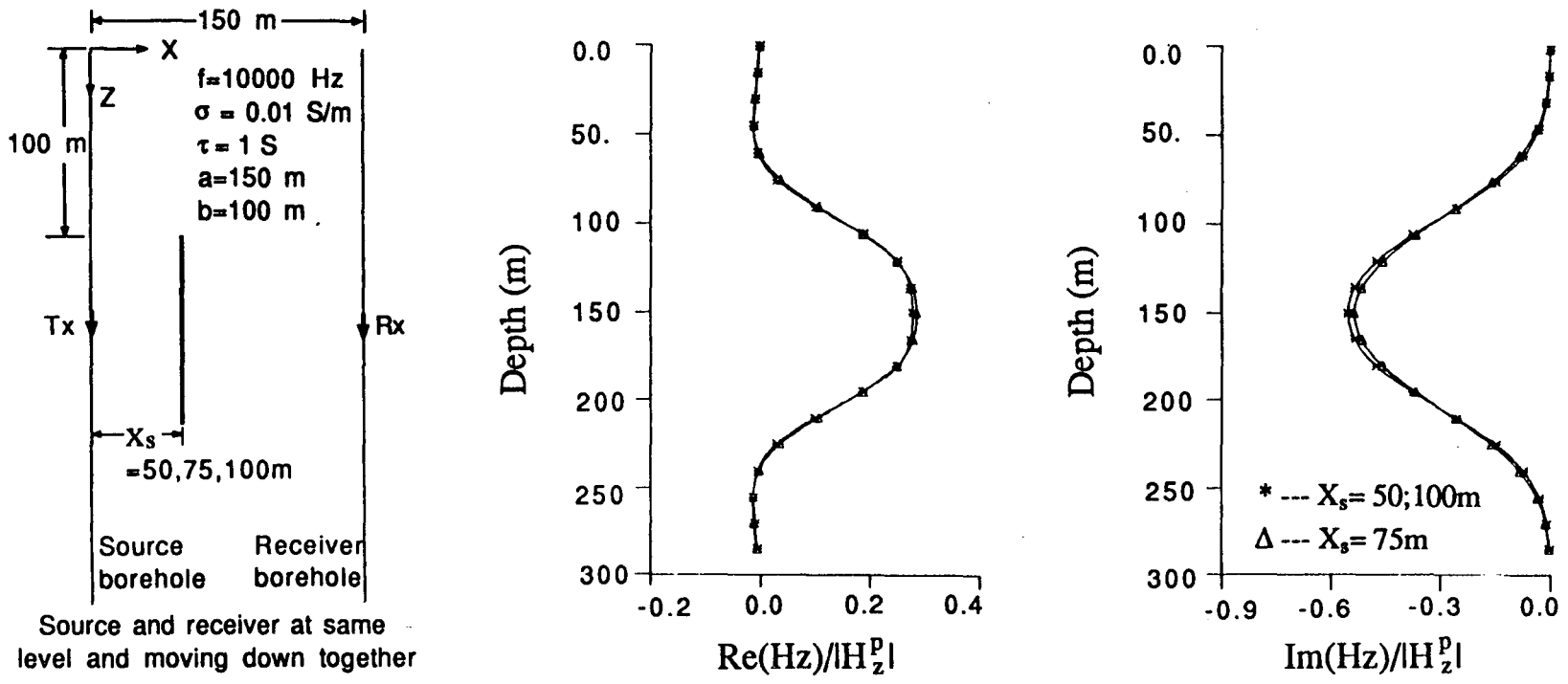

(a) Model

(b) Magnetic field

Figure 4-4-1 Cross-hole parallel source-receiver (one conductor)

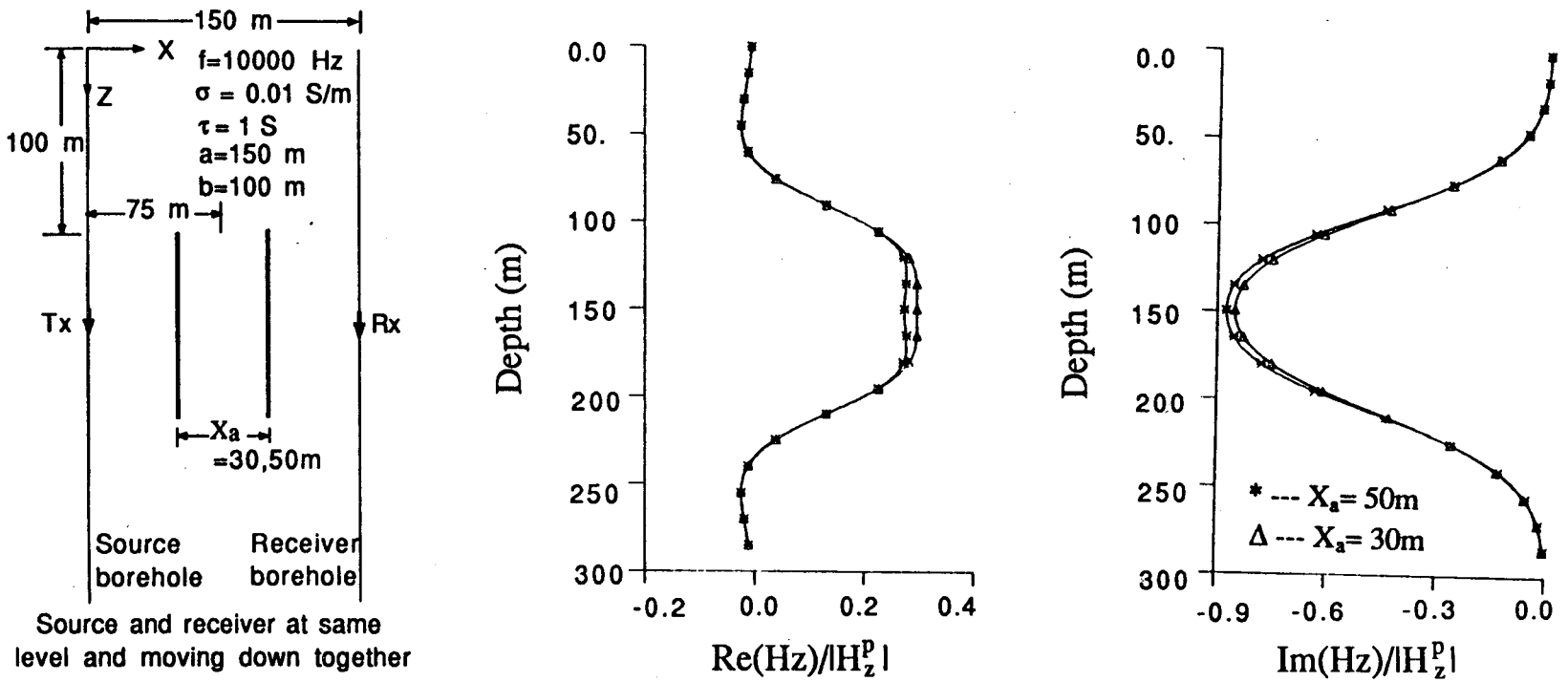

(a) Model

(b) Magnetic field

Figure 4-4-2 Cross-hole parallel source-receiver (two conductors)

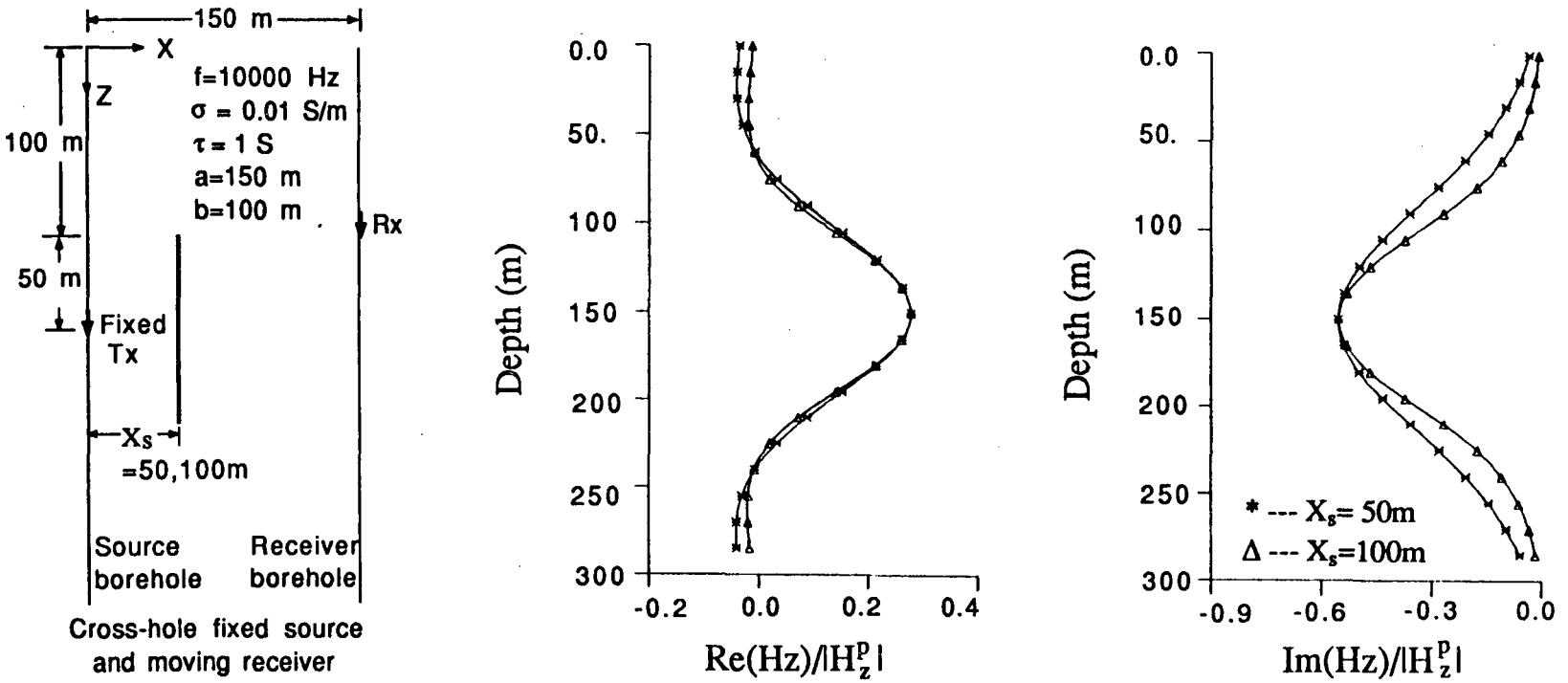

(a) Model

(b) Magnetic field

Figure 4-4-3 Cross-hole fixed source and moving receiver (one conductor)

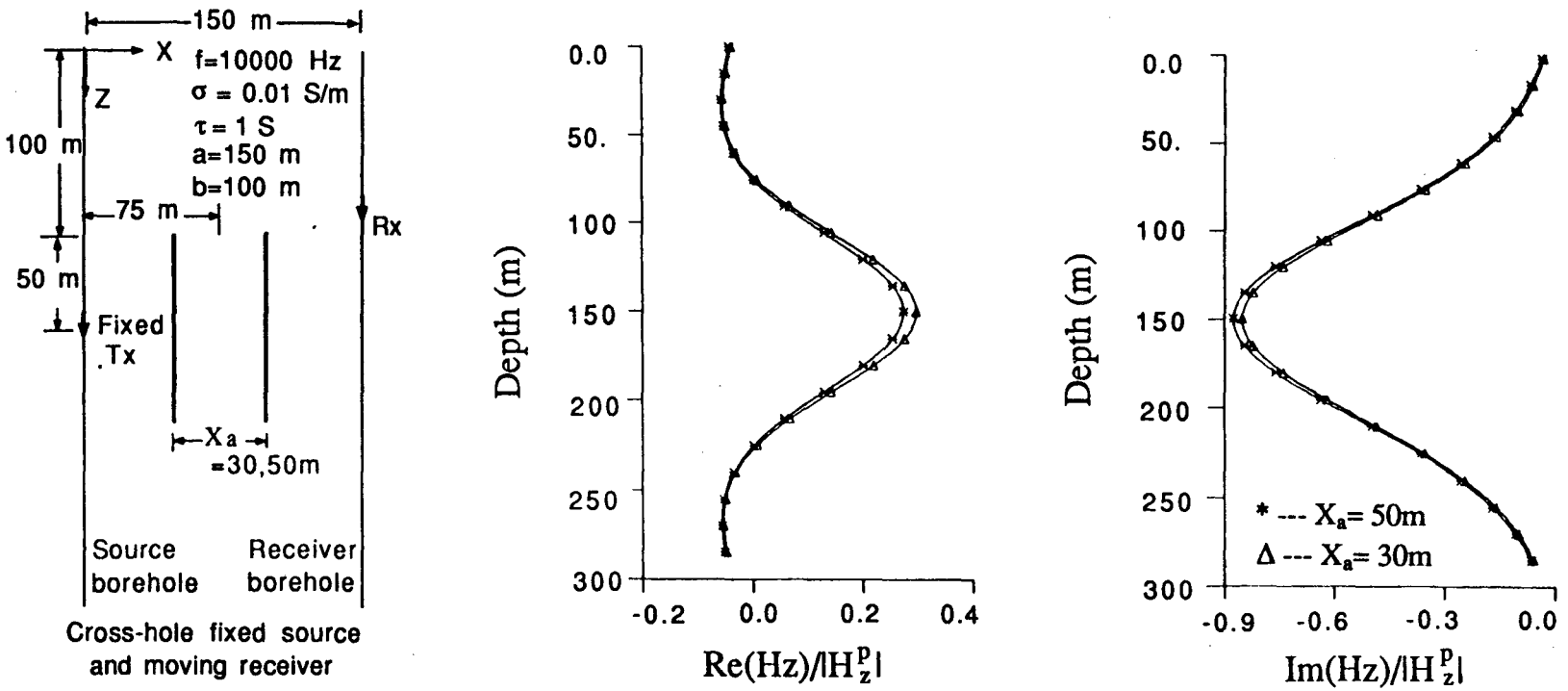

(a) Model

(b) Magnetic field

Figure 4-4-4 Cross-hole fixed source and moving receiver (two conductors)

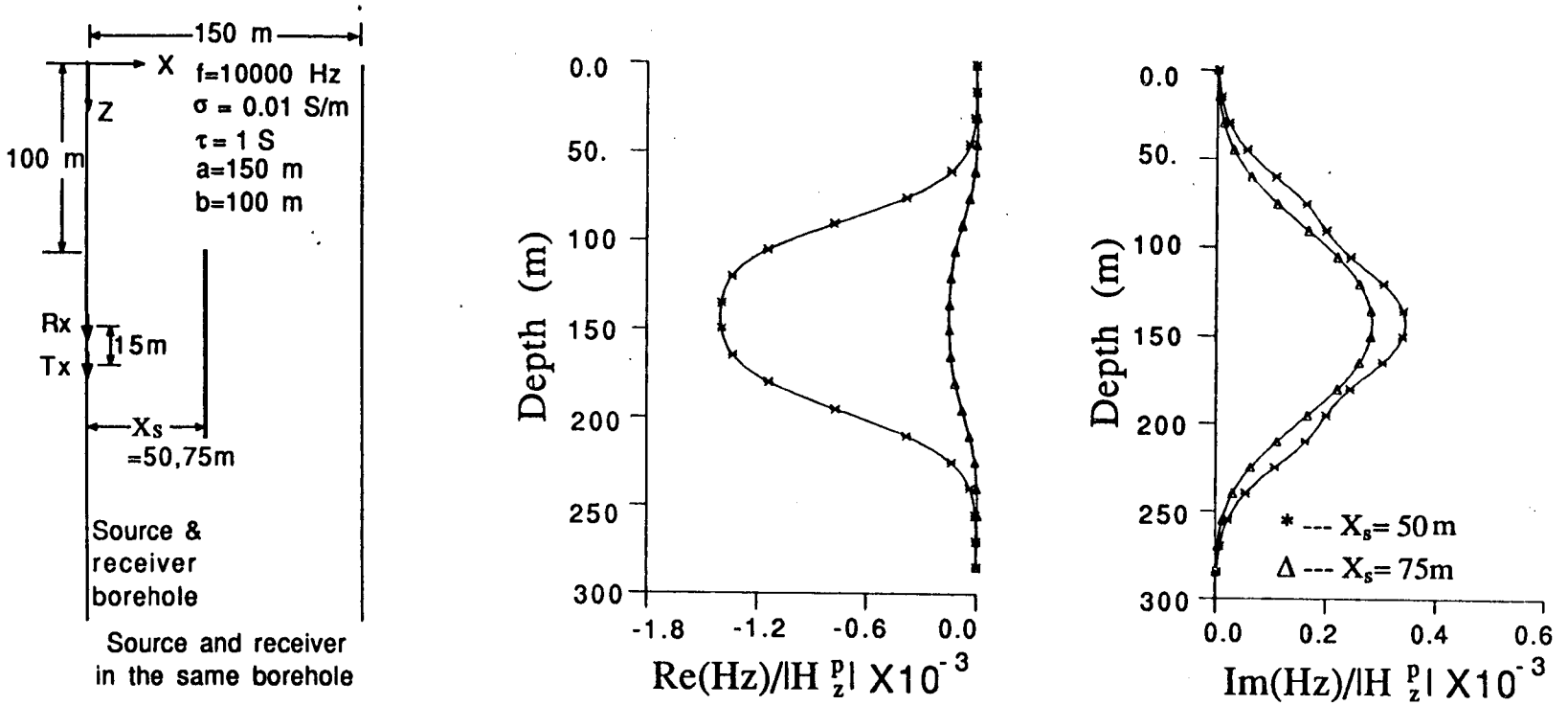

(a) Model

(b) Magnetic field

Figure 4-4-5 Single hole moving source and receiver (one conductor)

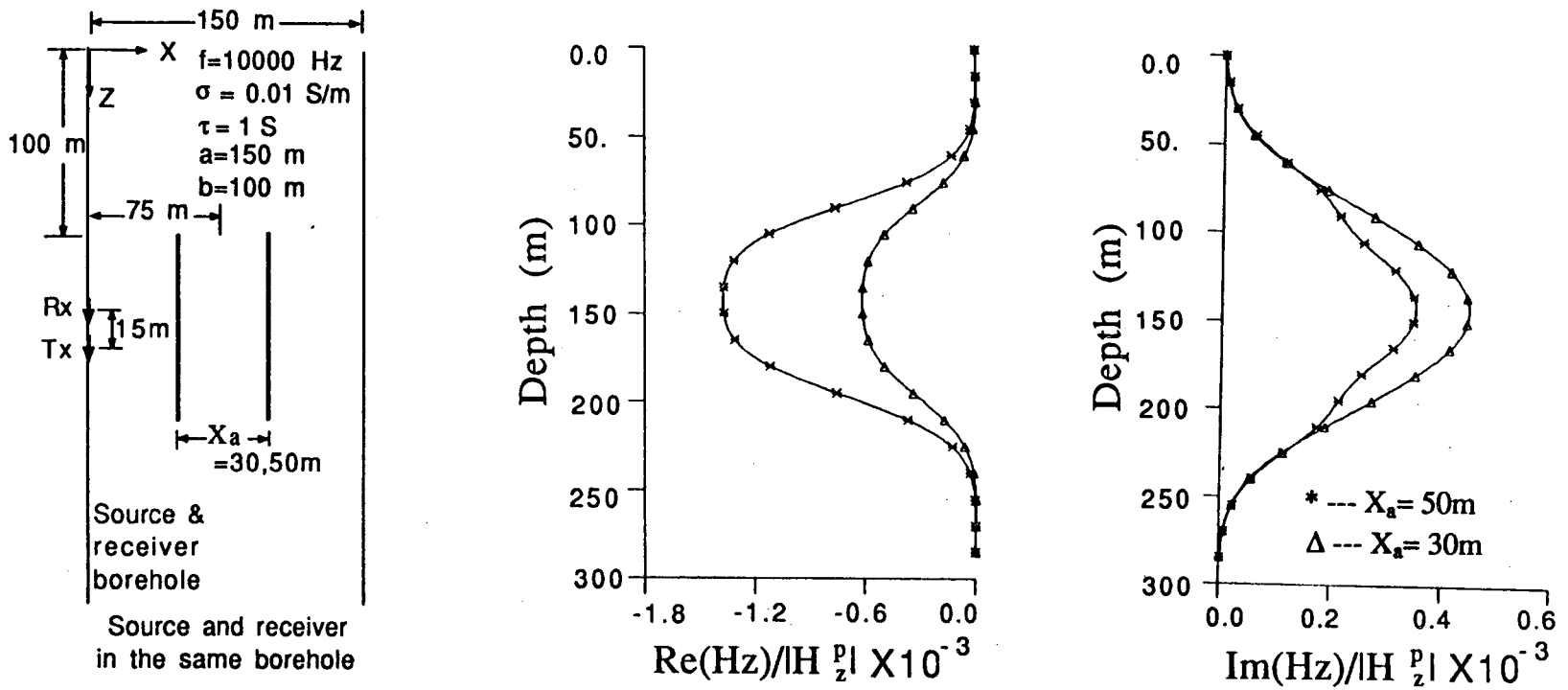

(a) Model

(b) Magnetic field

Figure 4-4-6 Single hole moving source and receiver (two conductors)

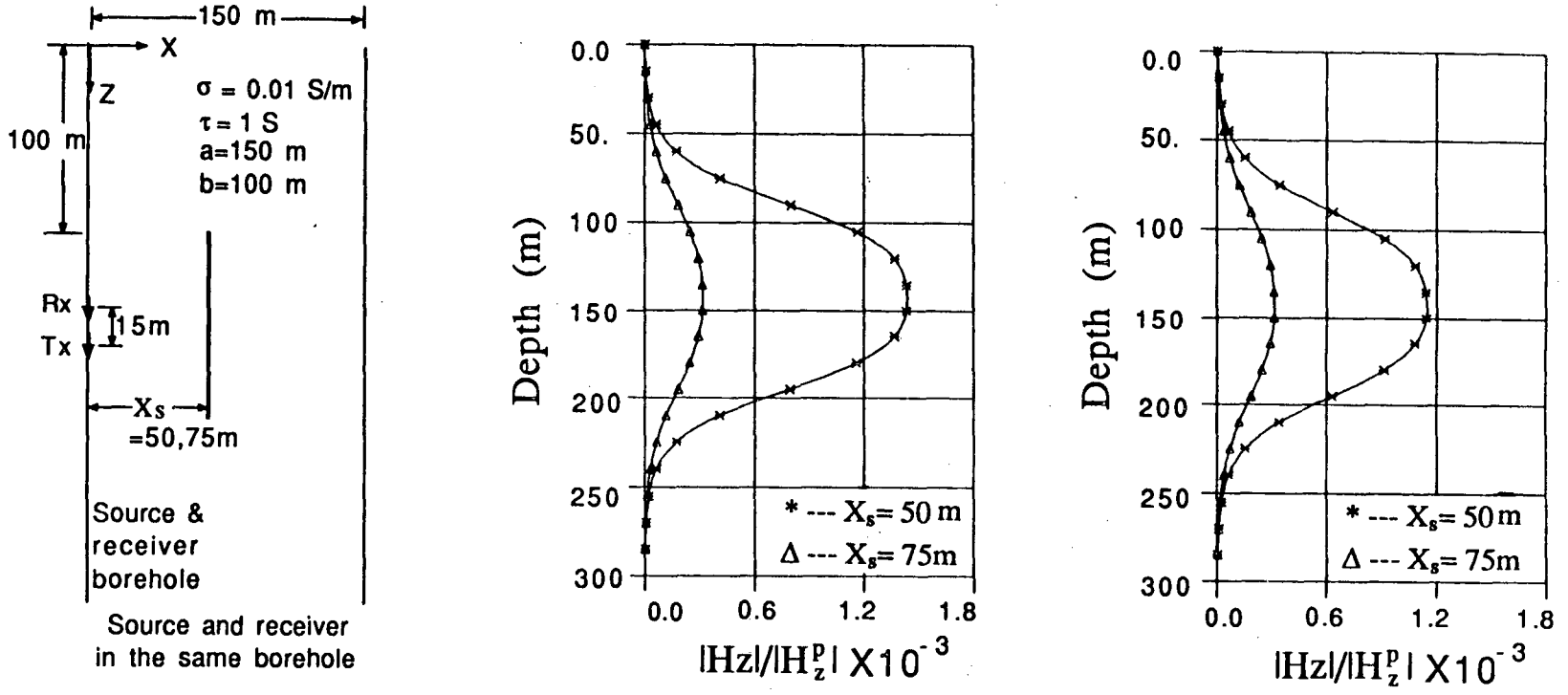

(a) Model (b) f=10K Hz (c) f=5K Hz

Figure 4-4-7 Single hole source-receiver configuration under different operating frequency

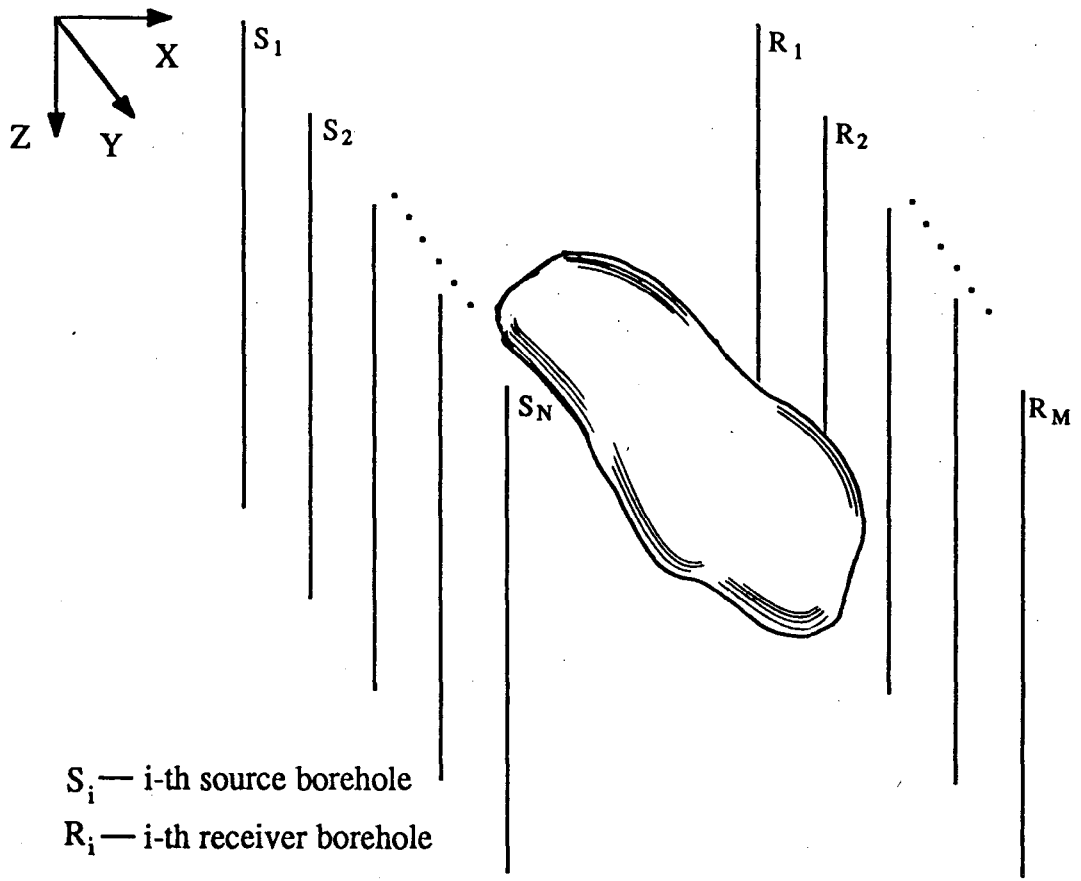

Figure 4-5-1 General three-dimensional target with multiple source and receiver boreholes

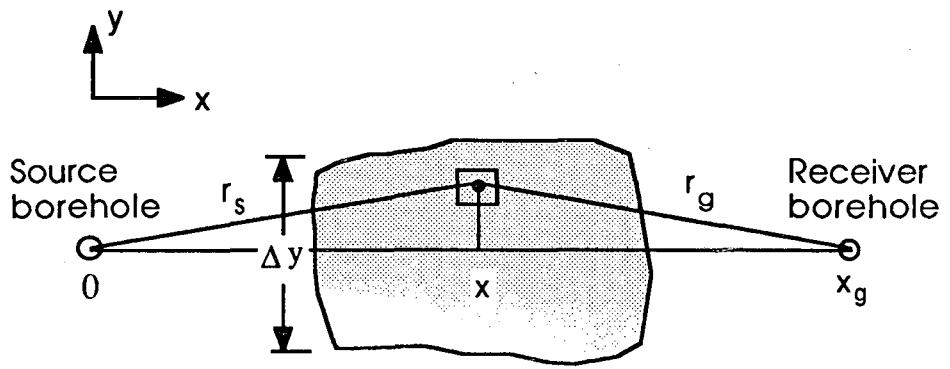

Figure 4-5-2 Three-dimensional target with only one pair of source and receiver boreholes

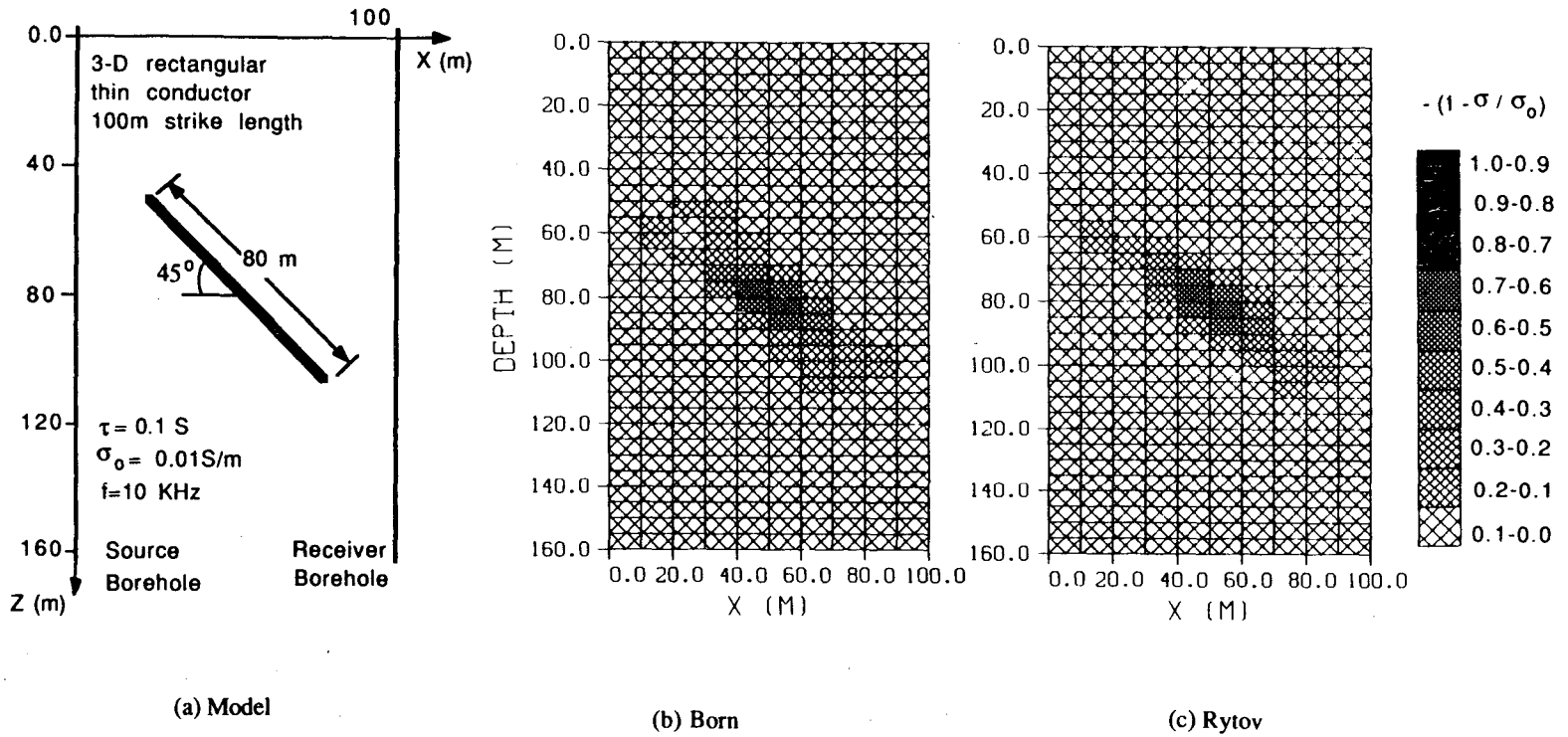

(a) Model (b) Born (c) Rytov

Figure 4-5-3 Solution for a dipping thin conductor with the 2-D method using a correction factor derived under far field approximation

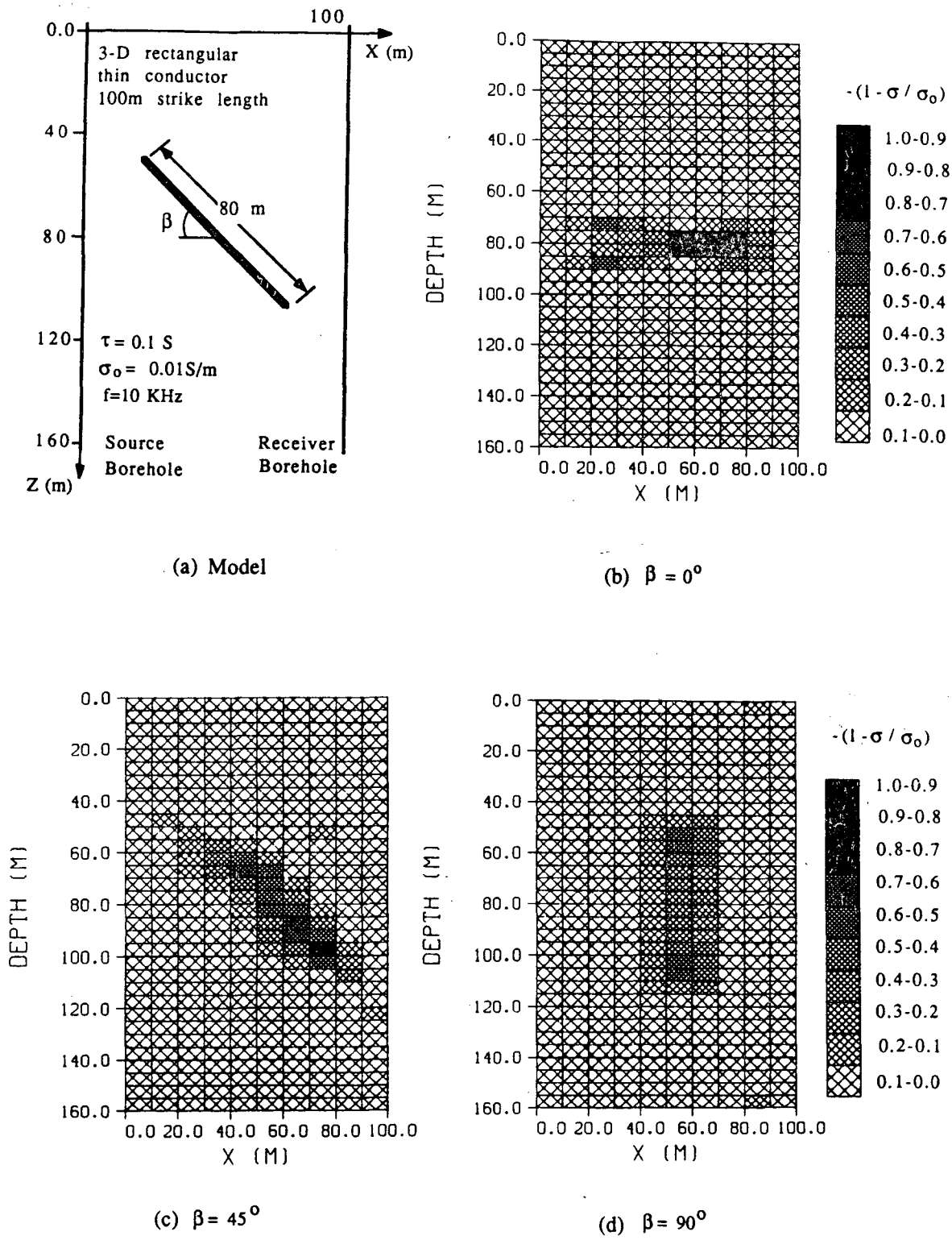

Figure 4-5-4 Born approximation solution for a dipping thin conductor

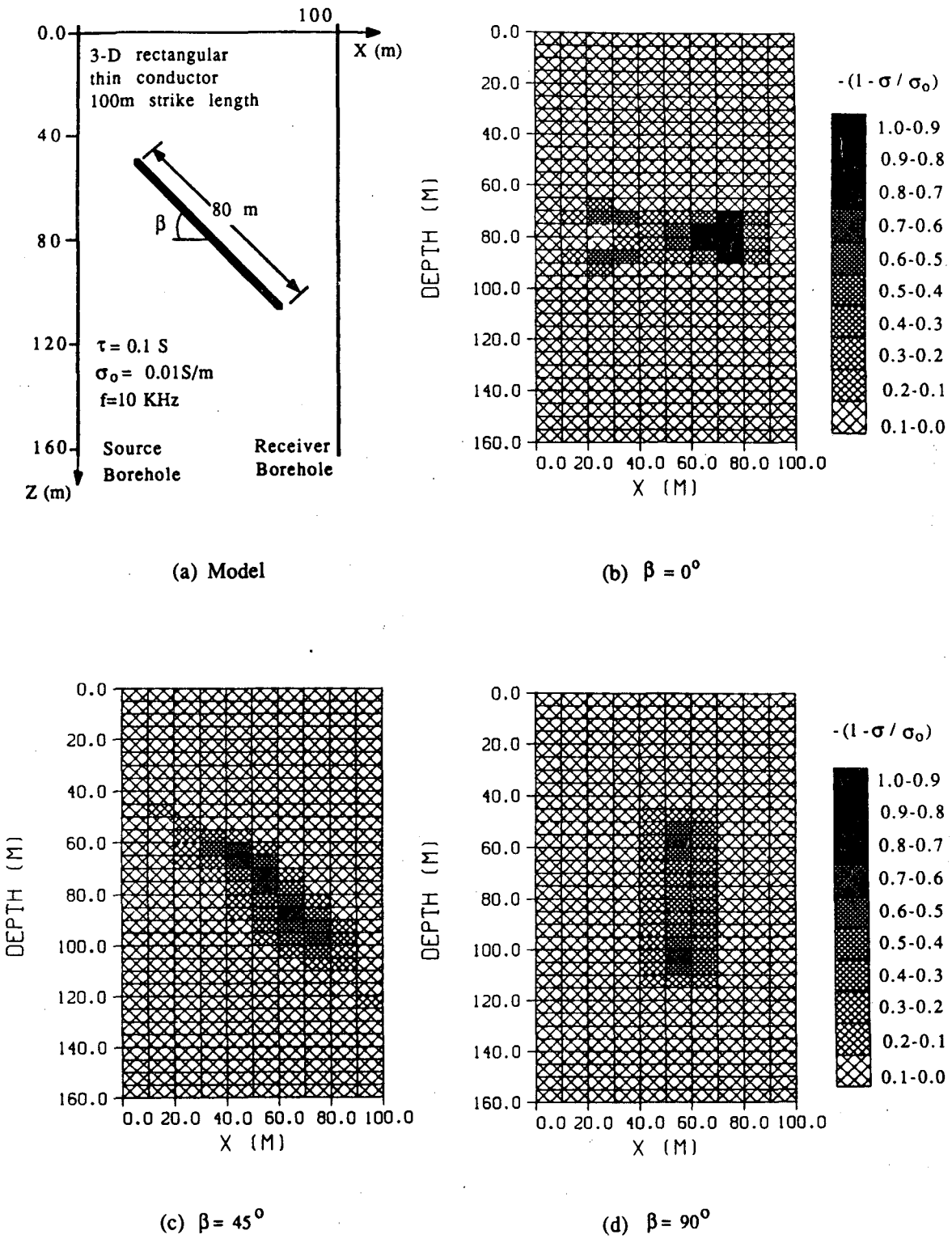

Figure 4-5-5 Rytov approximation solution for a dipping thin conductor

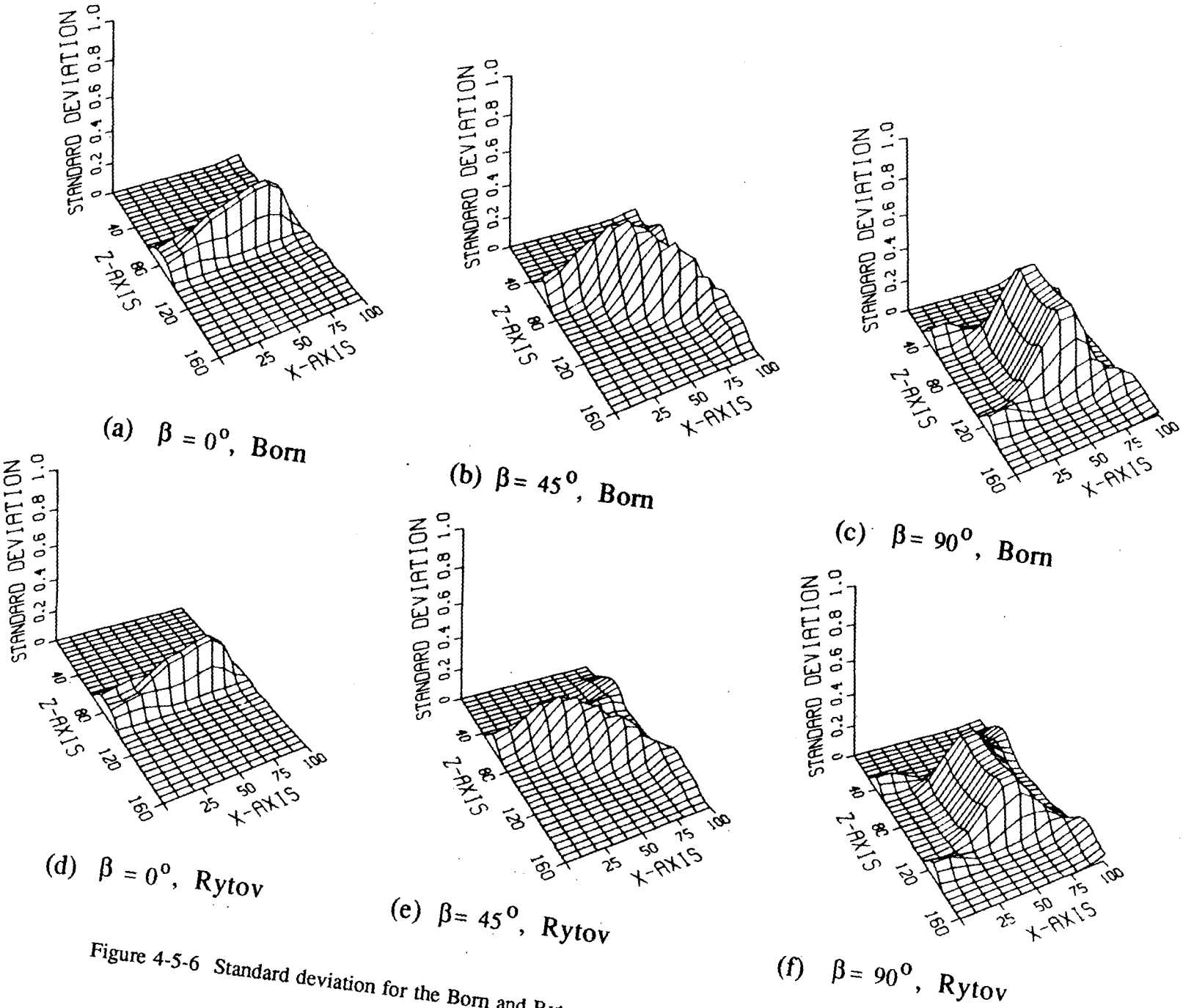

Figure 4-5-6 Standard deviation for the Born and Rytov solutions for the proceeding example

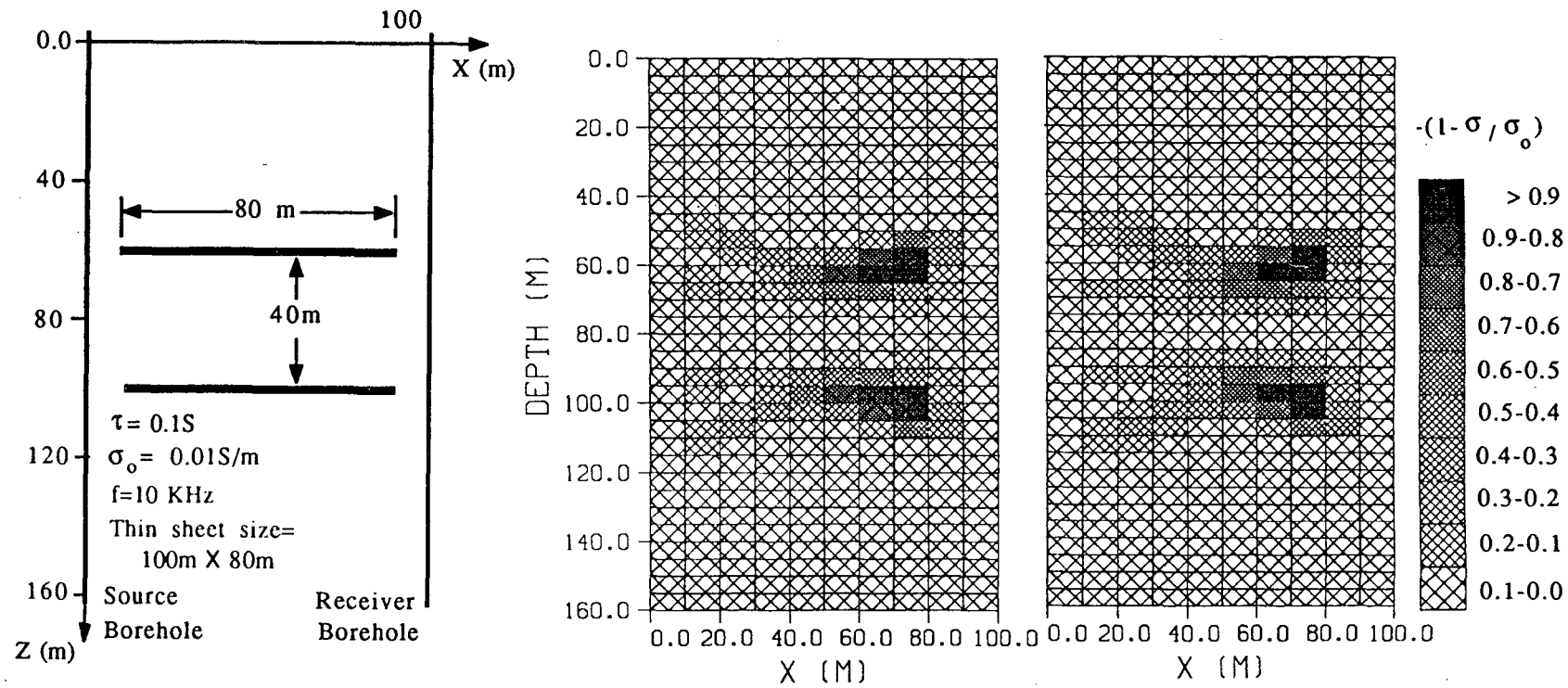

(a) Model (b) Born approximation (c) Rytov approximation

Figure 4-5-7 Images of two horizontal conductors

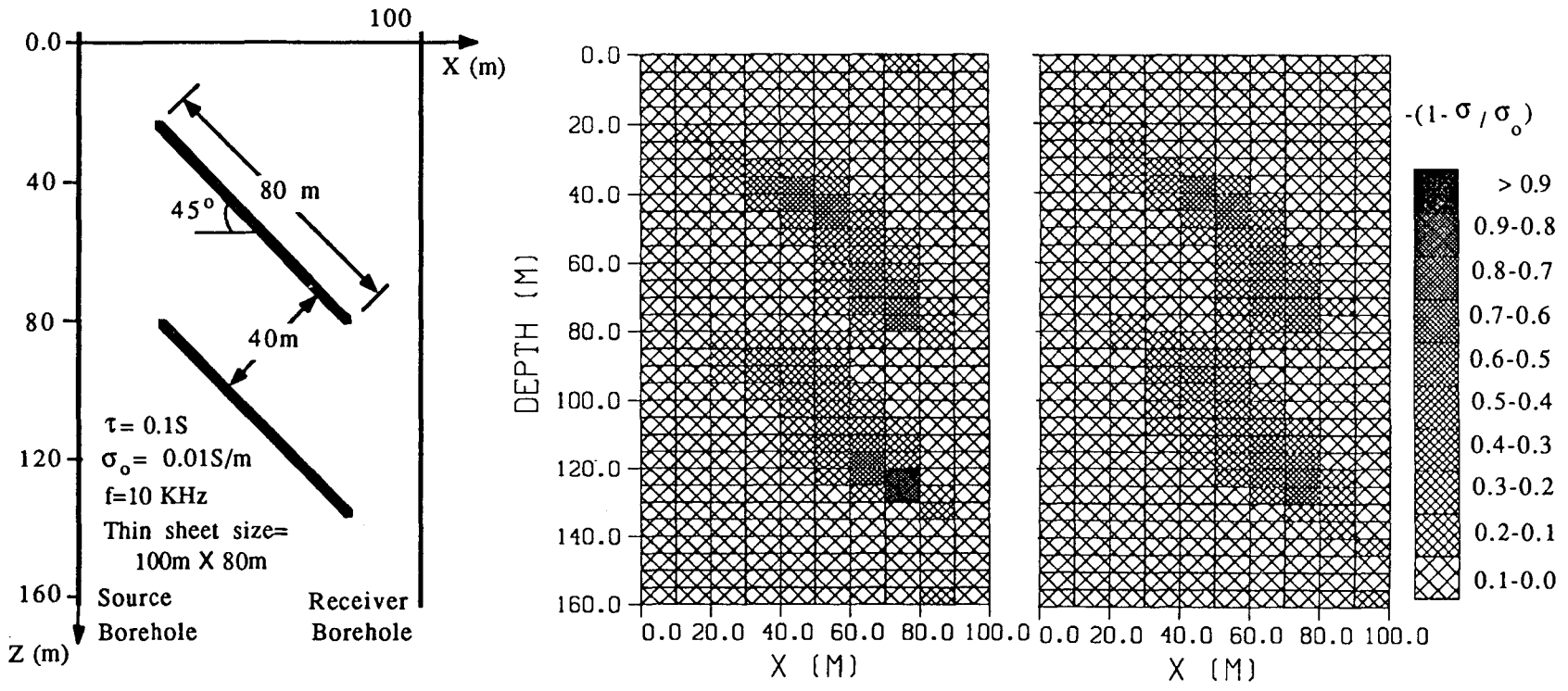

(a) Model (b) Born approximation (c) Rytov approximation

Figure 4-5-8 Images of two dipping conductors

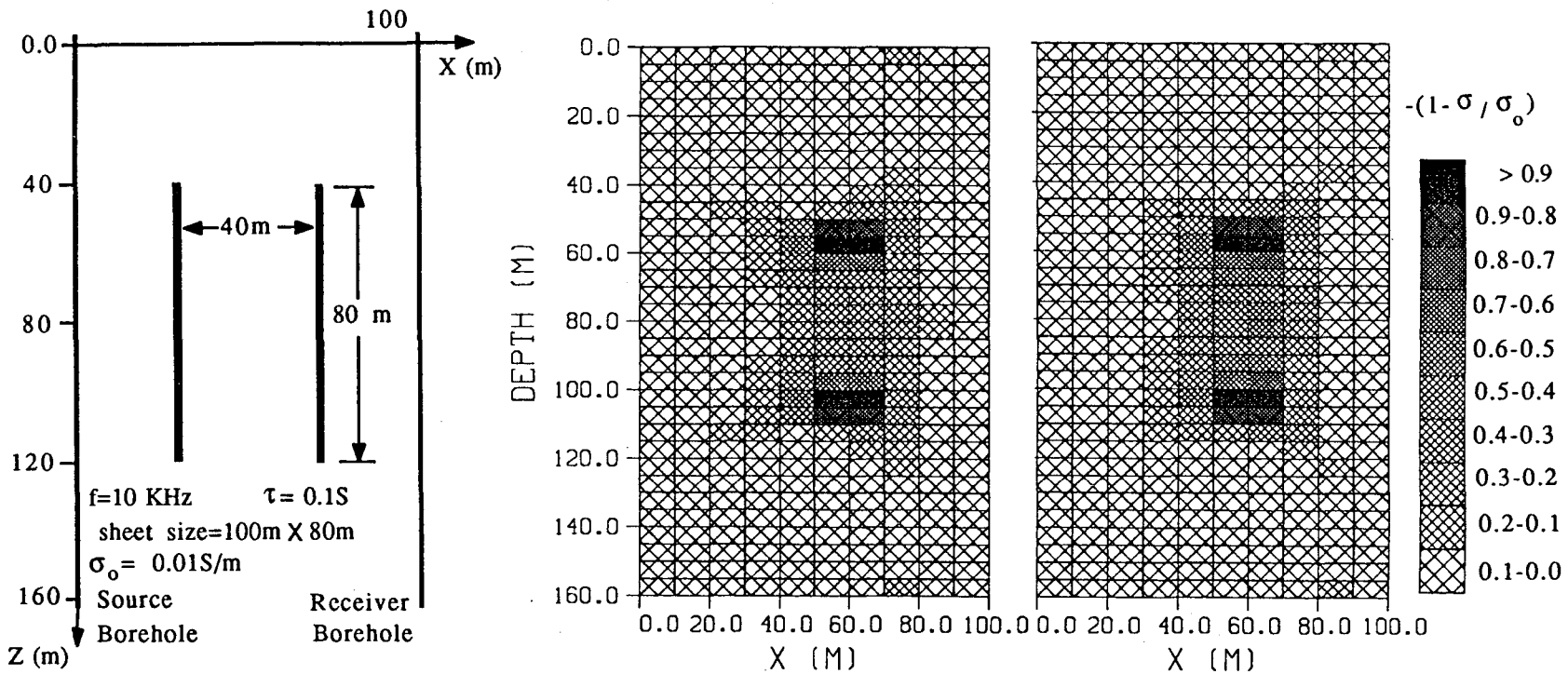

(a) Model (b) Born approximation (c) Rytov approximation

Figure 4-5-9 Images of two vertical conductors

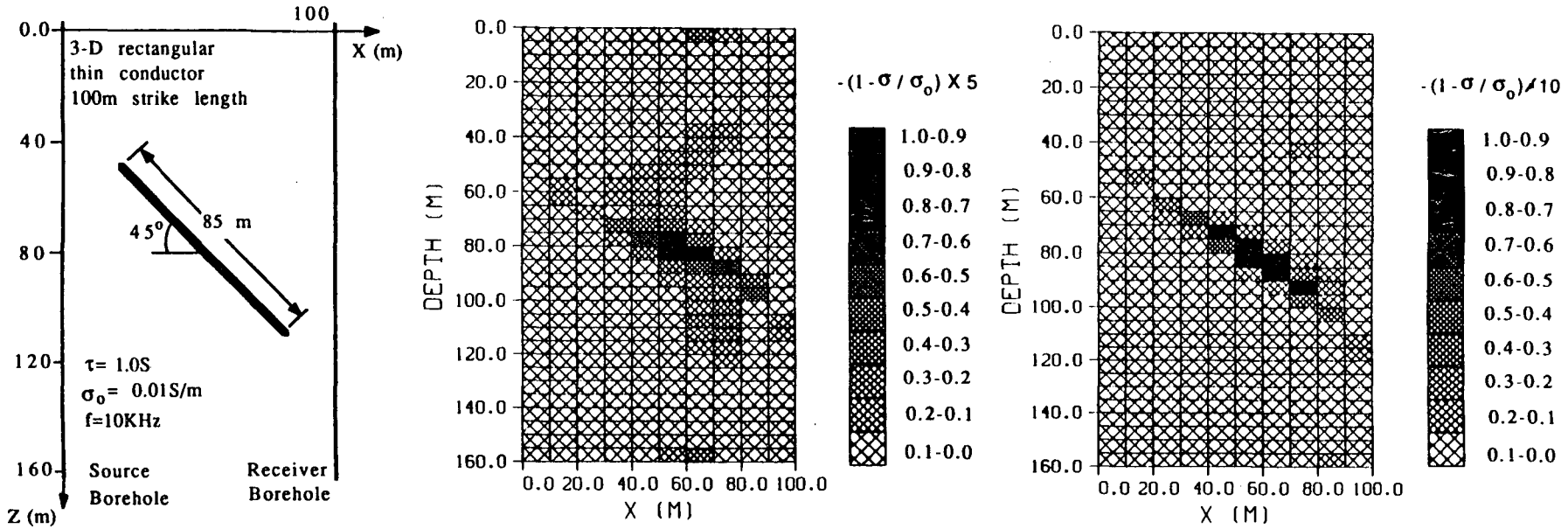

(a) Model (b) Born approximation (c) Rytov approximation

Figure 4-5-10 Comparison between Born and Rytov approximations for a dipping conductor ($\tau = 1.0S$)

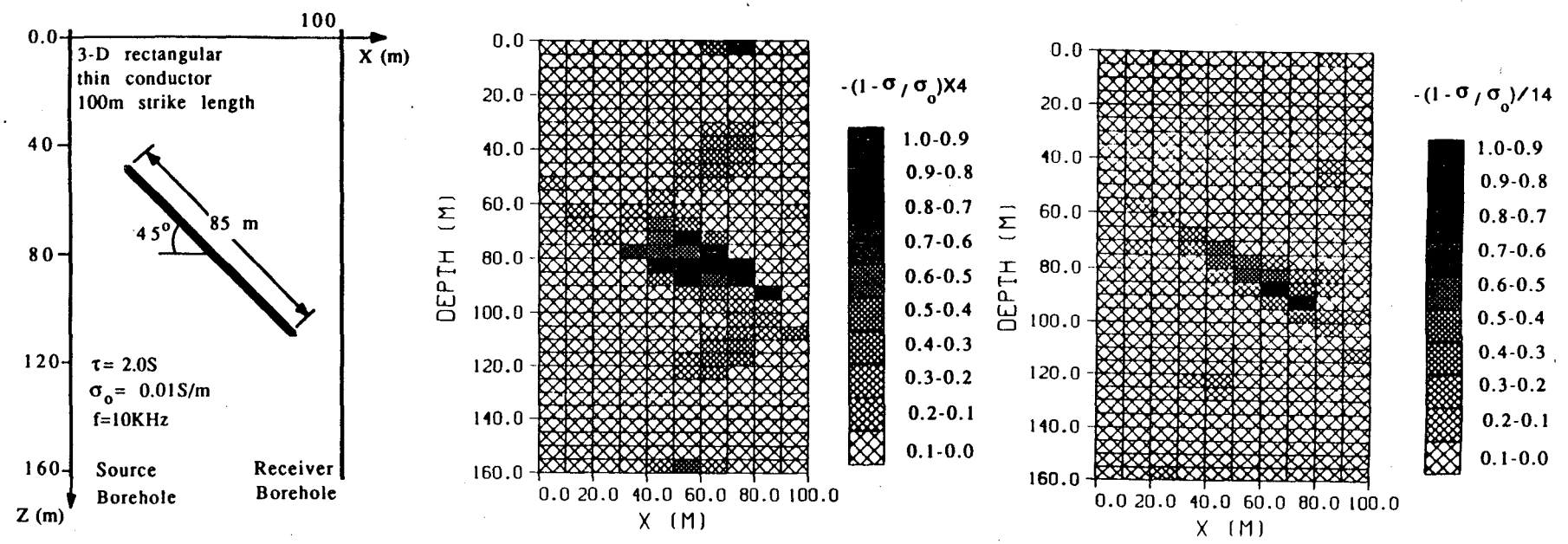

(a) Model (b) Born approximation (c) Rytov approximation

Figure 4-5-11 Comparison between Born and Rytov approximations for a dipping conductor ($\tau = 2.0S$)

Chapter 5
Conclusions and recommendations for further research

5.1 Conclusions

Integral equations can be solved numerically to model the cross-hole audio-frequency electromagnetic response of three types of conductive targets. The conductors considered are two-dimensional with Cartesian or cylindrical symmetry geometry. A more complicated situation involving finite size thin sheet conductors embedded in a conductive space can also be modeled. Both numerical and physical modeling checks reveal that the code accuracy is satisfactory. Forward modeling serves two purposes, it furnishes the necessary synthetic data for inversion studies and provides an understanding of the inverse problem.

Once the three forward modeling codes are available, the inverse problem can be investigated using a tomographic method which, by analogy with acoustic diffraction tomography, we have named electromagnetic diffusion tomography. Since the target (fracture) zones under consideration have small electric conductance or thickness-conductivity product, a weak scattering approximation (Born or Rytov) can be applied to simplify the problem. Under this assumption, the target resolution of the audio-frequency electromagnetic method can be examined through numerical experiments and by investigating the wave number domain coverage of the object, or conductivity, function. The target detectability is found to be related to the source-receiver array arrangement and the source operating frequency.

For 2-D Cartesian geometry, the wave number domain coverage for various source-receiver configurations is similar to that seen in the acoustic diffraction tomography (Devaney, 1984; and Wu and Toksöz 1987). However, due to the diffusive nature for the audio-frequency electromagnetic field in an electrically conductive medium, the coverage in the EM case is much lower than that for the acoustic problem. The wave number domain analysis tells us that the inverted conductivity image is extremely band limited in the wave number domain.

For cross-hole source-receiver configuration, the horizontal coverage is much smaller than the vertical coverage and thus the space resolution in the lateral direction is poorer than that in the vertical. The maximum lateral coverage is related to the operating frequency used. One should use the highest frequency whenever possible. Also, the lateral resolution can be enhanced greatly if one uses both the cross-hole and single-hole measurements.

The wave number domain coverage also reveals that target characteristics, such as the dip angle of the thin conductors considered in most of the numerical experiments, should be properly recovered since there is no rotation or shift in the wave number domain. The distortion due to the incomplete coverage (missing high wave number) only makes the image blurred.

Because of the narrow band of coverage of the object function in the wave number domain and in order to enhance and stabilize the inversion result, constraints should be used whenever possible. On the other hand, if no prior information is imposed on the inversion process, one should always solve for the smoothest image because any rapid change is artificial and unstable. In order to incorporate the constraint that the target is more conductive than the background, the derived explicit solution for the object function can not be used. Instead, the integral equation relating the secondary response and the unknown conductivity is discretized to form a linear system of equations. Then a constrained least squares method or a quadratic programming algorithm can be used to obtain the inverse solution.

Under an additional far field approximation, the 2-D cylindrical symmetry and the 3-D models are found to have the same inversion characteristics as the 2-D Cartesian model. After a correction of the geometrical factor, the 2-D inversion methods are applicable to these more complicated situations.

Numerical experiments with different target geometries demonstrate the results with the cross-hole source-receiver configuration and the combined cross-hole and single-hole source-receiver arrays. It is also found from the numerical calculations that the Rytov approximation is superior to the Born one.

5.2 Recommendations for future work

Our inversion analysis is carried out under a weak scattering Born or Rytov approximation. In order to have wider application, it is necessary to extend the approach to a more general situation involving higher conductivity contrasts. By analogy with the acoustic problem (Slaney and Kak, 1985), it may be possible for our weak scattering EM problem to be extended somewhat by using the Born series. Nevertheless, such an approach has its shortcomings in convergence. Other conventional iterative inversion methods may be of help, however, at present, the large amount of computing time involved and the convergence problem may prohibit this approach from being widely used in routine data interpretation.

In solving for the three-dimensional situation, both weak scattering and far-field approximations are applied. These approximations imply that the channeling current is dominant over the induced current in the target, as might be expected for a conductive background and a low conductivity contrast between the target and the background medium. If one wants to extend our technique to high resistivity background, a new algorithm must be developed to take care of both types of currents which cause a totally different EM response (Newman et al., 1989).

The scheme for obtaining the conductivity distribution involves a matrix inversion, which is time consuming if there is a large number of unknowns. Therefore, techniques which do not demand matrix inversion would be preferred. The backpropagation algorithm (Devaney, 1982) used in the acoustic diffraction tomography might be one of the approaches that one might be able to use. Here, the difficulty lies in incorporating the necessary constraints to enhance and stabilize the EM inversion result.

The numerical inversion analysis in this thesis principally deals with the cross-hole source-receiver configuration. Studies based on the back-scattered field (i.e. source and receivers in the same borehole) should be helpful in increasing the resolution. In that case, as indicated by the wave number domain coverage a multifrequency approach should be taken.

Appendix A
Seismic tomographical methods

Two general types of seismic tomographical methods are available. The first is ray tomography, which employs a straight ray optical model. The other is diffraction tomography, which utilizes either the Born or the Rytov weak scattering approximation. A brief review of both methods is given here to provide additional background for our treatment of the EM inverse problem.

A.1 Ray tomography

Ray tomography was first applied in medical radiology and astrophysics. Early papers can be found from Bracewell (1956), Cormack (1963,1964), Bracewell and Riddle (1967), and a number of others. Later, it was adapted to seismic travel time data (Bois et al., 1972; Wang et al., 1983; and Peterson, 1986). By taking advantage of similarity between the physical phenomena involved, ray tomography has also been applied to study the high frequency electromagnetic problem in a highly resistive background medium (Dines and Lytle, 1979; Daily, 1984) Seismic ray tomography relies on the well known fact that the time delay between transmitting and receiving a signal is related to the source-geophone separation and the sound velocity in the medium, i.e. distance = time × velocity or time = distance × slowness, where slowness is the reciprocal of velocity.

For the cross-hole case (Figure A-1), the formation between boreholes is first divided into cells, or pixels. Under the straight ray optical assumption, the sonic wave traveling along the line connecting the source and receiver arrives at the geophone first. Thus for a single experiment, i.e. for a particular source-geophone combination, there is a linear equation relating the measured time delay with the medium property along the ray path.

$$\sum_{j=1}^{N} s_{ij} \, f_j = p_i \, , \tag{A-1}$$

where

s_{ij} --- the length of the segment of the i th ray intersecting the j th pixel;

f_j --- the averaging of the slowness (1/velocity) inside j th pixel.

p_i --- the time interval for the i th source-geophone combination.

If we have M source-receiver combinations, for an imaging area of N pixels, a linear system of equations can be obtained.

$$S\ F = P\ , \tag{A-2}$$

where

$S = [s_{ij}]_{N \times M}$, a N by M sparse matrix related to the geometry;

$F = [f_1, f_2, \cdots, f_N]^T$, an N element vector to be solved;

$P = [p_1, p_2, \cdots, p_M]^T$, an M element vector from measurements.

Numerous studies to solve the linear system of equations with a sparse coefficient matrix have been done in medical tomographic applications (Gordon et al., 1970; Herman et al., 1973; Huesman et al., 1977; to name but a few). The most popularly used reconstruction method in seismic application is the algebraic reconstruction technique, or ART, which is an iterative reconstruction scheme (Peterson, 1986). Ray tomography, as discussed above, can be summarized by the projection and backprojection theory (Macovski, 1983) with variations for specific applications. A very extensive review on this subject can also be found from Mersereau and Oppenheim (1974).

A.2 Diffraction tomography

The theoretical development of diffraction tomography was done by Wolf (1969) although the term 'diffraction tomography' was not used then. Contributions to this area are also from Mueller et al., 1978, Mueller et al., 1979, and Johnson and Tracy, 1983, among the others. Devaney (1984) first investigated its geophysical application in seismic exploration. Later, Wu and Toksöz (1987) compared acoustic diffraction tomography with holography and prestack seismic migration. Recently laboratory investigations of the method and comparisons with ray tomography were carried out by Lo et al. (1988). Diffraction tomography is more mathematically complex than ray tomography. The basic steps involved, however, are as follows.

First, an integral relationship is established between the measured secondary response and the acoustic property of the medium. In a source free region the acoustic pressure wave within a two dimensional acoustic medium satisfies the following scalar wave equation (Wu and Toksöz, 1987),

$$\nabla^2 u(\mathbf{r}) + \frac{\omega^2}{C^2(\mathbf{r})} u(\mathbf{r}) = 0, \tag{A-3}$$

where $u(\mathbf{r})$ is pressure, ω is angular frequency, and ∇^2 is the Laplacian operator. The two-dimensional coordinate system is shown in Figure A-2. By decomposing $u(\mathbf{r})$ into incident (u^o) and scattered (U) waves, i.e.

$$u(\mathbf{r}) = u^o(\mathbf{r}) + U(\mathbf{r}) \tag{A-4}$$

and defining object function $O(\mathbf{r})$ as

$$O(\mathbf{r}) = 1 - \frac{C_o^2}{C^2(\mathbf{r})}, \tag{A-5}$$

an integral relation between the object function and the measured secondary response can be derived.

$$U(\mathbf{r}) = -\int_S k_o^2 O(\mathbf{r}') u(\mathbf{r}') G(\mathbf{r},\mathbf{r}') d\mathbf{r}', \tag{A-6}$$

where $k_o = \omega/C_o$ and C_o is the reference background velocity. The integration is on the area of interest and $G(\mathbf{r},\mathbf{r}')$ is the two dimensional Green's function.

$$G(\mathbf{r},\mathbf{r}') = -\frac{i}{4} H_o^{(1)}(k_o |\mathbf{r}-\mathbf{r}'|). \tag{A-7}$$

Here $H_o^{(1)}$ is zero order Hankel function of the first kind.

The second step is to assume that the inhomogeneity has a small contrast with the background medium. Thus Born approximation ($u \approx u^o = G$) can be applied to equation (A-6). Let $\mathbf{r}_s$ be the source position and $\mathbf{r}_g$ be the geophone position and assume unit source excitation,

$$U(\mathbf{r}_g, \mathbf{r}_s) = -k_o^2 \int_S O(\mathbf{r}) G(\mathbf{r},\mathbf{r}_s) G(\mathbf{r}_g,\mathbf{r}) d\mathbf{r}, \tag{A-8}$$

where the change of notation from $U(\mathbf{r})$ to $U(\mathbf{r}_g, \mathbf{r}_s)$ is for the clarity of coordinate relation.

Next, Fourier transforms along source and geophone lines (i.e. with respect to z_s and z_g) are taken respectively as an example in the cross-hole case (Figure A-2). After denoting k_s as the Fourier domain wave number along source line and k_g as that along the geophone line, we have

$$U(k_g, k_s) = \frac{k_o^2}{4\gamma_g \gamma_s} e^{(i\gamma_s x_s - i\gamma_g x_g)} \int_S O(\mathbf{r}) e^{-i(\gamma_s - \gamma_g)x - i(k_s + k_g)z} \, dxdz. \tag{A-9}$$

Where

$$\gamma_s^2 = k_o^2 - k_s^2; \qquad \gamma_g^2 = k_o^2 - k_g^2. \tag{A-10}$$

x_s and x_g are the horizontal coordinates of the vertical boreholes (Figure A-2).

Finally, the object function can be reconstructed by double inverse Fourier transforms. If the following substitutions are made,

$$\gamma_s - \gamma_g = k_x; \qquad k_s + k_g = k_z, \tag{A-11}$$

equation (A-9) becomes

$$U(k_g, k_s) \frac{4\gamma_g \gamma_s}{k_o^2} e^{-i\gamma_s x_s + i\gamma_g x_g} = \int_S O(\mathbf{r}) e^{-i k_x x - i k_z z} \, dxdz. \tag{A-12}$$

Thus the object function can be derived by inverse Fourier transforms in k_x and k_z on the left hand side of equation (A-12).

$$O(\mathbf{r}) = \frac{1}{(2\pi)^2} \int [\, U(k_g, k_s) \frac{4\gamma_g \gamma_s}{k_o^2} e^{-i\gamma_s x_s + i\gamma_g x_g} \,] \, e^{+i k_x x + i k_z z} \, dk_x dk_z. \tag{A-13}$$

The inverse problem is then solved. Besides the mathematical elegance of equation (A-13) in obtaining the object function, formula (A-11) provides the basis for studying system resolution. Since k_s and k_g can only have finite number of values, k_x and k_z are limited to certain values too. In addition, equation (A-10) tells us that k_s and k_g must be smaller than or equal to k_o since k_x must be real in order to take advantage of the inverse Fourier transform scheme. Thus the resolution, which is related to the highest Fourier domain wave number, is limited by k_o and the object function in wave number domain is band limited. In the cross-hole case, the wave number domain coverage of the object function is shown in Figure A-3 with the shadowed area being covered. It is obvious that poor resolution in the lateral direction (x-direction) is expected for this source-geophone configuration.

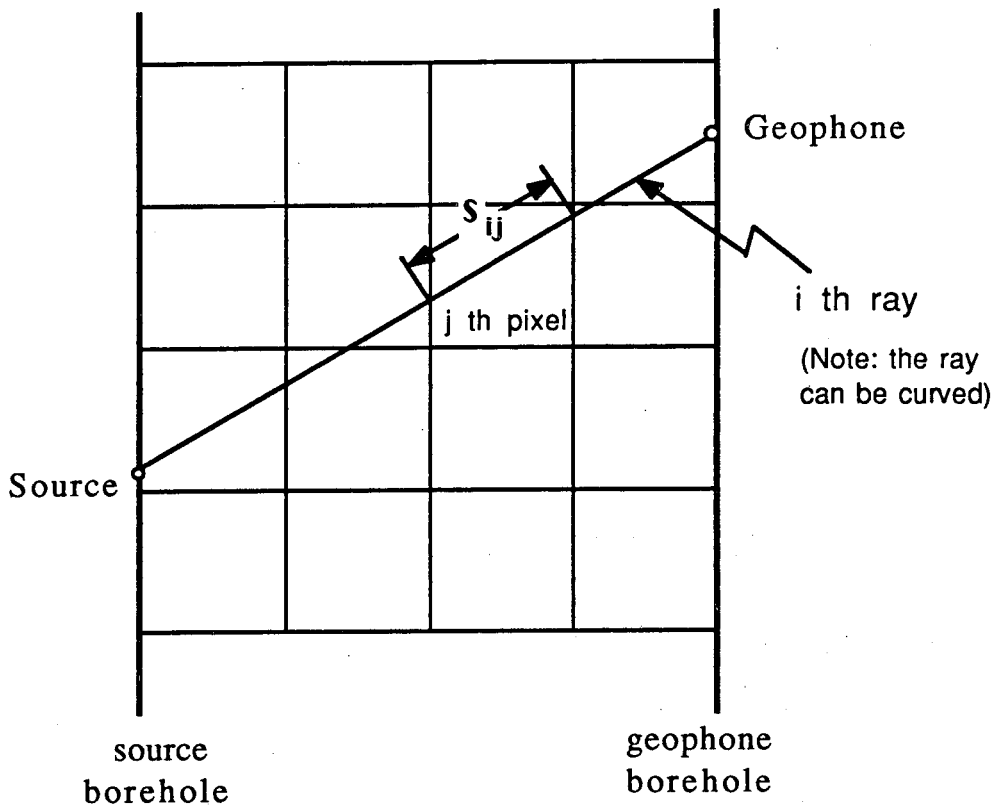

Figure A-1 The configuration for cross-hole ray tomography

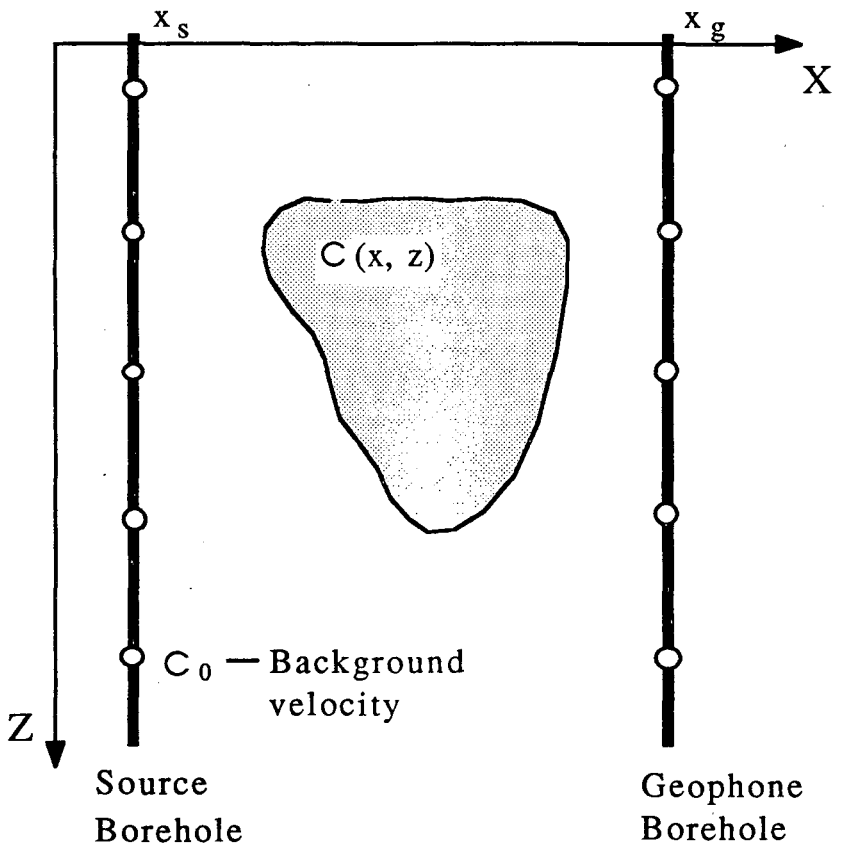

Figure A-2 The geometry for cross-hole diffraction tomography

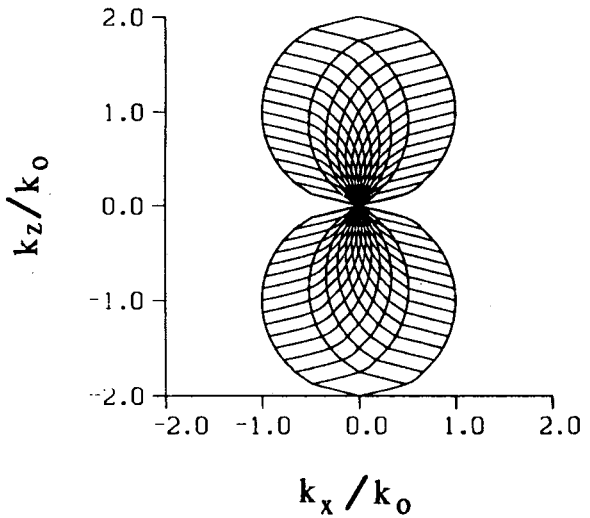

(a) Cross-hole configuration

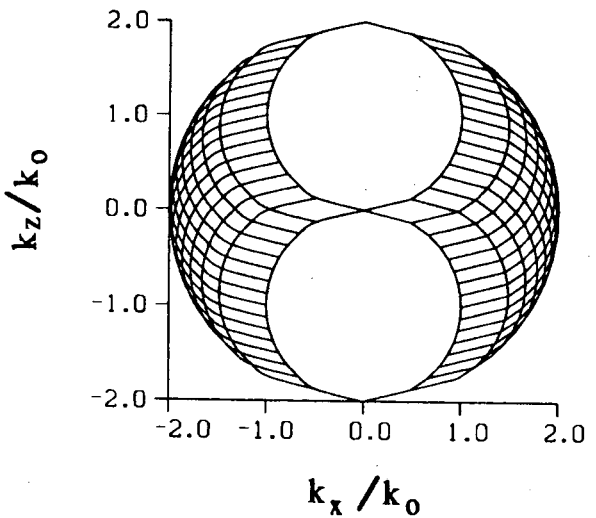

(b) Single-hole configuration

Figure A-3 Fourier domain coverage in acoustic diffraction tomography

Appendix B
Instability of Laplace transform of band limited data

It should be noted that the inverse Laplace transform of band limited data is very unstable. To show this fact, a simple δ function is used. Let

$$f(x) = \delta(x - x_0).$$

According to equation (2-2-12a), its Laplace transform is $F(s) = e^{-sx_0}$. With the inverse Laplace transform expression in (2-2-12b), the function $f(x)$ can be recovered from $F(s)$.

$$f(x) = \frac{1}{2\pi i} \int_{\tau - i\infty}^{\tau + i\infty} F(s) e^{sx}\, ds$$

$$= \frac{1}{2\pi i} \int_{\tau - i\infty}^{\tau + i\infty} e^{(x - x_0)s}\, ds\ ,$$

where τ (≥ 0) is a constant and the integration is along the line $Re(s) = \tau$. Make variable substitution,

$$s = \tau + iy\ ; \qquad ds = i\, dy\ .$$

Then we have

$$f(x) = \frac{1}{2\pi} \int_{-\infty}^{+\infty} e^{(x - x_0)\tau} e^{i(x - x_0)y}\, dy$$

$$= e^{(x - x_0)\tau} \frac{1}{2\pi} \int_{-\infty}^{+\infty} e^{i(x - x_0)y}\, dy$$

$$= e^{(x - x_0)\tau} \delta(x - x_0) = \delta(x - x_0)\ .$$

However for band limited data

$$f(x) = \frac{1}{2\pi i} \int_{\tau - i\, L/2}^{\tau + i\, L/2} F(s) e^{sx}\, ds$$

$$= e^{(x-x_0)\tau} \frac{1}{2\pi} \int_{-L/2}^{+L/2} e^{i(x-x_0)y}\, dy$$

$$= e^{(x-x_0)\tau} \frac{\sin[(x-x_0)L/2]}{\pi(x-x_0)} .$$

The exponential term $e^{(x-x_0)\tau}$ makes the inversion unstable and the unstability is integration path dependent (τ dependent). Since the actual integration path (Figure 2-5-1c) for our application is more complicated than the above one, precaution must be taken by incorporating constraints into the inverse process to stablize the problem.

Appendix C *

Mathematical expressions related to 3-D thin conductors

C.1 Green's Functions G_{ij} in $g(\mathbf{r}_o/\mathbf{r})$

The Green's functions will be considered in a three layer medium. A Cartesian coordinate system x_1, x_2, and x_3, is defined so that x_3 is perpendicular to the layer interfaces and x_1 and x_2 are parallel to them. The upper half space, $x_3<0$, is air which has a null conductivity ($\sigma_0= 0$). The overburden, $D>x_3>0$, has a conductivity of σ_1 and the lower half space, $x_3>D$, of σ_2. For source and receiver in the lower half space, the Green's functions satisfy

$$\nabla\times\nabla\times\mathbf{G}_i(\mathbf{r}_o/\mathbf{r}) + k_n^2(\mathbf{r})\mathbf{G}_i(\mathbf{r}_o/\mathbf{r})= \hat{\mathbf{x}}_i\,\delta(\mathbf{r}-\mathbf{r}_o)$$

and the tangential component of $\mathbf{G}$ and the normal component of $\sigma\mathbf{G}$ at the layer interfaces are continuous. Decompose the Green's function into G_{ij}^0 and G_{ij}^1, so that

$$G_{ij} = G_{ij}^0 + G_{ij}^1; \qquad i=1,2,3 \text{ and } j=1,2,3 .$$

Where G_{ij}^0 is the homogeneous whole space Green's function and is given by

$$\mathbf{G}_1^0= \left[+ \hat{\mathbf{x}}_1(1-\frac{1}{k_2^2}\frac{\partial^2}{\partial x_1^2}) - \hat{\mathbf{x}}_2\frac{1}{k_2^2}\frac{\partial^2}{\partial x_2\partial x_1} - \hat{\mathbf{x}}_3\frac{1}{k_2^2}\frac{\partial^2}{\partial x_3\partial x_1}\right]\frac{e^{-k_2R}}{4\pi R} ,$$

$$\mathbf{G}_2^0= \left[- \hat{\mathbf{x}}_1\frac{1}{k_2^2}\frac{\partial^2}{\partial x_1\partial x_2} + \hat{\mathbf{x}}_2(1-\frac{1}{k_2^2}\frac{\partial^2}{\partial x_2^2}) - \hat{\mathbf{x}}_3\frac{1}{k_2^2}\frac{\partial^2}{\partial x_3\partial x_2}\right]\frac{e^{-k_2R}}{4\pi R} ,$$

$$\mathbf{G}_3^0= \left[- \hat{\mathbf{x}}_1\frac{1}{k_2^2}\frac{\partial^2}{\partial x_1\partial x_3} - \hat{\mathbf{x}}_2\frac{1}{k_2^2}\frac{\partial^2}{\partial x_2\partial x_3} + \hat{\mathbf{x}}_3(1-\frac{1}{k_2^2}\frac{\partial^2}{\partial x_3^2})\right]\frac{e^{-k_2R}}{4\pi R} .$$

and G_{ij}^1 is given by

$$G_{11}^1= -\frac{1}{4\pi k_2^2}\frac{\partial^2}{\partial x_1^2}\int_0^\infty q_\phi J_0(ur)\frac{udu}{\alpha_2} + \frac{1}{4\pi}\int_0^\infty q_\psi J_0(ur)\frac{udu}{\alpha_2} +$$

$$+ \frac{1}{4\pi}\int_0^\infty (q_\psi-q_\phi)[J_2(ur)\cos^2\phi-\frac{1}{ur}J_1(ur)]\frac{udu}{\alpha_2} ,$$

* The mathematical expressions in this appendix are derived by following the method of Lajoie and West (1976). Some of the Green's functions are from a report by Weidelt (1981). Dr. K. Lee of Lawrence Berkeley Laboratory provided some of his personal notes to confirm the derived formula.

$$G^1_{12}=-\frac{1}{4\pi k_2^2}\frac{\partial^2}{\partial x_1\partial x_2}\int_0^\infty q_\phi J_0(ur)\frac{udu}{\alpha_2}+\frac{1}{4\pi}\int_0^\infty(q_\psi-q_\phi)J_2(ur)\frac{udu}{\alpha_2}\cos\phi\sin\phi\ ,$$

$$G^1_{13}=-\frac{1}{4\pi k_2^2}\frac{\partial^2}{\partial x_1\partial x_3}\int_0^\infty q_\phi J_0(ur)\frac{udu}{\alpha_2}\ ,$$

$$G^1_{21}=-\frac{1}{4\pi k_2^2}\frac{\partial^2}{\partial x_2\partial x_1}\int_0^\infty q_\phi J_0(ur)\frac{udu}{\alpha_2}+\frac{1}{4\pi}\int_0^\infty(q_\psi-q_\phi)J_2(ur)\frac{udu}{\alpha_2}\cos\phi\sin\phi\ ,$$

$$G^1_{22}=-\frac{1}{4\pi k_2^2}\frac{\partial^2}{\partial x_2^2}\int_0^\infty q_\phi J_0(ur)\frac{udu}{\alpha_2}+\frac{1}{4\pi}\int_0^\infty q_\psi J_0(ur)\frac{udu}{\alpha_2}+$$

$$+\frac{1}{4\pi}\int_0^\infty(q_\psi-q_\phi)[J_2(ur)\sin^2\phi-\frac{1}{ur}J_1(ur)]\frac{udu}{\alpha_2}\ ,$$

$$G^1_{23}=-\frac{1}{4\pi k_2^2}\frac{\partial^2}{\partial x_2\partial x_3}\int_0^\infty q_\phi J_0(ur)\frac{udu}{\alpha_2}\ ,$$

$$G^1_{31}=\frac{1}{4\pi k_2^2}\frac{\partial^2}{\partial x_3\partial x_1}\int_0^\infty q_\phi J_0(ur)\frac{udu}{\alpha_2}\ ,$$

$$G^1_{32}=\frac{1}{4\pi k_2^2}\frac{\partial^2}{\partial x_3\partial x_2}\int_0^\infty q_\phi J_0(ur)\frac{udu}{\alpha_2}\ ,$$

$$G^1_{33}=\frac{1}{4\pi k_2^2}\frac{\partial^2}{\partial x_3^2}\int_0^\infty q_\phi J_0(ur)\frac{udu}{\alpha_2}-\frac{1}{4\pi}\int_0^\infty q_\phi J_0(ur)\frac{udu}{\alpha_2}\ ,$$

where

$$q_\phi=\frac{(\sigma_2\alpha_1-\sigma_1\alpha_2)+(\sigma_2\alpha_1+\sigma_1\alpha_2)e^{-2\alpha_1 D}}{(\sigma_2\alpha_1+\sigma_1\alpha_2)+(\sigma_2\alpha_1-\sigma_1\alpha_2)e^{-2\alpha_1 D}}\ e^{-\alpha_2(z+z_o-2D)}\ ,$$

$$q_\psi=\frac{(\alpha_2-\alpha_1)(\alpha_1+u)+(\alpha_2+\alpha_1)(\alpha_1-u)e^{-2\alpha_1 D}}{(\alpha_2+\alpha_1)(\alpha_1+u)+(\alpha_2-\alpha_1)(\alpha_1-u)e^{-2\alpha_1 D}}\ e^{-\alpha_2(z+z_o-2D)}\ ,$$

$$\alpha_m^2=u^2+k_m^2\ ,\qquad k_m^2=i\,\omega\mu_o\sigma_m\qquad(m=1,2)\ ,$$

$$\mathbf{r}=x_1\hat{\mathbf{x}}_1+x_2\hat{\mathbf{x}}_2+x_3\hat{\mathbf{x}}_3\ ,\qquad \mathbf{r}_o=x_{10}\hat{\mathbf{x}}_1+x_{20}\hat{\mathbf{x}}_2+x_{30}\hat{\mathbf{x}}_3\ ,$$

$$R=|\mathbf{r}-\mathbf{r}_o|\ ,\qquad r=\sqrt{(x_1-x_{10})^2+(x_2-x_{20})^2}\ ,$$

$$\cos\phi=(x_1-x_{10})/r\ ,\qquad \sin\phi=(x_2-x_{20})/r\ ,$$

and $J_0(ur)$, $J_1(ur)$ and $J_2(ur)$ are the zero, first and second order Bessel functions respectively.

C.2 The Green's Function $g_s(\mathbf{r}_o/\mathbf{r})$

To solve equation (4-2-10), the Green's function g_s must be calculated first. Equation (4-2-8) is rewritten here in a simplified way

$$g(\mathbf{r}_o/\mathbf{r})=\begin{bmatrix} G_{11} & G_{12} & G_{13} \\ G_{21} & G_{22} & G_{23} \\ G_{31} & G_{32} & G_{33} \end{bmatrix}$$

with the unit vectors omitted. The expressions for G_{ij} (i=1,2,3; j=1,2,3) can be found in Appendix C.1. Two coordinate systems x_i, y_i, z_i and x_j, y_j, z_j are introduced in the same way as the reference coordinate x_1, x_2, x_3. Then the x_i, y_i, z_i system is rotated horizontally by an angle γ_i and the x_j, y_j, z_j system by γ_j. Supposing the sources are in x_i, y_i, z_i directions and the observations are made in x_j, y_j, z_j directions, then

$$g_{ij}=\begin{bmatrix} G_{x_ix_j} & G_{x_iy_j} & G_{x_iz_j} \\ G_{y_ix_j} & G_{y_iy_j} & G_{y_iz_j} \\ G_{z_ix_j} & G_{z_iy_j} & G_{z_iz_j} \end{bmatrix}$$

$$=\begin{bmatrix} \cos\gamma_i & \sin\gamma_i & 0 \\ -\sin\gamma_i & \cos\gamma_i & 0 \\ 0 & 0 & 1 \end{bmatrix}\begin{bmatrix} G_{11} & G_{12} & G_{13} \\ G_{21} & G_{22} & G_{23} \\ G_{31} & G_{32} & G_{33} \end{bmatrix}\begin{bmatrix} \cos\gamma_j & -\sin\gamma_j & 0 \\ \sin\gamma_j & \cos\gamma_j & 0 \\ 0 & 0 & 1 \end{bmatrix}.$$

Next the coordinate system x_i, y_i, z_i or x_j, y_j, z_j is rotated along the axis x_i or x_j by an angle β_i or β_j so that the sources are in $\hat{\mathbf{a}}_i$ and $\hat{\mathbf{b}}_i$ directions and the observation points are in $\hat{\mathbf{a}}_j$ and $\hat{\mathbf{b}}_j$ directions. The Green's functions with source in $\hat{\mathbf{c}}_i$ direction or with the measurements in $\hat{\mathbf{c}}_j$ direction are not used, therefore they are not given in the following.

$$g_s=\begin{bmatrix} G_{a_ia_j} & G_{a_ib_j} \\ G_{b_ia_j} & G_{b_ib_j} \end{bmatrix}$$

$$=\begin{bmatrix} 1 & 0 & 0 \\ 0 & \cos\beta_i & \sin\beta_i \end{bmatrix}\begin{bmatrix} G_{x_ix_j} & G_{x_iy_j} & G_{x_iz_j} \\ G_{y_ix_j} & G_{y_iy_j} & G_{y_iz_j} \\ G_{z_ix_j} & G_{z_iy_j} & G_{z_iz_j} \end{bmatrix}\begin{bmatrix} 1 & 0 \\ 0 & \cos\beta_j \\ 0 & \sin\beta_j \end{bmatrix}$$

$$= \begin{bmatrix} \cos\gamma_i & \sin\gamma_i & 0 \\ -\sin\gamma_i\cos\beta_i & \cos\beta_i\cos\gamma_i & \sin\beta_i \end{bmatrix} \begin{bmatrix} G_{11} & G_{12} & G_{13} \\ G_{21} & G_{22} & G_{23} \\ G_{31} & G_{32} & G_{33} \end{bmatrix} \begin{bmatrix} \cos\gamma_j & -\sin\gamma_j\cos\beta_j \\ \sin\gamma_j & \cos\beta_j\cos\gamma_j \\ 0 & \sin\beta_j \end{bmatrix} .$$

More explicitly, we have $G = G^0 + G^1$ with G^0 and G^1 given by

$$G^0_{a_i a_j} = \left[\cos(\gamma_i - \gamma_j) - \frac{1}{k_2^2}\frac{\partial^2}{\partial a_i \partial a_j}\right] \frac{e^{-k_2 R}}{4\pi R} ,$$

$$G^0_{a_i b_j} = \left[\cos\beta_j \sin(\gamma_i - \gamma_j) - \frac{1}{k_2^2}\frac{\partial^2}{\partial a_i \partial b_j}\right] \frac{e^{-k_2 R}}{4\pi R} ,$$

$$G^0_{b_i a_j} = \left[\cos\beta_i \sin(\gamma_j - \gamma_i) - \frac{1}{k_2^2}\frac{\partial^2}{\partial b_i \partial a_j}\right] \frac{e^{-k_2 R}}{4\pi R} ,$$

$$G^0_{b_i b_j} = \left\{\left[\cos\beta_i \cos\beta_j \cos(\gamma_i - \gamma_j) + \sin\beta_i \sin\beta_j\right] - \frac{1}{k_2^2}\frac{\partial^2}{\partial b_i \partial b_j}\right\} \frac{e^{-k_2 R}}{4\pi R} ,$$

$$G^1_{a_i a_j} = -\frac{1}{k_2^2}\frac{\partial^2}{\partial a_i \partial a_j} A + \left[E\cos\gamma_i \cos\gamma_j + F\sin\gamma_i \sin\gamma_j + G\cos(\gamma_i + \gamma_j) + H\sin(\gamma_i + \gamma_j)\right] ,$$

$$G^1_{a_i b_j} = -\frac{1}{k_2^2}\frac{\partial^2}{\partial a_i \partial b_j} A + \left[-E\sin\gamma_j \cos\gamma_i + F\cos\gamma_j \sin\gamma_i - G\sin(\gamma_i + \gamma_j) + H\cos(\gamma_i + \gamma_j)\right] \cos\beta_j ,$$

$$G^1_{b_i a_j} = -\frac{1}{k_2^2}\frac{\partial^2}{\partial \bar{b}_i \partial a_j} A + \left[-E\sin\gamma_i \cos\gamma_j + F\cos\gamma_i \sin\gamma_j - G\sin(\gamma_i + \gamma_j) + H\cos(\gamma_i + \gamma_j)\right] \cos\beta_i ,$$

$$G^1_{b_i b_j} = -\frac{1}{k_2^2}\frac{\partial^2}{\partial \bar{b}_i \partial b_j} A + \left[E\sin\gamma_i \sin\gamma_j + F\cos\gamma_i \cos\gamma_j - G\cos(\gamma_i + \gamma_j) - H\sin(\gamma_i + \gamma_j)\right] \cos\beta_i \cos\beta_j$$

$$-A\sin\beta_i \sin\beta_j ,$$

where

$$A = \frac{1}{4\pi}\int_0^\infty q_\phi J_0(ur)\frac{udu}{\alpha_2} , \qquad B = \frac{1}{4\pi}\int_0^\infty q_\psi J_0(ur)\frac{udu}{\alpha_2} ,$$

$$C = \frac{1}{4\pi}\int_0^\infty q_\phi J_1(ur)\frac{\frac{udu}{\alpha_2}}{\alpha_2} , \qquad D = \frac{1}{4\pi}\int_0^\infty q_\psi J_1(ur)\frac{\frac{udu}{\alpha_2}}{\alpha_2} ,$$

$$E = B\sin^2\phi + A\cos^2\phi , \qquad F = B\cos^2\phi + A\sin^2\phi ,$$

$$G = (D-C)\,\frac{\cos 2\phi}{r}\,, \qquad H = [(A-B) + (D-C)\frac{2}{r}]\,\cos\phi\sin\phi\,,$$

$$\frac{\partial}{\partial a_i} = \frac{\partial}{\partial x}\cos\gamma_i + \frac{\partial}{\partial y}\sin\gamma_i\,, \qquad \frac{\partial}{\partial a_j} = \frac{\partial}{\partial x}\cos\gamma_j + \frac{\partial}{\partial y}\sin\gamma_j\,,$$

$$\frac{\partial}{\partial b_j} = \frac{\partial}{\partial x}(-\sin\gamma_j\cos\beta_j) + \frac{\partial}{\partial y}\cos\beta_j\cos\gamma_j + \frac{\partial}{\partial z}\sin\beta_j\,,$$

$$\frac{\partial}{\partial \bar{b}_i} = \frac{\partial}{\partial x}(-\sin\gamma_i\cos\beta_i) + \frac{\partial}{\partial y}\cos\beta_i\cos\gamma_i - \frac{\partial}{\partial z}\sin\beta_i\,.$$

Note that the above Green's functions can be rearranged into the form

$$\mathbf{G}_{a_i s_j} = \mathbf{S}_{a_i} + \frac{1}{k_2^2}\nabla_{s_j}\phi_{a_i}\,, \tag{C-1a}$$

$$\mathbf{G}_{b_i s_j} = \mathbf{S}_{b_i} + \frac{1}{k_2^2}\nabla_{s_j}\phi_{b_i}\,, \tag{C-1b}$$

so that $\mathbf{S}$ and ϕ are unrelated with $\frac{1}{k_2^2}$.

C.3 Incident Fields $\mathbf{E}_n$ and $\mathbf{H}_n$

The same coordinate definitions as in section C.1 are used. If both the source and receiver are in the lower half space, the incident electric and magnetic fields are as following.

(1) Grounded vertical electric dipole (G.V.E.D.) source of unit moment

$$H_{n\phi} = \frac{1}{4\pi}\left\{(1+k_2R)\frac{r}{R^3}e^{-k_2R} - \int_0^\infty \frac{u^2}{\alpha_2}q_\phi J_1(ur)\frac{udu}{\alpha_2}\right\}.$$

$$H_{nx_1} = -H_{n\phi}\sin\phi\,. \qquad H_{nx_2} = H_{n\phi}\cos\phi\,.$$

$$H_{nx_3} = 0\,.$$

$$E_{nr} = \frac{i\omega\mu_o}{4\pi}\left[\frac{r(x_3-x_{30})}{(k_2R)^2}(3+3k_2R+(k_2R)^2)\frac{e^{-k_2R}}{R^3} - \int_0^\infty \frac{u^2}{k_2^2}q_\phi J_1(ur)\frac{udu}{\alpha_2}\right].$$

$$E_{nx_1} = E_{nr}\cos\phi\,. \qquad E_{nx_2} = E_{nr}\sin\phi\,.$$

$$E_{nx_3}=\frac{i\omega\mu_o}{4\pi}\left\{\left[(1+3\frac{1+k_2R}{(k_2R)^2})\frac{(x_3-x_{30})^2}{R^2}-(1+\frac{1+k_2R}{(k_2R)^2})\right]\frac{e^{-k_2R}}{R}-\int_0^\infty\frac{u^2}{k_2^2}\frac{u}{\alpha_2}q_\phi J_0(ur)\frac{udu}{\alpha_2}\right\}.$$

(2) Vertical magnetic dipole (V.M.D.) source of unit moment

$$H_{nr}=\frac{r(x_3-x_{30})}{R^4}(3+3k_2R+(k_2R)^2)\frac{e^{-k_2R}}{4\pi R}+\frac{1}{4\pi}\int_0^\infty q_\psi J_1(ur)u^2\frac{udu}{\alpha_2}.$$

$$H_{nx_1}=H_{nr}\cos\phi. \qquad H_{nx_2}=H_{nr}\sin\phi.$$

$$H_{nx_3}=\left[-\frac{1}{R^2}(1+k_2R+(k_2R)^2)+\frac{(x_3-x_{30})^2}{R^4}(3+3k_2R+(k_2R)^2)\right]\frac{e^{-k_2R}}{4\pi R}$$

$$+\frac{1}{4\pi}\int_0^\infty q_\psi J_0(ur)\frac{u^3}{\alpha_2}\frac{udu}{\alpha_2}.$$

$$E_{n\phi}=-\frac{i\omega\mu_o}{4\pi}\left[\frac{r}{R^2}(1+k_2R)\frac{e^{-k_2R}}{R}+\int_0^\infty q_\psi J_1(ur)\frac{u^2}{\alpha_2}\frac{udu}{\alpha_2}\right].$$

$$E_{nx_1}=-E_{n\phi}\sin\phi. \qquad E_{nx_2}=E_{n\phi}\cos\phi.$$

$$E_{nx_3}=0.$$

(3) Horizontal magnetic dipole (H.M.D.) source of unit moment

$$H_{nx_1}=\left[-\frac{1}{R^2}(1+k_2R+(k_2R)^2)+\frac{(x_1-x_{10})^2}{R^4}(3+3k_2R+(k_2R)^2)\right]\frac{e^{-k_2R}}{4\pi R}$$

$$+\frac{1}{4\pi}\int_0^\infty(\alpha_2^2q_\psi\cos^2\phi+k_2^2q_\phi\sin^2\phi)J_0(ur)\frac{u\frac{udu}{\alpha_2}}{\alpha_2}$$

$$-\frac{1}{4\pi}\int_0^\infty(\alpha_2^2q_\psi-k_2^2q_\phi)J_1(ur)\frac{\frac{udu}{\alpha_2}}{\alpha_2}\frac{\cos2\phi}{r}.$$

$$H_{nx_2}=\frac{(x_1-x_{10})(x_2-x_{20})}{R^4}(3+3k_2R+(k_2R)^2)\frac{e^{-k_2R}}{4\pi R}$$

$$+\frac{1}{4\pi}\int_0^\infty(\alpha_2^2q_\psi-k_2^2q_\phi)J_0(ur)\frac{u\frac{udu}{\alpha_2}}{\alpha_2}\sin\phi\cos\phi-\frac{1}{4\pi}\int_0^\infty(\alpha_2^2q_\psi-k_2^2q_\phi)J_1(ur)\frac{\frac{udu}{\alpha_2}}{\alpha_2}\frac{\cos2\phi}{r}.$$

$$H_{nx_3}=\frac{(x_1-x_{10})(x_3-x_{30})}{R^4}(3+3k_2R+(k_2R)^2)\frac{e^{-k_2R}}{4\pi R}-\frac{1}{4\pi}\int_0^\infty q_\psi J_1(ur)u^2\frac{udu}{\alpha_2}\cos\phi\ .$$

$$E_{nx_1}=\frac{i\omega\mu_o}{4\pi}\left[\int_0^\infty(q_\psi-q_\phi)J_0(ur)u\frac{udu}{\alpha_2}\sin\phi\cos\phi-\int_0^\infty(q_\psi-q_\phi)J_1(ur)\frac{udu}{\alpha_2}\frac{\cos2\phi}{r}\right].$$

$$E_{nx_2}=\frac{i\omega\mu_o}{4\pi}\left[\frac{x_3-x_{30}}{R^2}(1+k_2R)\frac{e^{-k_2R}}{R}\right.$$

$$\left.-\int_0^\infty(q_\psi\cos^2\phi+q_\phi\sin^2\phi)J_0(ur)u\frac{udu}{\alpha_2}+\int_0^\infty(q_\psi-q_\phi)J_1(ur)\frac{udu}{\alpha_2}\frac{\cos2\phi}{r}\right].$$

$$E_{nx_3}=\frac{i\omega\mu_o}{4\pi}\left[-\frac{x_2-x_{20}}{R^2}(1+k_2R)\frac{e^{-k_2R}}{R}+\int_0^\infty q_\phi\frac{u^2}{\alpha_2}J_1(ur)\frac{udu}{\alpha_2}\sin\phi\right].$$

C.4 Green's Functions $\mathbf{H}_{a,b}$ ($\mathbf{H}_{a,b}=\nabla\times\mathbf{G}_{a,b}$)

The Green's Function $\mathbf{H}_a$ and $\mathbf{H}_b$ relate the induced current on the thin conductors to the magnetic response at the receiver. Similar to the coordinate definitions in Appendix C.1, for source and field points in the lower half space $\mathbf{H}_{a,b}(\mathbf{r}_o/\mathbf{r})$ will be given by the following formulas.

$$H_{ax_1}=\frac{1}{4\pi}\frac{\partial}{\partial x_{10}}\int_0^\infty(q_\psi-q_\phi)J_1(ur)\frac{udu}{\alpha_2}\sin\phi\ .$$

$$H_{ax_2}=-\frac{1}{4\pi}\frac{x_3-x_{30}}{R^3}(1+k_2R)e^{-k_2R}+$$

$$+\frac{1}{4\pi}\frac{\partial}{\partial x_{20}}\int_0^\infty q_\psi J_1(ur)\frac{udu}{\alpha_2}\sin\phi+\frac{1}{4\pi}\frac{\partial}{\partial x_{10}}\int_0^\infty q_\phi J_1(ur)\frac{udu}{\alpha_2}\cos\phi\ .$$

$$H_{ax_3}=\frac{1}{4\pi}\frac{x_2-x_{20}}{R^3}(1+k_2R)e^{-k_2R}+\frac{1}{4\pi}\int_0^\infty q_\psi J_1(ur)\frac{u^2}{\alpha_2}\frac{udu}{\alpha_2}\sin\phi\ .$$

$$H_{bx_1}=\frac{1}{4\pi}\frac{x_3-x_{30}}{R^3}(1+k_2R)e^{-k_2R}\cos\beta-\frac{1}{4\pi}\frac{x_2-x_{20}}{R^3}(1+k_2R)e^{-k_2R}\sin\beta-$$

$$-\frac{1}{4\pi}\frac{\partial}{\partial x_{10}}\int_0^\infty q_\psi J_1(ur)\frac{udu}{\alpha_2}\cos\phi\cos\beta-\frac{1}{4\pi}\frac{\partial}{\partial x_{20}}\int_0^\infty q_\phi J_1(ur)\frac{udu}{\alpha_2}\sin\phi\cos\beta$$

$$+\frac{1}{4\pi}\int_0^\infty q_\phi J_1(ur)\frac{u^2}{\alpha_2}\frac{udu}{\alpha_2}\sin\phi\sin\beta\ .$$

$$H_{bx_2}=\frac{1}{4\pi}\frac{x_1-x_{10}}{R^3}(1+k_2R)e^{-k_2R}\sin\beta-$$

$$-\frac{1}{4\pi}\frac{\partial}{\partial x_{10}}\int_0^\infty(q_\psi-q_\phi)J_1(ur)\frac{udu}{\alpha_2}\sin\phi\cos\beta-\frac{1}{4\pi}\int_0^\infty q_\phi J_1(ur)\frac{u^2}{\alpha_2}\frac{udu}{\alpha_2}\cos\phi\sin\beta\ .$$

$$H_{bx_3}=-\frac{1}{4\pi}\frac{x_1-x_{10}}{R^3}(1+k_2R)e^{-k_2R}\cos\beta-\frac{1}{4\pi}\int_0^\infty q_\psi J_1(ur)\frac{u^2}{\alpha_2}\frac{udu}{\alpha_2}\cos\phi\cos\beta\ .$$

The definitions for $\cos\phi$, $\sin\phi$, α_2, R, r are the same as before and β is the dip angle. The unit vector $\hat{\mathbf{b}}$ is in the dip direction. $\hat{\mathbf{a}}$ and $\hat{\mathbf{x}}_1$ are in the same direction. If they are different, a coordinate rotation must be made.

C.5 Numerical solution of the integral equations

(1) The tangential electrical fields on the conductors

Equation (4-2-10) can be rewritten into, for the $\hat{\mathbf{a}}_i$ component on the i *th* conductor in the strike direction,

$$E_{a_i}=E_{na_i}-i\omega\mu_o\sum_{j=1}^{ns}\int_{s_j}\mathbf{G}_{a_is_j}\cdot\tau\mathbf{E}_{s_j}\,ds\ , \tag{C-2}$$

where E_{na_i} is given by Appendix C.3. Define $\mathbf{J}_{s_j}=\tau\mathbf{E}_{s_j}$ as the tangential current on the j *th* conductor and assume

$$\mathbf{J}_{s_j}=\nabla\times(\hat{\mathbf{c}}_j\psi_j)+k_2^2\nabla_{s_j}\phi_j \tag{C-3}$$

with $\psi=0$ on the four sides of each rectangular thin conductor. The tangential electrical field will be solved indirectly by solving for ψ and ϕ first. Thus, as was found by Weidelt (1981), the numerical error due to small k_2^2 or σ_2 will be avoided. Putting equation (C-1a) and (C-3) into equation (C-2), one arrives at

$$E_{a_i}=E_{na_i}-i\omega\mu_o\sum_{j=1}^{ns}\int_{s_j}[\mathbf{S}_{a_i}+\frac{1}{k_2^2}\nabla_{s_j}\phi_{a_i}]\cdot[\nabla\times(\hat{\mathbf{c}}_j\psi_j)+k_2^2\nabla_{s_j}\phi_j]\,ds$$

Then the critical term with $\frac{1}{k_2^2}$ or $\frac{1}{\sigma_2}$ will be

$$I = -\frac{1}{\sigma_2}\sum_{j=1}^{ns}\int_{s_j} \nabla_{s_j}\phi_{a_i}\cdot\nabla\times(\hat{\mathbf{e}}_j\psi_j)\, ds$$

$$= -\frac{1}{\sigma_2}\sum_{j=1}^{ns}\int_{s_j}[\frac{\partial}{\partial a_j}(\phi_{a_i}\frac{\partial\psi_j}{\partial b_j}) - \frac{\partial}{\partial b_j}(\phi_{a_i}\frac{\partial\psi_j}{\partial a_j})]\, ds$$

$$= \frac{1}{\sigma_2}\sum_{j=1}^{ns}\int_{\partial s_j}[\phi_{a_i}\frac{\partial\psi_j}{\partial b_j}db_j + \phi_{a_i}\frac{\partial\psi_j}{\partial a_j}da_j]$$

$$= \frac{1}{\sigma_2}\sum_{j=1}^{ns}\int_{\partial s_j}\phi_{a_j}\, d\psi_j \equiv 0\,,$$

where ∂s_j is the boundary of s_j. Therefore

$$E_{a_i}(\mathbf{r}_o) = E_{na_i}(\mathbf{r}_o) - i\,\omega\mu_o\sum_{j=1}^{ns}\int_{s_j}[\mathbf{S}_{a_i}\cdot(\nabla\times(\hat{\mathbf{e}}_j\psi_j) + k_2^2\nabla_{s_j}\phi_j) + \nabla_{s_j}\phi_{a_i}\cdot\nabla_{s_j}\phi_j]\, ds\,, \tag{C-4a}$$

and similarly the tangential electrical field in dip direction is

$$E_{b_i}(\mathbf{r}_o) = E_{nb_i}(\mathbf{r}_o) - i\,\omega\mu_o\sum_{j=1}^{ns}\int_{s_j}[\mathbf{S}_{b_i}\cdot(\nabla\times(\hat{\mathbf{e}}_j\psi_j) + k_2^2\nabla_{s_j}\phi_j) + \nabla_{s_j}\phi_{b_i}\cdot\nabla_{s_j}\phi_j]\, ds\,. \tag{C-4b}$$

Equation (C-3) gives

$$\tau_i E_{a_i,mn} \approx \frac{1}{2\Delta b_{i,m}}[\psi_{i,m,n-1} - \psi_{i,m-1,n-1} + \psi_{i,m,n} - \psi_{i,m-1,n}] +$$

$$+ \frac{k_2^2}{2\Delta a_{i,n}}[\phi_{i,m-1,n} - \phi_{i,m-1,n-1} + \phi_{i,m,n} - \phi_{i,m,n-1}]\,, \tag{C-5a}$$

$$\tau_i E_{b_i,mn} \approx -\frac{1}{2\Delta a_{i,n}}[\psi_{i,m-1,n} - \psi_{i,m-1,n-1} + \psi_{i,m,n} - \psi_{i,m,n-1}] +$$

$$+ \frac{k_2^2}{2\Delta b_{i,m}}[\phi_{i,m,n-1} - \phi_{i,m-1,n-1} + \phi_{i,m,n} - \phi_{i,m-1,n}]\,, \tag{C-5b}$$

where $\Delta a_{i,n}$ and $\Delta b_{i,m}$ are the width and length of each individual cell on the rectangular targets. $\phi_{i,m,n}$ or $\psi_{i,m,n}$ are the values of ϕ or ψ on the grid point (m,n) of the i *th* thin conductor (Figure C-1). The electrical fields $E_{a_i,mn}$ and $E_{b_i,mn}$ are taken as constants on each cell.

It is also found that the substitutions

$$\phi_{i,k,l} \;\text{->}\; \begin{cases} \phi_{i,k,l} + c_1\,; & k+l \;\; even \\ \phi_{i,k,l} + c_2\,; & k+l \;\; odd \end{cases} \qquad (c_1 \;\&\; c_2 \; constant)$$

will not alter the values given by equation (C-5). Therefore two of the ϕ's on each target can be set to zero or any other values. The total number of independent ϕ and ψ is $\sum_{i=1}^{ns} 2\times N_{ai}\times N_{bi}$.

A linear complex system of equations for the potentials ϕ and ψ will be established from equations (C-4) and (C-5). After ϕ and ψ are solved, $\mathbf{E}_s$ can then be derived from equation (C-5).

(2) Solving for the magnetic fields at the points of interest

Equation (4-2-11) can be rearranged as

$$\mathbf{H}(\mathbf{r}) = \mathbf{H}_n(\mathbf{r}) + \sum_{j=1}^{ns} \int_{s_j} \tau[E_{a_j}(\mathbf{r}_o)\mathbf{H}_{a_j}(\mathbf{r}_o/\mathbf{r}) + E_{b_j}(\mathbf{r}_o)\mathbf{H}_{b_j}(\mathbf{r}_o/\mathbf{r})]\, ds_o \;,$$

where

$$\mathbf{H}_{a_j} = H_{a_j x_1}\hat{\mathbf{x}}_1 + H_{a_j x_2}\hat{\mathbf{x}}_2 + H_{a_j x_3}\hat{\mathbf{x}}_3, \qquad \mathbf{H}_{b_j} = H_{b_j x_1}\hat{\mathbf{x}}_1 + H_{b_j x_2}\hat{\mathbf{x}}_2 + H_{b_j x_3}\hat{\mathbf{x}}_3$$

are given by $\mathbf{H}_{a_j,b_j} = \nabla\times\mathbf{G}_{a_j,b_j}$ (Appendix C.4) with $\hat{\mathbf{a}}_j$ and $\hat{\mathbf{x}}_1$ in the same direction. If $\hat{\mathbf{a}}_j$ is not in the direction of $\hat{\mathbf{x}}_1$, coordinate rotations must be made for the magnetic fields from each conductor. The incident field $\mathbf{H}_n(\mathbf{r})$ is listed in Appendix C.3.

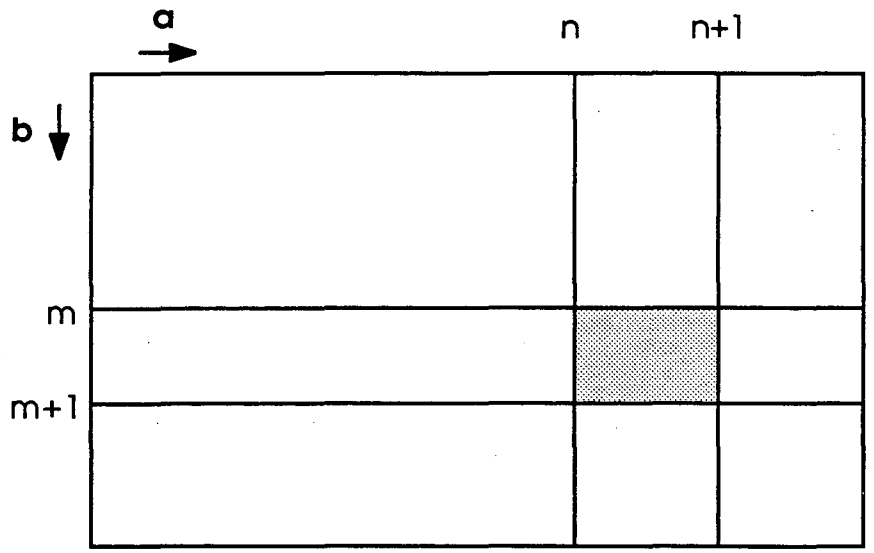

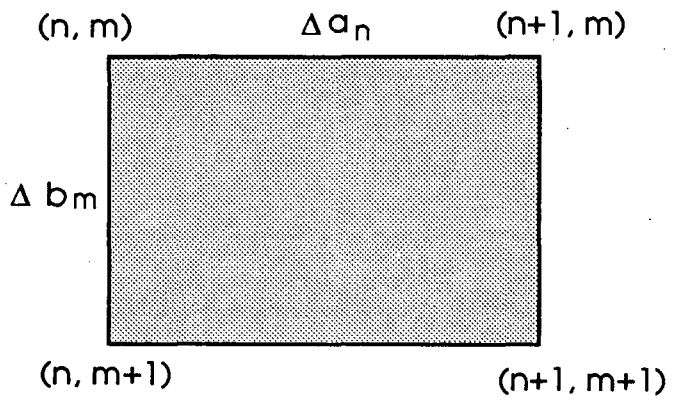

Figure C-1 The notations on one of the cells in calculating thin conductor EM response

References

Achenbach, J. D., and Viswanathan, K., 1980, Seismic detection of water-filled cracks, in Hot Dry Rock Reservoir Characterization and Modeling: Los Alamos National Laboratory Report LA-8343-MS, 121-154.

Adm, A., 1984, Fractures as conducting dykes and corresponding two-dimensional models: Geophysical Prospecting, 32, 543-553.

Aguilera, R., 1980, Naturally fractured reservoirs: The Petroleum Publishing Company, Tulsa.

Anderson, B., and Chang, S. K., 1982, Synthetic induction logs by the finite element method: The Log Analyst, 23, 17-26.

Archie, G. E., 1942, The electrical resistivity log as an aid in determining some reservoir characteristics: Trans. AIME, 146, 54-62.

Bertero, M., 1982, On the recovery and resolution of exponential relaxation rates from experimental data - value analysis of the Laplace transform inversion in the presence of noise: Proc. R. Soc. Lond. A383, 15-29.

Bertero, M., Brianzi, P., and Pike, E. R., 1983, Singular value decomposition of the Laplace transform inversion with discrete data: Series title: Pubblicazioni dell'Istituto di analisi globale e applicazioni. Serie "Problemi non ben posti ed inversi"; No. 1.

Beylkin, G., and Burridge, R. (Schlumberger-Doll Research), 1989, Linearized inverse scattering problems in acoustic and elasticity: Paper submitted to Geophysics.

Bleistein, Norman, 1984, Mathematical methods for wave phenomena: Academic Press, Inc.

Brace, W. F., 1982, A note on downhole detection of conductive fractures: USGS open-file rep. 82-1075, 624-628.

Bracewell, R. N., 1956, Strip integration in radio astronomy: Aust. J. Phys., 9, 198-217.

Bracewell, R. N., and Riddle, A. C., 1967, Inversion of fan-beam scans in radio astronomy: Astrophys. J., vol. 150, 427-434.

Bois, P., LaPorte, M., Lavergne, M., and Thomas, G., 1972, Well to well seismic measurements: Geophysics, 37, 471-480.

Chang, H. T., 1984, Feasibility of a borehole VHF radar for fracture mapping: Geotherm. Resour. Council, Trans., 8, 485-488.

Chang, H. T., Suhler, S. A., and Owen T. E., 1984, Evaluation of bore hole electromagnetic and seismic detection of fractures: Sandia National Laboratories, Report SAND 84-7109, 75p.

Cheng, G., 1984, Exact and approximate solutions to some geophysical inverse problems: Ph.D. thesis, University of California at Berkeley.

Constable, S. C., Parker, R. L., and Constable C. G., 1987, Occam's inversion: A practical algorithm for generating smooth models from electromagnetic sounding data: Geophysics, 52, 289-300.

Cormack, A. M., 1963, Representation of a function by its line integrals with some radiological applications - I: J. appl. phys. 34, 2722- 2727.

Cormack, A. M., 1964, Representation of a function by its line integrals with some radiological applications - II: J. appl. phys. 35, 2908- 2913.

Crary, S., Boyeldieu, C., Brown, S., et al, 1987, Fracture detection with logs: The Technical Review, 37, 22-34.

Cull, J. P. and Cobcroft R., 1986, Omni-directional downhole EM probes: Geophysical Prospecting, 34, 569-579.

Daily, W., 1984, Underground oil-shale retort monitoring using geotomography: Geophysics, 49, 1701-1707.

Deadrick, F. J., Ramirez, A. L., Lytle, R. J., 1982, In-situ fracture mapping using geotomography and brine tracers: IEEE Trans. on Nuclear Science, NS-29, No.1.

Deniels, J. J., 1983, Hole-to-surface resistivity methods: Geophysics, 48, 87-97.

Dines, K. A., and Lytle, R. J., 1979, Computerized geophysical tomography: Proceedings of the IEEE, 67, 1065-1073.

Devaney, A. J., 1981, Inverse-scattering theory within the Rytov approximation: Optics Letters, 6, 374-376.

Devaney, A. J., 1982, A filtered backpropagation algorithm for diffraction tomography: Ultrasonic Imaging 4, 336-350.

Devaney, A. J., 1984, Geophysical diffraction tomography: IEEE transactions on geoscience and remote sensing, GE-22, No. 1. 3-13.

Dyck, A. V., M. Bloore, and M. A. Vallee, 1980, User manual for programs PLATE and SPHERE: Res. in Applied Geophysics. No.14, Uni. of Toronto.

Eaton, Perry A. and Hohmann, Gerald W., 1988, Three dimensional electromagnetic inversion: SEG 58th annual international meeting and exposition, Oct.30-Nov.3, 229-233.

Edwards, R. N., 1974, The magnetometric resistivity (MMR) method and its application to the mapping of a fault: Can. J. Earth Sci., 11, 1136-1156.

Emerson, D. W. (Editor), 1987, Special issue on downhole electromagnetic methods: Exploration Geophysics, Sept. 1987.

Esmersoy, Cengiz, 1986, The backpropagated field approach to multidimensional velocity inversion: Ph.D. thesis, Massachusetts Institute of Technology.

Fehler, M., and Pearson, C., 1984, Cross-hole seismic surveys: Applications for studying subsurface fracture systems at a hot dry rock geothermal site: Geophysics, 49, 37-45.

Fehler, M., Turpening, R., Blackway, C., and Mellen, M., 1982, Detection of a hydrofrac with shear wave vertical seismic profiles: Extended abstract, Technical Program Abstracts and Biographies, SEG 52nd Annual International Meeting and Exposition, Dallas, 159-161.

Fitterman, D. V., 1989, Detectability levels for central induction transient soundings: Geophysics, 54, 127-129.

Flovenz, O. G., 1984, Application of the head-on resistivity profiling method in geothermal exploration: Geothermal Resources Council, Trans., 8, 493-398.

Franklin, J. N., 1970, Well-posed stochastic extensions of ill-posed linear problems: Journal of mathematic analysis and applications, 31, 682-716.

Gill, P. E., Murray, W. and Wright, M. H., 1981, Practical optimization: Academic Press, London.

Goldstein, N. E., 1985, Fracture detection and characterization for geothermal reservoir definition: Presented at the 10th Annual Workshop on Geothermal Reservoir Engineering, Stanford University, Stanford, CA, Jan. 22-24, 1985.

Gordon, R., Bender, R., and Herman, G. T., 1970, Algebraic reconstruction techniques (ART) for three-dimensional electron microscopy and X-ray photography: J. Theor. Biol., 29, 471-481.

Gradshteyn, I. S., Ryzhik, I. M., 1980, Table of integrals, series, and products: Academic Press, Inc.

Green, A. G., and Mair, J. A., 1983, Sub-horizontal fracture in a granitic pluton: Their detection and implications for radioactive waste disposal: Geophysics, 48, 1428-1499.

Frischknecht, F. C., 1987, Electromagnetic physical scale modeling, in Nabighian, M. N. Ed., Electromagnetic methods in applied geophysics - Theory: Investigations in geophysics No.3, Society of Exploration Geophysicists.

Hearst, J. R., and Nelson, P. H., 1985, Well logging for physical properties: R. R. Donnelley & Sons Company.

Hulen, J. B., 1982, Structure, stratigraphy, and permeability in the Redondo Creek project area, in Goldstein, N. E., Holman, W. R., and Molloy, M. W., eds., Final Report of the Department of Energy Reservoir Definition Review Team of the Baca Geothermal Demonstration Project: Lawrence Berkeley Laboratory Report LBL-14132, 7-14.

Herman, G. T., Lent, A., and Rowland, S. W., 1973, ART: Mathematics and applications: J. theor. Biol., 42, 1-32.

Hohmann, G. W., 1971, Electromagnetic scattering by conductors in the earth near a line source of current: Geophysics, 36, 101-131.

Hohmann, G. W., 1988, Numerical modeling for electromagnetic methods of geophysics, in Nabighian, M. N. Ed., Electromagnetic methods in applied geophysics - Theory: Investigations in geophysics No.3, Society of Exploration Geophysicists.

Hopper, M. J., 1979, HARWELL subroutine library - A catalogue of subroutines: AERE, Harwell, Didcot, Oxon, OX11 ORA, England.

Huesman, R. H., Gullberg, G. T., Greenberg, W. L., and Budinger, T. F., 1977, Users manual: Donner algorithms for reconstruction tomography: Lawrence Berkeley Laboratory, University of California, Report PUB- 214, 285p.

Jamtlid, A., Magnusson, K., Olsson, O., and Stenberg, L., 1984, Electrical borehole measurements for the mapping of fracture zones in crystalline rock: Geoexploration, 22, 203-216.

Johannsen, H. K. and K. Sorensen, 1979. Fast Hankel transforms. Geophysical Prospecting, 27, 876-901.

Johnson, S. A., and Tracy, M. L., 1983, Inverse scattering solutions by a sinc basis, multiple source, moment method -- Part I, theory: Ultrasonic Imaging, 5, 361-375.

Jones, J. W., Simpson, E. S., Neuman, S. P., and Keys, W. S., 1985, Field and theoretical investigations of fractured crystalline rock near Oraele, Arizona: Department of Hydrology and Water Resources, University of Arizona, NUREG/CR-3736, 104p.

Joshi, M. S., Gupta, O. P., and Negi, J. G., 1988, On the effects of thickness of the half-plane model in HLEM induction prospecting over sulphide dykes in a highly resistive medium: Geophysical Prospecting, 36, 551-558.

Katsube, T. J., and Hume, J. P., 1987, Permeability determination in crystalline rocks by standard geophysical logs: Geophysics, 52, 342-352.

Keller, J. B., 1969, Accuracy and validity of the Born and Rytov approximations: Journal of the Optical Society of America, 59, 1003- 1004.

Kostura, J. R., 1977, Fracture-controlled production: AAPG Reprint Series No. 21, Tulsa, 221p.

Lajoie, J. J. and West, G. F., 1976, Electromagnetic response of a conductive inhomogeneity in a layered earth: Geophysics, 41, 1133-1156.

Lawson, C. L. and Hanson, R. J., 1974, Solving least squares problems: Prentice-Hall, Chpt. 23.

Lee, K. H., Pridmore, D. F., and Morrison, H. F., 1981, A hybrid three-dimensional electromagnetic modeling scheme. Geophysics, 46, 796-805.

Lippmann, M. J., Goldstein, N. E., Halfman, S. E., and Witherspoon, P. A., 1984, Exploration and development of the Cerro Prieto geothermal field: J. Petro. Techn., 1579-1591.

Lo, T. W., Toksöz, M. N., Xu, S. H., and Wu, R. S., 1988, Ultrasonic laboratory tests of geophysical tomographic reconstruction, Geophysics, 53, 947-956.

Lytle, R. J., E. F. Laine, D. L. Lager, and D. T. Davis, 1979, Cross-borehole electromagnetic probing to locate high-contrast anomalies: Geophysics, 44, 1667-1676.

Macovski, A., 1983, Medical imaging systems: Prentice-Hall, Inc. Ch. 7.

Mair, J. A., and Green, A. C., 1981, High-resolution seismic reflection profiles reveal fracture zones within a "homogeneous" granite batholith: Nature, 294, 439-442.

Menke, William, 1984, Geophysical data analysis - Discrete inverse theory: Academic Press, Inc.

McCracken, K. G., Oristaglio, M. L., and Hohmann, G. W., 1986a, A comparison of electromagnetic exploration systems: Geophysics, 51, 810-818.

McCracken, K. G., Oristaglio, M. L., and Hohmann, G. W., 1986b, Minimization of noise in electromagnetic exploration systems: Geophysics, 51, 819-823.

Mersereau, R. M., and Oppenheim, A., 1974, Digital reconstruction of multidimensional signals from their projections: Proceedings of the IEEE, 62, 1319-1338.

Morse, P. M. and Feshbach, H., 1953, Methods of theoretical physics: McGraw-Hill, New York.

Mueller, R. K., Kaveh, M., and Iverson, R. D., 1978, A new approach to acoustic tomography using diffraction techniques: Acoustical Imaging, Plenum Press, New York, 8, 599-615.

Mueller, R. K., Kaveh, M., and Wade, G., 1979, Reconstructive tomography and applications to ultrasonics: Proceedings of the IEEE, 67, 567-587.

National Bureau of Standards, 1972, Handbook of mathematical functions with formulas, graphs, and mathematical tables: John Wiley & Sons, New York.

Nelson, P. H., Magnusson, K. A., and Rachiele, R., 1980, Application of bore hole geophysics at an experimental waste storage site: Lawrence Berkeley Laboratory, LBL-

11982/SAC-3a, 50p.

Nelson, Ronald A., 1985, Geologic analysis of naturally fractured reservoirs: Gulf Publishing Company, Houston.

Newman, G. A., Anderson, W. L., and Hohmann, G. W., 1989, Effect of conductive host rock on borehole transient electromagnetic responses: Geophysics, 54, 598-608.

Olsson, O., Black, J., Cosma, C., and Pihl, J., 1987, Crosshole investigations: Final report: Swedish Geological Co., Engineering Geology, Report ID-no. IRAP 87392.

Olsson, O., Duran, O., Jamtlid, A., and Stenberg, L., 1984, Geophysical investigations in Sweden for the characterization of a site for radioactive waste disposal- an overview: Geoexploration, 22, 187-201.

Oristaglio, M. L., 1985, Accuracy of the Born and Rytov approximations for reflection and refraction at a plane interface: Journal of Optical Society of America, 1987-1993.

Oristaglio, M. L. and Worthington, M. H., 1980, Inversion of surface and borehole electromagnetic data for two-dimensional conductivity models: Geophysical Prospecting, 28, 633-657.

Pai, David M. and Huang, Ming, 1988, A generalized Haskell matrix method for borehole electromagnetics - Theory and applications: Geophysics, 53, 1577-1586.

Paillet, F. L., 1981, A comparison of fracture characterization techniques applied to near-vertical fractures in a limestone reservoir: SPWLA 22nd Annual Logging Symposium. Paper XX.

Palmasson, G., 1976, Geophysical methods in geothermal exploration: Proc., 2nd U. N. Symposium on the Development and Use of Geothermal Resources, San Francisco, 2, 1175-1184.

Palmer, S. P., Smith, J. A., and Waters, K.H., 1981, fracture detection in crystalline rock using ultrasonic reflection techniques: Int. J. Rock Mech. and Min. Sci., 18, 403-414.

Parkhomenko, E. I., 1967, Electrical Properties of Rocks: Plenum Press, New York.

Peterson, J. E., 1986, The application of algebraic reconstruction techniques to geophysical problems: Ph.D. thesis, University of California. 188p.

Price, A. T., 1949, The induction of electric currents in non-uniform thin sheets and shells: Quart. Journ. Mech. and Applied Math., 2, 283-310.

Ramirez, A. L., and Lytle, R. L., 1983, Alterant geophysical tomography: IGRASS Vol.2, Paper FA2-9.

Slaney, M., and Kak, A. C., 1985, Imaging with diffraction tomography: School of Electrical Engineering, Purdue University, Report TR-EE 85- 5, 211p.

Soumekh, M., 1983, Inverse scattering with application to acoustic tomography: Ph.D. thesis, University of Minnesota. 140p.

Stark, Philip B., 1987, Strict bounds and applications: Proceedings of RCP 264 Recontre Interdisciplinaire Problemes Inverses Montpellier, France.

Stearns, D. W., and Friedman, M., 1972, Reservoirs in fractured rock, in Stratigraphic oil and gas fields: AAPG Memoir 16, Tulsa, 82-106.

Stinson, Donald C., 1976, Intermediate mathematics of electromagnetics: Prentice-Hall, Inc., Englewood Cliffs, NJ.

Suau, J., and Gartner, J., 1980, Fracture detection from well logs: The log analyst, 21, 3-13.

Tai, Chen-To, 1971, Dyadic Green's functions in electromagnetic theory: INTEXT Educational Publishers.

Treitel, S. and Lines, L., 1988, Geophysical examples of inversion: Geophysics: The leading edge of exploration, 7, No. 11, 32-35.

Van Golf-Racht, T. D., 1982, Fundamentals of fractured reservoir engineering: Elsevier Scientific Publishing Company.

Vogelsang, D., 1987, Examples of electromagnetic prospecting for karst and fault systems: Geophysical Prospecting, 35, 282-291.

Wait, J. R., and Hill, D. A., 1980, Fields of a horizontal loop of arbitrary shape buried in a two-layer earth: Radio Science, 15, 903-912.

Wang, J., Hurley P. and West G. F., 1983, Crosshole seismology and seismic imaging in crystalline rocks: Geophysical research letters, 10, 686-689.

Wannamaker, Philip E., Hohmann, Gerald W., and SanFilipo, William A., 1984, Electromagnetic modeling of three-dimensional bodies in layered earths using integral equations; Geophysics, 49, 60-74.

Ward, S. H., and Hohmann, G. W., 1988, Electromagnetic theory for geophysical applications, in Nabighian, M. N. Ed., Electromagnetic methods in applied geophysics - Theory: Investigations in geophysics No.3, Society of Exploration Geophysicists.

Weidelt, P., 1981, Report on dipole induction by a thin plate in a

Supplement
List of the developed FORTRAN codes

A list of the developed numerical codes are provided here. The details of the input parameters and output results are given in each program.

(1) Program 'TWODSH' calculates the frequency domain electromagnetic response of thin conductors in a two-dimensional Cartesian coordinates by an integral equation approach. The targets are located in a homogeneous conductive whole space. Electrical line source is used. The output is the secondary electrical field.

(2) Program 'TAHDCY' simulates the frequency domain electromagnetic response of a cylindrical symmetry medium. The target is located in a homogeneous conductive whole space. VMD source is along the axis of symmetry which is also the z-axis. The magnetic anomaly is solved by an integral equation approach.

(3) Program 'SHEETS' calculates the electromagnetic response from multiple tabular conductors. The conductive targets are located in a homogeneous conductive half space with overburden on top of it. An integral equation approach is used in solving the magnetic anomaly excited by magnetic dipole source.

(4) Program 'EMTOMO' computes the conductivity distribution of a two-dimensional medium under Born approximation. The target is assumed to be located in a homogeneous conductive whole space (2-D). Electrical line sources are used and the input is the secondary electrical field. With an additional far-field approximation, this program can be used to compute the conductivity images of 2-D cylindrical symmetry or 3-D situations with VMD dipole source excitation and the secondary magnetic field as input data.

(5) Program 'TOMO2H' computes the conductivity distribution of a cylindrical symmetry medium under Born approximation. The target is located in a homogeneous conductive whole space. Vertical magnetic dipole sources are along the axis of symmetry while the secondary magnetic field is measured in another borehole or in the same one.

LAWRENCE BERKELEY LABORATORY
TECHNICAL INFORMATION DEPARTMENT
1 CYCLOTRON ROAD
BERKELEY, CALIFORNIA 94720